Thèse

présentée à

L'Université des Sciences et Technologies de Lille

Ecole Doctorale des Sciences de la Matière,
du Rayonnement et de l'Environnement

- U.F.R. de Chimie -

pour obtenir le grade de

Docteur

Discipline: Molécules et Matière Condensée

par

Nina Forler

A Multinuclear Solid-State NMR Approach to the Weathering of Model Phosphate Glasses.

Soutenue le 25 janvier 2011

Membres du Jury

Dr. J.-J. Videau	ICMCB, Université de Bordeaux 1	Rapporteur
Dr. F. Angeli	CEA, Marcoule	Rapporteur
Prof. G. Silly	ICG, Université Montpellier 2	Examinateur
Prof. L. Montagne	UCCS, Université Lille 1	Directeur de thèse
Dr. L. Delevoye	UCCS, Université de Lille 1	Co-Directeur de thèse

The present manuscript focuses on the investigation of phosphate glass weathering by multinuclear solid-state magnetic resonance. Weathering, that is aqueous attack and aging of the phosphate glass under humid atmosphere, becomes important in application domains where high resistance against aqueous attack is an essential property. In particular, this is the case for phosphate glass matrices for the immobilization of nuclear waste.

In the frame of this work, binary (Na_2O-P_2O_5) and ternary (Na_2O-Al_2O_3-P_2O_5) model glass systems are considered. The aim is to obtain further insight into fundamental processes and structural changes that are taking place upon weathering attack on the glass.
Solid-state nuclear magnetic resonance is used as the main tool for structural characterization. ^{1}H, ^{27}Al, ^{31}P and ^{17}O are employed as probe nuclei. A number of one- and two-dimensional techniques allows for insight into the glass structure on the low and intermediate range.

The interpretation of ^{17}O NMR data is accompanied by a complementary approach. Therefore, the reliability of calculated ^{17}O NMR parameters of *protonated* crystalline phosphate phases has been validated for the first time. Relationships between ^{17}O NMR parameters and the structural environment of the nucleus could be drawn.
Those relationships prove to be helpful for the characterization of oxygen environments emerging in weathered $NaPO_3$ glass based on the chemical shift (δ_{CS}, δ_{iso}) and the quadrupolar parameters (C_Q, η_Q).

Keywords: Phosphate glass weathering; nuclear magnetic resonance; ^{17}O

Thèse

présentée à

L'Université des Sciences et Technologies de Lille

Ecole Doctorale des Sciences de la Matière,
du Rayonnement et de l'Environnement

- U.F.R. de Chimie -

pour obtenir le grade de

Docteur

Discipline: Molécules et Matière Condensée

par

Nina Forler

Etude multinucléaire du vieillissement des verres de phosphate modèles sous atmosphère humide

Soutenue le 25 janvier 2011

Membres du Jury

Dr. J.-J. Videau	ICMCB, Université de Bordeaux 1	Rapporteur
Dr. F. Angeli	CEA, Marcoule	Rapporteur
Prof. G. Silly	ICG, Université Montpellier 2	Examinateur
Prof. L. Montagne	UCCS, Université Lille 1	Directeur de thèse
Dr. L. Delevoye	UCCS, Université de Lille 1	Co-Directeur de thèse

Les travaux de cette these portent sur la compréhension du processus du vieillissement des verres de phosphate à la base des études de résonance magnétique nucléaire (RMN) des solides.
Le terme vieillissement se traduit dans ce cas par l'attaque aqueuse du verre sous atmosphère humide. Ce processus est d'un intérêt particulier dans tous les domaines où une haute résistance des verres de phosphate contre cette attaque constitue une propriété essentielle. Notamment c'est le cas pour la vitrification des déchets nucléaires.

Dans le cadre de cette étude des systèmes modèles ont été étudiés (Na_2O-P_2O_5 et Na_2O-Al_2O_3-P_2O_5) pour connaître les changements structuraux qui ont lieu pendant l'attaque aqueuse sous atmosphère humide.
La résonance magnétique multinucléaire des solides (^{1}H, ^{27}Al, ^{31}P et ^{17}O) étant l'outil principal, des expériences en 1D et en 2D permettent de caractériser l'environnement proche des noyaux ainsi que leur environnement intermédiaire (connectivité hétéro- et homonucléaire).

L'interprétation des données RMN de l'oxygène-17 est accompagnée d'une approche complémentaire. Des paramètres RMN calculés de l'oxygène-17 (DFT / GIPAW) des hydrogénophosphates crystallines ont été vérifiés et validés expérimentalement.
Des corrélations entre les paramètres RMN de l'oxygène-17 (δ_{CS}, δiso, C_Q, η_Q) et l'environnement structural du noyau ont été obtenues. Ces dernières permettent de caractériser les environnements du noyau oxygène-17 qui sont générés pendant le vieillissement d'un verre Na_2O-P_2O_5 ($NaPO_3$).

TABLE OF CONTENTS

CHAPTER 3

New insights into ^{17}O environments generated during phosphate glass alteration: A combined ^{17}O NMR and first principles calculations study

CHAPTER 4

The weathering of a binary model phosphate glass ($NaPO_3$) investigated by solid-state NMR

CHAPTER 5

Structure and weathering of a ternary model phosphate glass (x Al_2O3 – (100-x) $NaPO_3$) investigated by solid-state NMR

Ce travail de thèse a été effectué au sein de l'Unité de Catalyse et de Chimie du Solide (UCCS, UMR CNRS 8181) de l'Université des Sciences et Technologies de Lille (Université Lille 1). Il a été financé par le Ministère de l'Education et de l'Enseignement Supérieur.

Je tiens à remercier à mon directeur de thèse, le Professeur Lionel Montagne, de m'avoir accueillie au sein de l'UCCS. Je voudrais lui ainsi que mon co-directeur de thèse, Dr. Laurent Delevoye, remercier sincèrement pour la formation scientifique et pédagogique que j'ai reçue au cours de mes trois années au sein de l'équipe verres et RMN. Je les prie de bien vouloir trouver ici l'expression de mon plus grand respect.
Egalement, je tiens à remercier Dr. Grégory Tricot pour l'intérêt qu'il a porté à mes travaux, pour des discussions intéressantes et pour sa pugnacité quant aux aluminophosphates.
Je remercie les rapporteurs de ce manuscrit, Dr. Frédéric Angeli et Dr. Jean-Jacques Videau, et le président du jury, Prof. Gilles Silly, pour avoir accepté d'y participer et juger ce travail.

Je tiens aussi à remercier Dr. Sylvain Cristol et Dr. Filipe Vasconcelos pour leur apport à ce travail au long des trois années. Sans leur coopération et leur motivation, la réalisation de certaines parties de ce projet basé sur deux axes n'aurait pas été possible.

Je voudrais remercier Véronique Alaimo, Laurence Burylo et Nora Djelal pour les manipulations au sein de l'équipe verres, pour les analyses de diffraction rayon X sur poudre et pour les analyses thermiques. Ici aussi un grand merci à Jérémy Maton, toujours bien patient et souriant, pour ses nombreux « services » quand l'opératrice n'était plus compatible avec son matériel informatique. Merci à Nico Renaud et à Edouard Capoen pour leur support technique. Edouard, tu restes un phénomène, toujours capable de trouver tout à un certain endroit du labo! ☺ Je tiens à remercier Claudine Devynck et Nathalie, toujours gentilles, pour les nombreux services qu'elles m'ont rendus tout au long de ma thèse.

Egalement je tiens à remercier aux gens « logés » au bâtiment C4. Les RMNistes Bertrand Revel, Pierre Watkin et Marc Bria pour leur patience et pour tous les services et tout le support technique. Je voudrais aussi remercier à Hervé Vezin, l'homme habillé tout en noir (sans oublier les chaussures !)☺, et à Nadja. Merci pour les cafés nespresso et l'aide de récupération des bouchons rotors 4mm dans le siphon des toilettes de femmes !
J'aimerais aussi remercier sincèrement à Julien Trebosc pour son aide au « 800 », ses explications, sa patience (même quand la grippe était en train de « monter » et la climatisation rendait tout pire …) et l'enthousiasme avec lequel il m'a introduite dans l'équipement.

En fin de cette page, je tiens à remercier la Professeur Rose-Noëlle Vannier et Dr. Caroline Pirovano qui m'ont accueillie dans ce labo pendant mon stage ERASMUS en 2005. Merci encore une fois à vous deux pour l'accueil chaleureux que vous m'aviez fait et merci pour votre encadrement !

Au cours de mes trois années de thèse, j'ai eu de nombreux « colocataires » de bureau auxquels j'aimerais remercier pour l'amusement, les petites pauses de recréation, les sorties, les discussions et leur soutien ! Merci à « l'équipe actuelle », Prashant, Sandra, Thomas, Aline et Kuldeep. Merci aussi à Daniel qui était dans mon dos pendant tout le temps de ma thèse : Merci, Danxel, pour les conversations super-intéressantes après 19h00. Je n'oublierai jamais Petit Poney. … Merci également à son encadrant François Méar pour le « second dégrée » ! Ici, finalement, je peux avouer que j'aurais aussi choisi une Mini, si j'avais eu les moyens ☺. Je vous souhaite tous une Bonne Continuation !

Egalement, je tiens à remercier aux doctorants (et aux post-doctorants !) « logés » au deuxième étage. Merci pour le café l'après-midi, merci pour les blagues, merci pour l'humour. J'ai trop apprécié les nombreux tests de WELSH sur Lille (qui est l'inventeur de cet excès merveilleux de Cheddar ?). Par contre, j'ai pas du tout apprécié vos efforts de me faire aimer les pâtes du RU Pariselle (ce n'était pas une réussite … ☺), mais je les ai survécus.

Merci à Hend (Hendbook ☺), merci à Arvind (Ananthanarayanan, dit Anananananthanarayayayayayan-anan ☺), merci à Sandra pour Flandres en été et en hiver! Merci Véro, merci Aline : désolée que l'angine était plus en forme que moi quand on voulait profiter des soldes – on les fera, promis! Un énorme merci à AnaGil et à Diana pour leur soutien lors de l'organisation de ma thèse. Merci à Ana pour son enthousiasme d'organisation (les tomates …) et son hospitalité, merci à Diana (et Andres) pour sa (leur) patience et sa pugnacité lors de la préparation des dernières choses! Merci pour les nombreuses soirées et week-end après-midis, également ! Vous allez tant me manquer !
Merci à Nicolas (celui qui s'appelle Nicolassss) pour tous les dessins. J'ai particulièrement apprécié l'autobus (2009) et le bateau avec la tortue qui reçoit un cadeau (2011) et je les garderai, c'est sûr !!!

Merci aussi à Kirsten, Stefan, Esma, Fabian, Martin, Claudia, Axel, Roman. Stefan : réussite ! Parfois j'ai failli mourir de rire ! Martin : Merci pour tous les articles et toutes les discussions ☺ Axel, Roman : Merci pour les séances parfaites de Sushi ! Claudia : Merci pour la maîtrise parfaite de la préparation de presque tous les plats. Merci également pour de nombreuses discussions, des super-soirées, des fêtes. Merci de m'avoir donné l'occasion de peintre une cuisine entière tout en vert foncé ! Kirsten : Merci de toujours être prête à prêter un cheval pour brosser pendant une heure (ou plus ☺), tout ça accompagné d'un bon discours. Egalement merci pour tous les bons temps à Kaiserslautern !
Merci aussi à Nina (W.) : Style, l'Alfa ! ☺ Reste comme ça !
Merci à un certain P.R. (aus S. bei L. ☺) pour sa pugnacité. Ainsi j'ai eu l'occasion de vérifier que je suis capable de grimper de Villa Ludwigshöhe à Rietburg en pleine nuit sans connaître la route en pleines conditions hivernales en 33 minutes (23h26 – 23h59 - qqn d'autre qui était plus vite ?) ☺ Merci aussi pour m'avoir fait faillir de mourir de rire à de nombreuses occasions – comme ça, c'est o.k. pour les coups de fil en pleine nuit.

Finalement, je remercie affectueusement mes parents pour tout leur soutien tout au long de ma formation !
Un énorme merci aussi à mon grand-père !

Villeneuve d'Ascq, le 16 mars 2011

General Introduction

The electronic configuration of phosphorus does not allow for the same degree of P_2O_5 network polymerization as it is the case for silicium and SiO_2 networks. The fifth electron being promoted into a π-orbital, each PO_4^{3-} structural unit possesses one formal double bond and, in consequence, at least one non-bridging oxygen. This, in turn, influences the stability of the P-O-P bonds in phosphate networks. It is weaker (90 kcal mol^{-1}) than the Si-O-Si bond (110 kcal mol^{-1}) in silicate networks. As a result, P_2O_5 networks and phosphate glasses show more rapid degradation upon exposure to aqueous environments compared to their silicate counterparts. In addition, they are generally less hard, show lower T_g and soften at a lower temperature than comparable silicate glasses.

Nevertheless, phosphate glasses are of great interest, since in many domains, their highly varying chemical durability is a key property. It can vary over several orders of magnitude, depending on the nature and the extent of additional network forming or modifying oxides in the compound. Hence, a given phosphate glass may be easily soluble or extremely durable based upon its individual composition that has been adapted to its field of application.

As an example, glassy $NaPO_3$ dissolves rapidly in aqueous solutions. It is used as a sequestrant for boiler water and industrial cooling cycles and as the food additive E521i (www.reading.ac.uk). For several years, it has been the main constituent of commercially available water softening agents such as Calgon® (vanWazer1950). Controlled complete dissolution is also one of the key properties of phosphate glass fertilizers, e.g. AVA™® (www.agrovit.org). Granular pellets of varying composition range have been established as environmentally friendly fertilizer compounds of prolonged action. By varying their chemical composition, release and dissolution rates can be adapted to suit individual geographical conditions (Karapetyan2002). Controlled degradation of phosphate glass composites is also promising for biomedical applications. They are employed in the field of tissue engineering for hard tissue surgery, for neural repair or for oral healthcare (Knowles2003). In addition, their controlled dissolution rates have made them good candidates for drug delivery systems and bacterial control devices (Gilchrist1991).

Contrarily, high chemical durability is a key property of the phosphate glasses used in the domain of optical applications. As an example, as laser host matrices they need to be resistant against damage from high optical powers and stable in various environmental conditions (Schülzgen2008). Interest in chemically inert phosphate glass systems for the immobilization of high-level nuclear waste has developed over several decades (Tuthill 1967). This interest is motivated by phosphate glasses exhibiting lower aqueous corrosion rates combined with lower processing temperatures and reduced melt viscosities than comparable borosilicate glasses. Moreover, they can be loaded with higher concentrations of elements such as sulfur. Sodium aluminophosphate glass,

iron aluminum phosphate glass and iron phosphate glass (Sales 1984; Boatner1989; Ewing2002; Kim2003) are promising amorphous waste immobilization matrices. At Mayak (Urals, Russia), approximately 1000 m^3 of nuclear waste have been immobilized in a phosphate glass (Kushnikov1995). Vitrification using a sodium aluminum phosphate glass continues even today at the Mayak Production Association in Chelyabinsk (Ewing2002).

The examples presented above illustrate that the chemical durability and the degradation of phosphate glass systems are of considerable environmental, technological and scientific interest. Therefore, this dissertation presents studies of the *weathering* of model phosphate glasses. In the frame of this thesis, the term weathering is used as a synonym for degradation of the material in an atmosphere saturated with water vapor. Reproducible experimental weathering assays have been developed with the aim to create environmental conditions that can be found in several application domains. As an example, weathering is of particular interest in the case of fertilizers, optical devices or for the immobilization of nuclear waste. The systematic weathering studies of phosphate glasses stand in contrast to previously reported ones where phosphate glass degradation was investigated mainly in solution or where weathering conditions were not reported to be reproducible (Wenslow1998, Alam2005). In addition, most of the phosphate glass alteration studies focused on the parameters affecting the hydrolysis rates and not on a mechanistic and structural understanding of the degradation process.

Two model glass systems shall be considered: $NaPO_3$ and x Al_2O_3 - (100-x) $NaPO_3$.

$NaPO_3$, sodium "metaphosphate", is a binary phosphate glass built up from long chains of phosphate tetrahedra. Sodium modifier cations compensate the formally negative charges at the non-bridging oxygen sites of the phosphate tetrahedra. $NaPO_3$ has been chosen for its simple structure that has been reported in the literature (vanWazer1950) and characterized by multinuclear solid-state NMR methods (Brow1991, Alam2005). Moreover, it has been used as a model glass system for aqueous attack in previous studies (Alam2001, Wenslow1998). 1D ^{1}H and ^{31}P MAS NMR experiments were performed together with 2D ^{1}H-^{31}P heteronuclear correlation techniques to resolve sites and to elaborate model mechanisms for aqueous attack. However, none of these studies employed $NaPO_3$ glass systems that were submitted to reproducible weathering conditions. Moreover, ^{17}O, the nucleus that is present at the sites of structural changes, has not been studied, so far.

x Al_2O_3 - (100-x) $NaPO_3$ is a ternary model system that has been chosen with regard to applications in the domain of nuclear waste immobilization. As well as a Fe_2O_3 phosphate glasses, it exhibits superior chemical durability that is attributed to increased network reticulation. However, Fe_2O_3 containing phosphate glasses are not particularly suited to NMR studies owing to the paramagnetic nature of iron. Considering our focus on NMR investigations, the ternary model glasses have been prepared with Al_2O_3 incorporation. Of particular interest in this case are the reticulation of the aluminophosphate network and the coordination states of aluminum during weathering. The various types of connectivity between aluminate and PO_4^{3-} polyhedra demand the characterization of the glass structure on the intermediate length scale. The different coordination states of aluminum reach from tetrahedral network forming aluminum to octahedral network modifying aluminum. (-OP) bonds may be coordinated as well as hydroxyl (-OH) groups or entire water molecules to the central aluminum. Yet, the role of aluminum in phosphate glass fortification and its evolution in the weathering phosphate glass system is not yet completely understood.

Solid-state NMR is a powerful probe to detect local structural changes that take place at the different sites of a nucleus in a weathering glass. Hence, it complements diffraction techniques: It provides short range information without requiring for any periodic long range organization and it probes crystalline and amorphous phases simultaneously and quantitatively.

NMR being an element-specific probe under constant development, further insight can be gleaned using a number of modern techniques that enable the recording of high resolution spectra of quadrupolar nuclei, mapping of homo- and heteronuclear correlations and the probing of spatial proximities between the observed nuclei. Hence, the scope of solid-state NMR is nowadays extended on the intermediate range to probe connectivity and network reticulation in a glass and its evolution due to weathering. Results can be combined to provide a comprehensive picture of the incorporation of water and of the network evolution in the glass system throughout the weathering process.

The degradation of the two model glass systems is mainly studied by ^{31}P, ^{1}H and ^{27}Al NMR. Due to their relatively high natural abundance and magnetogyric ratios, quantitative 1D one pulse spectra of these nuclei can be obtained within a short timescale, usually reaching from several minutes to several hours. In some cases, ^{17}O, a low abundant probe nucleus with low magnetogyric ratio, is employed as an isotopic probe. This allows for studying oxygen environments that are generated by weathering the glass under $H_2{}^{17}O$ water vapor, selectively.

During the last decade, interest in the combination of first-principles calculations with NMR has been growing constantly. Especially for nuclei such as ^{17}O, a key nucleus in materials chemistry, spectral analysis and the extraction of accurate shielding and quadrupolar parameters are still challenging in MQMAS spectra. This is mainly due to the poor signal-to-noise ratio, even in spectra of ^{17}O-enriched samples.

The gauge including projector augmented planewave (GIPAW) formalism allows for sufficiently rapid calculation of shielding and quadrupolar tensors. Thus, experimental NMR data can be complemented, their assignment can be rendered unambiguous (Ashbrook2007) or the costly experiment can be replaced fully. Periodic as well as non-periodic systems are accessible by this simulation approach and thus it is attractive for crystalline systems as well as for glasses. Preliminary to the simulation of NMR parameters, the electronic structure of the real system is described by means of density functional theory (DFT), where optimization of the exact geometry of the studied system can be challenging.

With regard to the interest of phosphate glasses in our group, this combined methodology has been elaborated for a series of non-protonated crystalline sodium phosphate (reference) phases (Vasconcelos2008). In the context of the NMR weathering studies, it was desirable to develop a robust calculation protocol for hydrogen sodium phosphate phases. So far, the present study is the first to combine high-resolution ^{17}O NMR with simulation of the corresponding NMR parameters for *hydrogen* phosphate phases (Forler2010). Even for silicate systems, studies of hydrous phases have only been reported recently for a first time (Griffin2009).

The calculation approach for sodium hydrogen phosphates could be validated, though the exact DFT based geometry optimization of hydrogen containing phases is a difficult task with regard to the precision of neutron- or X-ray diffraction reference data. Focusing on ^{17}O, systematic relationships between different structural environments and simulated solid-state NMR data have been established. The latter built a basis for the interpretation of ^{17}O NMR studies of weathered phosphate glasses (Chapter4; *Fig.I.1*).

To conclude, the aim of this thesis is to obtain insights into the structural changes taking place during weathering of phosphate glasses using modern multinuclear solid-state NMR techniques. Therefore, reproducible weathering assays have been put into practice, recent methodologic approaches have been extended and systematic NMR analysis protocols have been established. Based on our NMR results, we achieve a further understanding of certain mechanistic details.

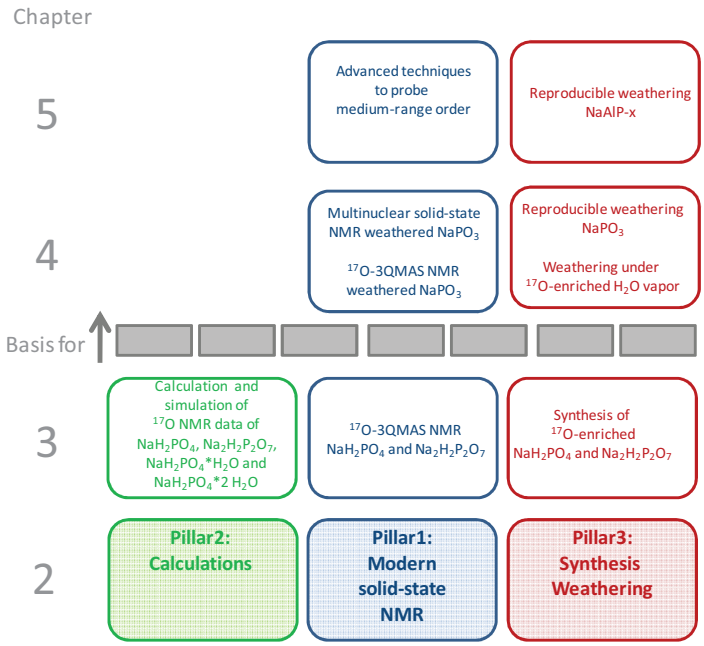

Fig. I.1:
Flowchart that illustrates the combined methodology used in this work.

The present thesis comprises five chapters.

Chapter 1 presents an introduction into phosphate glasses and considers their applications. A review of the literature is presented, with emphasis on chemical durability and the ramification of this for various applications. Particular attention is paid to the structure of ternary aluminophosphate glass systems and the studies of degradation of phosphate glasses exposed to weathering attack.

Chapter 2 is dedicated to the experimental procedures and analysis techniques employed in the frame of this thesis. It consists of two parts. In the first part, the NMR techniques used for the investigation of phosphate glass weathering will be presented. A summary of the calculation approach applied to NMR parameters of crystalline hydrogen phosphates will be given. In the second part of Chapter 2, exprimental protocols of microsynthesis of ^{17}O-enriched, phase pure sodium hydrogen phosphates are presented. The preparation of the binary and ternary model glasses will be described, followed by an elaboration of the weathering conditions for the glasses.

Chapter 3 focuses on the combination of first-principles calculation with solid-state NMR, emphasis lying on ^{17}O. High resolution NMR of ^{17}O-enriched phase-pure sodium hydrogen phosphate phases will be presented together with a complementary first-principles calculation approach. DFT calculations allow for structural optimization that is followed by simulation of the NMR spectra based on GIPAW-calculated NMR parameters. The NMR results are used to validate the calculation approach on hydrogen containing crystalline sodium phosphate phases. Notably, the quadrupolar nature of ^{17}O shall be exploited to obtain an understanding of the relationships between the symmetry and the chemical composition of its proximate surroundings and its NMR parameters.

Chapter 4 presents studies on the weathering of sodium metaphosphate glass, $NaPO_3$. The modification of the glass structure is investigated by multinuclear NMR techniques using nuclei such as ^{1}H, ^{31}P and ^{17}O. Based upon the evolution of structural units in the glass with weathering time, it has been attempted to achieve an initial understanding of the nature of water vapor attack. The aim is to investigate whether mechanistic scenarios presented in the literature (Brow1990, Wenslow1998) are valid and whether preferred sites of attack exist. In particular, ^{17}O NMR is used to monitor the changes in the oxygen environment.

In Chapter 5 we extend our analysis to the ternary model system Na_2O-Al_2O_3-P_2O_5. In such systems, an understanding of the role played by Al_2O_3 during weathering is not available in the literature. Hence, in a first approach, the evolution of the glass network structure is monitored by multinuclear solid-state NMR. The techniques used in this chapter are based on ^{1}H, ^{31}P and ^{27}Al NMR. As an example, REDOR experiments are performed in order to achieve a further insight into the underlying mechanisms, e.g. sites of water and proton incorporations.

This opening chapter constitutes the basis for further NMR investigation strategies of ternary glass systems.

Bibliography General Introduction

Alam2005
Alam, T.M., Tischendorf, B.C., Brow, R.K.
Solid State Nuclear Magnetic Resonance (2005), **27 (1-2),** 99-111

Ashbrook2007
Ashbrook, S.E., Le Pollès, L., Pickard, C.J., Berry, A.J., Wimperis, S., Farnan, I.
Physical Chemistry Chemical Physics (2007), **9**, 1587-1598

Boatner1989
Boatner, L.A., Sales, B.C.
U.S. patent no 4,847,008 (1989)

Ewing2002
Ewing, R.C. and Wang, L.
Reviews in Mineralogy and Geochemistry (2002), 48

Forler2010
Forler, N., Vasconcelos, F., Cristol, S., Paul, J.-F., Montagne, L., Charpentier, T., Mauri, F., Delevoye, L.
Phys. Chem. Chem. Phys. (2010), **12**, 9053-9062

Gilchrist1991
Gilchrist, T., Healy, D.M., Drake, C.
Biomaterials (1991), **12**, 76-78

Griffin2009
Griffin, J.M., Wimperis, S., Berry, A.J., Pickard, C.J., Ashbrook, S.E.
J. Phys. Chem. C (2009), **113**, 465-471

Karapetyan2002
Karapetyan, G., Karapetyan, K., Maksimov, L.
Proceedings of IMPHOS, Jena (Germany), July 10-13 2002

Kim2003
Kim, C.W., Ray, C.S., Zhu, D., Day, D.E., Gombert, D., Aloy, A., Mogus-Milankovich, A., Karabulut, M.
Journal of Nuclear Materials (2003) **322**, 152-164.

Knowles2003
Knowles, J.C.
J. Mater. Chem. (2003), 13, 2395-2401.

Kushnikov1995
Kushnikov, V.V., Mayunin, Y.I., Smelova, T.V., Demin, A.V.
Materials Research Society Symposium Proceedings (1997) **465**, 55

Sales1984a
Sales, B.C., Boatner, L.A.
Science (1984) **226 (4670)**, 45-48.

Schülzgen2008
Schülzgen, A., Li, L., Zhu, X., Suzuki, S., Temyanko, V.L., Albert, J., Peyghambarian, N.
Materials Research Society Symposium Proceedings, (2008) **1076**, 65-73

Tuthill1967
Tuthill, E.J., Weth, G.G., Emma, L.C., Strickland, G., Hatch, L.P.
Ind. Eng. Chem.: Process Design and Development (1967) **6 (3)**, 314-321

vanWazer1950
Van Wazer
J. Amer. Chem. Soc. (1950), 72, 644-647

Vasconcelos2008
Vasconcelos, F., Cristol, S., Paul, J.-F., Tricot, G., Amoureux, J.-P., Montagne, L., Mauri, F., Delevoye, L.
Inorg. Chem. (2008), 47 (16), 7327-7337

Wenslow1998
Wenslow, R.M., Mueller, K.T.;
Journal of Physical Chemistry B (1998) **102 (45)**, 9033

(www.agrovit.org)
www.agrovit.org/en/production

(www.reading.ac.uk)
www.reading.ac.uk/foodlaw/additive.htm

Chapter 1

Introduction to the subject

CHAPTER 1

Introduction to the subject

The present chapter shall introduce to the subject of this thesis:

Structural and mechanistic studies on the weathering of binary and ternary model phosphate glass systems with regard to their future implication as nuclear waste hosts.

Therefore, the first part of this chapter will give an introduction into the basic built-up principles of phosphate glass networks.

In the second part of the present chapter, an overview of the main application domains of phosphate glasses shall be given. A number of examples from the literature shall outline that phosphate glasses possess unique properties that render them attractive for numerous applications in industries, in medicine, in optics and electronics and many other domains. The immobilization of nuclear waste will be considered as the final point, pointing towards NMR studies on model phosphate glass systems that exhibit high chemical durability in the following section.

With regard to the future development of highly durable phosphate glasses, the structure and the weathering shall be studied on an atomic scale level. The few works on this subject that have been published in the literature shall be summarized in the two last paragraphs. In Section 1.3, the structure of ternary aluminophosphate glass systems shall be considered, in Section 1.4, NMR studies on the structural changes and mechanistic aspects of phosphate glass weathering shall be summarized.

1.1 Structure of phosphates and phosphate glasses

1.1.1 The glassy state

In the following, an introduction to the basic structural principles of phosphate compounds is presented. Those principles and the nomenclature are valid for crystalline phosphates and phosphate glasses. In the frame of this thesis, emphasis lies on phosphate glasses. Therefore, the main characteristics of the glassy state that are important in the frame of the following studies shall be recapitulated for oxide glasses (Doremus1994).

- A glass is a supercooled liquid, a frozen in state of an oxide melt.
- A glass does not show any long range order.
- A glass shows distributions of bond lengths and angles.

Contrarily, these parameters are periodically repeated with exactitude in crystalline compounds.

Tab. 1.1 gives an overview about the ranges of structural order in a glass.

The short range structure (I; *Tab. 1.1*) includes the first coordination spheres of the glass-constituting atoms: its chemical composition, local bond lengths and angles towards neighbors. In most cases, analogies between the first coordination spheres of glasses and crystal compounds of identical composition can be drawn. By taking into account the crystalline reference data, the immediate environment of nuclei in glassy structures can be elucidated.

Intermediate (II and III; *Tab. 1.1*) and long range structure concerns connectivity, that is how the basic building units are linked together to form large macroscopic networks.

Tab. 1.1:
Overview about the ranges of structural order in a glass (from Doremus1994).

	Name	Features	Characterization parameters
I	Short range order	Central atom and its next nearest neighbors	Coordination number, bond length, bond angles
II	Interconnections of adjacent units	Packing of 1 units around central unit	Connection mode, connectivity
III	Intermediate	Ordered arrangements several atom distances from a central atom	Small clusters of structural units (plains and chains and their dimensions)
IV	Long range	Density and compositional fluctuations	Size and composition fluctuations.

1.1.2 Basic structural unit

In crystalline and amorphous phosphate phases, the basic structural units are PO_4^{3-} tetrahedra. The electronic configuration of phosphorus

$$[Ne]\ 3s^2\ 3p^3$$

results in the formation of four $3sp^3$ hybrid orbitals that undergo covalent P-O bonds with oxygen. The fifth valence electron is promoted into a 3d orbital.

The phosphate tetrahedra link through bridging oxygens (P-O-P linkages) to form various phosphate anions. The maximum number of bridging oxygens (BO) in each phosphate unit is three, since the fifth valence electron in the 3d orbital requires to undergo one formal π bond with oxygen. In pure P_2O_5, this π bond is localized to form a P=O double bond in each structural unit. However, it can be partly delocalized, if phosphate units possess more than one non-bridging oxygen (NBO). This case is represented by the dashed lines in *Fig. 1.1*. The more localized the double bond is, the weaker the remaining P-O single bonds are. Hence, Q^3 units possess the weakest P-O bonds, Q^0 tetrahedra the strongest ones.

1.1.3 Network polymerization and nomenclature

The tetrahedral units in phosphate networks are classified using the Q^n terminology where *n* denotes the number of P-O-P linkages per tetrahedron (*Fig. 1.1*). In mixed networks, the Q^n_m notation is employed, *m* denoting the number of connected atoms of the additional network former (e.g. Q^0_4 in $AlPO_4$). This notation has been extended by van Wüllen *et al.* for aluminophosphate networks (vanWüllen2007) by specifying the nature of aluminum coordination: $Q^n_{m,AlOx}$.

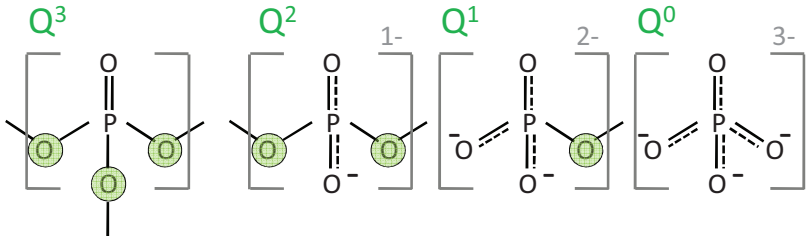

Fig. 1.1:
Phosphate tetrahedra are the basic structural units phosphate networks are built up from. The Q^n notation allows for their characterization. The superscript n denotes the number of bridging oxygens (green) in each tetrahedron.

It is common to classify phosphate networks based on their degree of P-O-P network polymerization. The latter depends on the oxygen-to-phosphorous-ratio, [O]/[P]. [O]/[P] determines the average number of bridging oxygens in each tetrahedron and hence the dominating Q^n species. The different types of phosphate glass networks are illustrated in *Fig. 1.2*.

Ultraphosphates show an [O]/[P] ratio < 3.0. They consist mainly of Q^3 ([O]/[P]→ 2.5) and Q^2 ([O]/[P]→3.0) units.

The oxygen-to-phosphorus ratio in metaphosphate glasses is 3.0. Ideally, their structure is built up from Q^2 phosphate chains of infinite length.

In polyphosphate glasses, [O]/[P] is higher than 3.0, resulting in decreasing Q^2 chain lengths and an increasing fraction of Q^1 structural units.

In the case of pyrophosphates, the oxygen-to-phosphorus ratio is 3.5. Pyrophosphates are built up from dimeric Q^1 units.

Orthophosphates exhibit an [O]/[P] ratio of 4,0 and consist of isolated PO_4^{3-} tetrahedra.

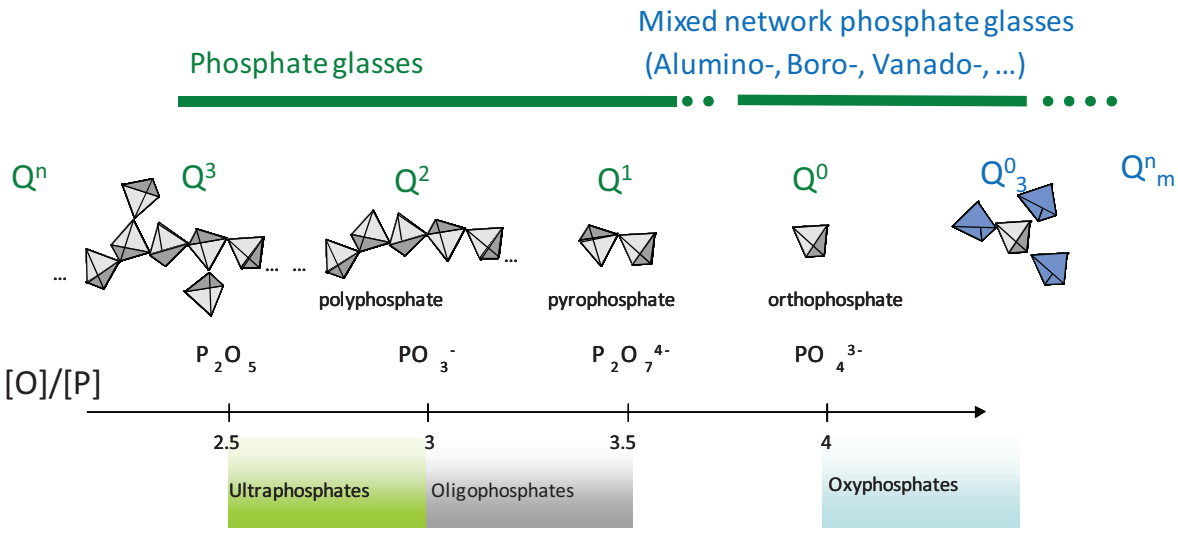

Figure 1.2:

The different degrees of condensation in M_xO_y-P_2O_5 phosphates versus the [O]/[P] ratio, and the corresponding Q^n notation. In addition, an example of the Q^n_m notation is given.

Variations in the [O]/[P] ratio are achieved by introducing additional compounds, mostly oxides, that can take the role of modifiers or intermediates between network formers and modifiers.

1.2 Phosphate glass applications

Unless they are less widespread than silicate glasses, phosphate glasses have found interest in many application domains, nowadays. One of the main benefits of phosphate glass systems is that their chemical durability can vary extremely. In the course of this thesis, the term chemical durability stands for the resistance towards aqueous attack and weathering influences.

In the following, phosphate glass systems shall be subdivided into two groups: phosphate glasses with low chemical durability and those with high chemical durability. First, the most important application domains for phosphate glasses with low chemical durability shall be considered. A presentation of the implementation fields of phosphate glass systems with high chemical durability follows.

1.2.1 Phosphate glasses with low chemical durability

Phosphate glass compositions with low chemical durability find their main applications for hard water treatment, as fertilizers and as biomaterials.

a) Hard water treatment

Amorphous $NaPO_3$ has found use as a sequestering agent for hard water treatment in industries, since it dissolves rapidly in aqueous solutions. For several years, it has been the main constituent of commercially available water softening agents such as Calgon® (van Wazer1958) and still it is commercially available.

b) Phosphate glass fertilizers

Glassy phosphate fertilizers have been introduced in the early 1980s to overcome the problems of conventional mineral fertilizers: weathering and washing away from the soil, causing fertilizer loss and environmental pollution in subsoil waters (Drake 1979). Granular phosphate glass pellets present a new generation of environmentally friendly fertilizers of prolonged action.

As an example, they may consist of glasses of the compositional base system K_2O-CaO-MgO-P_2O_5 (AGROVIT; Karapetyan2002; Ivanenko2007). Variations in the phosphate glass composition allow for controlling decomposition and ionic release rates. Complete dissolution can occur within time intervals of several days to several years (AGROVIT). In addition, the fertilizer glass composition can be charged with microelements that are needed for plant nutrition.

c) Phosphate glass biomaterials

As biomaterials, phosphate glasses possess applications in the field of hard and soft tissue engineering, as antibacterial devices and for the controlled release of drugs.

With a chemical composition out of the inorganic phase of bone, P_2O_5-CaO-Na_2O glasses are promising materials for the repair and the reconstruction of those (www.novabone.com). They play - in contrast to inert implants - an active part in the process of bone regeneration. First, they decompose completely in the physiological environment and can be replaced gradually by bone tissue. Hence, surgery removal is not needed, once their function is fulfilled (Pickup2007). Second, the ionic environment created during the degradation of bioglass materials may stimulate the growth of bone tissue. As an example, Ca^{2+} cations can stimulate osteoblast-like cell proliferation and differentiation (Knowles2003; Abou Neel2009).

Related application domains are the field of dental healthcare (Perioglass®) and the area of soft-tissue repair (Knowles2003; Abou Neel2009).

Moreover, phosphate glasses offer potential alternatives to the treatment of infections. Ions with antibacterial effects such as copper, silver and gallium can be included in the glass (Valappil2007). The material can be placed at the site of the infection with the aim of releasing antibacterial ions upon degradation. The use of these devices could be extended to the prevention of implant- or biomaterial- related infections. In addition, the current infection prophylaxis by systematically administred antibiotics could be replaced (Abou Neel2009).

In practical terms, silver-releasing phosphate glasses are used clinically to combat long term infection in indwelling catheters (Gilchrist1991).

Finally, phosphate bioglasses can act as drug carriers for medical applications (Knowles2003). As an example, soluble phosphate glasses containing elements such as copper, cobalt and selenium are manufactured under the trade name of Cosecure®. These glasses are used for oral treatment of trace element deficiencies in animals.

1.2.2 Phosphate glasses with high chemical durability

Extremely high chemical durability is a key feature of phosphate glasses that find their application as laser hosts, as sealing glasses and as matrices for the immobilization of nuclear waste.

a) Optical applications

Beneficial properties of phosphate glasses used for high power laser applications are their low thermooptical coefficients and their ability to tolerate high rare earth cation contents (Schülzgen2008). Thus, they can benefit from large rare earth stimulated cross sections.

As an example, Schott's APG-2® phosphate laser glass is a Nd-doped phosphate glass composition that may be used as an ultrashort pulse laser source or as a broadband oscillator. Niobium phosphate glasses possess a high third-order susceptibility $\chi 3$ (Flambard 2004; Flambard2008) and attract interest for ultra-fast optical switches.

b) Sealing glasses

Hermetic seals between glasses and high expansion metals, e.g. aluminum or stainless steel, are required in a variety of application domains such as industries or electronics. Phosphate glasses are suitable materials for their low glass transition temperatures that allow for effective sealing *below* the fusion temperatures of metals such as aluminum. In addition, their thermal expansion coefficients match those of the materials that are to seal. As an example, durable phosphate sealing glasses have been developed on the basis of Li_2O / Na_2O / K_2O - Al_2O_3 - P_2O_5 glass compositions that may contain additional BaO or CaO (Brow 1991).

c) Storage of nuclear waste

At the present time, borosilicate glasses are the widely used reference standard for the immobilization of nuclear waste. However, in the U.S., iron phosphate glasses (base compositions: Na_2O-Fe_2O_3-P_2O_5 and PbO-Fe_2O_3-P_2O_5) have been implemented as host matrices for the immobilization of radioactive waste for several decades, now (Tuthill1967; Krause1973; Kim2003; Ewing2002). In Russia, nuclear waste has been immobilized in glasses of the base composition Na_2O-Al_2O_3-P_2O_5 at the Mayak facility in Ozersk (Mukhamet-Galeyev1995; Kushnikov1995; Oelkers2008).

Beneficial properties of waste immobilization phosphate glasses are their lower melting and operating temperatures and their higher waste loading capacities. Sales and Boatner (Sales1984a, Sales1984b) and Boatner and Sales (Boatner1989) demonstrated that phosphate-bearing glasses had dissolution rates that were 100 to 1000 times lower, processing temperatures that were 100-250°C lower and melt viscosities that were in the regime from 800-1000°C lower than those of borosilicate glasses. Recently, Bingham et al. (Bingham2006) demonstrated that BaO-FeO-Fe_2O_3-P_2O_5 glasses are ultra durable, thermally stable and low melting and that they possess a large glass-forming range. The relatively low thermal stabilities of phosphate glasses can be overcome by addition of B_2O_3 (Bingham2009).

Within the frame of this thesis, emphasis lies on the structural and mechanistic aspects of phosphate glass weathering. Our studies are carried out with regard to the further implementation of phosphate glass systems as host matrices for the immobilization of nuclear waste. Above, the two main base compositions of such systems have been presented: iron phosphate glasses ($Fe_2O_3 – P_2O_5$) and aluminophosphate glasses ($Al_2O_3 – P_2O_5$).

The main tool of our structural investigations being solid-state NMR, aluminophosphate systems will be investigated, owing to the paramagnetic nature of iron.

It is common to investigate in a first step simple model systems in order to gain insight into the structural role of the base compounds. In the following paragraph, the NMR works that have been carried out to elucidate the structure of simple aluminophosphate model glass systems, shall be presented together with their most important outcomes.

1.3 NMR studies on ternary aluminophosphate glass systems

It is known that addition of Al_2O_3 to a phosphate glass in the regime of low alumina content (0 < x < 15 mol %) strengthens the glass network and increases the chemical durability of the glass (Kreidl1941, Brow1993). The strengthening of the glass network in the regime of low alumina content is mainly attributed to cross-linking of the phosphate chains by AlO6 octahedra.

^{31}P and ^{27}Al NMR reveal changes in the atomic level and intermediate range of the glass network as aluminum is added. Understanding of the changes on these levels is an essential step for establishing correlations between glass composition and glass performance. Not many NMR studies of the ternary model systems M_2O- Al_2O_3 - P_2O_5 (M = Na; K) have been carried out that were able to characterize these ternary aluminophosphate glass systems on an intermediate range level.

Early works implemented 1D ^{31}P and 1D ^{27}Al NMR to monitor structural changes that occur on an atomic level upon addition of Al_2O_3 (Brow1990; Brow1993). Brow *et al.* (Brow1993) observed in the x Al_2O_3 - (100-x) $NaPO_3$ system dramatic changes in the dominating AlOx coordination state when the glass network reaches the pyrophosphate composition limit ([O]/[P] =3.5; ca. 15 mol % of Al_2O_3). They explained this change in AlOx coordination based on their model of local charge compensation for binary Al_2O_3 - P_2O_5 model systems. Hence, the [O]/[P] ratio determines the dominating coordination state of aluminum.

However, based on empirical considerations, ^{31}P resonances could not be resolved and attributed unambiguously in these earlier works, since the presence of ^{31}P-^{27}Al connectivity leads to overlapping ^{31}P resonances.

Resolution of the 1D ^{31}P spectra and of the concealed ^{31}P-^{27}Al connectivity information developed with the advent of the routine implementation of 2D techniques. Egan *et al.* (Egan2000) employed 2D ^{27}Al-{^{31}P} cross-polarization on a x $NaAlO_2$ - (100-x) $NaPO_3$ glass system. These experiments enabled these authors to determine the number and the nature of connectivity between ^{31}P resonances and AlO6, AlO5 and AlO4. However, besides the connectivity information, the specific assignment of 1D ^{31}P Q^n_{AlOx} resonances to $Q^n_{m,AlOx}$ species was mainly based on chemical shift values of crystalline references and on empirical considerations.

Lang *et al.* (Lang2001) used ^{31}P-{^{27}Al} and ^{31}P-{^{23}Na} TRAPDOR experiments to detect how the addition of aluminum influences the phosphorus environment with regard to sodium and aluminum in the 50 Na_2O - x Al_2O_3 - (50-x) P_2O_5 glass series (0<x<17.5).

They concluded that **adding aluminum to the glass composition results in the formation of P-O-Al environments and the reduction of P-O-P environments. The sodium environment of phosphorus nuclei remains invariant. Hence, any observed changes in the physical properties such as an increase of the chemical durability of the glass must be a result of changes in the Al-O-P and P-O-P bonding environments.**

Van Wüllen *et al.* (van Wüllen2007; Wegner2008) were the first to specify connectivity in the ternary aluminophosphate system 50 K_2O - x Al_2O_3 - (50-x) P_2O_5 in terms of $Q^n_{m,AlOx}$ in detail, based on experimental evidence and not on empirical considerations. ^{31}P-{^{27}Al} CP HETCOR NMR was employed to characterize ^{31}P-^{27}Al connectivity, ^{31}P – {^{27}Al} REAPDOR NMR and ^{27}Al – {^{31}P} REDOR to determine the number of ^{27}Al in proximity to ^{31}P and *vice versa*. Further, ^{31}P-J-RES NMR spectroscopy was used to determine ^{31}P polymerization. The outcome of these experiments was used to draw a picture of the glass network (*Fig. 1.3*) and to follow the effects of increasing Al_2O_3 addition in the 50 K_2O – x Al_2O_3 – (50-x) P_2O_5 system quantitatively.

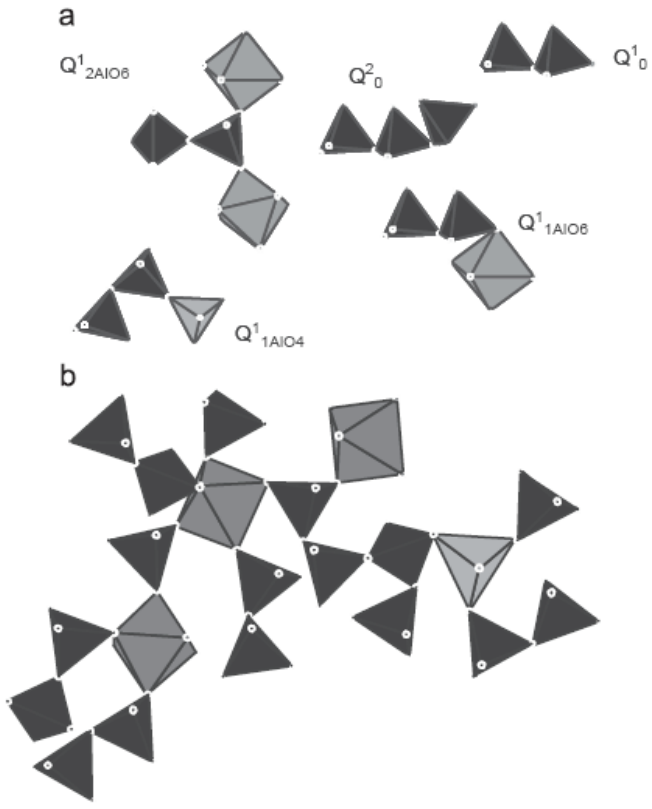

Fig. 1.3:
Structural model of the 50 K_2O - 10 Al_2O_3 - 40 P_2O_5 glass network given by van Wüllen et al. (from van Wüllen2007). Part a) shows the basic structural units identified by the authors. Part b) of the picture gives an impression of the network organization.

Concluding:

- Few NMR studies on aluminophosphate glass systems exist. Nevertheless, all authors agree that the addition of Al_2O_3 to the ternary glass network results in creation of Al-O-P linkages and reduction of P-O-P linkages. In the regime of low alumina content, these Al-O-P linkages are at the origin of glass strengthening and changes in other physical properties of the glass.

- Al-O-P linkages generate a multitude of connectivity types $Q^n_{m,AlOx}$. Nowadays, the implementation of an advanced NMR protocol allows for identification, specification and quantification of all $Q^n_{m,\ AlOx}$ species present in the ternary glass network.

- With regard to our interest in phosphate glass weathering, the monitoring of the evolution of the weathering ternary phosphate glass network is of interest. Particular emphasis lies on the moisture resistance of Al-O-P bonds and the structural role of aluminum throughout the weathering process.

1.4 NMR studies on phosphate glass weathering

1.4.1 Phosphate glass weathering model

A qualitative model of the aqueous attack of a phosphate glass is illustrated schematically in *Fig. 1.4*. Nowadays, this model is generally accepted in the literature. It distinguishes alteration conditions where the phosphate glass is attacked in solution and those where the phosphate glass is exposed to humid atmosphere. It is noteworthy that in most studies phosphate glasses with chain like structure are considered.

Aqueous attack on a phosphate glass can be subdivided into two main steps, the first one being the same in solution and under weathering conditions.

1) Hydration:
   In a first step, water molecules are adsorbed at the phosphate glass surface and hydrate the phosphate chains and the modifier cations.

2) The following processes depend on the exact conditions of aqueous attack. In solution conditions, removal of entire phosphate chains and modifier cations occurs. Congruent dissolution has been observed for sodium phosphate glasses as well as sodium aluminum phosphate glass systems. After the dissolution of entire chains, hydrolysis of the dissolved phosphate chains may occur. Depending on the ionic conditions of the solution, precipitation of the hydrolysis products on the phosphate glass surface may occur (Clément1999).
   Under weathering conditions, phosphate chain hydrolysis occurs. Surface crystallization, mainly into orthophosphate phases, has been observed (Tischendorf2004).

Only few studies exist where the structure of *weathered* phosphate glass systems has been investigated on an atomic scale and a first understanding of the weathering mechanisms that occur on this level has been developed. In the domain of phosphate glasses, NMR has become a powerful tool to gain insight into the alteration processes of phosphate glasses on an atomic scale level. It is commonly accepted to use simple model systems to monitor the fundamental processes of phosphate glass weathering in a first approach. Hence, in the following, the NMR studies on simple model systems that contributed to the understanding of phosphate glass weathering shall be presented.

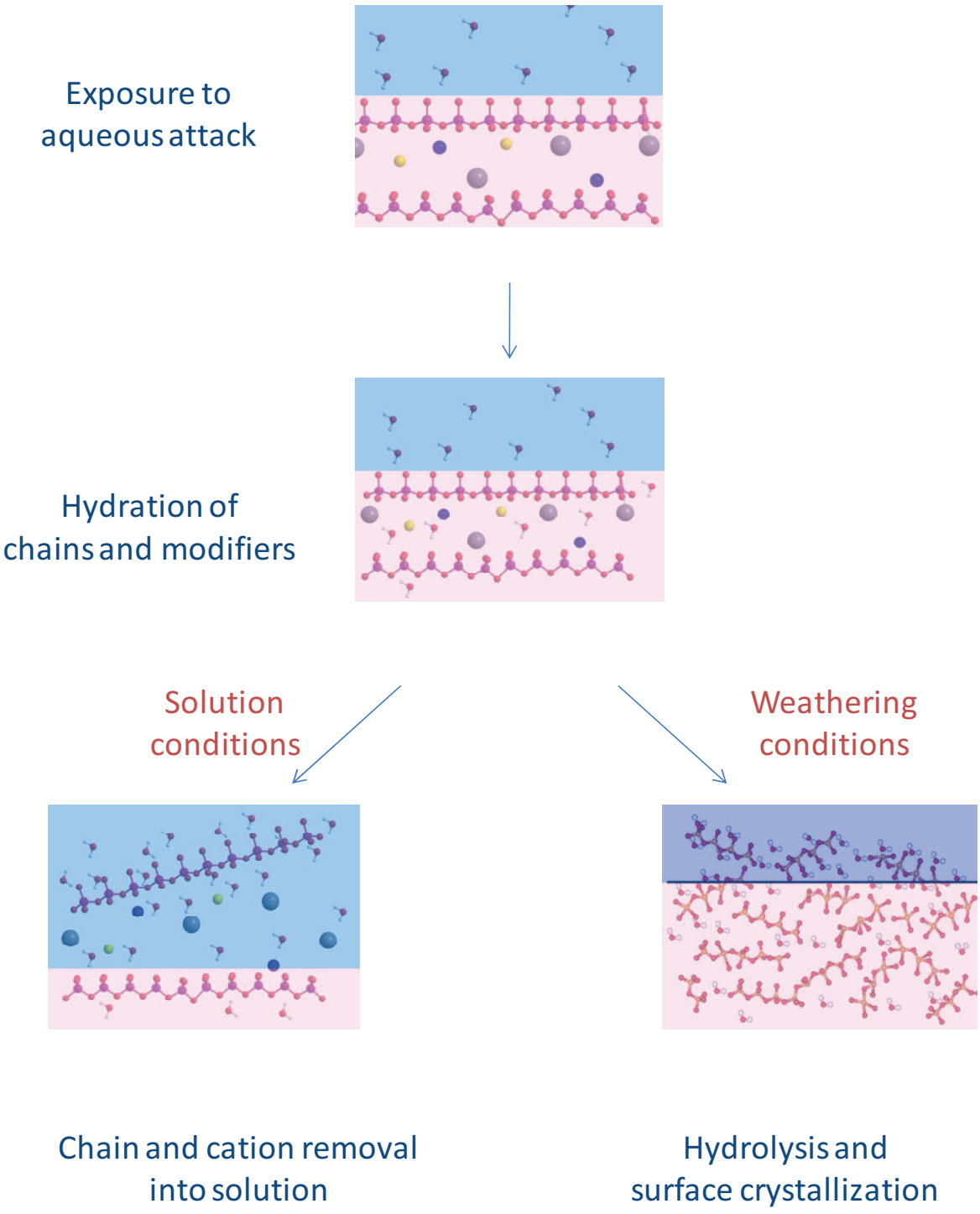

Fig. 1.4:
A qualitative model for the aqueous attack on phosphate glass systems. Glass corrosion in solution conditions and glass corrosion under weathering conditions have to be distinguished (from Tischendorf2004).

1.4.2 Phosphate glass weathering studies: contributions from NMR

a) Contributions from 1D ^{31}P NMR

From 1D ^{31}P NMR, phosphate species generated during the weathering process could be identified. Those attributions were mainly based on chemical shift values of comparable sites in crystalline reference phases. Brow *et al.* observed strong indication for phosphate glass chain hydrolysis upon weathering (Brow1990), as well as Hartmann *et al.* (Hartmann1994) who attributed signals at -8.6 ppm to Q^1_H species resulting from Q^2 chain hydrolysis after weathering.

b) Contributions from 1D ^{1}H NMR

Works from Palavit *et al.* (Palavit1998), Wenslow *et al.* (Wenslow1998), Mercier et al. (Mercier1999) and Alam *et al.* (Alam2005) focused on proton environments that are created when phosphate glass is exposed to aqueous attack under humid atmosphere. The assignment of protons is mainly based on empirical correlations between proton chemical shift values and hydrogen bond lengths in crystals such as given by Jeffrey and Yeon (Jeffrey1986)

$$\delta\ ^1\text{H ppm} = 44.68 - 19.3 * d_{(O\ldots H)} \text{ (A)}$$

In general, all authors whose works are presented above observed signals in the range between 0 to +10 ppm attributed to surface adsorbed water molecules as well as signals in the region between +10 and +20 ppm attributed to strong (O…H) bonds. Whereas adsorbed surface water points towards hydration of phosphate chains, protons that are involved in strong hydrogen bonding are a strong indicator for phosphate chain hydrolysis and simultaneous generation of P-OH sites.

During the last years, resolution in ^{1}H NMR increased considerably. As an example, Alam *et al.* (Alam2005) were able to identify seven or eight different contributions to the ^{1}H signal in weathered K_2O-Al_2O_3-P_2O_5 glass (*Fig. 1.5*).

In the works of Wenslow (Wenslow1998), Mercier (Mercier1999) and Alam (Alam2005), the specification of the identified proton species has been refined by complementary 2D experiments that shall be presented in the following paragraph, 1.4.2. c).

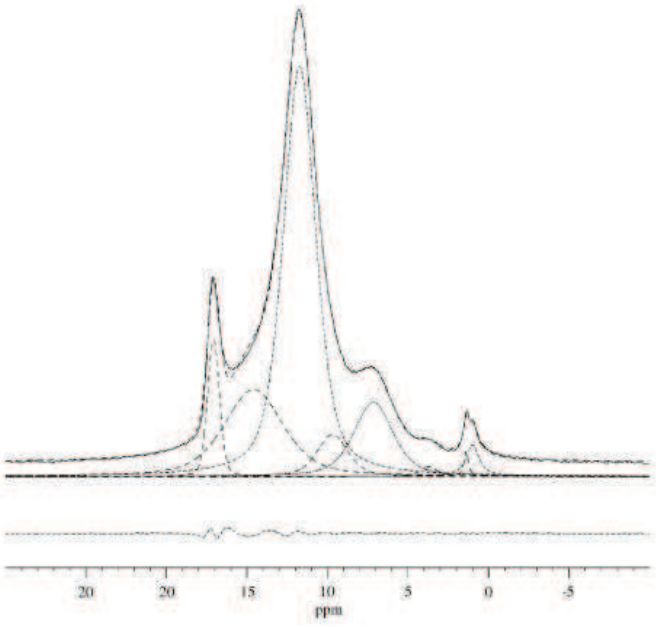

Fig. 1.5:
1D ^{1}H NMR spectrum of weathered 30 K_2O – 10 Al_2O_3 – 60 P_2O_5 glass (14.1 T; spinning speed 30 kHz). The authors identified seven individual contributions of ^{1}H species generated throughout weathering (from Alam2005).

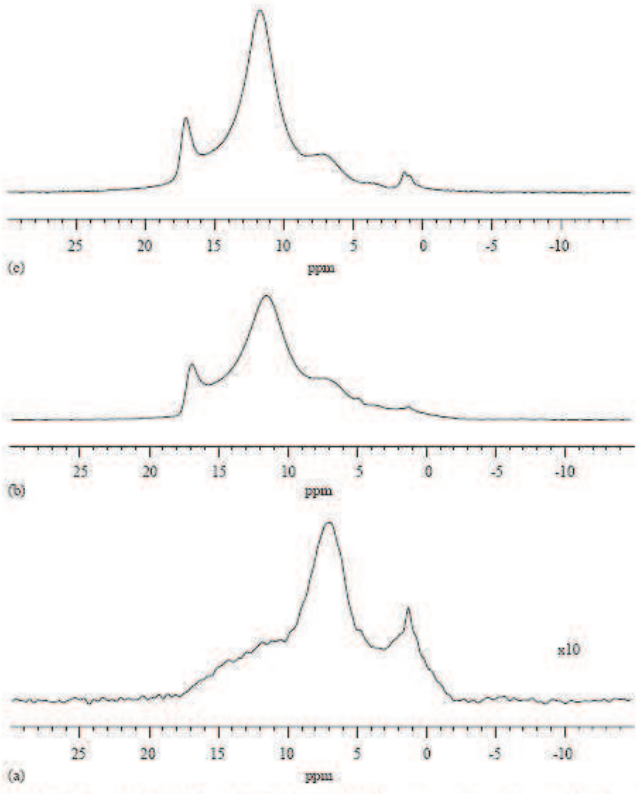

H MAS NMR spectra of the KAP glass, obtained at 600.13 MHz using a rotor-synchronized Hahn echo at a nction of exposure time to 80% RH at 50 °C: (a) 0 days, (b) 2 days, and (c) 7 days.

Fig. 1.6:
1D ^{1}H NMR spectrum of weathered K_2O – Al_2O_3 – P_2O_5 glass (14.1 T; spinning speed 30 kHz). The spectral evolution allowed to draw conclusions about the time dependent occurrence of surface hydration and hydrolysis processes (from Alam2005).

c) Contributions from high resolution techniques

By implementing cross-polarization (CP) transfer from ^{1}H to ^{31}P, Wenslow *et al.* (Wenslow1998) were able to classify the phosphate sites that are present in weathered Na_2O-P_2O_5 glass with near-metaphosphate structure. Two types of hydrogen-bond proton environments (O…H) could be distinguished by means of ^{1}H MAS NMR and cross-polarization performed at variable contact times (0.2 ms to 7.0 ms). A complementary 2D ^{31}P - $\{^{1}H\}$ CP experiment (0.2 ms) revealed the presence of three connectivities between ^{31}P sites and the two ^{1}H environments (*Fig. 1.7*). Overall, five distinct ^{31}P sites could be identified in the attacked glass network, namely Q^2_{Na}, Q^1_{Na}, $Q^1_{Na,H}$, Q^1_H and Q^0_H.

Based on the identified ^{31}P species in the weathered $NaPO_3$ glass, the authors proposed two simple model pathways for the hydrolysis attack on a phosphate chain of finite length (*Fig. 1.8*).

- **Pathway / Scenario 1**

  Phosphate chains are hydrolyzed at interior positions of the chains. Resulting in generation of Q^1_H moieities.

- **Pathway / Scenario 2**

  Phosphate chains are hydrolysed at the end of the chains, resulting in generation of Q^1_H and Q^0_H units.

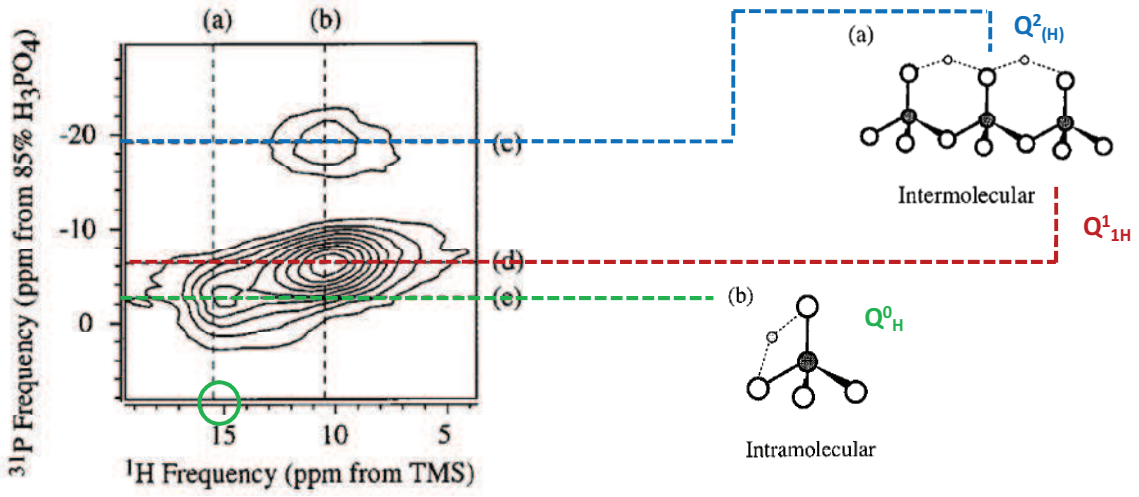

Fig. 1.7:
Specifiation of protonated ^{31}P sites in a near-metaphosphate glass after water vapor attack. Q^0_H represents an orthophosphate site with strong intramolecular hydrogen bonding, Q^1_H with exhibiting weaker hydrogen bonding. The Q^1_H site is connected to a $Q^2_{(H)}$ backbone unit attracting loosely its proton. The $Q^2_{(H)}$ unit may stem from the same phosphate backbone or from a neighboring one (from Wenslow1998).

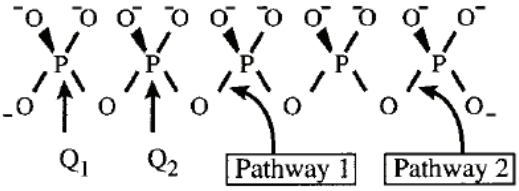

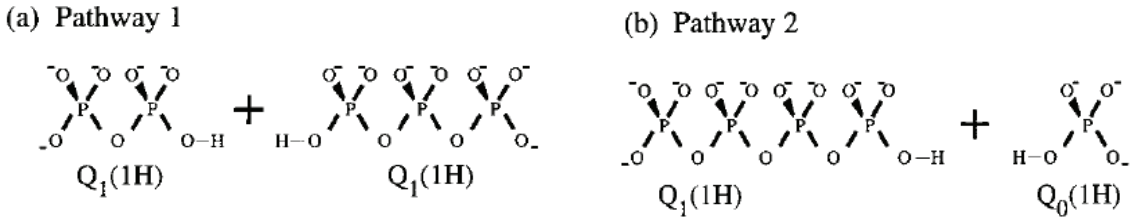

Fig. 1.8:
Two model pathways for hydrolytic attack on a phosphate chain of finite length (from Wenslow1998).

In a similar investigation, Mercier and coworkers implemented 1D ^{31}P - $\{^{1}H\}$ cross-polarization transfer at variable contact times to distinguish protonated ^{31}P sites in zinc ultraphosphate glasses containing large amounts of hydroxyl groups (Mercier1998) and for zinc ultraphosphate glasses weathered under humid air at 140°C (Mercier1999).
In a study conducted by Montagne and coworkers (Montagne2006) 1D ^{31}P - $\{^{1}H\}$ cross-polarization experiments revealed the presence of *crystalline* Q^{1}_{H} and Q^{0}_{H} sites generated throughout aqueous attack on $NaPO_3$ glass at 110°C and 200°C for 60 h. 4 to 5 hydrogen phosphate phases were identified by means of 2D ^{1}H-^{31}P Cross-polarization whereas XRD only revealed the presence of NaH_2PO_4.

Alam *et al.* **(Alam2005)** also implemented 2D ^{31}P - $\{^{1}H\}$ cross-polarization in order to specifiate the assignment of the ^{1}H resonance contributions presented in *Fig. 1.5.* In the same study, the authors monitored the evolution of these resonances during the weathering of the glass *(Fig. 1.6).* **This allowed them to refine the mechanistic propositions given by Wenslow and Mueller (Wenslow1998) for the weathering process of their model phosphate glass, 30 K_2O-10 Al_2O_3-60 P_2O_5.**

- **The initial steps of weathering involve the association of H_2O species with the glass surface**, denoted as surface hydration within the frame of this work. Primarily, Q^2 species are concerned by this process. The wide range of different ^{1}H NMR chemical shifts observed for these H_2O species suggest that different adsorption acidities are present due to hydration processes of both, the phosphate chains and the cations present in the glass.

- The growing intensity of ^{1}H NMR resonances > 10 ppm is an indicator for **subsequent hydrolysis of P-O-P bonds and generation of P-OH bonds**. Subsequent reaction of The Q^{1}_{H} moieities with additional H_2O produces Q^{0}_{H} species.

Alam and Lang (Alam2001) proposed the implication of a ^{31}P - $\{^{1}H\}$ CP edited ^{31}P RFDR experiment to detect selectively ^{31}P-^{31}P correlation signals that arise from hydrogen phosphate phases on the surface of aged Na_2O-P_2O_5 glass of near-metaphosphate composition.

Concluding:

All studies conducted by NMR helped to identify species and structural changes present in weathered phosphate glasses. These studies have lead to mechanistic propositions for the weathering attack on phosphate glasses (Wenslow1998, Alam2005). Nevertheless, a number of questions still subsist.

- Under humid atmosphere, hydration and subsequent hydrolysis of the phosphate chains has been observed. It is of interest, to monitor this evolution for shorter time intervals in order to gain detailed insight, *when* hydrolysis commences.

- Based on the fact that P-O bond stabilities differ depending on the degree of phosphate polymerization, it is of interest to investigate whether one of the both pathways proposed by Wenslow and Mueller is preferred for hydrolytic attack.

- The weathering of phosphate glass systems has been studied exhaustively by ^{1}H and ^{31}P NMR. However, it is remarkable that for ternary systems involving ^{27}Al (Alam2005), this nucleus has not been the subject of interest, so far. Nevertheless, the understanding of its role during the weathering process is of crucial importance for the amelioration of the weathering properties of Na_2O - Al_2O_3 - P_2O_5 glass systems.

- Finally, ^{17}O has not been implemented as a probe nucleus for weathering studies, so far. Nevertheless, oxygen is at the site of reaction, whenever aqueous attack on a glass occurs. Therefore, the implication of ^{17}O NMR studies is of interest.

Conclusion and Perspectives Chapter 1

In the present chapter, an introduction into phosphate glass structure (Section 1.1) and into the most important application domains of these glasses has been presented (Section 1.2). Finally, we focused our interest on durable glass systems for the storage of nuclear waste and on their durability properties.

With regard to the future development of highly durable phosphate glasses, NMR studies on model aluminum phosphate glasses have been presented in section 1.3. Authors agree that Al-O-P linkages are at the origin of glass strengthening and changes in other physical properties of the glass.

With regard to the impact of weathering on the future implementation of phosphate glasses as nuclear waste hosts, NMR strategies for the investigation of the weathering process have been presented in Section 1.4. Under humid atmosphere, hydration and subsequent hydrolysis of the phosphate chains has been observed (Tischendorf2004). Mechanistic propositions for the weathering attack on phosphate glasses (Wenslow1998, Alam2005) have been presented.

The major aim of the present thesis is to further understand the weathering process of phosphate glasses on an atomic scale level. Therefore, NMR investigation strategies from Section 1.3 and 1.4 have to be reconciled with systematic weathering assays. Moreover, the scope of the probe nuclei shall be extended towards ^{17}O and ^{27}Al.

- ^{17}O is directly involved in aqueous attack. A strategy for the interpretation of ^{17}O NMR spectra and for the implementation of ^{17}O as a selective marker has to be developed.

- The role of aluminum in the weathering process has not been investigated in detail, so far, unless Al-O-P linkages are supposed to be at the origin of changes in physical properties of the phosphate glasses such as their durability. In particular, we are interested in the moisture resistance of the Al-O-P linkages.

Bibliography Chapter 1

Abou Neel2009
Abou Neel, E.A., Pickup, D.M., Valappil, S.P., Newport, R.J., Knowles, J.C.
Journals of Materials Chemistry (2009) 19 (6), 690

AGROVIT
1) www.agrovit.org/en/production
2) http://idw-online.de/pages/de/news218121

Alam2001
Alam, T.M., Lang, D.P.
Chemical Physics Letters (2001) **336 (5-6)** 385

Alam2005
Alam, T.M. Tischendorf, B.C., Brow, R.K.
Solid State Nuclear Magnetic Resonance (2005) **27**, 99

Bingham2006
Bingham, P.A., Hand, R.J., Forder, S.D., Lavaysierre, A., Deloffre, F., Kilcoyne, S.H., Yasin, I.
Physical Chemistry of Glasses: Eur. J. Glass Sci. Technol. B (2006) **47 (4)**, 313

Bingham2009
Bingham, P.A., Hand, R.J., Hannant, O.M., Forder, S.D., Kilcoyne, S.H.
Journal of Non-Crystalline Solids (2009) **335**, 1526

Boatner1989
Boatner, L.A., Sales, B.C.
U.S. patent no 4,847,008 (1989)

Brow1990
Brow, R.M., Kirkpatrick, R.J., Turner, G.L.
Journal of the American Ceramic Society (1990) **73 (8)**, 2293

Brow1991
Brow, R.K., Day, D.E.
U.S. patent, no. 5,045,508 (1991)

Brow1993
Brow, R.K.
Journal of the American Ceramic Society (1993) **76 (4)**, 913

Clément1999
Clément, J., Manero, J.M. Planell, J.A.
Journal of Materials Science: Materials in Medicine (1999) **10**, 429

Doremus1994
Doremus, R.H.
Glass Science, Second Edition, John Wiley & Sons, New York, 1994

Drake1979
DrakeC.F.
U.S. patent no 4,148,623 (1979)

Egan2000
Egan, J.M., Wenslow, R.M., Mueller, K.T.
Journal of Non-Crystalline Solids (2000) **261**, 115

Ewing2002
Ewing, R.C. and Wang, L.
Reviews in Mineralogy and Geochemistry (2002), 48

Flambard2004
Flambard, A., Montagne, L., Delevoye, L., Palavit, G., Amoureux, J.-P., Videau, J.-J.
Journal of Non-Crystalline Solids (2004) **345-346**, 75

Flambard2008
Flambard, A., Videau, J.-J., Delevoye, L., Cardinal, T., Labrugère, C., Rivero, C.A., Couzi, M., Montagne, L.
Journal of Non-Crystalline Solids (2008) **354 (30)**, 3540

Gilchrist1991
Gilchrist, T., Healy, D.M., Drake, C.
Biomaterials (1991) **12**, 76

Hartmann1994
Hartmann, P., Vogel, J., Schnabel, B.
Journal of Non-Crystalline Solids (1994) **176 (2-3)** 157

Ivanenko2007
Ivanenko, V., Karapetyan, G., Lipovskii, A., Maksimov, L., Rusan, V., Tagantsev, D., Tatarintsev, B., Fleckenstein, J., Schnug, E.
Landbauforschung Völkenrode (2007) **4 (57)**, 323

Jeffrey1986
Jeffrey, G.A., Yeon, Y.
Acta Crystallographica (1986) **B42**, 410

Junge1969
Junge, A.E.
U.S. patent, no 3,845,646 (1969)

Karapetyan2002
Karapetyan, G., Karapetyan, K., Maksimov, L.
Proceedings of IMPHOS, Jena (Germany), July 10-13 2002

Kim2003
Kim, C.W., Ray, C.S., Zhu, D., Day, D.E., Gombert, D., Aloy, A., Mogus-Milankovich, A., Karabulut, M.
Journal of Nuclear Materials (2003) **322**, 152

Knowles2003
Knowles, J.C.
J. Mater. Chem. (2003), **13**, 2395

Krause1973
Krause, H.
Chemie-Ing.-Techn. (1973) **45. Jahrgang 10a**, 658

Kreidl1941
Kreidl, N.J., Weil, W.A.
Journal of the American Ceramic Society (1941) **24**, 372

Kushnikov1995
Kushnikov, V.V., Mayunin, Y.I., Smelova, T.V., Demin, A.V.
Materials Research Society Symposium Proceedings (1997) **465**, 55

Lang2001
Land, D.P., Alam, T.M., Bencoe, D.
Chemistry of Materials (2001) **13**, 420

Mercier1998
Mercier, C., Montagne, L., Sfihi, H., Palavit, G., Boivin, J.C., Legrand, A.-P.
Journal of Non-Crystalline Solids (1998) **224 (2)**, 163

Mercier1999
Mercier, C., Montagne, L., Sfihi, H., Palavit, G.
Journal of Non-Crystalline Solids (1999) **256 & 257,** 124.

Montagne2006
Montagne, L., Delevoye, L., Trebosc, J., Revel, B.
Réunion du GDR RMN Grand Bassin Parisien, May 2006, Versailles, France.

Mukhamet-Galeyev1995
Mukhamt-Galeyev, A.P., Magazina, O.L., Levin, K.A., Samotoin, N.D., Zotov, A.V., Omelianenko, B.I.
Materials Research Society Symposium Proceedings (1995) **353**, 79

NOVABONE
www.novabone.com

Oelkers2008
Oelkers, E., Montel, J.-M.
Elements (2008) **4**, 113

Palavit1998
Palavit, G., Mercier, C., Montagne, L., Drache, M., Abe, Y.
Journal of the American Ceramic Society (1998) **81 (6),** 1521

Pickup2007
Pickup, D.M., Ahmed, I., Guerry, P., Knowles, J.C., Smith, M.E., Newport, R.J.
J. Phys.: Condens. Matter (2007) **19**, 415116

Sales1984a
Sales, B.C., Boatner, L.A.
Science (1984) **226 (4670)**, 45

Sales1984b
Sales, B.C., Boatner, L.A.
Materials Letters (1984) **2 (4)**, 301

Schülzgen2008
Schülzgen, A., Li, L., Zhu, X., Suzuki, S., Temyanko, V.L., Albert, J., Peyghambarian, N.
Materials Research Society Symposium Proceedings, (2008) **1076**, 65

Tischendorf2004
Tischendorf, B., Brow, R.;
XX. International Congress on Glass, Oct. 2004, Kyoto, Japan.

Tuthill1967
Tuthill, E.J., Weth, G.G., Emma, L.C., Strickland, G., Hatch, L.P.
Ind. Eng. Chem.: Process Design and Development (1967) **6 (3)**, 314

Valappil2007
Valappil, S.P., Pickup, D.M., Carroll, D.L., Hope, C.K., Pratten, J., Newport, R.J.
Antimicrobial Agents and Chemotherapy 51 (12), 4453

vanWazer1958
vanWazer, J.R.
Phosphorus and its compounds, vol.1
Interscience, New York, 1958

van Wüllen2007
van Wüllen, L., Tricot, G., Wegner, S.
Solid State Nuclear Magnetic Resonance **(2007) 32 (2)**, 44

Wegner2008
Wegner, S., van Wüllen , L., Tricot, G.
Journal of Non-Crystalline Solids (2008) **354 (15-16)**, 1703

Wenslow1998
Wenslow, R.M., Mueller, K.T.;
Journal of Physical Chemistry B (1998) **102 (45)**, 9033

Xue2009
Xue, X., Kanzaki, M.
Journal of the American Ceramic Society (2009) **92 (12)** 2803

Chapter 2

A combined approach for the study of weathering phosphate glass systems: methods and experimental techniques

CHAPTER 2:

A combined approach for the study of weathering phosphate glass systems: Methods and experimental techniques

Our work is based on three pillars, namely NMR, DFT-GIPAW calculations and the experience of the glass group in ^{17}O-enrichment. Those shall be introduced in the frame of the present chapter that focuses on methodological aspects.

As solid-state NMR constitutes the main structural investigation tool, section 2.1 to 2.3 are dedicated to this structural analysis technique. The basic interactions are introduced (2.1) and the probe nuclei are presented (2.2). Finally, an overview over the advanced solid-state NMR techniques that were used for structural studies in this work shall be presented (2.3). Emphasis lies on the practical aspects and on the information content of each technique.

The second pillar, the calculation approach, is presented in section 2.4. Emphasis lies on the protocol elaborated in the frame of the studies of crystalline *hydrogen* phosphates.

The protocols of newly developed ^{17}O-enrichment techniques and weathering assays are given in sections 2.5 and 2.6. In section 2.5, a protocol for the synthesis of ^{17}O-enriched phase-pure crystalline hydrogen phosphates is introduced. In section 2.6, a protocol for weathering assays on phosphate glass systems will be presented.

2.1 The basic interactions in solid-state NMR

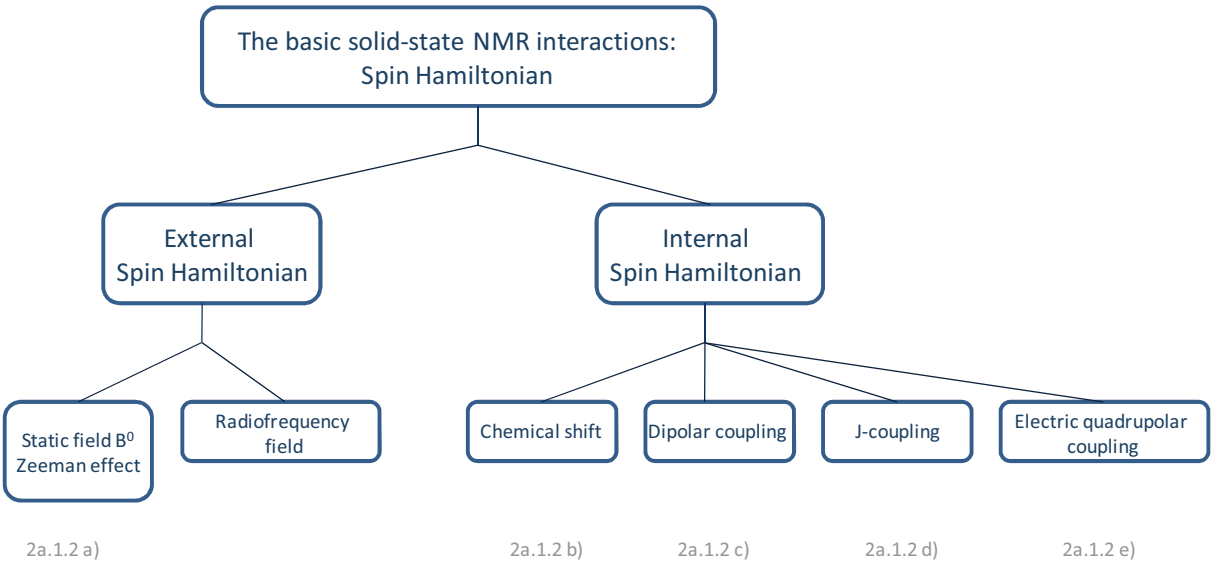

Fig. 2.1:
Schematic representation of the basic interactions present in solid-state NMR. The spin Hamiltonian is divided into an external and an internal part. At the bottom of the cases the paragraphs describing the interactions are indicated. External perturbations from radiofrequency fields will be discussed in detail in 2.1.2.

The basic NMR interactions in solid-state NMR are represented in *Fig. 2.1* where the spin Hamiltonian has been divided into an external and an internal part. Each interaction possesses an anisotropic part and certain of them contain an isotropic part. This will be discussed in detail in the following sections (2.1.2a-e), as indicated at the bottom of *Fig. 2.1*.

In contrast to liquid-state NMR, where most anisotropic interactions cannot be observed due to motional averaging, anisotropic interactions are conserved in NMR of powder samples. Thus, formally, the nuclear spin interaction Hamiltonian can be decomposed into its isotropic and its anisotropic part

$$I = I_{iso} + I_{aniso}$$

Nowadays, solid-state NMR has become almost a synonym for magic angle spinning (MAS) solid-state NMR where the main part of the anisotropic interactions is removed to enhance spectral resolution by rotation of the sample at the magic angle.

2.1.1 Magic angle spinning

Powder samples consist of many crystallites with random orientations, their high number giving rise to a large distribution of spectral frequencies. Broad powder patterns are obtained, if the spectrum is recorded under static conditions. As a result, different crystallographic sites can overlap, concealing information. As mentioned above, this loss of spectral resolution can be eliminated in great part by magic angle spinning.

The basic principle of MAS is that most of the nuclear spin interactions present an orientation dependence of the following form

$$(3\ \cos^2\theta - 1)$$

where θ is the angle between the static field $\underline{B}^0$ and the principal z-axis of the tensor ellipsoid of the nuclear spin interaction (*Fig. 2.2*).

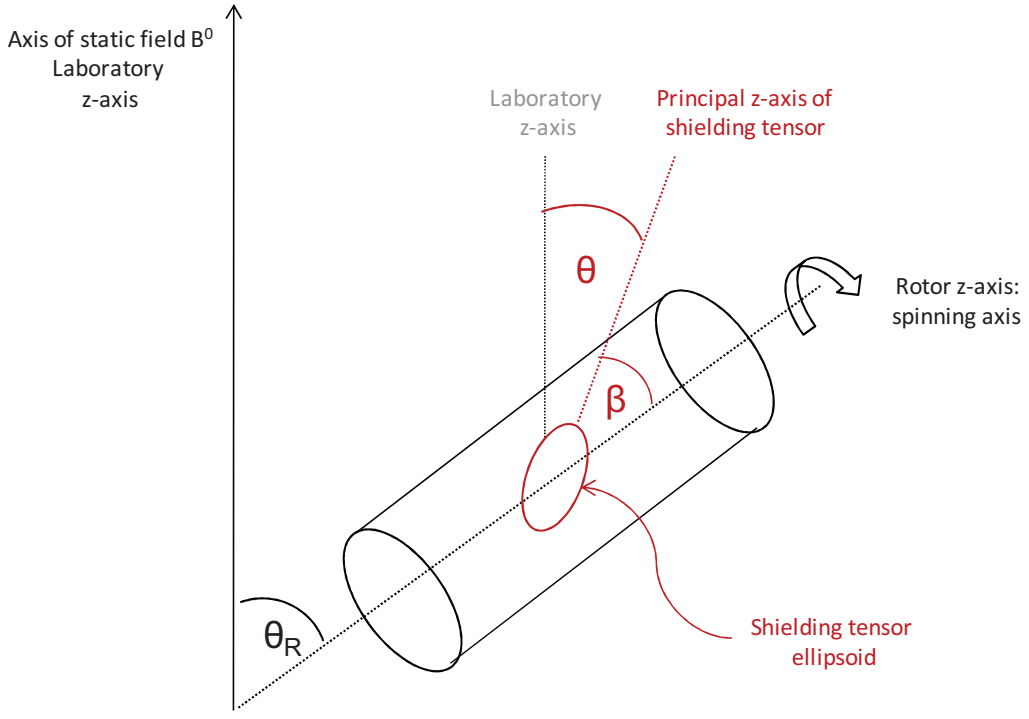

Fig. 2.2:

Schematic representation of the magic angle spinning experiment performed in a cylindrical rotor rotating at the magic angle θ_R=54,74°. Exemplarily, the chemical shielding tensor ellipsoid for one crystallite orientation is represented.

The aim of MAS is to average this term to zero. It takes advantage from the fact that the average of the nuclear orientation dependence under spinning can be shown to be

$$\left\langle 3\ \cos^2\theta - 1 \right\rangle = \frac{1}{2}\left(3\ \cos^2\theta_R - 1\right)\left(3\ \cos^2\beta - 1\right)$$

where θ_R is the angle between the spinning axis and the static field $\underline{B}^0$ and β is the angle between the spinning axis and the principal z-axis of the tensor ellipsoid of the nuclear spin interaction. If θ_R is set to be 54,74°, the magic angle, the term $\left\langle 3\ \cos^2\theta - 1 \right\rangle$ is zero under spinning conditions (*Fig. 2.2*).

At present, magic angle spinning is the most common technique to average out first-order anisotropic interactions in powder samples. Second-order anisotropic interactions are not completely averaged to zero. This can generally be explained by considering the evolution of I_{aniso} under magic angle spinning where the first-order anisotropic interaction is given by:

$$I_{aniso}^{(1)} = I_2^{(1)}(\theta,\theta_R) * P_2(\cos\theta_R)$$

and the second-order anisotropic interaction is given by:

$$I_{aniso}^{(2)} = I_0^{(2)} + I_2^{(2)}(\theta,\theta_R) * P_2(\cos\theta_R) + I_4^{(2)}(\theta,\theta_R) * P_4(\cos\theta_R)\,.$$

$P_2(\cos\theta_R) = \frac{1}{2}(3\cos^2\theta_R - 1)$ and $P_4(\cos\theta_R) = \frac{1}{8}(35\cos^4\theta_R - 30\cos^2\theta_R + 3)$ are Legendre polynoms. Since $P_4(\cos\theta_R) \neq 0$ under MAS conditions, only anisotropic interactions for spin-1/2 nuclei are removed whereas quadrupolar nuclei conserve parts of their second-order anisotropic interactions under magic angle spinning of the sample. This will be considered in 2.1.2e) and 2.3.1 where electric quadrupolar broadening and the MQMAS sequence are discussed.

To average the first-order anisotropic interaction efficiently, the spinning rate must be high enough compared to the anisotropy interaction that is a factor three or four (in frequency units).

2.1.2a) The Zeeman effect

The Zeeman effect results from an external perturbation of the spin system: Application of an external static magnetic field $\underline{B}^0$ annihilates the isotropy of space. The formerly degenerate energy levels split into $(2I+1)$ levels of energy

$$E_m = -m\gamma\hbar\underline{B}^0$$

where I represents the spin number of the nucleus, $m=(I,I-1,...,-I)$ the magnetic quantum number, γ its gyromagnetic ratio, and h is Planck's constant. The difference ΔE of two neighboring energy levels due to the Zeeman effect is directly field dependent. It is given by

$$\Delta E = \gamma\hbar\underline{B}^0$$

and determines the resonance frequency of a nucleus for a given field strength. Hence, it is one of the parameters that influence the sensitivity of a nucleus.

Owing to its magnitude, the nuclear Zeeman interaction is in general treated as the main interaction in solid state NMR. Thus, other nuclear interactions are considered as perturbations of the Zeeman interaction.

2.1.2b) Chemical shielding – chemical shift interaction

Each nucleus is „chemically shielded" by a cloud of electrons. The external magnetic field $\underline{B}^0$ induces ring currents in the electron clouds at the different crystallographic sites. These circulating currents, in turn, generate an induced magnetic field $\underline{B}^{ind}$

$$\underline{B}^{ind} = -\sigma\underline{B}^0$$

where σ is the magnetic shielding constant of the nucleus. $\underline{B}^{ind}$ is directly dependent on the external static field $\underline{B}^0$ and tends to oppose to the latter.
In solid-state NMR, the chemical shielding is orientation dependent and can reveal information about the close surroundings of the nucleus. The chemical shielding is represented by a tensor (ellipsoid)

that is diagonalized in its principal axis frame (PAF) (*Fig. 2.3*). The deviation of the tensor ellipsoid from spherical symmetry is an intuitive measure for the anisotropy of the chemical shielding.

The isotropic chemical shielding is the average value of the three tensor components

$$\sigma_{iso} = \frac{1}{3}(\sigma_{xx} + \sigma_{yy} + \sigma_{zz}) .$$

The chemical shielding anisotropy Δ_{CS} is defined as

$$\Delta_{CS} = \sigma_{zz} - \sigma_{iso} .$$

The asymmetry of the chemical shielding is defined as

$$\eta = \frac{\sigma_{xx} - \sigma_{yy}}{\Delta_{CS}} .$$

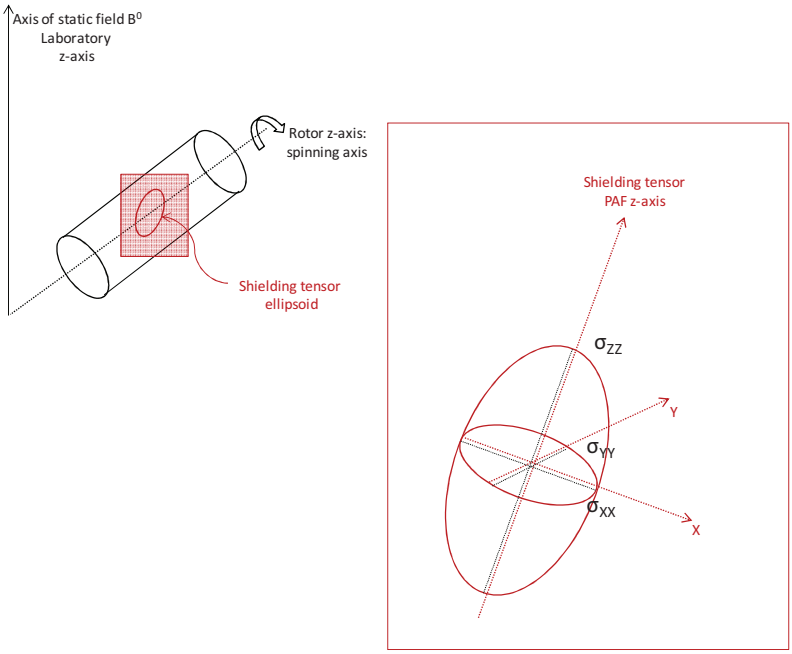

Fig. 2.3:
Orientation dependence of the chemical shielding. The chemical shielding tensor can be represented as an ellipsoid in its principal axis frame (PAF).

The effective field $\underline{B}^{eff}$ at the site of a nucleus is the sum of the external field $\underline{B}^{0}$ and the induced field $\underline{B}^{ind}$

$$\underline{B}^{eff} = \underline{B}^{0} + \underline{B}^{ind} = \underline{B}^{0} (1 - \sigma) .$$

$\underline{B}^{ind}$ is in the order of 10^{-4} of the static external field $\underline{B}^{0}$. However, $\underline{B}^{eff}$ is characteristic for a given crystallographic site, resulting in a slightly shifted resonance frequency.

$$\nu^{eff} = \nu^{0}\,(1-\sigma)\,.$$

By introducing the definition of the chemical shift δ

$$\delta = \frac{\nu^{eff} - \nu^{ref}}{\nu^{ref}} * 10^{6}$$

the $\underline{B}^{0}$ dependence of the resonance shift is removed. Additionally, the originally small effect of the chemical shielding is multiplied by a factor 10^{6}. δ is defined in units of part per million (ppm), ν^{ref} is the resonance frequency of the nucleus in a reference compound. Resonances that tend towards negative values of the δ (ppm) scale are termed *shielded* or *shifted upfield*. Resonances that tend towards positive chemical shift values (ppm) are termed *deshielded* or *shifted downfield*.

2.1.2c) Dipolar coupling

Due to its dipolar magnetic moment, each nuclear spin I generates a magnetic field surrounding it. Neighboring nuclear spins interact with this nuclear field directly through space. Each spin I is the source of a magnetic field and, in turn, experiences those generated by neighboring spins S. In the case of homonuclear dipolar coupling the spins I and S are of the same species. In the case of heteronuclear dipolar coupling the spins I and S are different.

The dipolar interaction can be described by substituting the quantum mechanical magnetic moment operator into the classical expression for the interaction between two point magnetic dipoles

$$\hat{H}_{dd} = -\left(\frac{\mu_0}{4\pi}\right)\gamma_I\gamma_S\hbar\left\{\frac{\underline{I}\bullet\underline{S}}{r^3} - 3\frac{(\underline{I}\bullet\underline{r})(\underline{S}\bullet\underline{r})}{r^5}\right\}$$

where I and S are the spin magnetic moments with their respective gyromagnetic ratios γ_I and γ_S. $\hbar$ is Planck's constant and μ_0 is the permittivity of the vacuum. r is the internuclear distance between I and S.

This description of dipolar coupling illustrates best that the strength of the dipolar interaction between two nuclei depends in first approximation on the inverse of the cubic distance between them, that is $\widehat{H}_{dd} \propto \frac{1}{r^3}$.

Dipolar coupling does not have any isotropic contribution. Its orientation dependence is of the form

$$(3\cos^2\theta - 1)$$

and hence it averages to zero under magic angle spinning.

Since the dipolar interaction between two nuclei depends in first approximation on the inverse of the cubic distance between them, $\widehat{H}_{dd} \propto \frac{1}{r^3}$, it can be exploited to probe spatial proximities between nuclei. Therefore, the dipolar interaction can be *reintroduced* by sequences like RFDR, HMQC, REDOR or REAPDOR. In particular REDOR and REAPDOR can be employed to achieve information about the number and the distance between heteronuclei in spatial proximity to each other.

2.1.2d) Scalar coupling (J-coupling)

Nuclear spins interact with each other via the bonding electrons they share. The terms scalar coupling or J-coupling are frequently used for this indirect coupling. The participation of the bonding electrons gives rise to an orientation dependence that is different from the one for dipolar coupling. As a result, there exists an isotropic component that contributes to scalar coupling and persists even under magic angle spinning conditions in solids or Brownian motion in liquids.

Scalar coupling is mainly observed in liquid state NMR. There it gives rise to multiplet signals splitted into resonances that are separated by the coupling constant J (in units of Hz).

In solid-state NMR, scalar coupling is a relatively weak interaction. During the last decade, HMQC probing scalar coupling in solid-state NMR has been introduced (J-HMQC; Lesage, 1998). It enables selective detection of chemical bonds between heteronuclei.

2.1.2e) Electric quadrupole coupling

All nuclei with a spin $I > 1/2$ have a non-spherical charge distribution that gives rise to a nuclear electric quadrupole moment that interacts with the electric field gradient at the site of the nucleus. This interaction can be described in Cartesian tensorial form

$$\hat{H}_Q = \frac{eQ}{2I(2I-1)\hbar} \underline{I} \bullet \underline{\underline{V}}^{PAF} \bullet \underline{I}$$

Q being the quadrupolar moment of the nucleus, $\underline{I}$ its nuclear spin vector and $\underline{\underline{V}}^{PAF}$ the traceless electric field gradient tensor. $\underline{\underline{V}}^{PAF}$ is defined in its principal axis frame (PAF). Quadrupolar coupling is not completely removed by MAS. A second-order term persists, giving in many cases rise to characteristically broadened resonances that can be characterized by the quadrupolar coupling constant C_Q and the asymmetry parameter η_Q.

The asymmetry parameter η_Q characterizes the shape of the $\underline{\underline{V}}^{PAF}$ interaction tensor ellipsoid

$$\eta_Q = \frac{V_{xx}^{PAF} - V_{yy}^{PAF}}{V_{zz}^{PAF}}$$

and covers values from 0 to 1.
The quadrupolar coupling constant

$$C_Q = \frac{e^2 qQ}{\hbar}$$

can be defined in units of MHz.

In practice, C_Q indicates the strength of the quadrupolar coupling between the nucleus and the electric field gradient of its proximate surroundings. It determines the linewidth of the NMR signal. η_Q is a measure for the electronic symmetry of the proximate environment and gives rise to the characteristic shape of the NMR signal in the MAS dimension.

For the study of binary and ternary phosphate glass systems Na_2O-P_2O_5 and Na_2O-Al_2O_3-P_2O_5, ^{17}O, ^{23}Na and ^{27}Al represent quadrupolar nuclei whose investigation by solid-state NMR is of particular interest.

2.2 NMR probe nuclei

In the following section, the probe nuclei employed for the study of hydrogen sodium phosphates and the weathering of model phosphate glass systems will be presented. Emphasis lies on the information about the local structure that can be gained from 1D NMR experiments.

Table 2.1:
NMR probe nuclei used in the frame of this work (natural abundance, gyromagnetic ratio and sensitivity with respect to ^{1}H).

Nucleus	Spin	Quadrupole moment (mb)	Natural abundance (%)	γ (MHz / T)	Sensitivity (wrt. ^{1}H)
^{31}P	1/2	-	100	17,226	$6{,}642*10^{-2}$
^{1}H	1/2	-	99.985	42,553	1
^{17}O	5/2	-25,6	0.037	5,774	$1{,}081*10^{-5}$
^{27}Al	5/2	146,6	100	11,102	$2{,}070*10^{-1}$

2.2.1 ^{31}P as a probe nucleus

The phosphate units present in the studied phosphate glasses were identified by comparing their isotropic chemical shift δ ^{31}P (ppm) with those of known phosphate structures. In phosphate glasses, the isotropic chemical shift δ ^{31}P (ppm) can be associated at two main influences: the degree of condensation of the respective phosphate unit Q^n and the nature of network modifying or network forming atoms present in the phosphate glass. First, Q^n units tend to be more shielded with higher degree of condensation. Second, ^{31}P sites become more shielded with increasing character of covalence between the network modifying or -forming atom and its neighboring oxygen (P-O-M).
The chemical shift ranges for the various Q^n units are presented in *Fig. 2.4*.

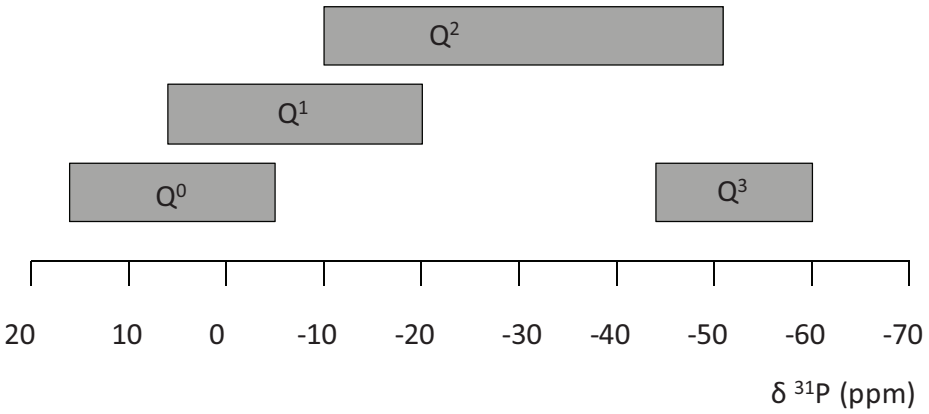

Fig. 2.4:
^{31}P chemical shift ranges for various degrees of polymerization.

2.2.2 ^{27}Al as a probe nucleus

^{27}Al experiences quadrupolar coupling with the EFG of its proximate environment. However, due to its high natural abundance and its fast relaxation times ^{27}Al is a favorable NMR nucleus.
The chemical shift of ^{27}Al is determined by its coordination state and the nature of the atoms present in its first sphere of coordination. The chemical shift range reaches from about -60 ppm to 80 ppm. 1D ^{27}Al NMR spectra are mainly employed to distinct between the three different coordination states, AlO4, AlO5 and AlO6. The characteristic resonance regions are shown in *Fig. 2.5*.

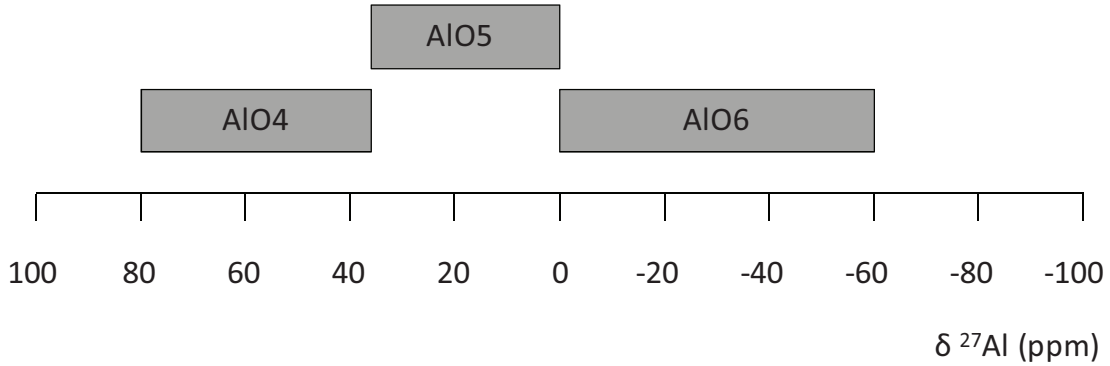

Fig. 2.5:
^{27}Al chemical shift ranges for different coordination states of aluminum.

2.2.3 ^{17}O as a probe nucleus

Of the three stable isotopes of oxygen, only ^{17}O is accessible to NMR. It is a quadrupolar nucleus of extremely low natural abundance and low gyromagnetic ratio *(Tab. 2.1).* Hence, it is necessary to employ high resolution NMR techniques such as MQMAS, DOR or DAS and to use ^{17}O-enriched samples in combination with high static fields to overcome these three obstacles.

However, ^{17}O exhibits a large chemical shift range that reaches in case of hydrogenated sodium phosphates from -40 ppm to 140 ppm. The quadrupolar interaction (η_Q, C_Q; Chap. 2.1.2e) can, in combination with the chemical shift, provide information about the immediate surroundings of the nucleus. As an example, the quadrupole coupling interaction has been reported to be a strong function of the covalency of the metal-oxygen bond (MacKenzie2002). In Chapter 3, chemical shift in combination with quadrupolar parameters will be used to establish systematic relationships between ^{17}O NMR parameters and structure for a group of crystalline sodium and sodium hydrogen phosphate compounds.

^{17}O NMR is sensitive to short-range interactions of the oxygen atoms that are located throughout the glass network. These oxygen atoms, in turn, are the centers of structural change when alteration of an oxide glass occurs. Therefore, in Chapter 4, ^{17}O has been implemented as a selective isotropic probe to monitor the incorporation of H_2O in a weathering $NaPO_3$ glass.

2.2.4 ^{1}H as a probe nucleus

Fast relaxation times, its natural abundance of nearly 100% and its high gyromagnetic ratio render ^{1}H attractive for solid state NMR. However, ^{1}H-^{1}H dipolar coupling must be overcome by implementation of homonuclear decoupling or spinning the sample at very fast spinning speeds.

1D ^{1}H NMR is useful for the speciation of the protons in the weathered glass structure. ^{1}H nuclei from H_2O vapor may either be present in intact structural hydrate water or as surface-adsorbed H_2O species. Alternatively, they may be part of hydroxyl groups (-OH) or take the form of structural acid protons.

The chemical shift range of ^{1}H in hydrous phosphate glasses reaches from about 0 ppm to about 20 ppm. ^{1}H in intact water molecules gives rise to signals in the range of 0 to 10 ppm whereas (-OH) hydroxyl groups exhibit resonances in the range from 10 to 20 ppm. With increasing hydrogen bonding strength of the protons involved (-OH…$^{-}$O), the nucleus is deshielded and its resonances are shifted upfield (Xue2009).

In spectra exhibiting a number of spinning sidebands, the chemical shielding anisotropy reflected in the spinning sideband intensities may be exploited to distinct more symmetric (-OH) sites from H_2O sites.

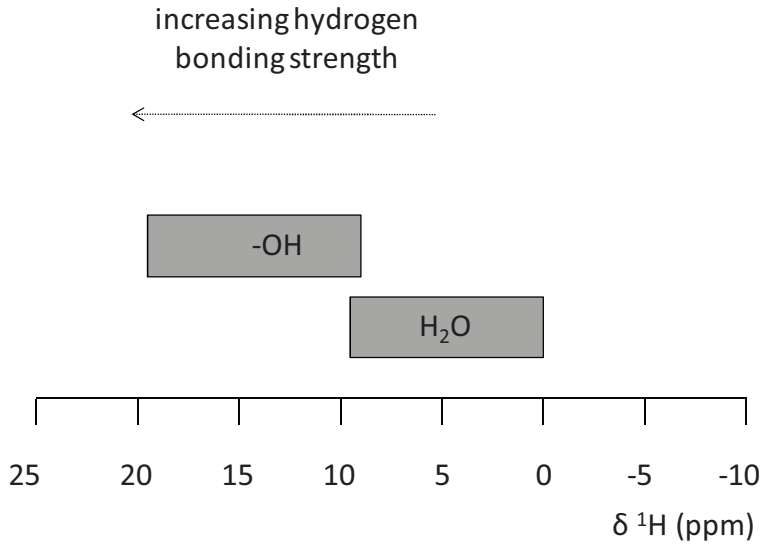

Fig. 2.6:
^{1}H chemical shift ranges for H_2O and protons involved in hydrogen bondings (-OH groups).

2.3 NMR pulse sequences

2.3.1 MQMAS (Multiple-quantum magic angle spinning)

High resolution spectra of quadrupolar nuclei

Quadrupolar nuclei conserve the second-order anisotropy under MAS. Spinning the sample under the magic angle ($\theta_R = 54,74°$) averages the Legendre polynome $P_2(\cos\theta_R)$ and hence their first-order anisotropy to zero, but not $P_4(\cos\theta_R)$.

Two main strategies exist to eliminate the remaining second-order anisotropy contribution to quadrupolar interaction. One consists in spinning the sample at angles of $\theta_R = 30,56°$ and $\theta_R = 70,12°$ to fulfill the condition $P_4(\cos\theta_R) = 0$. This can be done by employing DAS (dynamic angle spinning) between alternating angles of $\theta_R = 30,56°$ and $\theta_R = 70,12°$ (Llor1988) or by employing DOR (double rotation) that is spinning two rotors simultaneously at $\theta_R = 30,56°$ and $\theta_R = 70,12°$ (Samoson1988). Both techniques require special probeheads and have not fund widespread application.

MQMAS (Frydman1995) uses a second strategy to achieve high-resolution NMR spectra that is to correlate the evolution of multiple quantum coherence with the evolution of single quantum coherence in order to annihilate the remaining anisotropy contribution. Since it is available on modern solid-state NMR spectrometers with common MAS probeheads and without crucial technological limitations, MQMAS has become *the* routine technique for the acquisition of high-resolution NMR spectra of quadrupolar nuclei.

The basic MQMAS pulse sequence proposed by Frydman (Frydman1995, Medek1995) is illustrated in *Fig. 2.7* together with the corresponding coherence transfer pathway.

The first pulse p_1 excites multiple-quantum coherence $+m \rightarrow -m$ that evolves during the evolution time t_1. This multiple quantum coherence is selected by appropriate phase cycling. At the end of t_1, p_2 transfers the remaining multiple-quantum coherence into single quantum (-1) coherence. Evolution is allowed for a second period kt_1 where k is derived from the following expression:

$$\frac{\left[18I(I+1)-34{m_{MQ}}^2-5\right]m_{MQ}}{\left[18I(I+1)-34{m_C}^2-5\right]m_C}$$

with nuclear spin I, the quantum number defining the initial level in the MQ transition m_{MQ} and the quantum number defining the initial level for the central transition m_C. Under these conditions, the evolution of second-order anisotropy during the first evolution period t_1 is annulated.

At the end of kt_1 an echo without first- and second-order anisotropic contributions is recorded. A two-dimensional dataset is collected by incrementing t_1. After Fourier transformation, a two-dimensional frequency NMR spectrum of the quadrupolar nucleus is obtained where the purely isotropic high-resolution dimension f_1 is correlated with the anisotropic powder pattern in the f_2 dimension (MAS dimension). The isotropic signals in the high-resolution dimension consist of contributions from multiple-quantum and single-quantum isotropic shifts.

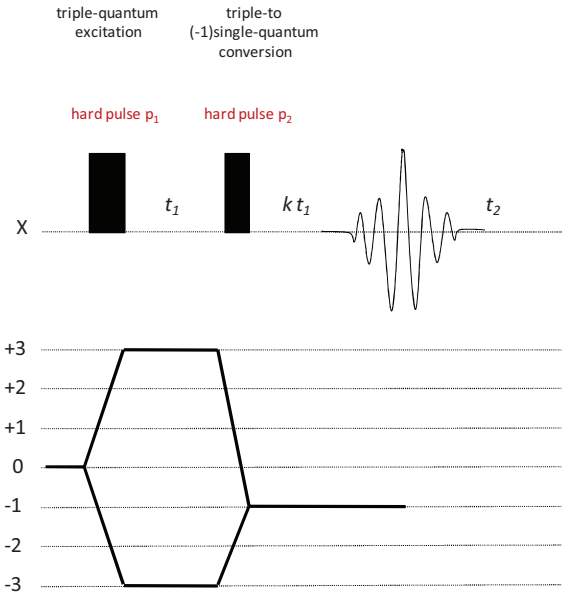

Fig. 2.7:
Initial MQMAS pulse sequence (Frydman1995) and corresponding coherence transfer pathway (bottom). This example illustrates best the working scheme of the MQMAS technique.

In order to obtain pure absorption spectra, a z-Filter three-pulse MQMAS sequence has been proposed by Amoureux *et al.* (Amoureux, 1996; *Fig. 2.8*). Before echo acquisition, MQ coherence is transferred to 0-coherence along $\underline{B}_0$ where it evolves during a second evolution period zt. An additional selective pulse then transfers the remaining magnetization into observable magnetization in the xy plane (-1 coherence). The crucial advantage of this sequence is the symmetric coherence transfer pathway. It allows for the efficiency of coherence transfer being the same for $\pm 3 \rightarrow 0$.

Hence, the amplitudes of both coherence pathways are the same in the final FID collected at t_2 and spectral distortions can be avoided.

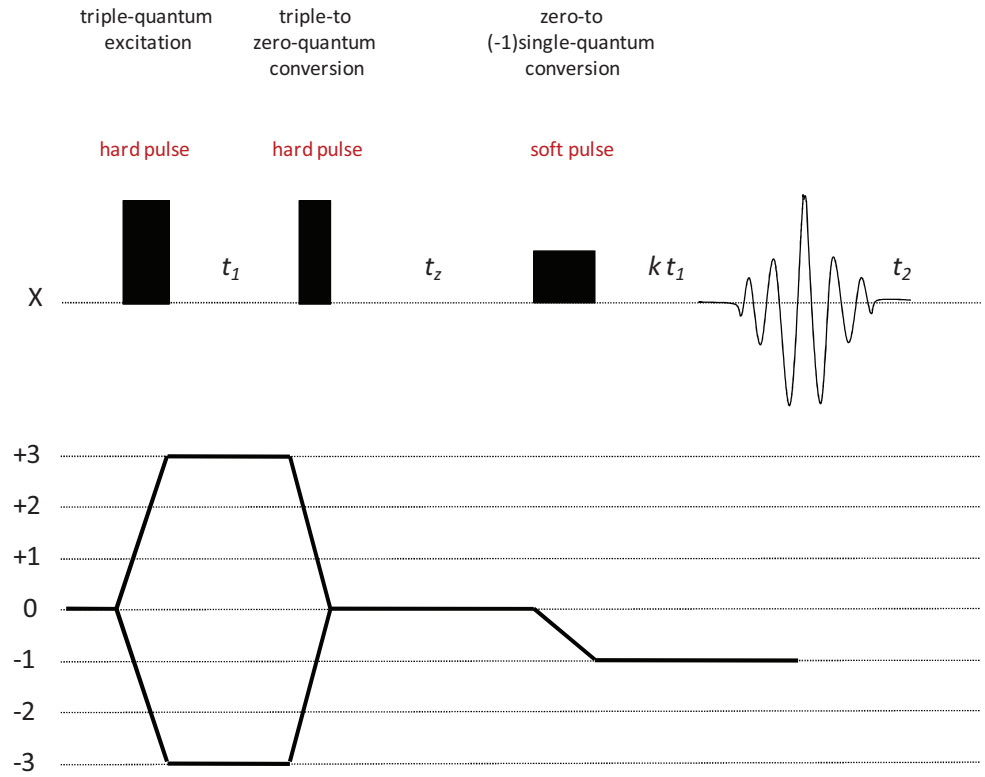

Fig. 2.8:
MQMAS sequence with z-Filter (Amoureux1996). The symmetric coherence transfer pathways allow for undistorted acquisition of whole echoes.

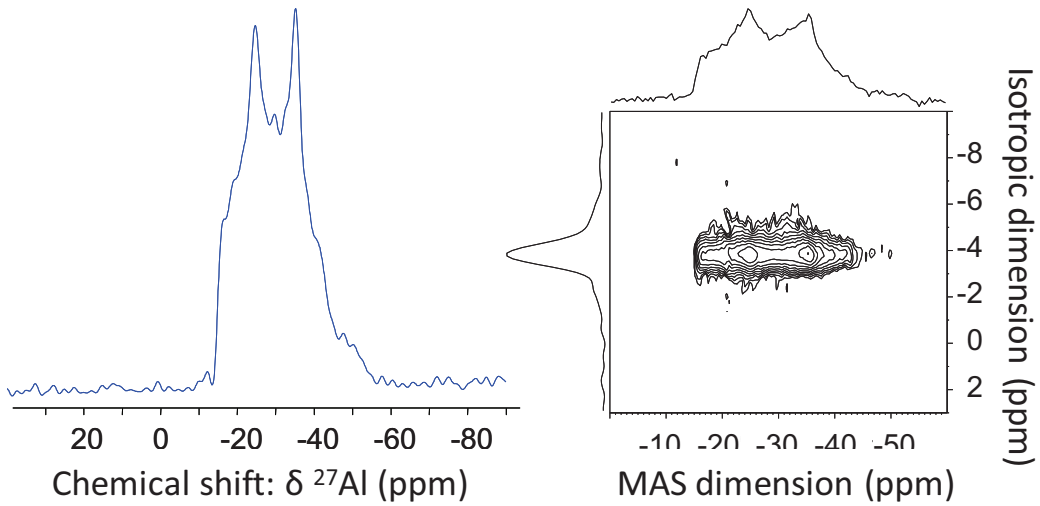

Fig.2.9:
1D ^{27}Al MAS NMR spectrum and 2D ^{27}Al 3Q-MAS spectrum of $Na_7(AlP_2O_7)_4PO_4$. The latter correlating anisotropic information from the first (MAS dimension) with high resolution information (high-resolution dimension; isotropic dimension).

The excitation efficiency for the generation of multiple quantum coherence depends on the crystallite orientation and on the quadrupolar coupling constant C_Q of the chemical site. As a result, MQMAS spectra are never quantitative and certain sites may not or only weakly be represented. However, a quantitative interpretation of MQMAS spectra is accessible by simulating the two-dimensional spectra using the DFT / GIPAW calculation approach. These simulations take the differences in excitation efficiency into account and lead to exploitable results for complex disordered mixtures. An example will be presented in Chapter 3 for ^{17}O 3QMAS spectra of weathered sodium phosphate glass.

In the frame of this thesis, MQMAS has been used for the acquisition of high-resolution spectra of ^{17}O in crystalline phases (Chap. 3) and in weathered phosphate glasses (Chap. 3, Chap. 4).

2.3.2 RFDR (Radio frequency driven dipolar recoupling)

RFDR exploits the homonuclear dipolar interaction between two spin-1/2 nuclei. It was introduced by Bennett et al. (Bennett1992).

The RFDR pulse sequence is illustrated in *Fig. 2.10*. An initial 90° pulse creates transverse magnetization. Single-quantum coherence is allowed to evolve during t_1 and subsequently converted into longitudinal magnetization (zero-quantum coherence) by a second 90° pulse. During the following mixing period, the longitudinal magnetization undergoes a series of 180° pulses. The number of 180° pulses / rotor cycles $[\frac{\tau_R}{2} - 180° - \frac{\tau_R}{2}]$ is called the mixing time. It is a crucial parameter in the RFDR experiment, since it determines the scope of the probed dipolar coupling. At the end of the longitudinal mixing period, a 90° pulse transfers longitudinal magnetization (zero-quantum coherence) into observable transverse magnetization (-1 coherence).

RFDR is a robust technique. The longitudinal mixing prevents significant loss of observable magnetization that could occur by “forbidden” transverse mixing during a transverse mixing period. Additionally, RFDR allows for effective dipolar recoupling over a large spectral window.

Fig. 2.11 shows a simulated RFDR spectrum together with the corresponding 1D MAS spectrum of a compound consisting of two different crystalline phases. *Fig. 2.11* illustrates the case where the mixing time was chosen to be sufficiently long to allow transfer of magnetization between all crystallographic sites in the same crystalline phase. All diagonal peaks (ω_A, ω_A; ω_B, ω_B; ω_C, ω_C) arise from magnetization transfer between crystallographically identical sites.

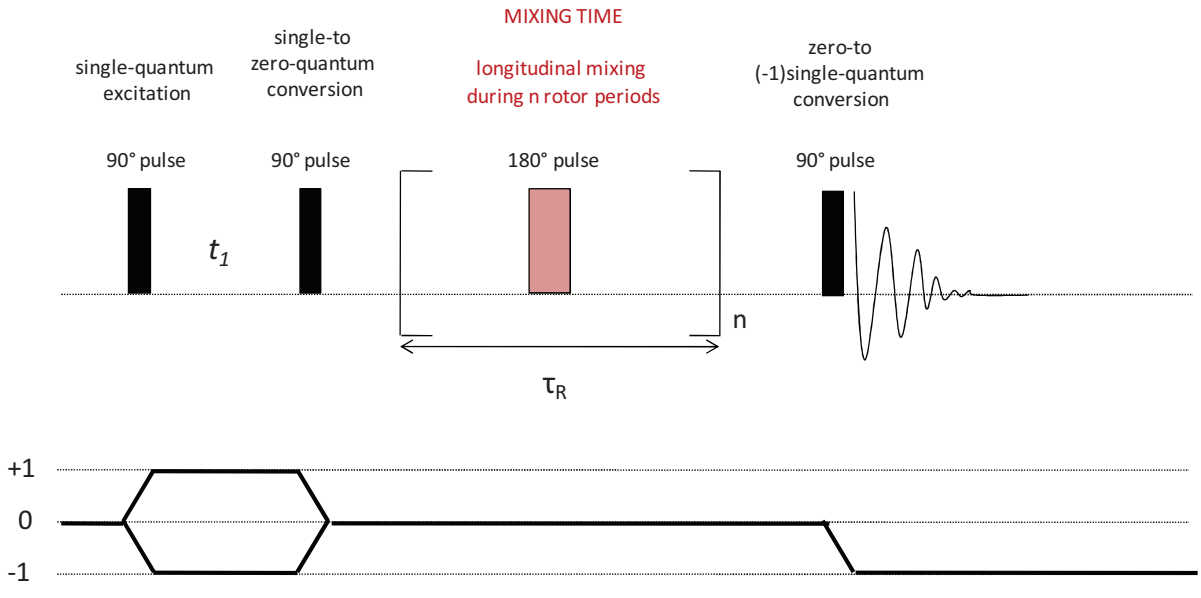

Fig. 2.10:
RFDR pulse sequence (Bennett1992) and corresponding coherence transfer pathway.

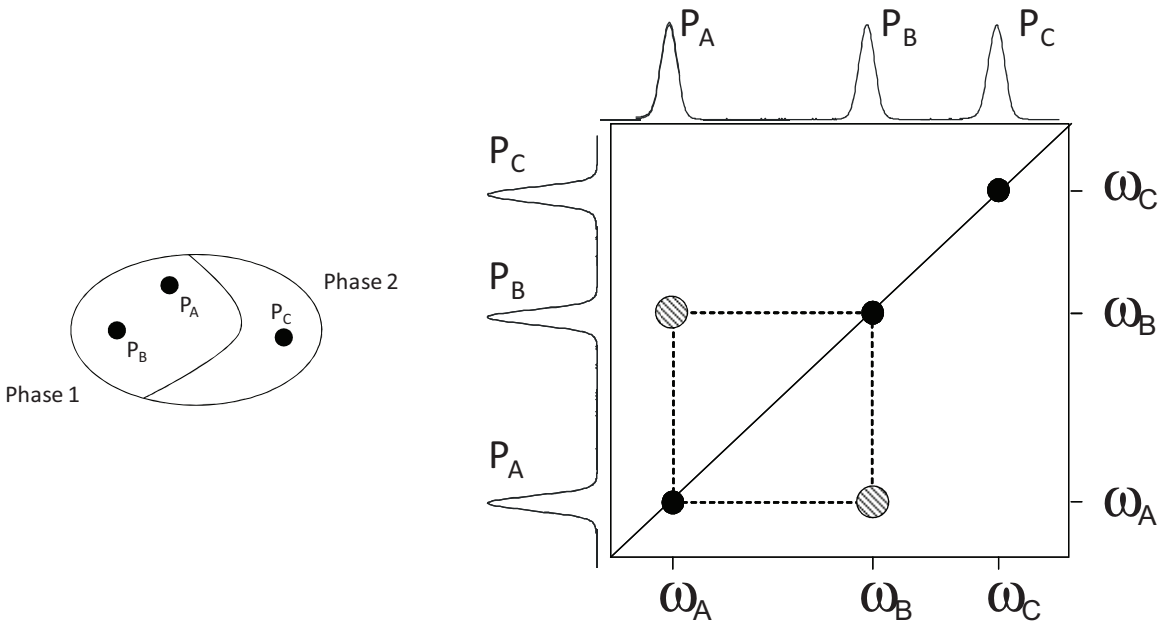

Fig. 2.11:
Simulated 2D RFDR spectrum (right side).For better examination, the 1D projections are given on the horizontal and the vertical axis.Off diagonal cross-peaks result from crystalline sites P_A and P_B that are both from Phase 1.

Sites P_A and P_B give rise to off-diagonal correlation signals at (ω_A, ω_B) and (ω_B, ω_A), and thus they are part of the same phase, phase 1. Site P_C does not give rise to any correlation peak with P_A or P_B. It is the single crystallographic site of another crystalline phase, phase 2.

In the frame of this thesis, RFDR has been used in the context mentioned above (Chapter 4). Different phases that give rise to signals in 1D ^{31}P MAS spectra of weathered $NaPO_3$ glass should be

distinguished and their corresponding peaks should be attributed. Similar to the work published by Alam *et al.* (Alam2005), the RFDR sequence was preceded by a ^{31}P-{^{1}H} cross-polarization (CP) transfer (see 2.3.3) in order to minimize experimental time and to detect selectively signals from ^{31}P sites in spatial proximity to ^{1}H nuclei.

2.3.3 CP (Cross-polarization)

Cross-Polarization exploits the dipolar interaction between two heteronuclear spins I and S.
Originally the technique has been used to enhance sensitivity of dilute spins by allowing cross-polarization magnetization transfer from an abundant species (Hartmann1962). At present, CP is mainly employed to probe spatial proximity between two spin species either in one or two dimension(s). CP can be considered as a proximity-filtering sequence, too.
It is noteworthy that the relaxation delay of the CP experiment is determined by the relaxation time of nucleus I . Thus, careful choice of the spy nucleus can reduce experimental time significantly.

The cross-polarization pulse sequence is illustrated in *Fig. 2.12 (left side)*. A first 90° pulse transfers I magnetization into the xy-plane where it is "spin locked". During the contact time spins I transfer magnetization to spins S in the xy-plane. This transfer of magnetization is possible, if the Hartmann-Hahn condition is fulfilled. The energy gaps between two spin states have to be equal for both nuclei. During acquisition of the spectrum of nucleus S , proton decoupling is usually applied.
The 2D MAS D-HETCOR sequence allows for correlating through space connectivities between two heteronuclei by introducing an additional evolution time t_1 (*Fig. 2.12; right side*).

In practice, the Hartmann-Hahn condition has to be adapted to the experimental conditions (Duer2004). For two spin-1/2 nuclei,

static conditions: $\gamma^I B^I_{RF} = \gamma^S B^S_{RF}$ and $\omega^I_{RF} = \omega^S_{RF}$

have to be distinguished from

magic-angle spinning: $\omega^I_{RF} = \omega^S_{RF} + n \cdot \omega_{MAS}$.

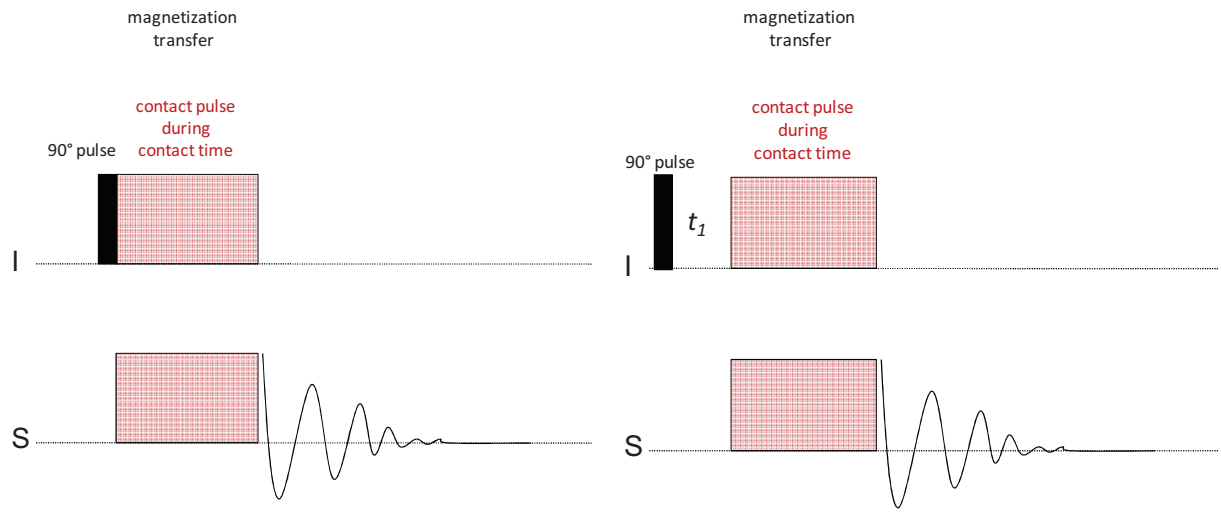

Fig. 2.12:
1D cross-polarization pulse sequence (CP; left side) and 2D cross-polarization sequence for heteronuclear correlation spectra based on CP transfer (CP-HETCOR; right side).

For cross-polarization transfer from spin I to a quadrupolar nucleus S, two regimes have to be distinguished for fulfillment of the Hartmann-Hahn condition: the adiabatic regime and the sudden regime (Duer2004, Amoureux2009). In most cases, in particular at fast MAS speed, the sudden regime is used. The corresponding Hartmann-Hahn matching condition is:

$$\omega_{RF}^{I} = \left(S + \frac{1}{2} \right) \omega_{RF}^{S} + n \cdot \omega_{MAS} \,.$$

Optimization of this type of experiments is very delicate, since selective excitation of the central transition coherence of the quadrupolar nucleus S is needed. Therefore, very weak RF fields have to be employed. This in turn renders the CP transfer very sensitive towards offset effects. Often, it is necessary to perform CPMAS D-HETCOR involving quadrupolar nuclei for several chemical shift offsets.

Another aspect for CP optimization is the contact time. It is a crucial parameter of each experiment, since it influences the scope of the dipolar coupling and hence the distance selectivity of the experiment. Short contact times allow for magnetization transfer to nuclei in close proximity, exclusively. Long contact times allow for nuclei at longer distances to be probed.

For the weathering of phosphate glasses, CP experiments involving ^{1}H are of considerable interest. As an example, ^{31}P-{^{1}H} CP experiments were performed in the frame of this work to detect protonated ^{31}P sites in weathered $NaPO_3$ glass selectively. In a similar experimental setup, variable contact times

were used to distinct surface water protons at longer distances from those incorporated into the close network structure of a weathered zinc ultraphosphate glass by Mercier *et al.* (Mercier1999). Wenslow and Mueller employed 2D ^{31}P -{^{1}H} CP experiments to characterize various protonated ^{31}P sites at the dissolution surface of alterated sodium phosphate glass (Wenslow1998).
More generally, 2D CP-HETCOR is a widespread correlation technique in solid-state NMR. As an example, it has been used to correlate ^{31}P chemical shifts with ^{27}Al shifts by Wegner *et al.* (Wegner2008) in order to probe connectivity types in a series of aluminophosphate glasses.

2.3.4 HMQC (Heteronuclear multiple-quantum correlation)

Initially, HMQC has been used to probe chemical bondings between heteronuclei (J-HMQC) in liquid state NMR. Nowadays, HMQC pulse sequences probing dipolar coupling (e.g. D-SFAM-HMQC) and scalar coupling (J-HMQC) are accessible for solid-state NMR. In particular, D-SFAM-HMQC can be an alternative to 2D CPMAS D-HETCOR techniques (Amoureux2009).

Understanding of the HMQC sequence demands knowledge of the product operator formalism and shall therefore not be considered in detail in the frame of this thesis.

All *D*-HMQC sequences require additional pulse blocks for the reintroduction of the dipolar coupling. D-SFAM-HMQC makes use of the SFAM recoupling block. It is a robust sequence for the acquisition of 2D correlation spectra, presenting several advantages over the conventional CP HETCOR technique presented above (see 2.3.3). First, for heteronuclear correlation experiments involving quadrupolar nuclei, optimization of the experimental conditions is not as delicate as in the case of 2D CPHETCOR. The sensitivity towards offsets effects can be avoided and one single (SFAM-)D-HMQC experiment can cover the entire range of chemical shifts in a sample. Second, experimental time is further reduced by enhanced sensitivity of the method (Amoureux2009).

In the frame of this work, ^{27}Al-{^{31}P} D-SFAM-HMQC has been used for acquisition of 2D heteronuclear correlation spectra of Na_2O-Al_2O_3-P_2O_5 glass systems (Chapter 5). As recommended by Amoureux *et al.* (Amoureux2009), the quadrupolar nucleus, ^{27}Al has been chosen to be the observed nucleus. As mentioned above, the recent sequence allowed for significant reduction of experimental time whilst providing the same information as a 2D CP HETCOR experiment.

2.3.5 Techniques for *measuring* heteronuclear dipolar couplings: REDOR (Rotational-echo double resonance)

All techniques for *measuring* heteronuclear dipolar coupling between an observed spin I and a coupled spin S are based on echo experiments (Duer2004). Under MAS, the dipolar coupling would be refocused over each rotor period. By applying pulses on spin S, this refocusing is distorted.
The obtained curves in experiments such as REDOR (and similar pulse sequences) provide a means to measure to which extent the complete refocusing of the echo is prevented by the pulses applied on S. This, in turn, is a measure of the dipolar coupling strength.

As an example, the REDOR pulse sequence that is used to measure the strength of dipolar coupling between two spin-1/2 nuclei is illustrated in *Fig. 2.13*.
A 90° pulse creates transverse magnetization on spin I. During one rotor period τ_R dephasing of the transverse magnetization occurs. At times $2\tau_R$, $4\tau_R$, … 180° pulses are applied to refocus inhomogeneous interactions such as heteronuclear dipolar coupling. The remaining echo intensities at $2\tau_R$, $4\tau_R$, … are recorded as a reference dataset. The loss of echo intensity with increasing number of rotor periods is caused by transverse relaxation.
In a second step, echo intensities at $2\tau_R$, $4\tau_R$, …. are recorded again. This time, a series of 180° pulses are applied on spin S. They invert the phase of dipolar coupled spins S. The latter mediate this phase distortion via dipolar coupling to spins I. As a consequence, I echo intensities ($2\tau_R$, $4\tau_R$, ….) in the second REDOR curve are not only reduced by transverse relaxation, but also by incomplete refocusing due to the experienced phase distortion. Its extent is a measure for the strength of dipolar coupling between I and S.

In the frame of this thesis, REDOR has been implemented in order to detect differences in the strength of dipolar coupling between two heteronuclei (Chapter 5) in weathered Na_2O-Al_2O_3-P_2O_5 glass systems.

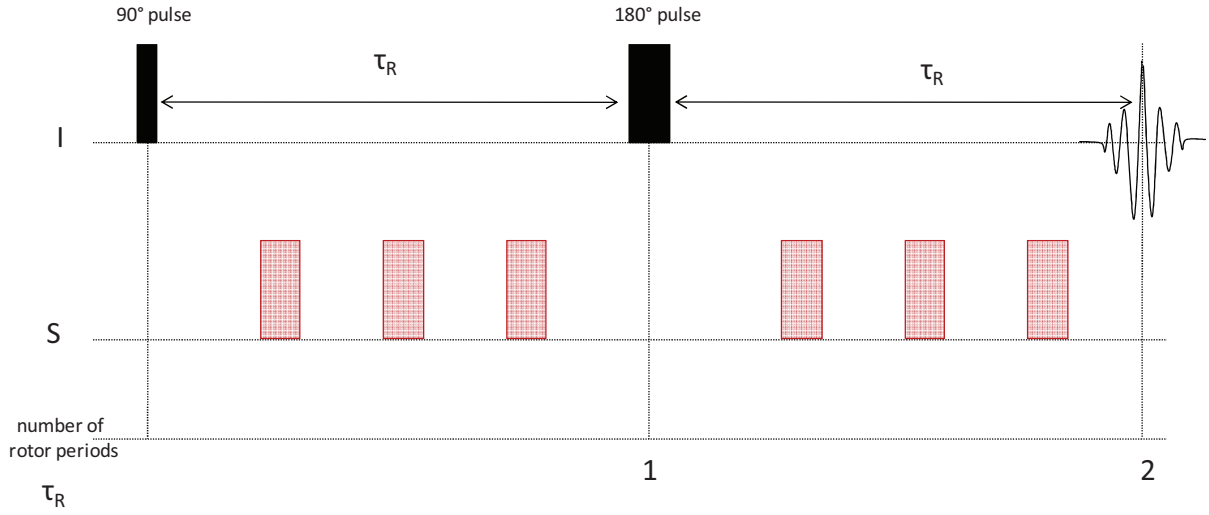

Fig. 2.13:
Schematic representation of the REDOR pulse sequence.

2.4 Calculation of NMR parameters

It is possible to compute NMR parameters in extended solids using DFT and periodic boundary conditions. The GIPAW approach (Pickard2001) reconciles the prediction of highly accurate absolute chemical shifts with the use of pseudopotentials and plane wave basis sets. In the frame of this work, a combined DFT / GIPAW approach has been used in order to calculate NMR chemical shift of ^{17}O and the quadrupole parameters of the nucleus in sodium hydrogen phosphate phases. Subsequently, ^{17}O 3QMAS spectra have been simulated.

In the following, the most important concepts shall be introduced in a brief manner.

2.4.1 Density functional theory (DFT)

Conventional approaches to quantum chemistry use the wave function as the central quantity. The latter being a good approximation to the ground state of the examined system, one can obtain all information about a particular state of the system of interest. In contrast to conventional approaches, DFT uses the electron density functional to reach a solution of the Schrödinger equation and to describe the state of a system of interest. The electron density provides the advantage to depend only on three spatial variables and to be therefore an object in the three-dimensional physical space.

The external potential is to (within a constant) a unique functional of the electron density. Since, in turn, the external potential fixes $\hat{H}$, we see that the full many particle ground state is a unique functional of the electron density (Hohenberg 1964; Kohn1965).

2.4.2 Pseudopotential approach (PAW and GIPAW formalism)

PAW is a general approach for calculation of all-electron properties from pseudopotential-based schemes (Blöchl1994). Pseudopotentials replace the Coulomb interaction of the core electrons by an effective potential. Instead, only valence electrons are taken into account. The interaction between the valence electrons and the ionic core is also taken into account by the pseudopotential. Outside a well chosen cutoff radius, the pseudo-wavefunctions correspond to the original all-electron wavefunctions.

The PAW (Blöchl1994) approach neglects the form of electronic wavefunctions near the nucleus. The pseudo-wavefunctions are chosen to be as smooth as possible in the core region, and the correct nodal structure of the wavefunctions is lost. This leads to a good approximation of total energies and properties for which the matrix elements are dominated by regions outside the core.

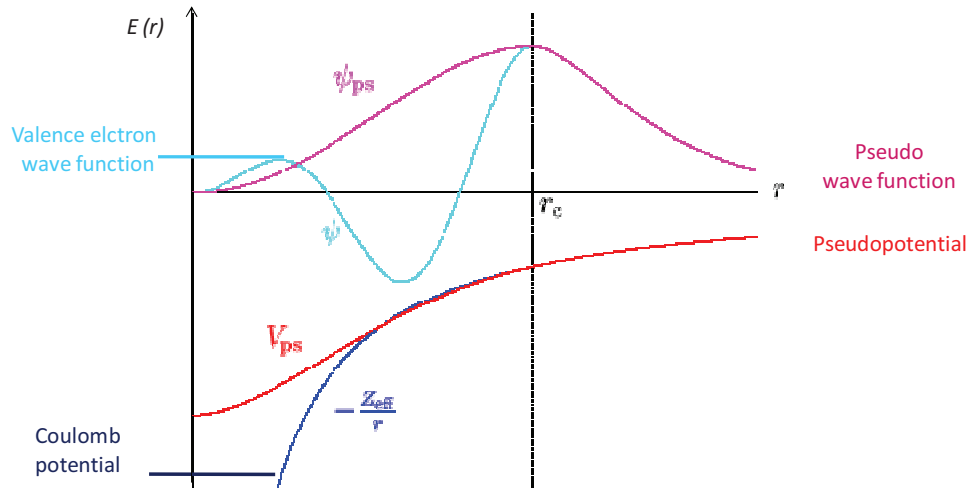

Fig. 2.14a:
Schematic diagram of the relationship between all-electron and pseudo- potentials and wave-functions. The strong Coulomb potential and core electrons (blue) are replaced by an effective pseudopotential (red). *The valence electron wave-functions that oscillate rapidly in the core (green) region are replaced by* pseudo-wave-functions *that vary smoothly in the core region (pink).*

However, it prevents a direct calculation of the properties that depend critically on the details of the wavefunction in the core region. Examples for those critically dependent properties are the electric field gradient at the site of the nucleus and NMR chemical shifts. In particular, chemical shifts require an accurate description of the induced currents near the nuclei.

Pickard and Mauri overcame this drawback of the PAW approach by extending the PAW formalism and introducing the gauge including projector augmented wave method (GIPAW) (Pickard2001). Calculations within the GIPAW formalism have been carried out by employing the PARATEC code (PARATEC).

2.4.3 Simulation of 2D NMR spectra

Charpentier and coworkers have proposed a simplified formalism for the analysis of coherence transfer processes in a rotating sample. All interactions and their time dependency are considered during the pulses, whereas computation efficiency has been considerably improved at the same time.

Based on this simplified formalism, a procedure for simulating MQMAS (as well as any 2D) NMR spectra has been introduced. As an example, it is possible to take into account the efficiency-dependence of multiple-quantum coherence excitation and -conversion on quadrupolar coupling constants. This allows for obtaining 'correct' signal intensity ratios in simulated MQMAS spectra.

2.4.3 The calculation protocol

Fig. 2.14b illustrates the calculation protocol step by step (grey).

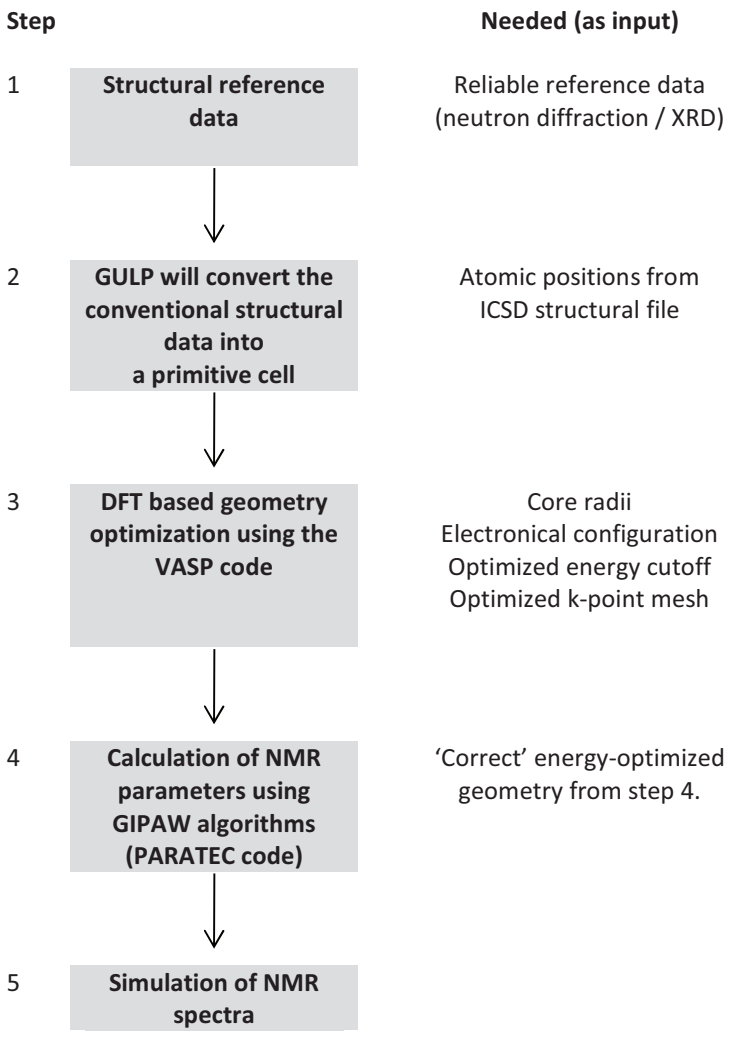

Fig. 2.14b:
Calculation protocol for ^{17}O NMR parameters.In a final step, 2D 3QMAS ^{17}O NMR spectra have been simulated using a software provided by Dr. T. Charpentier.

Step1: In order to achieve correct geometries, reliable structural reference data for geometry optimization have to be chosen from the Inorganic Crystal Structural Database (ICSD). In general, neutron diffraction data have been preferred over X-ray diffraction data, through XRD analysis, protons are quite invisible due to the large dependence of the scattering factor with the electron density. In step 2, structural parameters from the most suitable ICSD file are converted by GULP into a primitive cell structure. Thus, ideally, a smaller number of atoms still fully describe the structure. As a result, the computation time is minimized. In step 3, geometry optimization of the primitive cell structure is carried out. In step 4, NMR parameters were calculated using GIPAW algorithms (Pickard2001). Finally, in step 5, 2D 3Q MAS spectra have been simulated employing the simulation software developed by Charpentier and coworkers.

Acknowledgement:

We gratefully acknowledge Dr. T. Charpentier, CEA, IRAMIS (Gif-sur-Yvette, France) for providing the simulation program for simulation of ^{17}O 2D 3QMAS NMR spectra.

2.5 Micro-synthesis of ^{17}O-enriched *phase-pure* crystalline *hydrogen* phosphates

Owing to our interest in ^{17}O as a NMR probe nucleus, several ^{17}O-enrichment techniques have been developed and adapted in our group in the past.

Zeyer *et al.* (Zeyer2002) synthesized a series of ^{17}O-enriched x Na_2O - (100-x) P_2O_5 glasses by hydrolysis of PCl_5 and subsequent neutralization of $H_3P^{17}O_4$ with Na_2CO_3. As an example, final polymerization at 500°C and fusion at 800°C lead to sodium metaphosphate glass, $NaPO_3$. In 2006, Flambard *et al.* (Flambard2006) introduced a method for ^{17}O-enrichment under $H_2{}^{17}O$ vapor atmosphere at temperatures around 600°C. In this temperature regime, hydrolysis and condensation rates are accelerated and rapid enrichment can be achieved. However, this technique is only feasible for compounds that are thermally stable in the elevated temperature regime.

In the following, the synthesis protocol of phase-pure NaH_2PO_4 and $Na_2H_2P_2O_7$ shall be presented. In the present work, it has been introduced for the systematic ^{17}O NMR study of crystalline hydrogen phosphates (Chapter 3). So far, the synthesis of ^{17}O-enriched *phase-pure* reference phosphate compounds of this type has been limited to anhydrous phases (Prochnow2006). On a ml level, the synthesis presented below constitutes a challenge, since both hydrogen phosphate compounds are sensitive towards temperature fluctuations and the chosen hydrolysis route is strongly exothermic. E.g., condensation of NaH_2PO_4 into $Na_2H_2P_2O_7$ occurs within a relatively low temperature regime (Ghule2001). Moreover, phase-purity (>95%) of the orthophosphate is difficult to achieve on a ml level, since the quantity of $H_3P^{17}O_4$ is too small to determine the yield during step 1 of the synthesis of NaH_2PO_4 with exactitude. Hence, adjustment and optimization of the experimental parameters of this synthesis are time-demanding.

2.5.1a Synthesis of phase-pure NaH_2PO_4

For the synthesis of phase-pure NaH_2PO_4 hydrolysis of PCl_5 has been optimized on a ml level. This synthesis route provides the advantage that, in the ideal case, all oxygen atoms present in four ^{17}O-enriched water molecules are transferred into one H_3PO_4 molecule in the first reaction step. In step 2 of the synthesis procedure, oxygens in CO_2 and H_2O stem from Na_2CO_3.

Step 1: $$4\ H_2O + PCl_5 \rightarrow H_3PO_4 + 5\ HCl$$

Step 2: $$2\ H_3PO_4 + Na_2CO_3 \rightarrow 2\ NaH_2PO_4 + H_2O + CO_2$$

In **step 1**, reagent grade phosphorus pentachloride, PCl_5 (95%, Aldrich), was used together with ^{17}O-enriched water (40.6 %, Cortecnet) (Zeyer2002). The micro-synthesis was realized in the assembly shown in *Fig. 2.14*. Under a constant flux of dry nitrogen, 2.8 g of PCl_5 were added to 1.1 g of ^{17}O-enriched water. The dry gas was used to remove HCl and to avoid reaction of PCl_5 with atmospheric water. At the end of step 1, the ice-cooling was removed and the temperature was risen to 80°C in order to complete the hydrolysis reaction.

During **step 2**, the exothermic nature of the reaction had to be kept under control carefully by ice-cooling of the beaker containing the reaction mixture, *slow* mixing of the educts and permanent stirring. Thus, immediate condensation of newly generated NaH_2PO_4 into $Na_2H_2P_2O_7$ or uncontrolled reaction to $Na_4P_2O_7$ due to local excess of Na_2CO_3 could be circumvented. Further, the formation of unwanted products such as $Na_4P_2O_7$ could be avoided by taking into account the systematic yield loss occurring during reaction step 1. As a consequence, the quantity of Na_2CO_3 (99.5 %, extra pure, Acros) had to be reduced in step 2.

Systematically, a mixture of two crystalline phases, NaH_2PO_4 and $NaH_2PO_4{*}H_2O$, was obtained, as verified by X-ray diffraction. This mixture was subsequently dried under evacuated argon atmosphere at 40°C for 60 hours in order to obtain phase-pure NaH_2PO_4, exclusively.

2.5.1b Synthesis of phase-pure $Na_2H_2P_2O_7$

In **step 3**, complete condensation to ^{17}O-enriched pure crystalline sodium hydrogen pyrophosphate, $Na_2H_2P_2O_7$,

Step 3: $$2\ NaH_2PO_4 \rightarrow Na_2H_2P_2O_7 + H_2O$$

was achieved by heating ^{17}O-enriched phase-pure NaH_2PO_4 with controlled rate (1°C/min) up to 240°C (Ghule2001) and by maintaining this temperature for 45 min.

The purity of all crystalline ^{17}O-enriched sodium hydrogen phosphates was checked by powder X-ray diffraction and by 1D ^{1}H, ^{23}Na and ^{31}P NMR. It was greater than 95%.

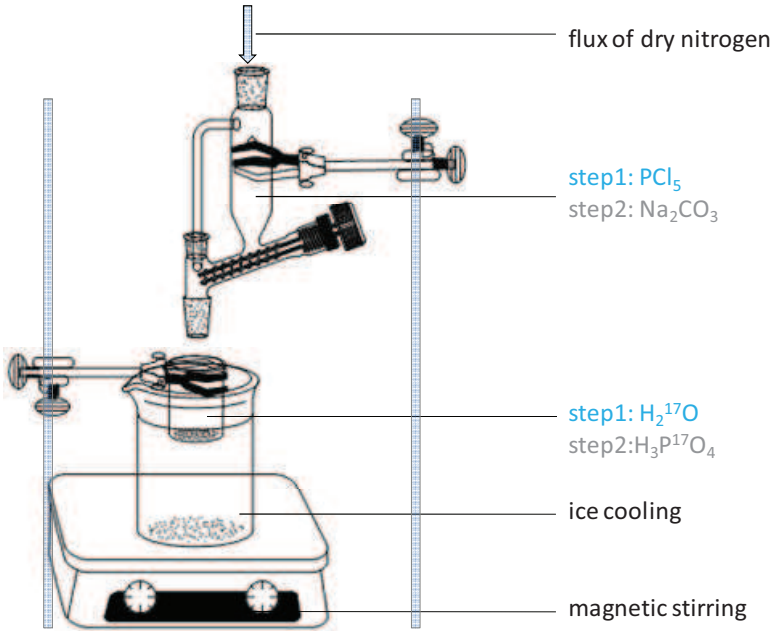

Fig. 2.14:
Assembly used for the synthesis of small amounts of ^{17}O-enriched NaH_2PO_4 by hydrolysis of PCl_5.

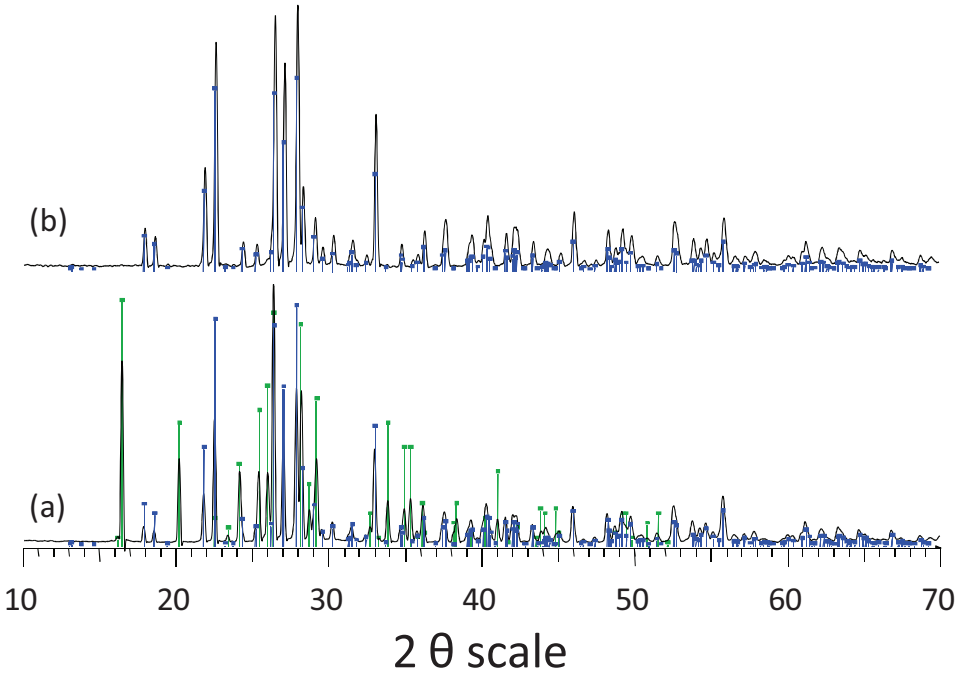

Fig. 2.15:
X-Ray diffractograms of ^{17}O-enriched crystalline hydrogen phosphates. Mixture of $NaH_2PO_4{*}H_2O$ and NaH_2PO_4 (a) that was obtained systematically immediately after synthesis. After drying, >95% phase-pure NaH_2PO_4 was obtained (b).

2.6 Weathering assays

The experimental conditions for the weathering assays on phosphate glasses (Chapter 4 and Chapter 5) had to be optimized with regard to costs, to parameters to obtain reproducibility and to appropriate kinetics. Experimental conditions for water vapor attack that were published in the literature served as a basis for the adjustment of the weathering conditions employed in the frame of this work. A recapitulation of the most important ones is given below.

In our group, Mercier *et al.* (Mercier1999) exposed zinc ultraphosphate glass to humid air at 140°C (88% relative humidity) in order to study the surface alteration mechanisms. Those studies did not need small water vapor reaction volumes, since ^{1}H and ^{31}P NMR were performed, exclusively.

In 2002, Masui *et al.* (Masui2002) weathered defined amounts of Na_2O-SiO_2 glass powders on a mg level (125-250 um) under an atmosphere saturated by water vapor at 80°C. Weathering times varied from 30 min to about 25 h.

Alam *et al.* (Alam2005) realized water vapor attack on powdered aluminophosphate glass systems at 50°C and 80% relative humidity in a controlled environmental chamber for 2 d to 7 d. Petri dishes were used as sample holders. After weathering, the samples were dried overnight in a vacuum chamber at 40°C to remove excess water and to prevent additional dissolution reactions from occurring during the subsequent NMR experiments. The samples were stored in desiccators when not being analyzed.

In the following, the weathering protocol for $NaPO_3$ and NaAlP-x is presented with emphasis on the most important points that had to be optimized:

2.6.1 Costs: Weathering in small reactors

The mass of $H_2{}^{17}O$ used for water vapor attack on glass powders should not exceed 1 g. At the same time, a controlled environmental chamber was needed for reproducible experiments. Hence, small glass reactors allowing for efficient weathering on a ml level were constructed in order to fulfill both conditions. A representation of such a model glass reactor is given in Fig. 2.16. A porcelain sample support was placed inside the horizontal reaction tube. Water in the reservoir was brought to evaporation to create an atmosphere saturated by water vapor.

2.6.2 Parameters: Uniformity of dimensions, educts, treatment and storage

- Dimensions

All reactors and porcelain supports were of uniform dimensions (*Fig. 2.16*).

- Sample preparation

Since commercial $NaPO_3$ contains significant amounts of water, it has to be remelted in order to remove -OH groups, immediately before starting the weathering assays. Thus, reagent grade crystalline $NaPO_3$ (Graham's salt, Merck) was ground in a porcelain mortar, brought to fusion for 30 minutes at 800°C and quenched rapidly on a steel plate at ambient temperature. The maximum storage time in a desiccator with P_2O_5 as the drying agent was 12 h.

The NaAlP-x [= (100-x) $NaPO_3$-x Al_2O_3] glass series were prepared using a standard melt-quench technique. Stoichiometric mixtures of Na_2CO_3, $Al(OH)_3$ and $(NH_4)_2HPO_4$ were thoroughly ground and homogenized in a porcelain mortar. Subsequently, a thermal treatment (1°C/min) up to 600°C (10 h) in a platinum crucible was applied to remove CO_2, H_2O and NH_3. The remaining batch composition was homogenized in a porcelain mortar and brought to fusion for 30 min at temperatures between 1050°C and 1400°C. After 15 min, the glass melt was agitated to ensure homogenization.

At the end of the fusion time, the glass was quenched rapidly between two steel plates. The NaAlP-x glasses used for weathering assays were stored in a desiccator with P_2O_5 as the drying agent.

Routinely, the amorphous nature of the glass was verified by X-ray diffraction. Differential scanning calorimetry (DSC) and 1D ^{1}H, ^{31}P and ^{27}Al solid-state NMR spectra served as further controls for glass transition temperatures (T_g) and homogeneity of the samples, respectively.

The pristine glass powder (see glass preparation) used for weathering assays was ground immediately before starting the experiment and routinely verified by 1D ^{31}P and ^{1}H NMR. 500 mg of glass powder with a maximum grain size of 100 µm were used for each experiment. The powder was distributed homogeneously in the porcelain sample support. By holding these parameters constant the attacked sample surface of pristine glass powder could be reproduced in each experiment.

➢ Sample treatment

The reservoir of the reactor was loaded with 1ml of H_2O for each weathering assay. The weathering assays were carried out in an incubator oven where ventilation and temperature could be adjusted exactly (±0,1 °C) (*Fig. 2.17; left side*). Before starting the experiment, thermal equilibration of the reactor system with its environment was allowed for 1 h in order to achieve the same degree of H_2O water vapor saturation in each reactor (*Fig. 2.17; right side*).

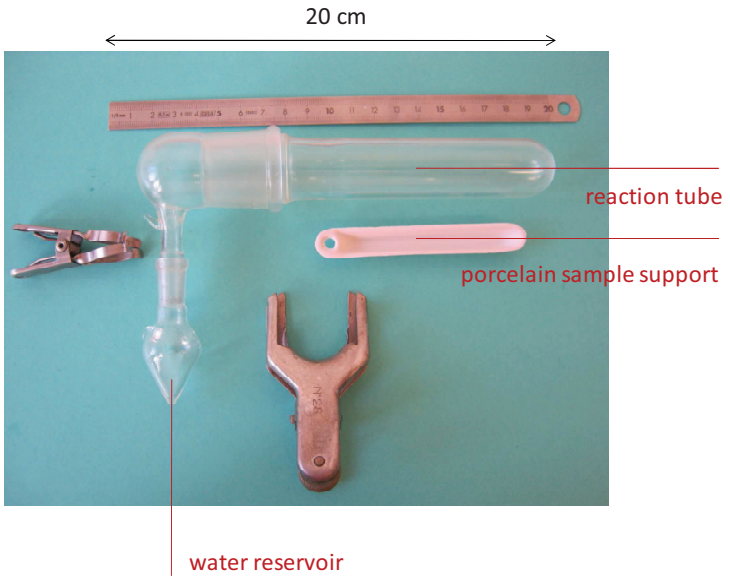

Fig. 2.16:
Reactor used for weathering assays. The water reservoir has to be charged with 1 ml of water, the sample support has to be loaded with 500 mg of powdered glass sample and placed inside the reaction tube.

Fig. 2.17:
Left side: Incubator oven used for weathering assays.
Right side: View inside the incubator oven. Reactor systems were placed on two grill levels. Ventilation (see rear wall) was used to homogenize the temperature inside the oven. The water reservoirs were kept in oil baths during weathering.

- Sample storage

After each experiment, the weathered sample was stored for 12 h under dynamic vacuum (10^{-4} bar) at room temperature in order to remove the great extent of loosely adsorbed surface water.

2.6.3 Reproducibility test

Finally, reproducibility of the weathering assays was verified by recording 1D ^{31}P NMR spectra of samples weathered for 4 h at 80°C in different reactors and at different dates. The relative Q^2, Q^1 and Q^0 unit fractions were determined by deconvolution over the entire range of spinning sidebands (Massiot2002).

The mean value and the corresponding standard deviation of each unit fraction of the series were calculated (*Tab. 2.2*). With regard to the small number of random samples the standard deviation cannot be considered as exact. However, it serves as a measure for the maximum experimental error and for the degree of reproducibility of each test that is in the range of about 2% of each unit fraction.

Fig. 2.18 shows 1D ^{31}P NMR results of four such tests. It is remarkable that the same crystalline phase, $NaH_2PO_4*H_2O$ (+2.1 ppm), has been reproduced in each of the four test samples.

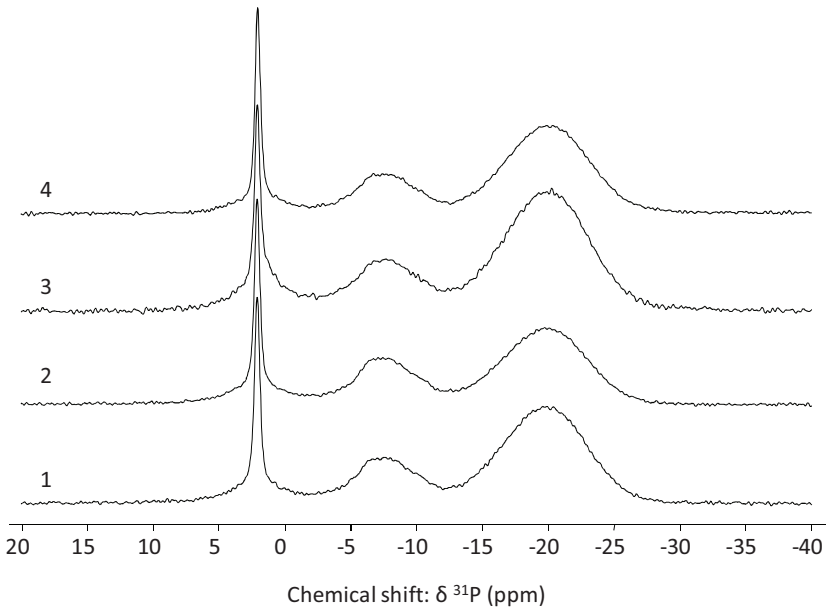

Fig. 2.18:
Reproducibility test. 1D ^{31}P NMR spectra 1, 2, 3, and 4 stem from samples weathered for four hours in different reactors at different days. Remarkable: $NaH_2PO_4*H_2O$ is reproduced in each assay.

Tab. 2.2:
Reproducibility test results from deconvolution of 1D ^{31}P NMR spectra over the entire range of spinning side-bands (Massiot2002).

	Reproducibility test number				Mean value (%)	Standard deviation (%)
	1	2	3	4		
Q^2 (%)	71,5	67,7	74,2	72,9	71,6	2,8
Q^1 (%)	16,5	18,1	14,1	15,0	16,0	1,8
Q^0 (%)	12,0	14,2	11,7	12,1	12,5	1,1

2.6.4 Weathering kinetics adjustment:

In a final step, the conditions of the weathering kinetics were adapted. Therefore the weathering temperature was varied. Suitable weathering kinetics had to fulfill several conditions:

- They had to lead to reproducible results. Therefore a multitude of competing and unselective processes, mostly occurring at elevated temperatures, had to be avoided.
- They had to allow for time-resolution of processes that are eventually occurring consecutively.
- They had to allow for weathering kinetics that are fast enough to generate many points on the weathering timescale.

Fig. 2.19 shows 1D ^{31}P NMR spectra of $NaPO_3$ glass for three different weathering temperatures. For $NaPO_3$, a weathering temperature of 80°C was chosen, based on the outcome of the weathering tests at different temperatures that fulfill the above conditions. In *Tab. 2.3*, the weathering conditions for the $NaPO_3$ glass (Chapter 4) and the NaAlP-x glass series (Chapter 5) are shown.

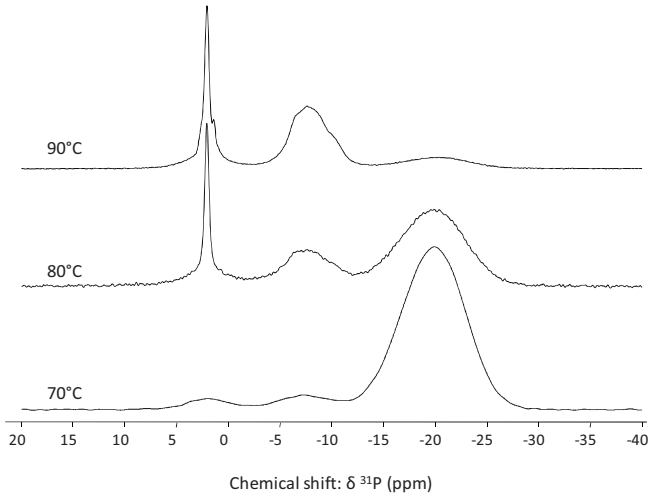

Fig. 2.19:
Adjustment of weathering kinetics, example for $NaPO_3$ glass weathered for four hours.

Tab. 2.3:
Overview over the weathering assays and the corresponding weathering conditions.

Glass system	Temperature	Duration	Experiment	
$NaPO_3$	80°C	4 h	reproducibility tests	Chapter 2
	60°C 70°C 80°C	4 h	kinetics optimization	Chapter 2
	80°C	1 h min to 70 h max	$NaPO_3$ weathering studies.	Chapter 4
NaAlP-x	45°C	4 h min to 24 h max	NaAlP-x weathering studies.	Chapter 5

Summary and Conclusion Chapter 2

Summary:

The simultaneous detection of crystalline and amorphous phases constitutes one of the main advantages of solid-state NMR, a structural analysis technique that has been presented in the first part of this chapter (2.1-2.3). In addition, NMR can provide quantitative information. This constitutes an important advantage with regard to subsequent studies on weathering glass systems (Chapters 4 and 5).

In the second part of this chapter (2.4), an approach for the calculation of NMR parameters and the simulation of the corresponding spectra has been introduced. In the following (Chapter 3), this calculation approach will be employed to complement ^{17}O NMR information. NMR, in turn, will be implemented to consolidate the reliability of the calculation approach.

The synthesis protocols of ^{17}O-enriched NaH_2PO_4 and $Na_2H_2P_2O_7$ have been presented in section 2.5. They extend the synthesis repertoire of ^{17}O-enriched compounds within our group (Zeyer2002, Flambard2006).

In section 2.6, the experimental conditions of the weathering assays have been presented in detail. With regard to subsequent assays under ^{17}O-enriched water vapor, the protocol has been elaborated for very small quantities of H_2O. Within our group, the experimental setup has been refined with regard to costs, reproducibility and kinetics of two different glass systems.

Conclusion:

The variety of methods above illustrates how NMR, calculations, synthesis of ^{17}O-enriched phosphate compounds and weathering assays build an effective symbiosis for the studies of phosphate glass systems and their weathering.
New synthesis protocols of phase-pure ^{17}O-enriched hydrogen phosphates have been established and the calculation approach for the generation of NMR data has been extended to hydrogen containing crystalline sodium phosphate systems. So far, *both* methodological approaches have not been reported in the literature.

Bibliography Chapter 2

Alam2005,
Alam, T.M., Tischendorf, B.C., Brow, R.K.
Solid State Nuclear Magnetic Resonance (2005) **27 (1-2)** 99

Amoureux1996
Amoureux, J.-P., Fernandez, C., Steuernagel, S.
Journal of Magnetic Resonance (1996) **A123** 116

Amoureux2009
Amoureux, J.-P., Trebosc, J., Delevoye, L., Lafon, O., Hu, B., Wang, Q.
Solid-State Nuclear Magnetic Resonance (2009) **35** 12

Bennett1992
Bennett, A.E., Ok, J.H., Griffin, R.G., Vega, S.
Journal of Chemical Physics (1992) **96** 8624

Blöchl1994
Blöchl, P.E.
Physical Review B (1994) **50 (24)** 17953

Duer2004
Duer, M.J.,
Introduction to solid-state NMR spectroscopy
Blackwell Science (2004)

Flambard2006
Flambard, A., Montagne, L., Delevoye, L.
Chemical Communications (2006) 3426

Frydman1995
Frydman, L., Harwood, J.S.
Journal of the American Chemical Society (1995) **117 (19)** 5367

Fyfe1993
Fyfe, C. A., Mueller, K. T., Grondey, H. Wong-Moon, K.C.
Journal of Physical Chemistry (1993) **97** 13484

Ghule2001
Ghule, A., Ramaswamy, M., Chang, H.
Inorganic Chemistry (2001) **40** 5917.

Hartmann1962
Hartmann, S.R., Hahn, E.L.
Physics Reviews (1962) **128** 2042

Hohenberg1964
Hohenberg, P., Kohn, W.
Physical Review B (1964) **136 (3B)** 864

Kohn1965
Kohn, W. Sham, L.
Physics Review (1965) **140 (4A)** 1133

Lesage1998
Lesage, A., Sakellariou, D., Steuernagel, S., Emsley, L.
Journal of the American Chemical Society (1998) **120 (50)**, 13194

Llor1988
Llor, A., Virtel, J.
Chemical Physics Letters (1988) **2** 285

MacKenzie2002
MacKenzie, K. J. D., Smith, M.E.
Multinuclear Solid-State NMR of Inorganic Materials, Pergamon Materials Series Vol. 6
Elsevier Science (2002)

Massiot2002
Massiot, D., Fayon, F., Capron, M., King, I., Le Calvé, S., Alonso, B., Durand, J.-O., Bujoli, B., Gan, Z., Hoatson, G.
Magnetic Resonance in Chemistry (2002) **40 (1)** 70

Masui2002
Masui, H., Danping, C., Tomoko, A., Tetsuo, Y.
Zeitschrift für Naturforschung (2002) **57a** 473

Medek1995
Medek, A., Harwood, J.S., Frydman, L.
Journal of the American Chemical Society (1995) **117 (51)** 12779

Mercier1999,
Mercier, C., Montagne, L., Sfihi, H., Palavit, G.
Journal of Non-Crystalline Solids (1999) **256** 124

PARATEC,
Pfrommer, B., Raczkowski, D., Canning, A., Louie, S.G., Mauri, F., Cote, M., Yoon, Y., Pickard, C.J., Heynes, P.,
www.nersc.gov/projects/paratec

Pickard2001
Pickard, C.J., Mauri, F.
Physical Review B (2001) **63** 245101

Prochnow2006
Prochnow, D., Grimmer, A.-R., Freude, D.
Solid-State Nuclear Magnetic Resonance (2006) **30 (2)** 69

Samoson1988
Samoson, A., Lipmaa, E., Pines, A.
Molecular Physics (1988) **65** 1013

Thilo1955
Thilo, E., Grunze, H.
Zeitschrift für anorganische und allgemeine Chemie (1955) **281** 262.

Vasconcelos2008
Vasconcelos, F., Cristol, S., Paul, J-F., Tricot, G., Amoureux, J-P., Montagne, L., Mauri, F., Delevoye, L.
Inorganic Chemistry (2008) **47 (16)** 7327

Zeyer2002
Zeyer, M., Montagne, L., Kostoj, V., Palavit, G., Prochnow, D., Jaeger, C.
Journal of Non-Crystalline Solids (2002) **311 (3)** 223

Xue2009
Xue, X., Kanzaki, M.
Journal of the American Ceramic Society (2009) **92 (12)** 2803

Chapter 3

New insights into ^{17}O environments generated during phosphate glass alteration: A combined ^{17}O NMR and first principles calculations study

CHAPTER 3

New insights into ^{17}O environments generated during phosphate glass alteration: A combined ^{17}O NMR and first principles calculations study

Oxygen atoms are the most abundant species within the oxide glass framework and occupy a large variety of distinct sites. Thus, the ^{17}O NMR study enables valuable insights into the atomic structure of crystalline and amorphous phosphate phases that form during the aging of a glass. Oxygen is a choice probe to better understand the mechanisms involved in glass alteration, since it is also one of the constituents of the water molecule.
In a first step towards phosphate glass studies (Vasconcelos2008), our group worked at assigning ^{17}O MAS and 3QMAS spectra by using first-principles calculations for three crystalline anhydrous sodium phosphates in order to study phosphate glasses.

In the first part of this chapter, a NMR calculation / simulation approach shall be extended to and validated for crystalline sodium *hydrogen* phosphate phases. These phases are indeed generated throughout the weathering process of sodium phosphate glasses. The aim is to verify the reliability of the calculation approach by comparing calculated to experimentally obtained results. Reliable calculations can help assignment and interpretation of ^{17}O NMR spectra. Further, they allow for avoiding costly synthesis of ^{17}O-enriched crystalline reference phases and the subsequent time demanding acquisition of high-resolution reference spectra at high field.

The work on crystalline anhydrous sodium phosphates (Vasconcelos2008) allowed for drawing correlations between the NMR parameters δ_{CS}, C_Q and η_Q and the structural environment of the ^{17}O nucleus. In the second part of this chapter, the systematic study of these correlations shall be extended to the field of protonated phases. With regard to further studies of water alteration into sodium phosphate glass, the aim is to deduce structural features of oxygen sites within the sodium phosphate family based on the inspection of their corresponding NMR parameters.

Finally, the combined methodology, consisting of high resolution ^{17}O NMR studies at high field that are complemented by first principles calculations, shall be tested. Water alteration into a sodium phosphate glass, namely $NaPO_3$, shall be followed by taking snapshots at different alteration times. Oxygen environments in the complex phase mixture formed upon $NaPO_3$ glass degradation shall be characterized, based on the correlations previously deduced between the NMR parameters and the structural environment of ^{17}O.

NMR details Chapter 3

All ^{17}O MAS NMR experiments were performed on a Bruker Avance II spectrometer, equipped with a 18.8T narrow bore magnet, using a Bruker 3.2 mm (rotor diameter) tri-γ probehead operating at 108.47 MHz for ^{17}O.

The ^{17}O MAS spectra were obtained using a selective pulse of 11 µs at a radio frequency (RF) field strength of 7.5 kHz. The excitation pulse was preceded by a Double Frequency Sweep (DFS) pulse of 3 ms sweeping between 100 and 900 kHz at an RF field amplitude of 50 kHz in order to enhance the central transition polarization for half-integer quadrupolar nuclei (Iuga2000). The 3QMAS spectra were collected at a MAS speed of 20 kHz, using the z-filter sequence (Amoureux1996). It consisted of two hard pulses of 3.5 and 1.25 µs at an RF field of 100 kHz, for triple-quantum excitation and reconversion, respectively, followed by a soft pulse of 9 µs. The t_1 step was set to be a multiple (n=1 or 2) of the MAS period. The isotropic dimension has been referenced and scaled following the recommendation of Amoureux et al. (Amoureux2002).

The ^{31}P-^{17}O HMQC spectrum was obtained at a MAS speed of 20 kHz using the pulse sequence detailed by Massiot et al. (Massiot2003). An echo was applied to the observed ^{17}O nuclei with respective 90° and 180° pulses of 14 µs and 28 µs. Two 90° pulses of 4.5 µs were then applied on either sides of the ^{17}O 180° pulse. The evolution delay was set to 3.5 µs for an evolution under J-coupling. A total of 512 scans were accumulated with a recycling delay of 1s. All other relevant experimental parameters are given in the figure captions. The ^{17}O chemical shift values are given in ppm with respect to tap water.

3.1 Validation of the calculation approach for sodium hydrogen phosphates

3.1.1 Calculations

3.1.1a Structural data:

Wherever possible, structural data obtained from neutron diffraction (ND) have been preferred over data from X-Ray diffraction (XRD). Through XRD analysis, protons are quite invisible due to the large dependence of the scattering factor with the electron density. This uncertainty is not present in the case of neutron diffraction (ND) where the neutrons interact with the nucleus. ^{1}H positions in structures resulting from XRD analysis were considered with attention and treated carefully.
In *Fig. 3.1* (*a-d*) unit cells of the studied crystalline sodium hydrogen phosphates NaH_2PO_4, $Na_2H_2P_2O_7$, $NaH_2PO_4*H_2O$ and $NaH_2PO_4*2H_2O$ are presented together with their basic anion units (*Fig. 3.1 e-h*). Space groups, cell dimensions, cell volume and the number of formula units present in the unit cell are indicated on the right side of *Fig. 3.1 a, b, c* and *d*. In the following, the structural references whose reliability is a crucial issue for geometry optimization and subsequent calculations shall be presented.

The structure of sodium dihydrogen phosphate NaH_2PO_4 (*Fig. 3.1 a*) has been refined from neutron diffraction on a single-crystal sample by Choudhary et al. (Choudhary1981). It crystallizes in the monoclinic space group P $2_1/c$ (14) with four formula units per unit cell. Two crystallographic distinct sodium sites, two phosphorus sites, four hydrogen sites and eight oxygen sites are present. In each of the two anion units, four tetrahedrally arranged oxygen atoms are connected to the central phosphorus atom by covalent bonds. As the NaH_2PO_4 structure is built on Q^0 entities, exclusively, all oxygen atoms are non-bridging ones with covalent and/or ionic bonds towards sodium and hydrogen atoms in their immediate surroundings.
Based on the Rietveld method, the structure of disodium dihydrogen pyrophosphate, $Na_2H_2P_2O_7$ has been refined by Selevich et al. (Selevich2002) from X-Ray powder diffraction data (*Fig. 3.1 b*). $Na_2H_2P_2O_7$ crystallizes in the orthorhombic space group F d d d (70) with 16 formula units per unit cell. One sodium site, one phosphorus site, two hydrogen sites and four oxygen sites can be distinguished from the crystallographic point of view. The Q^1 entities form the basic anion units of

the $Na_2H_2P_2O_7$ structure: Two tetrahedra share one bridging oxygen atom located in the mirror plane of the pyrophosphate structural unit, $P_2O_7^{2-}$.

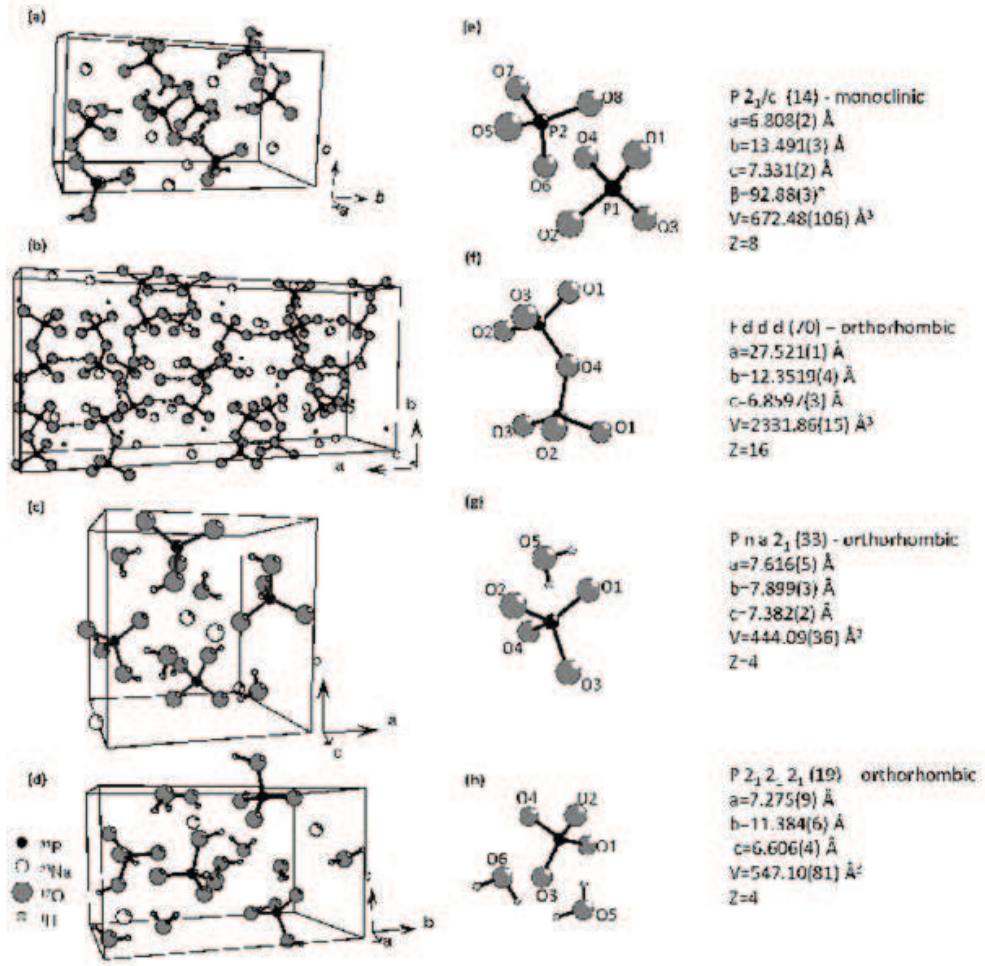

Fig. 3.1:
Unit cell structures of (a) NaH_2PO_4, (b) $Na_2H_2P_2O_7$, (c) $NaH_2PO_4*H_2O$, (d) $NaH_2PO_4*2H_2O$. Basic anion units for (e) NaH_2PO_4, (f) $Na_2H_2P_2O_7$, (g) $NaH_2PO_4*H_2O$, (h) $NaH_2PO_4*2H_2O$ are presented in the middle column. On the right sight, space group (first line), cell dimension (a,b,c), cell volume (V) and the number of formula units present in the unit cell are indicated.

Two hydrated sodium dihydrogen orthophosphate compounds, namely $NaH_2PO_4*H_2O$ and $NaH_2PO_4*2H_2O$ (*Fig. 3.1 c* and *d*, respectively), are also studied and discussed in the following sections. The two structures have been described by Catti and Ferraris (Catti1976) and Bartl et al. (Bartl1976), respectively. The structure of $NaH_2PO_4*H_2O$, orthorhombic phase, was determined using single crystal X-ray measurements and direct methods of refinement. It crystallizes in space group P n a 2_1 (33) with four formula units per unit cell. It contains one crystallographic sodium site and one phosphorus site, four oxygen and four proton sites. The structure of $NaH_2PO_4*2H_2O$ was determined using both X-ray and neutron data obtained on a single crystal phase. It crystallizes in the orthorhombic space group P 2_1 2_1 2_1 (19) with 4 formula units per unit cell. One phosphorus site, one

sodium site, six oxygen sites and six hydrogen sites are present. From a crystallographic point of view, two different water molecules are distinguished in the structure.

3.1.1b Calculation procedure

Subsequently, the calculation details will be described in a general manner. The calculated ^{17}O NMR data will be presented in *Tab. 3.1* for comparison with experimentally obtained NMR parameters.

Since the calculation of NMR parameters requires the accurate knowledge of the crystalline structure, geometry optimization preceded the calculation of NMR parameters. In the present work, XRD and ND structures have been systematically optimized by using DFT. The VASP code (Kresse1993, Kresse1996, VASP) was used for the geometric structure optimization. All degrees of freedom (ionic internal coordinates, cell shape, and cell volume) were taken into account for the geometric structure optimization. In a final step, cell parameters were rescaled to the experimental volume (Fig. right side) to avoid the DFT-GGA tendency to overestimate both, the distances and the cell volume.

The first principles calculations are based on a plane-wave pseudopotential method and density functional theory (DFT) (Hohenberg1964, Kohn1965). Calculations were performed using the PARATEC code (PARATEC). For the generalized gradient approximation (GGA) of the exchange-correlation functional, the PBE functional (Perdew1996) was used. The potentials due to the ions are represented by norm-conserving Troullier-Martins pseudopotentials (Trouillier1991). Further calculation details such as electronical configurations used for the pseudopotentials, k-point mesh and energy cutoff are given elsewhere (Vasconcelos2008). The calculation parameters are consistent with those used in our group for the systematic study of crystalline phosphates (Vasconcelos2008).

The calculation of the absolute chemical shielding was performed using GIPAW algorithms developed by Pickard and Mauri (Pickard2001). Experimental isotropic chemical shifts δ_{CS} and absolute isotropic chemical shielding σ are related through the definition of an isotropic reference shielding σ_{ref} defined by $\delta_{CS} = \sigma_{ref} - \sigma$.

In a previous work (Vasconcelos2008), the absolute chemical shift value was set to an unambiguous isolated resonance (site O6 of sodium trimetaphosphate $Na_3P_3O_9$; Vasconcelos2008) as an internal reference. Subsequently, correlations between experimentally observed and calculated chemical shift values for ^{17}O were deduced. The obtained correlation curves show slopes different from “1”.

However, within the same family of compounds, this procedure allows for determination of experimentally expected chemical shift values.
It turned out that the slope of correlation is sensitive to variations in the chemical composition of the studied compounds. Thus, the internal chemical shift reference formerly used in a sodium phosphate could not be employed in the case of *hydrogen* containing sodium phosphate phases. In the present work, the crystallographic site O3 of sodium dihydrogen phosphate NaH_2PO_4 was used as an internal reference for ^{17}O chemical shift values.

The electronic structure gives access to the electric field and thus to the electric field gradient tensor (EFG) through the reconstruction of the all-electron wavefunction that is obtained with the projector augmented wave (PAW) approach (Blöchl1994, Profeta2003). The EFG tensor is then diagonalized to obtain the principal components V_{xx}, V_{yy} and V_{zz} where by convention $|V_{xx}| < |V_{yy}| < |V_{zz}|$. These components are related to the quadrupolar coupling constant C_Q and the asymmetry parameter η_Q (Chapter2). In the present work, for ^{17}O Q=-25.58 $*10^{-31}$ m^2 was used (Pyykkö2001).

The high agreement between experimental and simulated NMR data (see following sections) confirmed this protocol for geometric structure optimization as accurate enough to lead to reliable results.

3.1.2 Validation of the combined methodology for ^{17}O NMR studies of crystalline hydrogen phosphate phases

In the following, experimental ^{17}O NMR data of the pure crystalline sodium hydrogen ortho- and pyrophosphates, NaH_2PO_4 (*Fig. 3.2, Fig. 3.3*) and $NaH_2P_2O_7$ (*Fig.3.4*) are presented. The different oxygen sites can be characterized by their chemical shift δ_{CS}, their quadrupolar constant C_Q and their asymmetry parameter η_Q (see Chapter 2). These ^{17}O NMR parameters are given in table *Tab. 3.1*.

Fig. 3.2 and top spectra (*Fig. 3.3 a and Fig. 3.4 a*) illustrate the 1D ^{17}O MAS spectra, showing second-order quadrupolar broadening, which remains under fast sample reorientation at the magic angle. *Fig. 3.2* allows for a direct comparison between the experimental and the simulated ^{17}O 1D MAS envelope of crystalline NaH_2PO_4. The latter consists of contributions from eight crystallographically distinct oxygen sites as illustrated by the simulated individual contributions at the bottom of *Fig. 3.2*.

The synthesized ^{17}O-enriched sodium hydrogen orthophosphate presents a high degree of crystallinity that gives rise to sharp discontinuities. Experimental and simulated data stand in excellent agreement. Nevertheless, an unambiguous deconvolution of the experimental spectrum is impossible within a conventional fit program (Massiot2002). This is mainly due to the severe overlap of ^{17}O resonances.

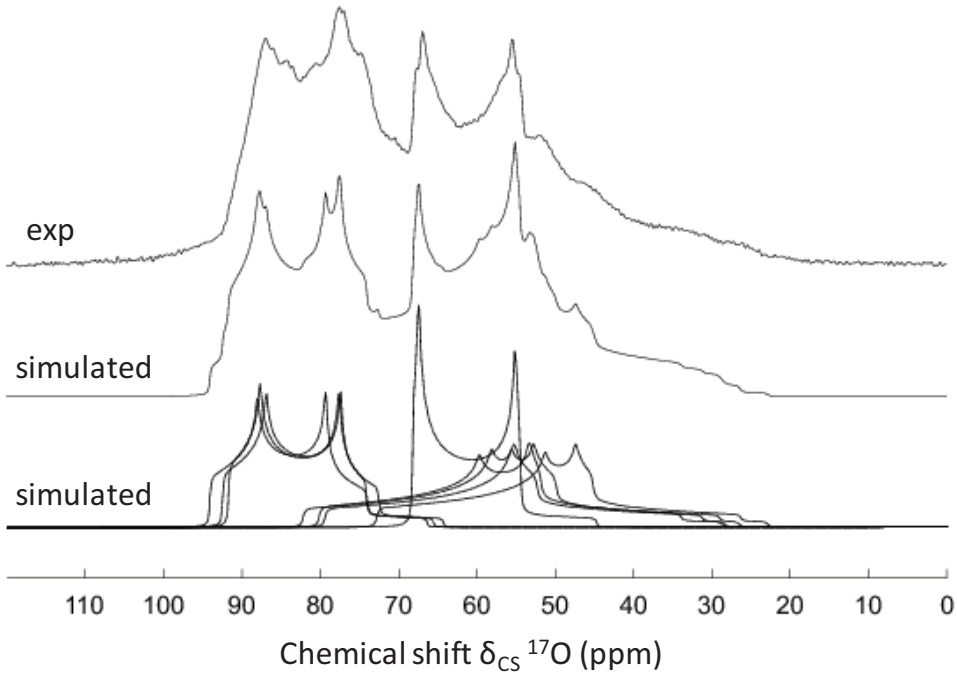

Fig.3.2:
Experimental (top) and simulated (middle) 1D ^{17}O MAS powder lineshape for NaH_2PO_4. The experimental data has been recorded at a static field of 18.8 T (MAS=20kHz; rotor diameter 3.2 mm). At the bottom, simulated contributions from eight crystallographic distinct sites are presented.

However, additional information is provided by the experimental 2D ^{17}O 3QMAS spectra of NaH_2PO_4 (*Fig. 3.3 b*) and $NaH_2P_2O_7$ (*Fig.3.4 b*). In the following, all individual slices along the ^{17}O MAS dimension, including those with poor signal intensity, have been fitted to estimate the quadrupolar parameters C_Q and η_Q and chemical shift values roughly (*Fig. 3.3 c* and *Fig. 3.4 c*).
Also, both, δ_{iso} values that are extracted by projecting the spectrum on the isotropic dimension of the MQMAS spectra, and δ_{CS} values (in brackets) deduced from fitting the individual resonance slices, are given in order to ease the visual inspection of the 2D MQMAS data.

In the 2D 3QMAS spectrum of NaH_2PO_4 (*Fig. 3.3 b*), four signals at δ_{iso} = 80 ppm, δ_{iso} = 89 ppm, δ_{iso} = 96 ppm and δ_{iso} = 102 ppm (δ_{CS} = 71.6 ppm, δ_{CS} = 85 ppm, δ_{CS} = 84 ppm and δ_{CS} = 94 ppm) are detected, all arising from non-bridging oxygens, whilst eight crystallographic distinct oxygen sites are present in NaH_2PO_4 (Choudhary1981). For each group of resonances, the individual anisotropic cross slice and its corresponding best-fit simulation are represented (*Fig. 3.3 c*). For NaH_2PO_4, two intense resonances (δ_{iso} = 80 ppm and δ_{iso} = 102 ppm) are identified at the edges of the chemical shift scale and two broad resonances of very weak signal intensity can be observed at δ_{iso} = 89 ppm and δ_{iso} = 96 ppm (δ_{CS} = 85 ppm and δ_{CS} = 84 ppm).
The 2D 3QMAS spectrum of $Na_2H_2P_2O_7$ (*Fig. 3.4 b*), exhibits two well-resolved groups of resonances at δ_{iso} = 88 ppm and δ_{iso} = 102 ppm (δ_{CS} = 80 ppm and δ_{CS} = 90 ppm) arising from non-bridging oxygens (NBO). A third one at δ_{iso} = 138 ppm (δ_{CS} = 112.5 ppm) arises from the bridging oxygen site (BO) in the pyrophosphate anion unit. It has not been considered in experimental and simulated $Na_2H_2P_2O_7$ NMR data, since we will focus exclusively on NBO sites in the following discussion. For a more detailed discussion of bridging oxygen NMR, see previously published work (Vasconcelos2008).
Hence, the 3QMAS spectrum of $Na_2H_2P_2O_7$ clearly distinguishes two groups of resonances in the region of NBO, whilst three crystallographically non-equivalent oxygen sites are expected.

For both sodium hydrogen ortho- and pyrophosphate, not all ^{17}O resonances appear well-resolved in their corresponding high-resolution spectra. We observe a clear discrepancy between the number of crystallographic NBO sites (eight in NaH_2PO_4 and three in $Na_2H_2P_2O_7$) and the number of ^{17}O resonances clearly extracted from the ^{17}O 3QMAS NMR (four in NaH_2PO_4 and two in $Na_2H_2P_2O_7$) at a magnetic field of 18.8 T. This discrepancy between the number of crystallographically distinct oxygen sites and the observed signals shall be elucidated by complementing experimental NMR results with data from first principles calculations.

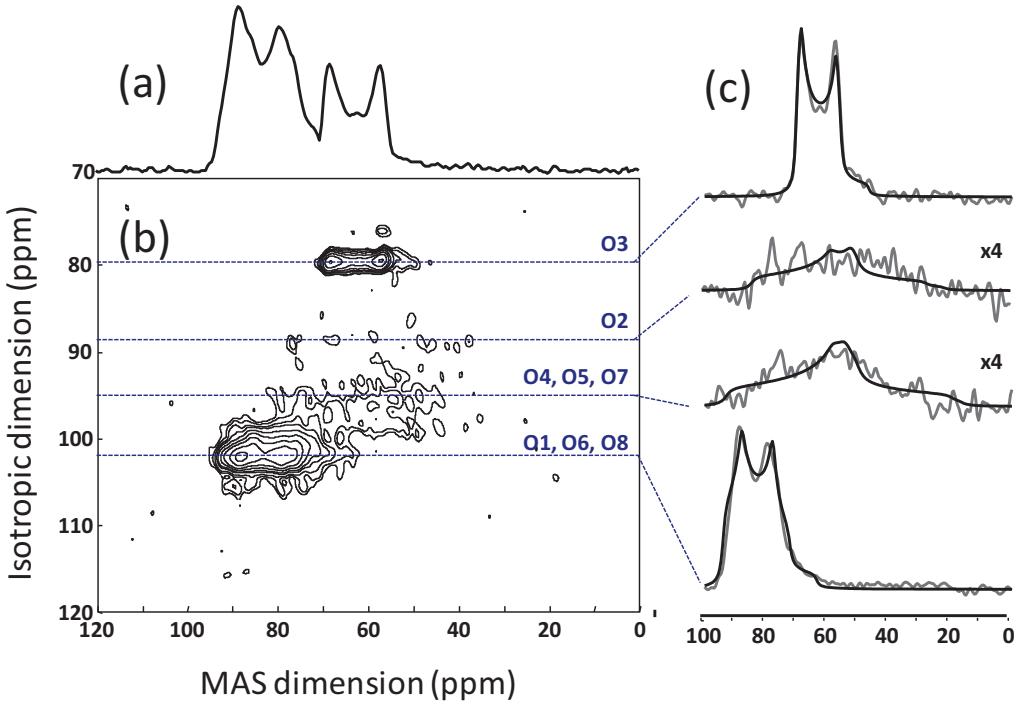

Fig. 3.3:
2D ^{17}O 3QMAS data of NaH_2PO_4 (b) together with its 1D MAS powder lineshape (a) and individual slices (c, cross sections) extracted to determine quadrupolar parameters C_Q and η_Q roughly. For experimental details see "NMR details" at the beginning of this chapter.

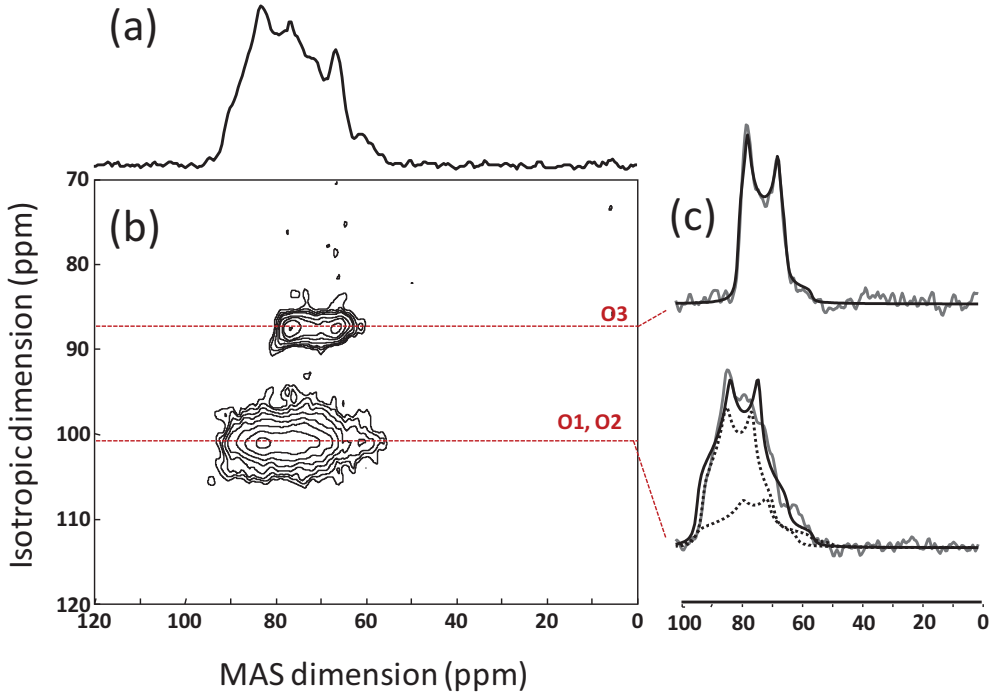

Fig. 3.4:
2D ^{17}O 3QMAS data of $Na_2H_2P_2O_7$ (b) together with its 1D MAS powder lineshape (a) and individual slices (c, cross sections) extracted to determine quadrupolar parameters C_Q and η_Q roughly. For experimental details see "NMR details" at the beginning of this chapter.

The parameters δ_{CS}, C_Q and η_Q, that were deduced from the PAW/GIPAW calculations, are grouped in *Tab. 3.1*. They were used in a simulation program (Charpentier1998) in order to generate the 2D ^{17}O 3QMAS spectra of NaH_2PO_4 and $Na_2H_2P_2O_7$ (*Fig. 3.5 a* and *b*). These simulated 2D ^{17}O 3QMAS spectra are consistent with the experimental results, enabling a complete assignment of the experimentally observed resonances.

It is useful to classify the oxygen atoms into subgroups depending on their immediate structural environment, in particular on the nature of [OH], [OP] bonding and the chemical composition of the first sphere of coordination. This eases the examination of systematic relationships between NMR parameters and different types of local environment. *Fig. 3.6* illustrates the site classification employed in *Tab. 3.1* and the following discussion.

For NaH_2PO_4, the signal at δ_{iso} = 80 ppm (δ_{CS} = 71.6 ppm) can be attributed to the crystallographic site O3 with a short O-P bond length (delocalized double bond character) and three sodium ions in its close vicinity (PO; *Fig.3.6*). The weak signal at δ_{iso} = 89 ppm (δ_{CS} = 85 ppm) corresponds to the crystallographic site O2, an oxygen with a covalent OH bond and two sodium ions. The weak signal at δ_{iso} = 96 ppm (δ_{CS} = 84 ppm) is a superposition of sites O4, O5 and O7 whose surroundings correspond to an oxygen with one sodium ion and a covalent O-H bond (POH; *Fig. 3.6*). A set of oxygen atoms with different bond lengths towards hydrogen and phosphorus gives rise to the resonance at δ_{iso} = 102 ppm (δ_{CS} = 94 ppm), resulting from contributions of sites O1, O6 and O8 (PO…H; *Fig. 3.6*). For $Na_2H_2P_2O_7$, the signal at δ_{iso} = 102 ppm (δ_{CS} = 90 ppm) is the result of the overlapping resonances of sites O1 and O2 which are sharing the same hydrogen (PO-H; *Fig. 3.6*). The oxygen site O3, with only one sodium ion in its close vicinity, gives rise to the resonance at δ_{iso} = 88 ppm (δ_{CS} = 80 ppm) (PO; *Fig. 3.6*).

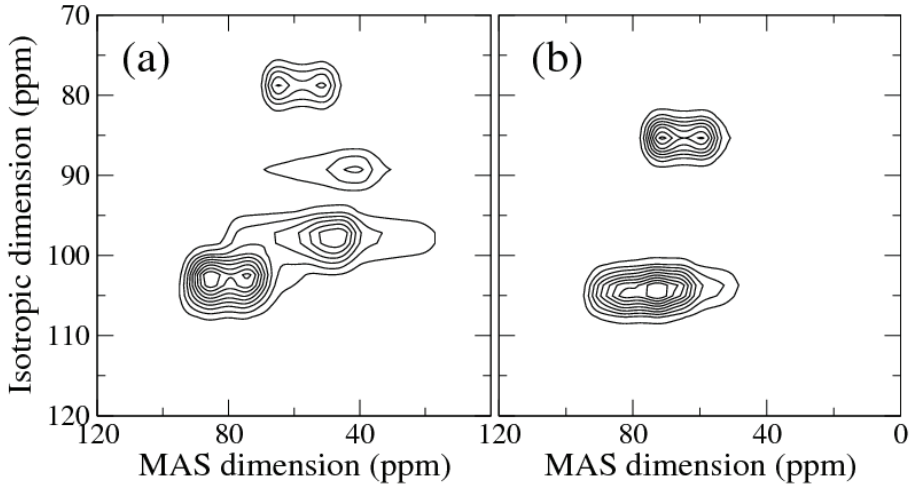

Fig. 3.5:
Simulated 2D ^{17}O 3QMAS NMR data for (a) NaH_2PO_4 and (b) $Na_2H_2P_2O_7$.

Tab. 3.1:
Comparison of experimental and calculated (blue) ^{17}O parameters for NaH_2PO_4 and $Na_2H_2P_2O_7$ together with calculated ^{17}O parameters of $NaH_2PO_4*H_2O$ and $NaH_2PO_4*2\ H_2O$.

Compound	O Site	^{17}O Type	δ_{iso} ^{17}O (ppm)	δ_{CS} ^{17}O (ppm)		C_Q ^{17}O (MHz)		η_Q ^{17}O	
				exp	calc	exp	calc	exp	calc
NaH_2PO_4	O3	PO	80	71.6	71.6	4.6	5.31	0.1	0.05
	O2	POH	89	85	73.00	6.7	6.82	0.7	0.84
	O7	POH	96	84 *	80.62	7.3	7.04	0.9	0.75
	O5	POH			79.53		6.97		0.84
	O4	POH			82.33		7.01		0.89
	O8	PO…H	102	94 #	94.40	5.0	5.40	0.3	0.33
	O6	PO…H			94.02		5.41		0.25
	O1	PO…H			95.76		5.46		0.37
$Na_2H_2P_2O_7$	O3	PO	88	80	81.29	4.6	5.19	0.2	0.18
	O1	PO-H	102	90 +	94.64	5.5	6.09	0.6	0.64
	O2	PO-H			97.90		5.75		0.44
	O4	POP		112.5	127.62	6.8	7.99	0.6	0.56
$NaH_2PO_4*H_2O$	O1	PO	n.d.	n.d.	88.46	n.d.	4.90	n.d.	0.18
	O3	POH			70.32		7.23		0.82
	O4	POH			78.39		6.81		0.98
	O2	PO…H			108.26		5.43		0.29
	O5	HOH			-29.55		8.78		0.78
$NaH_2PO_4*2H_2O$	O1	PO	n.d.	n.d.	87.06	n.d.	5.33	n.d.	0.39
	O3	POH			72.45		7.09		0.74
	O4	POH			83.00		6.69		0.82
	O2	PO…H			108.34		5.35		0.28
	O5	HOH			-23.69		8.53		0.87
	O6	HOH			-27.56		8.34		0.86

*NaH_2PO_4 *: Sites O4, O5, O7 are represented by one experimental slice at δ_{iso} 84 ppm. #: Sites O1, O-, O8 are represented by one experimental slice at δ_{iso} 94 ppm.*
$Na_2H_2P_2O_7$ +: Sites O1, O2 are rpresented by one experimental slice at δ_{iso} 90 ppm.

	Site nomenclature	Exemplary Site	NNN	Bond types	
BO	POP		2 P	2 [OP]:	covalent, SB
	HOH		2 H	2 [OH]:	covalent, SB
NBO	POH		1 P 1 H 1 Na	1 [OP]: 1 [OH]: 1 [ONa]:	covalent, SB covalent, SB ionic
	PO-H	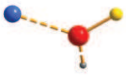	1 P 1 H 1 Na	1 [OP]: 1 [OH]: 1 [ONa]:	covalent, SB intermediate ionic
	PO…H		1 P 1 H 1 Na	1 [OP]: 1 [OH]: 1 [ONa]:	covalent, SB ionic ionic
	PO	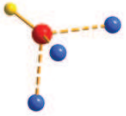	1 P 3 Na	1 [OP]: 3 [Na]:	covalent, DB ionic

Fig. 3.6:
Classification of ^{17}O sites employed in this chapter. Covalent bonds are represented by straight lines, ionic bonds are represented by dotted lines. BO and NBO stand for bridging and non-bridging oxygen, respectively. SB and DB stand for single bonding and double bonding, respectively.

In order to extend the NMR database for sodium hydrogen phosphates involved in the process of glass alteration, two hydrated phases, namely $NaH_2PO_4*H_2O$ and $NaH_2PO_4*2H_2O$ should be considered. The synthesis of ^{17}O-enriched phase-pure hydrated sodium phosphates is time-demanding, costly and difficult to achieve because of the low chemical stability under moderate temperature fluctuations. However, the good agreement between experimental and calculated NMR data of NaH_2PO_4 and $Na_2H_2P_2O_7$ presented above demonstrates the validity of the GIPAW approach. As a consequence, calculated NMR parameters replace experimental data completely in the case of $NaH_2PO_4*H_2O$ and $NaH_2PO_4*2H_2O$ (Tab. NMR data). Simulated 2D ^{17}O 3QMAS spectra replace experimental ones.

The NBO regions of the corresponding simulated 2D ^{17}O 3QMAS spectra are exhibited on *Fig. 3.7*. Bridging oxygen resonances arising from crystallographic H-O-H sites are given in the insets.

Both, the $NaH_2PO_4*H_2O$ (*Fig. 3.7 a*) and the $NaH_2PO_4*2H_2O$ (*Fig. 3.7 b*) spectrum, are very similar, presenting NBO resonances in the δ_{CS} range from 70 to 120 ppm. Signals at δ_{CS} 88.46 ppm in the $NaH_2PO_4*H_2O$ spectrum, respectively δ_{CS} 87.06 ppm in the $NaH_2PO_4*2H_2O$ spectrum, correspond to oxygen sites with a purely cationic Na environment (PO; *Fig. 3.6*), whereas resonances at δ_{CS} 70.32 ppm and δ_{CS} 78.39 ppm in the $NaH_2PO_4*H_2O$ spectrum, respectively δ_{CS} 72.45 ppm and δ_{CS} 83.00 ppm in the $NaH_2PO_4*2H_2O$ spectrum can be assigned to NBOs with a covalent OH bond (POH; *Fig. 3.6*). The ionic character of the same bond that is hydrogen bonding (PO…H; *Fig. 3.6*), in the same chemical environment results in shifted δ_{CS} values: δ_{CS} 108.26 ppm in the $NaH_2PO_4*H_2O$ spectrum, respectively δ_{CS} 108.34 ppm in the $NaH_2PO_4*2H_2O$ spectrum. One noticeable difference between the two simulated 2D ^{17}O 3QMAS spectra lies in the presence of an additional oxygen site (see insets in *Fig. 3.7 a* and *b*), in the crystal water chemical shift range for $NaH_2PO_4*2H_2O$. This allows for a clear experimental distinction between the two hydrated hydrogen orthophosphate phases.

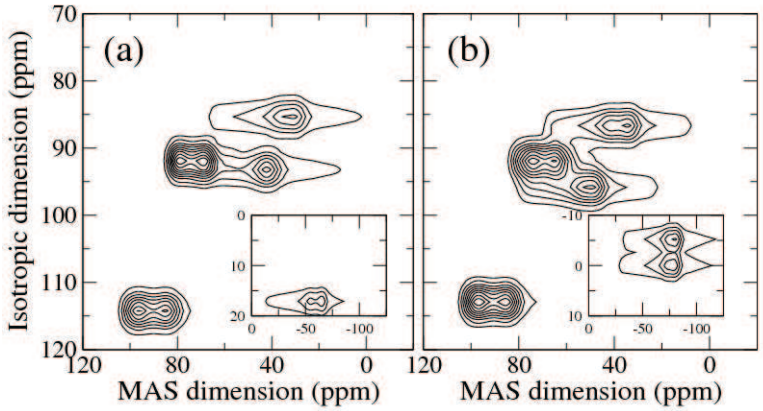

Fig. 3.7:
Simulated 2D ^{17}O 3QMAS NMR data for (a) $NaH_2PO_4*H_2O$ and (b) $NaH_2PO_4*2H_2O$. Simulated ^{17}O crystal water H_2O NMR resonances are given in insets. They allow for a clear distinction between the single- and the double-hydrated phase. So far, both compounds are not accessible by synthesis of ^{17}O-enriched phase-pure crystalline references.

3.2 Systematic relationships: ^{17}O structure – NMR parameters

In the following section, it shall be referred to calculated δ_{CS}, C_Q and η_Q values. Several reasons justify this procedure. First, NMR parameters extracted from experimental spectra often suffer from low sensitivity or strong overlap of ^{17}O sites. Second, a high consistence between experimental and calculated NMR parameters for NaH_2PO_4 and $Na_2H_2P_2O_7$ has been observed. In general, based on a calculation approach, NMR datasets can be reproduced reliably within the precision that they can be determined experimentally after a multi-parameter fitting procedure. The fact that quadrupolar coupling constants are generally overestimated by calculation (ca. 0.2 MHz) has been taken into account in the following considerations.

3.2.1 Chemical shift δ_{CS}

The chemical shift δ_{CS} is a widespread and conventional approach to interpret solid state NMR spectra. Nevertheless, it is limited by the fact that references from *comparable* systems must exist. The chemical shift is only useful to distinguish the deviation in chemical environment roughly. In case of small variations in the proximate surroundings of a nucleus, precise characterization often fails. Moreover, it has been demonstrated in previously published work about crystalline sodium phosphate phases that long-range effects induce strong overlap of the ^{17}O chemical shift regions (Vasconcelos2008).

A careful examination of the chemical shift ranges for each of the distinct oxygen environments extracted from *Tab. 3.1* and those presented by Vasconcelos et al. (Vasconcelos2008). The illustration of 1D chemical shift scales for the various ^{17}O site types reveals the following results (*Fig. 3.8*):

For bridging oxygen (POP), the data on hydrogen sodium pyrophosphate confirm the results previously published on pure sodium phosphate systems (Vasconcelos2008). These oxygens give rise to extraordinarily sharp signals in the range from δ_{CS}= 124.8 ppm to 136.7 ppm (including data from the reference mentioned above). Oxygen sites in crystal water (HOH) present chemical shifts in the range from -29.55 ppm to -23.69 ppm. These two types of oxygen environments are clearly distinguishable from NBO and therefore easily identified through their chemical shifts.

However, the distinction of the different NBO environments by a pure chemical shift approach is not full proof, due to the strong overlap of the different ranges of resonances.

As an example, oxygen environments with ionic bonds to sodium only (denoted as PO) present chemical shifts in a range of nearly 20 ppm (71.6 ppm for O3 in NaH_2PO_4 to 89.3 ppm for O3 in $Na_5P_3O_{10}$). Hence, within this range, no clear relationship can be drawn between the chemical shift and the number of sodium ions in the first sphere of coordination.

Non-terminal oxygen sites with covalent bonds to phosphorus and hydrogen show resonances from δ_{CS} = 70.32 ppm (O3 in $NaH_2PO_4*H_2O$) to 83.00 ppm (O4 in $NaH_2PO_4*2H_2O$). This chemical shift range cannot be distinguished from the previous one, rendering unambiguous assignment impossible. Other NBO sites show a covalent bond to phosphorus associated with hydrogen bonding (OH bond length around 1.5 Å) towards oxygen. They give δ_{CS} in a range from 94.02 to 108.34 ppm, clearly distinct from the two previous ones.

Sites O1 and O2 in $Na_2H_2P_2O_7$ (denoted as PO-H) require a special attention. The crystallographic data reveal OH bond lengths of 1.2 Å associated with chemical shifts δ_{CS} =94.64 ppm and 97.90 ppm. These values are intermediates to the calculated values for ionic (1.5 Å) and covalent (1.0 Å) OH bonds. This observation will be further addressed when considering the quadrupolar parameters.

To conclude, only limited trends can be drawn between the chemical shift and the local ^{17}O environments in sodium and sodium hydrogen phosphates. In the next paragraph, we will draw correlations between local ^{17}O environment and the corresponding quadrupolar parameters.

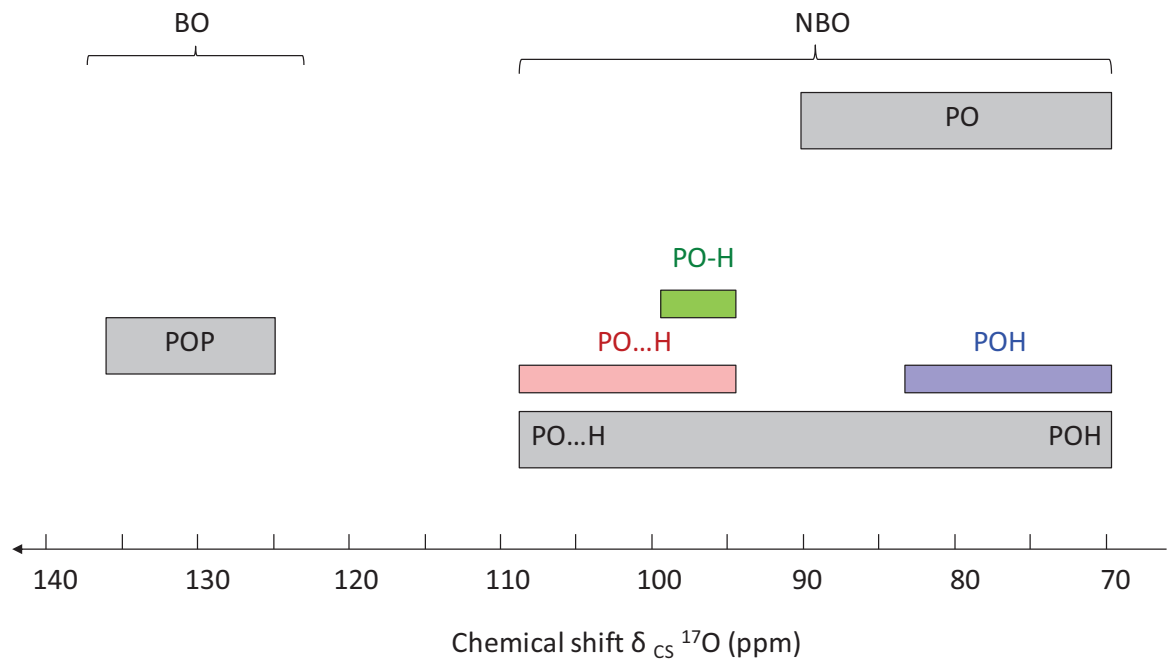

Fig. 3.8:
Chemical shift ranges for the various ^{17}O site types illustrated in Fig. 3.6. Chemical shift ranges of different ^{17}O environments overlap.

3.2.2 Quadrupolar parameters C_Q and η_Q

The quadrupolar parameters C_Q and η_Q can be used as a complementary source of structural information. Being sensitive probes for the local electric field gradient (Chapter 2), they provide valuable information about coordination and symmetry of the proximate surroundings of the observed oxygen sites (Vasconcelos2008, Ashbrook2007, MacKenzie2001).

Fig. 3.9 shows the characteristic C_Q ranges of the different types of oxygen environments. C_Q values in sodium hydrogen phosphates reach from about 4,9 MHz to 8,5 MHz.
Oxygen sites that exhibit ionic bonds towards their next nearest neighbors exhibit low C_Q values. As an example, PO sites with only Na^+ cations in their close surroundings have the smallest C_Q values [4,9 MHz; 5,4 MHz]. With increasing covalent contributions towards the proximate surroundings, C_Q values become larger. As an example, they increase with increasing covalence from PO…H [5,3 MHz] to POH (O-H distance: 1,0 A) [7,2 MHz] sites. Bridging oxygen sites establishing two covalent bonds towards their next nearest neighbors exhibit the highest C_Q values [7,7 MHz; 8,4 MHz].
The observed qualitative trends stand in agreement with those reported by several authors (MacKenzie2001, Schramm1984). On an empirical basis, the quadrupolar coupling constant is an indicator to determine the ionic / covalent nature of bonds within a group of similar materials. As an example, Schramm and Oldfield (Schramm1984) deduced in an early study a relationship for a family of compounds, including various oxides (MgO, K_2WO_4, ZnO, Mg_2SiO_4, $CaMgSi_2O_6$, α-Al_2O_3, B_2O_3). Their equation relates the ionic nature (I in %) of the respective O-M bonds with the corresponding quadrupolar coupling constants (in MHz):

$$\frac{e^2qQ}{h}\,(\mathrm{MHz}) = -0,203I(\%) + 14,78$$

Fig. 3.10 shows the characteristic η_Q ranges of the different types of oxygen environments. They cover the entire range of possible values [0,05; 0,98]. As it is the case for C_Q values, η_Q values become larger with increasing covalent contributions towards the proximate surroundings. PO sites with solely Na cations in their close surroundings exhibit the smallest η_Q values [0,05; 0,39]. Oxygen sites with Na, P and H in their proximate environment cover a wide range of η_Q values. In analogy to the observation for C_Q, η_Q increases with increasing covalent contribution in the O-H bond. PO…H exhibits the smallest η_Q values [0,25] whereas the covalent POH sites exhibit the highest η_Q [0,98].

Bridging oxygens (HOH and POP) exhibit high η_Q values [0,78; 0,84]. However, in contrast to the observations made for CQ, they do not exhibit the *highest* η_Q.

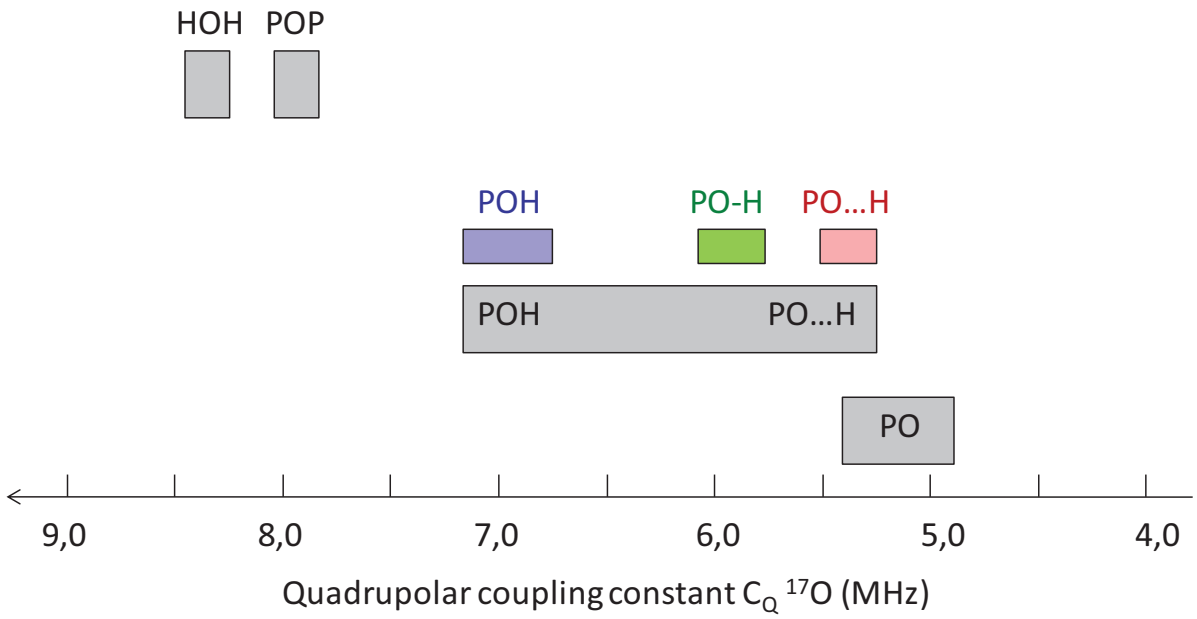

Fig. 3.9:
C_Q ranges for the various ^{17}O site types illustrated in Fig. 3.6. C_Q ranges of PO and PO…H ^{17}O environments overlap.

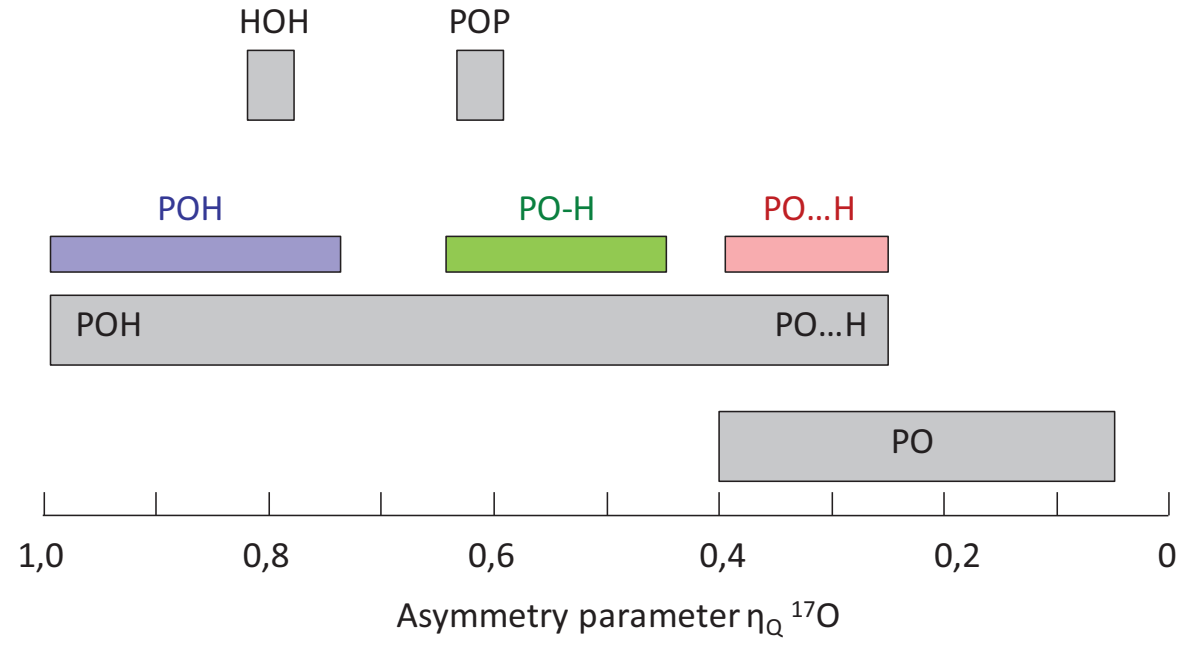

Fig. 3.10:
Asymmetry parameters for the various ^{17}O site types illustrated in Fig. 3.6. η_Q ranges of PO and PO…H and η_Q ranges of BO and NBO overlap.

To conclude, in the case of the sodium hydrogen phosphates investigated in the frame of this study and those sodium phosphates investigated in a previous work (Vasconcelos2008), both quadrupolar parameters C_Q and η_Q proved to be useful to classify the nature of the O-M and O-H bonds. The revealed trends are coherent with those found empirically (MacKenzie2001, Schramm1984), relating qualitatively the ionic / covalent nature of the O-M or O-H bonds with the quadrupolar parameter C_Q. Nevertheless, one single quadrupolar parameter does not allow for unambiguous determination of the ^{17}O environment. As an example, for both C_Q and η_Q, PO and PO…H ranges overlap. In the case of η_Q, bridging oxygens cannot be distinguished from highly covalent POH non-bridging oxygens.

3.2.3 2D correlation maps for unambiguous distinction

The combination of at least two NMR parameters allows for clear distinction of environments. *Fig. 3.11* shows the dispersion of calculated quadrupolar parameters for the sodium hydrogen phosphate phases presented in this work as well as values published previously (Vasconcelos2008).

In a two-dimensional dataset (*Fig. 3.11, top*), C_Q values are presented with their corresponding δ_{CS}. While ionic O-M and O-H bonds can be found in the lower range of C_Q values, O-H and O-P bonds exhibiting higher covalence lie in the higher C_Q range. This confirms results reported above. It is noteworthy that in the 2D map, each type of oxygen environment can be found in a distinct region. None of these regions presents any overlap with one another.

In a second two-dimensional dataset (*Fig. 3.11, bottom*), C_Q values are presented with their corresponding η_Q , mapping clearly distinguishable regions for ionic (C_Q = [4.5, 5.5 MHz]; η_Q = [0, 0.4]) and covalent C_Q = [6.5, 9 MHz]; η_Q = [0.5, 1.0]) bond types (Schramm1984). In the ionic region, there is an absence of correlation between the quadrupolar coupling strength and the asymmetry parameter value. Oxygen sites with ionic bonds towards hydrogen (PO…H oxygens, hydrogen bonding) show a constant C_Q value of 4.5 MHz, for example. However, as already observed in *Fig. 3.9* this region can be subclassified: PO…Na oxygens possess smaller C_Q and η_Q than hydrogen bonding PO…H oxygens.

Those oxygens involved exclusively in covalent bonds with phosphorus or hydrogen atoms (POH, HOH, POP) are found in a completely different range of C_Q and η_Q values, the covalent region (*Fig. 3.11*; *bottom*). Within this group, the three different compositions of the bonding environment are clearly distinguishable through their quadrupolar parameters.

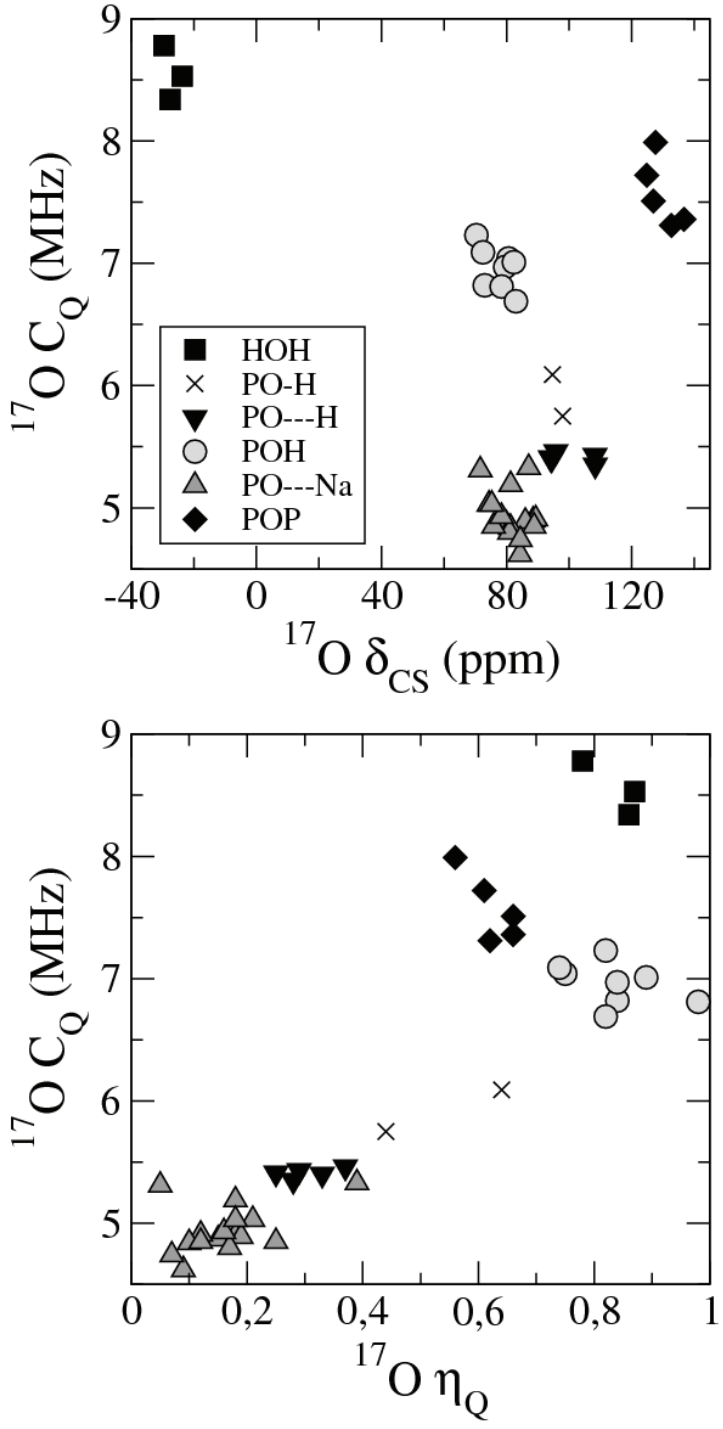

Fig. 3.11:
2D correlation maps of NMR parameters for different types of ^{17}O environments from this work (sodium hydrogen phosphates) and from Vasconcelos et al. (anhydrous sodium phosphates; Vasconcelos2008). Top: C_Q vs. δ_{CS}, bottom: C_Q vs. η_Q. Overlaps of regions are not observed. For further discussion see text.

HOH and POH oxygens, for example, are characterized by similar η_Q values positioned at the higher edge of the observation range. However, POP atoms show intermediate C_Q values of 7 MHz whereas HOH present high C_Q values close to 9 MHz. We notice that, this time, a correlation between the C_Q and the η_Q parameters exists, similar to the one reported for silicates (Clark2001, Charpentier2009).

3.2.4 Conclusion on systematic relationships:

While many empirical correlations can be observed, each of the ^{17}O NMR parameters δ_{CS}, C_Q and η_Q depends on a variety of structural features in the proximate (and long-range; Vasconcelos2008) environment of the nucleus. As an example, not only the O-M or O-H bond distance influences the quadrupolar coupling constant C_Q. The coordination number, the chemical composition of the close surroundings and bond angles influence the electron density and the symmetry of the ^{17}O environment, too. Various attempts have been made to establish relationships between quadrupolar parameters and the structural features mentioned above (Schramm1984, Timken1987, Ashbrook2006). Not only bond distances were studied systematically, Si-O-Si bond angles and P-O-P bond angles have been the subject of studies, too.
However, all approaches relate to groups of similar materials and focus on a restricted number of structural characteristics. This must not be neglected whilst considering the relationships elaborated above. Those are successfully applicable for the unambiguous determination of the ^{17}O environment in the case of sodium and sodium hydrogen phosphate systems. Absolute results cannot be applied to other families of compounds. It is not possible to take into account all changing variables that might influence C_Q and η_Q.

Nevertheless, the most widely applicable observation is the fact that bridging oxygens can be distinguished from non-bridging ones by their respective quadrupolar coupling constants (Ashbrook2007, Vasconcelos2008) as it has been confirmed in the frame of this work.
Moreover, the obtained results lead to relationships that are systematic within the sodium phosphate family. The 2D C_Q / η_Q map is a versatile tool to distinguish *at first sight*,

- BO from NBO
- O-Na from O-H bonds
- ionic from covalent O-H bonds
- POP from HOH.

3.3 Follow-up of water alteration of $NaPO_3$ glass by ^{17}O NMR

The previous results can be exploited for the NMR investigation of crystalline phosphate phases resulting from the alteration of a phosphate glass by water, namely $NaPO_3$. In the present study, our aim was to demonstrate the ability and versatility of ^{17}O NMR to identify the crystalline products generated under mild alteration conditions. Further, it will be demonstrated that the calculation approach gives access to a quantitative analysis of the 2D ^{17}O 3QMAS spectra of the aging glass.

Fig. 3.12 shows ^{17}O 3QMAS snapshots of the hydration of $NaPO_3$ glass at different stages of the alteration process, after 1, 10, 12 days and after two years of alteration in a thermostatic water bath at 60°C. In this particular case, the aim was not to simulate weathering. Emphasis was lying on identification and quantification of degradation products in a complex mixture, exclusively.

The water alteration into $NaPO_3$ leads to degradation of the glass and this in turn generates a complex mixture of crystalline and amorphous phases (*Fig. 3.12*). Most of the 2D ^{17}O 3QMAS snapshots exhibit overlapping resonances, arising from the formation and transformation of several crystalline and/or amorphous phosphate phases. Certain resonances show a low intensity. This may be due to the small concentration of the corresponding ^{17}O sites in the phase mixture or to inhomogeneous multiple-quantum excitation. ^{17}O sites with large C_Q values show small triple-quantum excitation efficiency compared to ^{17}O sites with small quadrupolar coupling interaction with the surrounding EFG.

3.3.1 Phase identification in snapshots:

The ^{17}O 3QMAS spectra of NaH_2PO_4 and $NaH_2P_2O_7$ (*Fig. 3.3 and Fig. 3.4*) can be used to characterize some of the phosphate phases that occur at different intermediate steps of the alteration of the $NaPO_3$ glass. The two NBO resonances of $NaH_2P_2O_7$ at δ_{iso} values of 88 ppm and 102 ppm, denoted as sites O3 and O1/O2, respectively, are present throughout the degradation process revealing the rapid formation of $Na_2H_2P_2O_7$ during degradation of the glass. The relative proportion of one of these resonances, the isolated O3 resonance for example, would give access to the possible quantification of this phase during the entire alteration process (see 3.3.2).

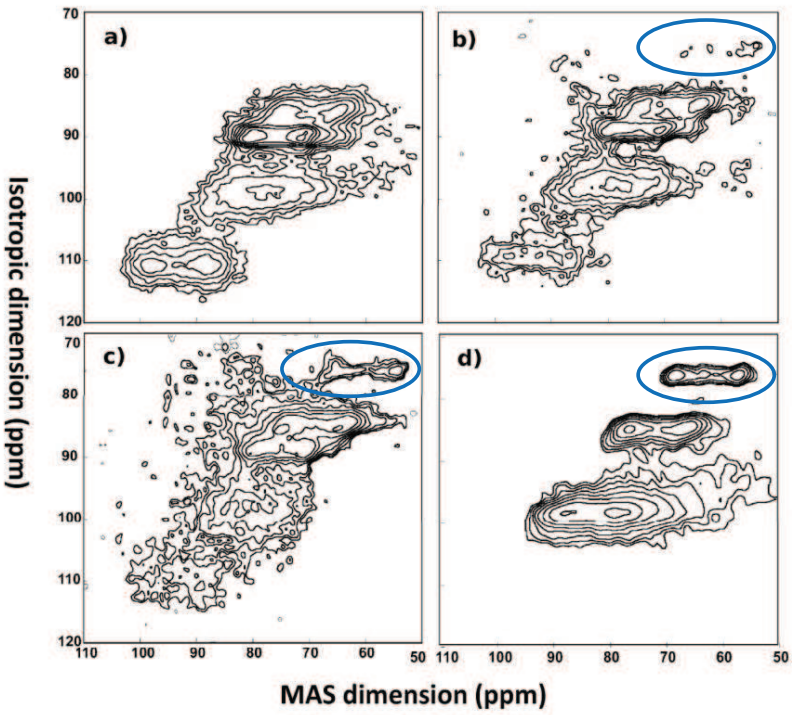

Fig. 3.12:
2D ^{17}O 3QMAS snapshots of NaPO3 glass after (a) 1 d, (b) 10 d, (c) 12 d and (d) 2 years of water alteration. Blue: Site O3 in NaH_2PO_4 is highlighted.

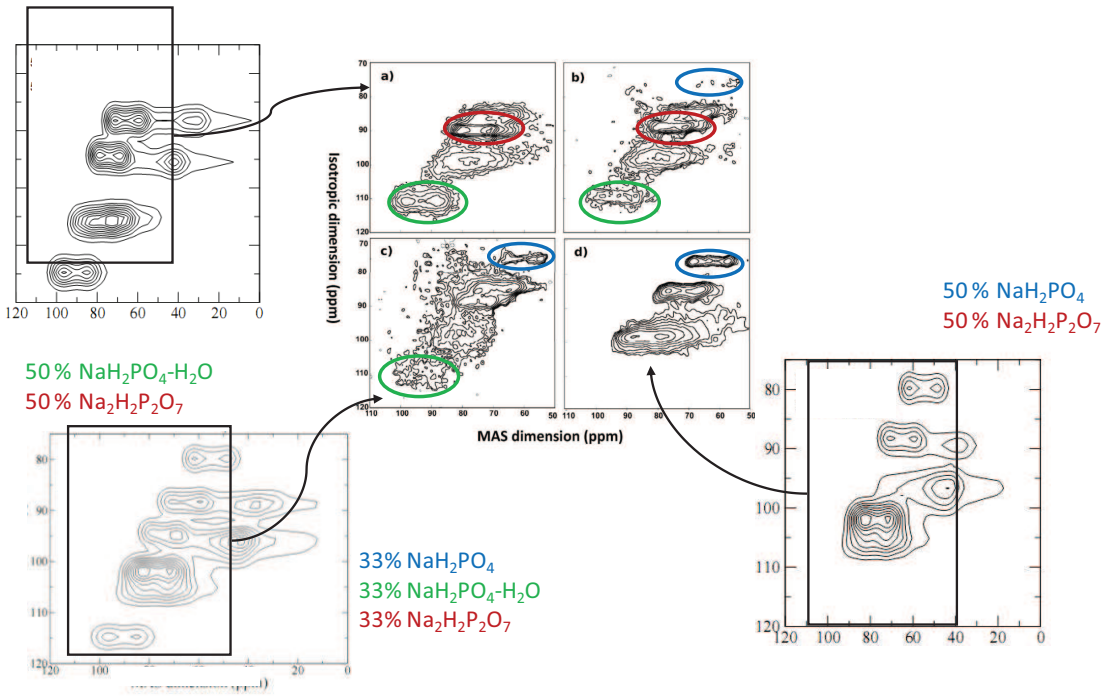

Fig. 3.13:
2D ^{17}O 3QMAS snapshots of NaPO3 glass after (a) 1 day, (b) 10 days, (c) 12 days and (d) 2 years of water alteration. Next to (a), (c) and (d) the simulated 2D ^{17}O 3QMAS spectra are presented. They allow for insight into relative proportions of phases present in the glass degradation mixture. Blue circles highlight crystallographic site O3 in NaH_2PO_4, red circles highlight site O3 in $Na_2H_2P_2O_7$ and green circles highlight crystallographic site O2 $NaH_2PO_4*H_2O$.

Based on the calculated NMR parameters that gave rise to the simulated spectra of $NaH_2PO_4*H_2O$ and $NaH_2PO_4*2H_2O$ in *Fig. 3.7*, one can observe that the site at δ_{iso} of about 110 ppm is characteristic for the presence of at least one of these phases in the first stages of alteration. A careful examination of the low chemical shift range (not shown), reveals that the doubly hydrated phosphate phase $NaH_2PO_4*2H_2O$ must be excluded due to the absence of a second oxygen site in the region of HOH (bridging) oxygen sites.

Later in the alteration process, the formation of NaH_2PO_4 can be observed, confirmed by the presence of the characteristic resonance at δ_{iso}=80 ppm assigned above to O3 and highlighted in red in *Fig. 3.12*. Simultaneously, resonances characteristic for $NaH_2PO_4*H_2O$ disappear.

After two years of evolution (*Fig. 3.12 d*), the snapshot presents crystalline NaH_2PO_4 and $Na_2H_2P_2O_7$ resonances. Hydrated sodium phosphate phases are no longer observed in the aged $NaPO_3$ glass.

To conclude, the ^{17}O NMR-based identification of crystalline phases generated throughout degradation of $NaPO_3$ glass is difficult due to the large variety of crystalline and amorphous phases that emerge throughout the transformation of the initial $NaPO_3$ glass. Nevertheless, from a purely qualitative point of view, the snapshots of $NaPO_3$ glass attacked by water provide crucial information: ^{17}O NMR data of hydrated sodium hydrogen $NaH_2PO_4*H_2O$ could be collected. Since this phase is not stable under moderate temperature fluctuations, the snapshots allow for the first time for verification of the calculated reference data (*Tab. 3.1, Fig. 3.5*).

3.3.2 Phase quantification in snapshots

Fig. 3.13 presents the snapshots of $NaPO_3$ exposed to aqueous attack together with simulated spectra of crystalline phase mixtures. The same local ^{17}O environments give rise to the same NMR parameters in crystalline and amorphous phases. In amorphous phases, distributions of these NMR parameters are observed, since the individual local geometries vary slightly. Nevertheless, the analogies in the local environments can be exploited to access the complex phase mixture quantitatively. Based on the reference NMR data of the four crystalline sodium hydrogen phases NaH_2PO_4, $Na_2H_2P_2O_7$, NaH_2PO_4*H2O and $NaH_2PO_4*2H_2O$, spectra of purely crystalline mixtures were simulated.

In the first snapshot taken after 1 day of water alteration into the glass, $NaH_2PO_4*H_2O$ and $Na_2H_2P_2O_7$ were identified (see section above). A simulated spectrum presenting equal fractions (50%) of both crystalline phases is presented in *Fig. 3.13* (next to snapshot *a*) where the experimental spectral window is highlighted in black. The main sites and their proportions present in the first simulated

snapshot correspond to those observed in the experimental data (*Fig. 3.13 a*). They are highlighted in green ($NaH_2PO_4*H_2O$) and red ($Na_2H_2P_2O_7$).
In the third snapshot taken after 12 days of water alteration into the glass, a simulated spectrum for a crystalline mixture containing equal fractions of $NaH_2PO_4*H_2O$, $Na_2H_2P_2O_7$ and NaH_2PO_4 (33%) stands in agreement with experimental observations.
After two years, equal fractions of $Na_2H_2P_2O_7$ and NaH_2PO_4 are present in the alterated $NaPO_3$ glass.

The challenge in the above section was to simulate NMR data for complex phase mixtures generated through transformation of $NaPO_3$ glass upon aqueous attack. It was possible to obtain simulated 2D ^{17}O 3QMAS spectra that stand in agreement with those experimentally observed in snapshots taken at different stages of water alteration into $NaPO_3$ glass. The simulated spectra lead to reliable results, since they take various experimental parameters (e.g. excitation efficiencies for different quadrupolar coupling constants) into account.
Thus, the combination of calculation / simulation approach and experimental ^{17}O 3QMAS snapshots allows for a first idea about the relative proportions of the different phases present at the different stages of aqueous attack.

3.3.3 Heteronuclear correlation: ^{31}P-^{17}O J-HMQC

Fig. 3.14 (top) exhibits a ^{31}P-^{17}O J-HMQC correlation spectrum of the snapshot taken after 12 days of aqueous attack on $NaPO_3$. The spectrum is accompanied by a ^{17}O 3QMAS spectrum (snapshot after 12 days, *Fig. 3.12 c*; *Fig. 3.14* bottom) in order to ease visual inspection and attribution of the correlations.
Only those ^{17}O sites that are chemically bonded to ^{31}P appear in the J-HMQC correlation spectrum. In the ^{31}P dimension (*Fig. 3.14, top*) Q^1 (around -10 ppm) and Q^0 resonances (about 0 ppm) can be observed. A high degree of crystallinity is present in the resonance range of Q^0 phosphorus sites. Their chemical shift difference corresponds to the one observed in crystalline NaH_2PO_4 reference data.
Relations between the HMQC spectrum and the corresponding resonances in the 2D ^{17}O 3Q MAS spectrum can be drawn. As expected, the NBO resonance attributed to site O3 in $Na_2H_2P_2O_7$ is correlated to the Q^1 type ^{31}P resonance at about -8 ppm (red arrows). The Q^0 type resonances at about 0 ppm in the ^{31}P dimension can be correlated to two NBO sites in the NaH_2PO_4 phase (blue and yellow arrows). *Fig. 3.14* illustrates the correlations visible in the ^{31}P-^{17}O J-HMQC spectrum.

The spectral window (isotropic dimension, *Fig. 3.14*, bottom) has been restricted to the region of NBO sites. The expected correlation between Q^1 phosphorus sites (*Fig. 3.14* top) and the BO resonance in $Na_2H_2P_2O_7$ (O4) has not been observed in the ^{31}P-^{17}O J-HMQC due to a lack of sensitivity.

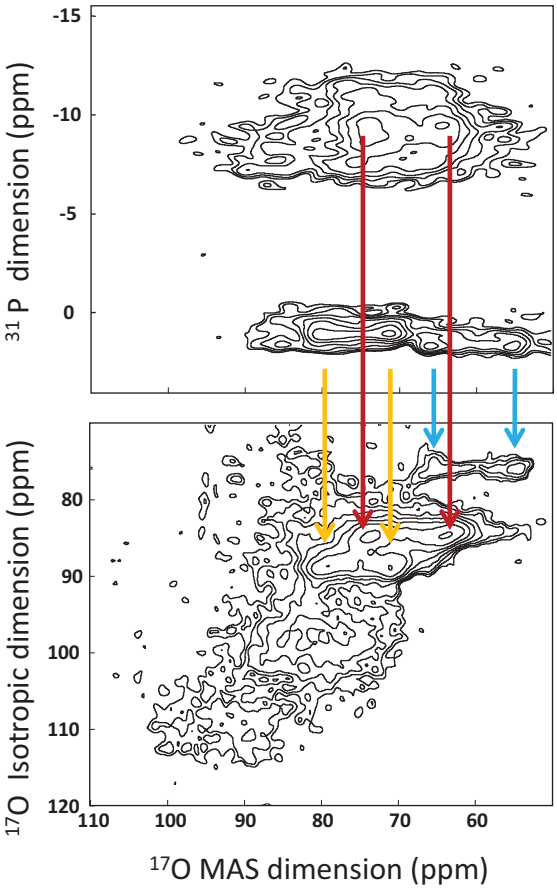

Fig. 3.14:
^{31}P - ^{17}O J-HMQC spectrum of $NaPO_3$ glass after 12 days of water alteration (top) together with the corresponding ^{17}O 3QMAS spectrum (bottom) to ease visual inspection.

The low efficiency of triple-quantum excitation of the POP site (large C_Q) and the low abundance of the $P^{17}OP$ site are factors that render detection of the corresponding signal extremely difficult: The maximum ^{17}O enrichment rate is 40%. From a crystallographic point of view, O4 sites are less represented in the phase than NBO crystallographic sites: O4:O1:O2:O3 = 1:2:2:2.

To conclude, in combination with 3QMAS, ^{31}P-^{17}O J-HMQC is a technique that enables correlation of ^{31}P and ^{17}O resonances observed through aging of $NaPO_3$. Former results (see section identification) have been confirmed by the combination of these techniques.

For future investigations, heteronuclear correlation techniques involving ^{17}O can be employed to complement high-resolution data and to ease assignment of multinuclear NMR spectra. Additionally, in the case of unidentified phases, structural information can be gained in a rapid way.

Summary and Conclusion Chapter 3

Summary:

In the present chapter special attention has been dedicated to ^{17}O as a NMR probe nucleus with regard to subsequent studies of weathering phosphate glasses. Three aims were pursued:

In the first part of this chapter, a NMR calculation / simulation approach should be validated for crystalline sodium *hydrogen* phosphate phases that are possibly generated throughout the weathering process of sodium phosphate glasses. It was of particular interest to complement experimental NMR data, to aid assignment and interpretation of ^{17}O NMR spectra and to establish a calculation protocol that allows the generation of reliable ^{17}O reference data for crystalline sodium hydrogen phosphate phases without performing costly and time-demanding ^{17}O-enrichment of reference samples.
A DFT / GIPAW approach was used to optimize the geometry of structural reference data of NaH_2PO_4 and $Na_2H_2P_2O_7$ and to calculate the corresponding NMR parameters subsequently. A simulation program (Charpentier1998) allowed for generation of simulated spectra based on the calculated NMR parameters. Simultaneously, ^{17}O-enriched crystalline NaH_2PO_4 and $Na_2H_2P_2O_7$ were synthesized and experimental NMR data were collected.
The calculation approach for hydrogen containing crystalline phosphate phases was successfully validated. Experimental and calculated / simulated ^{17}O NMR data of ^{17}O-enriched NaH_2PO_4 and $Na_2H_2P_2O_7$ stand in high agreement. In the case of ^{17}O NMR spectra, calculated / simulated NMR parameters allowed to overcome the limits of sensitivity and resolution of the 3QMAS NMR data and to assign all ^{17}O resonances present in the spectra unambiguously.
The successful validation of the calculation approach in the case of NaH_2PO_4 and $Na_2H_2P_2O_7$ allowed to include calculated data of two hydrated phosphate phases that are not accessible by synthesis, namely $NaH_2PO_4*H_2O$ and $NaH_2PO_4*2H_2O$, in the correlation studies carried out subsequently in this chapter.

The second aim of the work carried out in this chapter was to draw systematic correlations between the local environment of ^{17}O sites and their corresponding NMR parameters δ_{CS}, C_Q and η_Q. The trends that were revealed for sodium hydrogen phosphates were coherent with those reported by several authors (Schramm1984, MacKenzie2001) and previously published results within the group (Vasconcelos2008). The quadrupolar coupling constant C_Q proved to be a precise indicator for the

covalent or ionic bond nature: with increasing covalency between O and Na or H the quadrupolar coupling constant C_Q is increasing. In addition, η_Q shows the same trends.
Mapping ^{17}O NMR parameters in two-dimensional δ_{CS} vs. C_Q or C_Q vs. η_Q maps is a versatile tool for the discrimination of the different environments of ^{17}O. In particular in C_Q vs. η_Q maps, the chemical composition can be differentiated, e.g. P-O…Na from P-O…H. Ionic bonds are clearly separated from covalent ones. The latter can be subdivided into POP, HOH and POH bonds at first sight.
The possibility to distinct classify P-O…H, P-O-H and POH and HOH environments by ^{17}O NMR is of particular interest with regard to the hydrolytic depolymerization of phosphate glasses. Besides ^{1}H NMR and ^{1}H-^{31}P CP NMR, it allows for monitoring the way of water incorporation from a complementary point of view.

In the third part of this chapter, the aim was to implement the combination of NMR and first principles calculations presented above in order to study sodium phosphate glass alteration by water, namely $NaPO_3$, for the first time. The combined methodology proved to be a powerful tool to follow the process of degradation of the glass and to identify the generated crystalline and amorphous phases. As an example, the hydrated phase $NaH_2PO_4*H_2O$ whose reference NMR data are based on the DFT / GIPAW calculation approach solely (see 3.1.2), could be identified as an intermediate product of the early stages of the alteration process (see 3.3.1 and 3.3.2).
A complex mixture of crystalline and amorphous phases is generated upon aging of $NaPO_3$ glass. However, the similarities in the local environments of the same types of ^{17}O sites in crystalline and amorphous phases could be used to describe the aged mixture quantitatively. Based on the reference NMR data of the four crystalline sodium hydrogen phases, spectra of mixtures were simulated. This allowed for determining the relative proportions of the different phases present in the attacked $NaPO_3$ glass.

Conclusion:

So far, ^{17}O NMR parameters of *hydrogenated* crystalline phosphate phases have not been investigated by a combined NMR / DFT/ GIPAW approach and discussed in detail, since the exact determination of the proton positions represented a remarkable challenge for structure optimization. DFT / GIPAW investigations of NMR parameters of calcium hydrogen phosphates have been reported elsewhere, but the published calculated data for ^{17}O are not accompanied by experimental NMR controls (Pourpoint2008).

The combination of 2D 3QMAS ^{17}O NMR and DFT calculations helped to overcome the limits of sensitivity and resolution of the 2D ^{17}O 3QMAS experiment in a unique way. It enabled complete assignment of the observed resonances. These results build the first step towards a systematic study of cationic effects on quadrupolar parameters and thus on the immediate surroundings of oxygen sites in crystalline phosphate phases. This methodology is not restricted to the phosphates presented in this study and can be expanded to a variety of compounds, particularly to more complex crystalline and amorphous systems, as $Na_5P_3O_{10}$ for example.

In Chapter 4, interest in ^{17}O as a probe nucleus will be continued with respect to systematic weathering studies carried out on $NaPO_3$ glass. Using the results of the present chapter, ^{17}O-enriched water will be employed as a selective marker for sites of attack in a non-enriched phosphate glass exposed to ^{17}O-enriched humid or aqueous atmosphere. Compared to silicate materials, this domain still remains to be explored in phosphate glasses.

Bibliography Chapter 3

Alam2004
Alam, T. M., Segall, J. M.
Journal of Molecular Structure, Theochem (2004) **674** 167

Amoureux1996
J.-P. Amoureux, J.-P., Fernandez, C., Steuernagel, S.,
Journal of Magnetic Resonance (1996) **A123** 116

Amoureux2002
Amoureux, J.-P., Huguenard, C., Engelke, F., Taulelle, F.,
Chemical Physics Letters (2002) **356 (5-6)** 497-504

Angeli2008
Angeli, F., Charpentier, T., Gaillard, M., Jollivet, P.,
Journal of Non-Crystalline Solids (2008) **354 (31)** 3713-3722

Ashbrook2007
Ashbrook, S.E., Berry, A.J., Frost, D.J., Gregorovic, A., Pickard, C.J., Readman, J.E., Wimperis, S.
Journal of the American Chemical Society (2007) **129 (43)** 13213-13224

Ashbrook2007a,
Ashbrook, S.E., Le Pollès, L., Pickard, C.J., Berry, A.J., Wimperis, S., Farnan, I.
Physical Chemistry Chemical Physics (2007) **9 (13)** 1587-1598

Bartl1976
Bartl, H., Catti, M., Ferraris, G.
Acta Crystallographica Section B (1976) **32 (4)** 987-994

Benoit2005
Benoit, M., Profeta, M., Mauri, F., Pickard, C.J., Tuckerman, M.E.
Journal of Physical Chemistry B (2005) **109 (13)** 6052-6060

Blöchl1994
Blöchl, P.E.
Physical Review B (1994) **50 (24)** 17953-17979

Catti1976
Catti, M., Ferraris, G.
Acta Crystallographica Section B (1976) **32 (2)** 359-363

Charpentier1998
Charpentier, T., Fermon, C., Virlet, J.
The Journal of Chemical Physics (1998) **109 (8)** 3116-3130

Charpentier2004
Charpentier, T., Ispas, S., Profeta, M., Mauri, F., Pickard, C.J.
Journal of Physical Chemistry B (2004) **108 (13)** 4147-4161

Charpentier2009
Charpentier, T., Kroll, P., Mauri, F.
Journal of Physical Chemistry C (2009) **113 (18)** 7917

Choudhary1981
Choudhary, R. N. P., Nelmes, R. J., Rouse, K. D.
Chemical Physics Letters (1981) **78 (1)** 102-105

Clark2001
Clark, T.M., Grandinetti, P.J., Florian, P., Stebbins, J.F.
Journal (2001) 105 (49), 12257-12265

Clark2004
Clark, T. M., Philip J., Grandinetti, P. J., Florian, P., Stebbins, J. F.
Physical Review B (2004) **70** 064202

Coelho2007
Coelho, C., Benharbya, N., Gervais, C., Azais, T., Bonhomme-Coury, L., Laurent, G.,
Mauri, F., Bonhomme, C.
Materials Research Society Symposium Proceedings (2007) **984** 74-79

Du2007
Du, L. S., Peng, L., Stebbins, J. F.
Journal of Non-Crystalline Solids (2007) **353 (30-31)** 2910-2918

Forler2010
Forler, N., Vasconcelos, F., Cristol, S., Paul, J.-F., Montagne, L., Charpentier, T., Mauri, F., Delevoye, L.
Phys. Chem. Chem. Phys. (2010), **12**, 9053-9062

Frydman1995
Frydman, L., Harwood, J.S.,
Journal of the American Chemical Society (1995) **117 (19)** 5367-5368

Gan2000
Gan, Z.
Journal of the American Chemical Society (2000) **122 (13)** 3242-3243

Gervais2004
Gervais, C., Profeta, M., Babonneau, F., Pickard, C.J., Mauri, F.
Journal of Physical Chemistry B (2004) **108 (35)** 13249-13253

Hohenberg1964
Hohenberg, P., Kohn, W.
Physical Review B (1964) **136 (3B)** 864

Hussin1998
Hussin, R., Holland, D. Dupree, R.,
Journal of Non-Crystalline Solids **(1998) 232-234** 440-445

Iuga2000
Iuga, D., Schafer, H., Verhagen, R., Kentgens, A. P. M.
Journal of Magnetic Resonance (2000) **147** 192

Kohn1965
Kohn, W. Sham, L.
Physics Review (1965) **140 (4A)** 1133

Kresse1993
Kresse, G., Hafner, J.
Physical Review B (1993) **48** 13115

Kresse1996
Kresse, G., Furthmüller, J.
Physical Review B (1996) **54** 11169

Massiot2002,
Massiot, D., Fayon, F., Capron, M., King, I., Le Calvé, S., Alonso, B., Durand, J. O.,
Bujoli, B., Gan, Z., Hoatson, G.
Magnetic Resonance in Chemistry (2002) **40 (1)** 70-76

Massiot2003
Massiot, D., Fayon, F., Alonso, B., Trebosc, J., Amoureux, J. P.
Journal of Magnetic Resonance (2003) **164** 160

Mauri1996
Mauri, F., Pfrommer, B.G., Louie, S.G.,
PRL (1996) **77 (26)** 5300

Medek1995,
Medek, A., Harwood, J.S., Frydman, L.,
Journal of the American Chemical Society (1995) **117 (51)** 12779-12787

PARATEC,
Pfrommer, B., Raczkowski, D., Canning, A., Louie, S.G., Mauri, F., Cote, M., Yoon, Y., Pickard, C.J.,
Heynes, P.,
www.nersc.gov/projects/paratec

Perdew1996
Perdew, J.P., Burke, K., Ernzerhof, M.
Physics Review Letters (1996) **77** 3865

Pickard2001
Pickard, C.J., Mauri, F.
Physical Review B (2001) **63** 245101

Pourpoint2008,
Pourpoint, F., Gervais, C., Bonhomme-Coury, L., Mauri, F., Alonso, B., Bonhomme, C.
Comptes Rendus Chimie (2008) **11 (4-5)** 398-406

Prochnow2006
Prochnow, D., Grimmer, A.-R., Freude, D.
Solid-State Nuclear Magnetic Resonance (2006) **30 (2)** 69-74

Profeta2003
Profeta, M., Mauri, F., Pickard, C.J.
Journal of the American Chemical Society (2003) **125 (2)** 541-548

Pykkö2001
Pykkö, P.
Mol. Phys. (2001) **99 (19)** 1617

Schramm1984
Schramm, S., Oldfield, E.,
Journal of the American Chemical Society (1984) **106 (9)** 2502-2506

Selevich2002,
Selevich, K. A., Ivashkevich, L. S., Selevich, A. F., Lyakhov, A. S.
Russian Journal of Inorganic Chemistry (2002) **47 (10)** 1533-1536

Trouillier1991
Trouillier, N., Martins, J.L.
Physical. Review B (1991) **43** 1993

Vasconcelos2008
Vasconcelos, F., Cristol,S., Paul, J.-F., Tricot,G., Amoureux, J.-P., Montagne, L., Mauri,F. Delevoye, L.,
Inorganic Chemistry (2008) **47 (16)** 7327-7337

VASP
http://cms.mpi.univie.ac.at/vasp/

Chapter 4

The weathering of a binary model phosphate glass ($NaPO_3$) investigated by solid-state NMR

CHAPTER 4

The weathering of a binary model phosphate glass ($NaPO_3$) investigated by solid-state NMR

In the following chapter, degradation of a model phosphate glass, $NaPO_3$, under an atmosphere saturated with water vapor will be examined. Multinuclear solid state NMR has been implied as the major tool, employing ^{31}P, ^{1}H and ^{17}O as probe nuclei. It will be demonstrated that a combination of routine and advanced solid-state NMR techniques provide a means to achieve understanding of phosphate glass weathering on an atomic level.

In the first section of the following chapter, 1D ^{31}P and ^{1}H NMR will be employed to monitor changes in network polymerization and phase emergence qualitatively. In addition, ^{31}P RFDR will be employed to obtain information about unidentified crystalline phases present in 1D ^{31}P NMR spectra. ^{1}H-^{31}P CP will be useful to discern protonated from non-protonated phosphate tetrahedra and to correlate them to their respective proton environments.

Subsequently, in the second part of this chapter, ^{31}P NMR data is analyzed quantitatively. Kinetics do not provide exact mechanistic information, but can support or oppose proposed models for surface degradation under water vapor attack (Brow1990, Tischendorf2004). A polynomial analysis of the quantitative data will lead us to conclusions about preferred sites of attack.

Finally, ^{17}O will be employed as a selective isotopic probe nucleus to monitor sites of attack and the incorporation of water and its derivatives into the glass network. 2D 3QMAS NMR is the method of choice to achieve anisotropic-isotropic correlation spectra of the nucleus that can be compared with the NMR-structure relationships that have been elaborated in Chapter 3.

Sodium metaphosphate glass, $NaPO_3$, serves us as a model system of simple and well known structure, exhibiting suitable weathering kinetics. The details of glass preparation, handling and weathering conditions have been described in Chapter 2. The results and conclusions of the present chapter will help us to extend our view to ternary model systems in Chapter 5 where a first systematic NMR approach to the weathering of aluminophosphate glass systems will be presented.

NMR details Chapter 4

1D NMR spectra:

a) ^{1}H NMR

One-pulse 1D ^{1}H NMR experiments have been recorded at 9.4 T (ν_0 ^{1}H = 400.16 MHz) at MAS spinning speeds of 10 kHz. A 4 mm HX probe has been employed. The radiofrequency amplitude has been set to be (ν_{rf} ^{1}H) 50 kHz with a pulse length of 4 µs and a relaxation delay of 10 s.

^{1}H chemical shifts have been referred to tetramethylsilane (TMS).

The high resolution spectra and the ^{1}H spectra of samples weathered in $H_2{}^{17}O$ atmosphere have been recorded at 18.8 T with a resonance frequency of (ν_0 ^{1}H = 800.30 MHz). A 1.3 mm HX probe with MAS frequencies of 60 kHz was employed. For suppression of rotor and probe artifacts, the DEPTH sequence was used.

^{1}H chemical shift values are referred to adamantine.

b) ^{31}P NMR

1D ^{31}P NMR spectra have been recorded at 9.4 T. One-pulse ^{31}P spectra have been acquired using a 1.6 µs pulse length, a radiofrequency amplitude of (ν_{RF} ^{31}P) 50 kHz, 4 or 16 transients and a relaxation delay between 60 and 100 s, depending on the crystallinity of the sample. During acquisition, ^{1}H high power decoupling at an amplitude of (ν_{RF} ^{1}H) 73.5 kHz has been used, employing spinal 64.

1D ^{31}P NMR spectra of the samples weathered under $H_2{}^{17}O$ atmosphere have been recorded in a 3.2 mm HX probe at 18.8 T and MAS spinning speeds of 20 kHz. A one-pulse spectrum was acquired, the number of scans was set to be 1.

^{31}P chemical shift values are referred to 85% H_3PO_4.

^{31}P-{^{1}H} CP MAS

The ^{1}H-^{31}P cross-polarization experiment was performed in a 4 mm HX probe at a spinning frequency of 10 kHz, CP transfer was effected during 2 ms at a radiofrequency amplitude of 45 kHz, using a ramp. During acquisition, ^{1}H high power decoupling at an amplitude of (ν_{RF} ^{1}H) 60 kHz has been used, employing spinal 64.

The number of scans was set to be 128, the relaxation delay was 5 s.

^{31}P-{^{1}H} CP MAS edited RFDR

The ^{1}H-^{31}P cross-polarization edited RFDR experiment was performed in a 4 mm HX probe at a spinning frequency of 10 kHz. CP transfer was effected during 3 ms at a radiofrequency amplitude of 50 kHz, using a ramp. Magnetization exchange was allowed for 50 rotor cycles (10 ms). During acquisition, ^{1}H high power decoupling at an amplitude of (ν_{RF} ^{1}H) 70 kHz has been used, employing spinal 64.

The number of scans was set to be 16, the relaxation delay was 5 s.

^{17}O 3QMAS spectra

The ^{17}O MAS spectra have been recorded at 18.8 T, employing a 3.2 mm tri-γ probe operating at (ν_0 ^{17}O = 108.47 MHz). A selective pulse of 11 µs at a radio frequency (RF) field strength of 7.5 kHz was used for excitation. The excitation pulse was preceded by a Double Frequency Sweep (DFS) pulse of 3 ms sweeping between 100 and 900 kHz at a RF field amplitude of 50 kHz in order to enhance the central transition polarization for half-integer quadrupolar nuclei. The 3QMAS spectra were collected at a MAS speed of 20 kHz, using the z-filter sequence. It consisted of two hard pulses of 3.5 and 1.2 µs at an RF field of 100 kHz, for triple-quantum excitation and reconversion, respectively, followed by a soft pulse of 9 µs. The t_1 step was set to be a multiple (n=1 or 2) of the MAS period.

4.1 Phase emergence during weathering

4.1.1 Evolution of ^{31}P NMR spectra during weathering

Fig. 4.1 depicts the center band 1D ^{31}P NMR spectrum of pristine sodium metaphosphate ($NaPO_3$) glass, showing three broad resonances that are well resolved from each other. The resonances at about - 20 ppm, -8 ppm and 0 ppm can be assigned to Q^2_{Na}-, Q^1_H- (Hartmann1994) and Q^0_H or Q^1_{Na} units respectively. The ^{31}P chemical shift ranges of Q^2_{Na}, Q^1_H, Q^1_{Na}, Q^0_H and Q^0_{Na} signals are indicated at the bottom of *Fig. 4.1*. Ideally, sodium metaphosphate glass consists of infinite chains of Q^2 units. Contributions in the Q^1_H resonance region (-8 ppm) result from residual protons at phosphate chain ends (about 3.0 %). Those protons could not be removed during glass preparation despite its melting at high temperature. Signal intensity around 0 ppm arises from Q^1_{Na} units at phosphate chain ends (about 0.4 %), resulting from excessive sodium content in the batch composition. ^{1}H-^{31}P CP MAS (not shown) excluded the presence of Q^0_H units for pristine $NaPO_3$ glass.

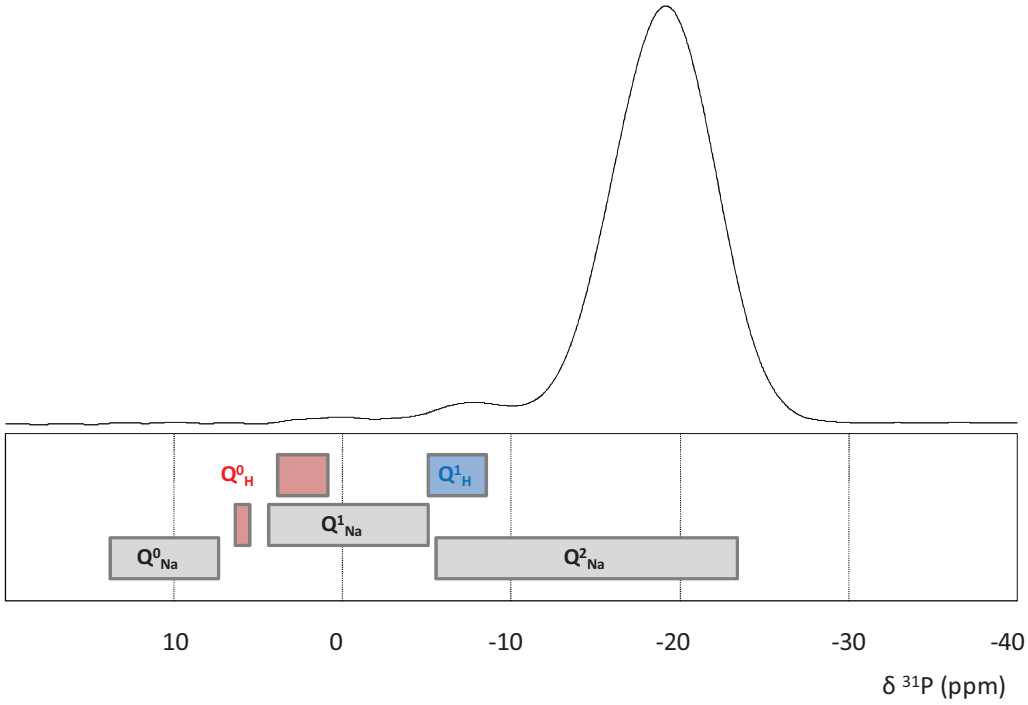

Fig. 4.1:

1D ^{31}P NMR spectrum of pristine $NaPO_3$ glass (top) together with chemical shift ranges for Q^n entities (bottom).

Figures 4.2a-c show the center bands of the 1D ^{31}P NMR spectra collected during $NaPO_3$ glass weathering. The exposure times varied from 1 h to 70 h and are indicated in the figures

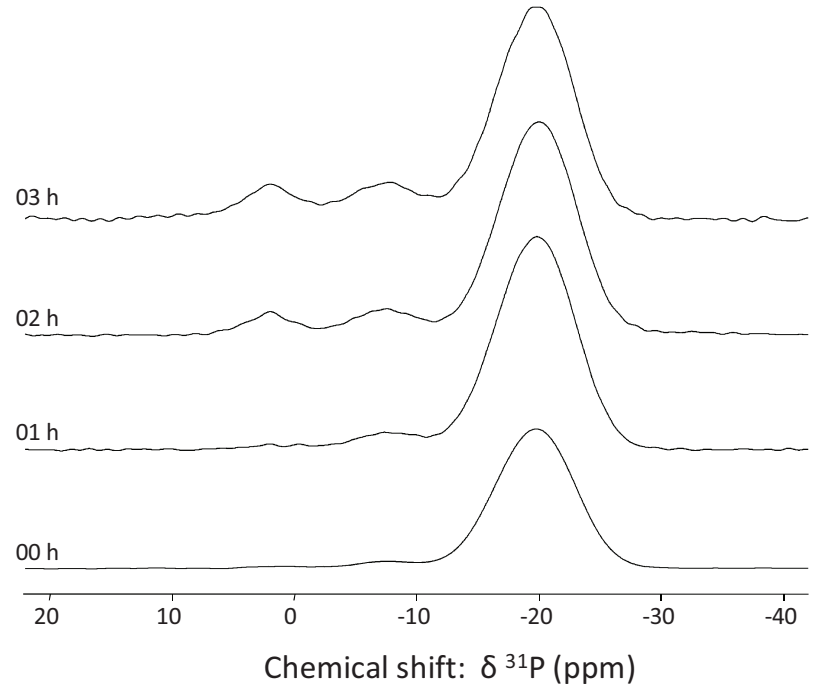

Fig. 4.2a:
1D ^{31}P NMR spectra during the first regime of the weathering process. Resonances are broad and characteristic of an amorphous material. Spectra are recorded at a static field of 9.4 T, MAS spinning speed 10 kHz (rotor diameter 4.0 mm), high power proton decoupling has been employed.

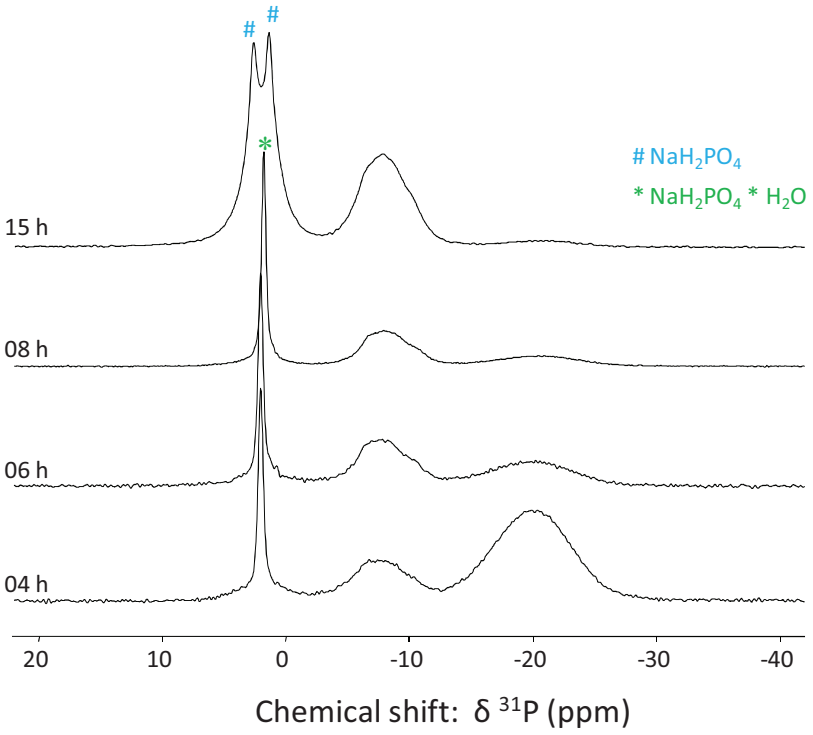

Fig. 4.2b:
1D ^{31}P NMR spectra for the intermediate phase of the weathering process. Broad resonances characteristic of an amorphous material coexist with crystalline peaks in the Q^0_H region. Spectra are recorded at a static field of 9.4 T, MAS spinning speed 10 kHz (rotor diameter 4.0 mm), high power proton decoupling has been employed.

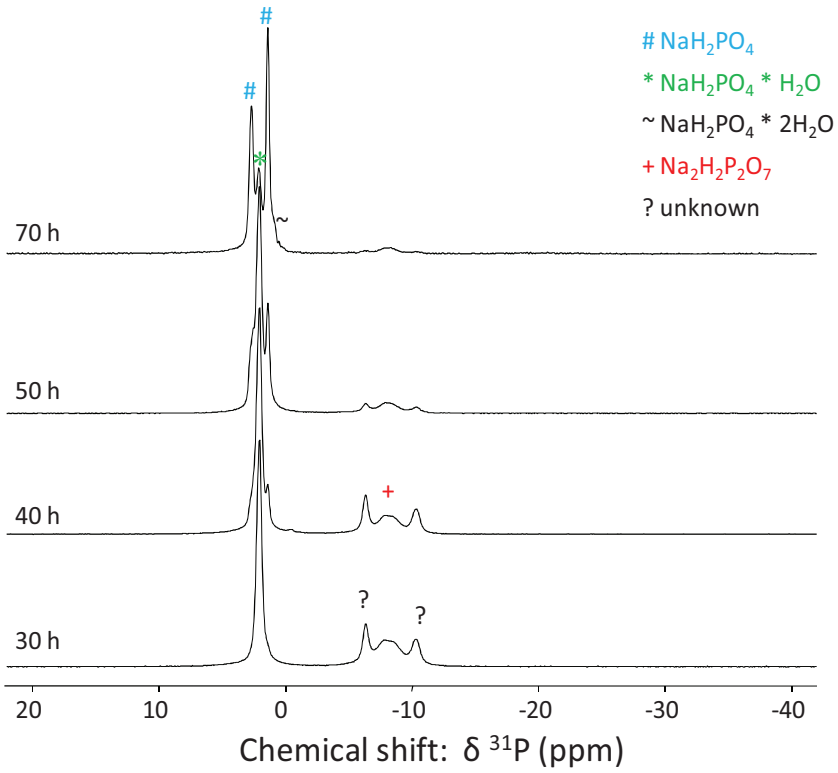

Fig. 4.2c:
*1D ^{31}P NMR spectra for the third regime of the weathering process. The majority of the signals is crystalline. Phases identified are NaH_2PO_4, NaH_2PO_4*H_2O, NaH_2PO_4*$2H_2O$. The $Na_2H_2P_2O_7$ contribution is still broad. Spectra are recorded at a static field of 9.4 T, MAS spinning speed 10 kHz (rotor diameter 4.0 mm), high power proton decoupling has been employed.*

The following consideration of the weathering process of $NaPO_3$ glass is subdivided into three regimes that are based on the crystallinity of the samples (*Fig. 4.2a, b* and *c*). In the first regime (*Fig. 4.2a*), the samples are completely amorphous. An evolution in glass network polymerization is observed and the intensity of the resonance at -20 ppm decreases, while resonance intensities at -8 ppm and 0 ppm increase. This implies, following the assignment presented in *Fig. 4.1*, progressive network depolymerization with weathering.

The second weathering regime commences at four hours of weathering (*Fig. 4.2b)*. It is characterized by further network depolymerization and by the coexistence of crystalline and amorphous phases. A crystalline resonance attributed to NaH_2PO_4*H_2O occurs at 2.1 ppm in the Q^0_H region and is marked by an asterisk in *Fig. 4.2b*. The observations indicate that isolated PO_4 tetrahedra are the first species to reorganize into an energetically favorable crystalline state. This tendency can be confirmed from the subsequent snapshots for 6 h, 8 h and 15 h of weathering *(Fig. 4.2b)* and from XRD data (*Fig. 4.3; Tab. 4.1*).

In the third weathering regime (*Fig. 4.2c*), the highly depolymerized nature of the glass network is evidenced by an absence of signal intensity in the Q^2 region (-20 ppm). The samples weathered for 30 h and longer are predominantly crystalline. In addition to $NaH_2PO_4*H_2O$ observed previously, $NaH_2PO_4*2H_2O$ (0.5 ppm) and NaH_2PO_4 (1.4 ppm and 2.7 ppm) can be identified in the Q^0_H resonance region. Further, crystalline resonances are observed in the Q^1_H chemical shift range corresponding to $Na_2H_2P_2O_7$ (-8.1 ppm). Two additional resonances appear at -6.7 ppm and -10.4 ppm. These two resonances could not be attributed to any phase reported in NMR or XRD databases (*Fig. 4.3, Tab. 4.1*).

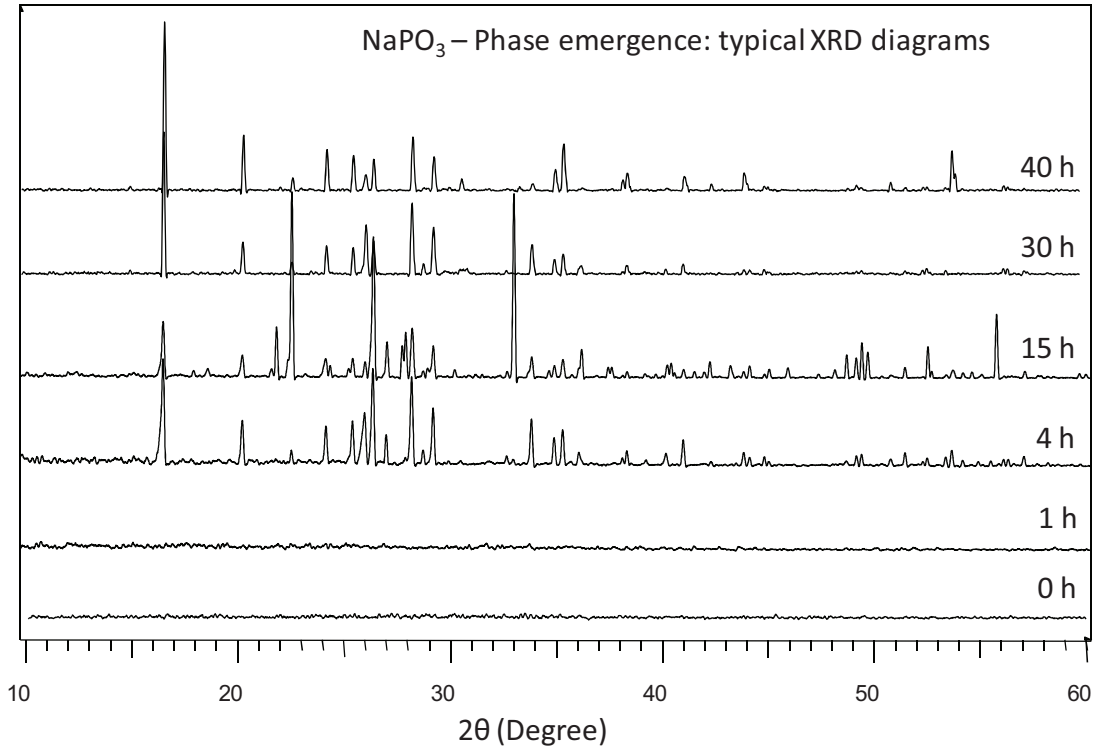

Fig. 4.3: XRD patterns of weathered $NaPO_3$ samples showing phase emergence of crystalline phases.

Table 4.1: Crystalline phases identified from XRD patterns in weathered $NaPO_3$ presented above (Fig. 4.3). The corresponding database file numbers are indicated.

Weathering time (hours)	**NaH_2PO_4**	**$NaH_2PO_4*H_2O$**	**$Na_2H_2P_2O_7$**	**Comments**
0	-	-	-	amorphous
1	-	-	-	amorphous
4	Identified ICSD 00-011-0659	Identified 00-011-0651	-	-
15	Identified ICSD 00-011-0659	Identified 00-011-0651	-	-
30	Identified ICSD 00-011-0659	Identified 00-011-0651	Identified 00-010-0192	*^{31}P NMR signals at - 6.7 ppm and - 10.4 ppm not identified by comparison with XRD databases.*
40	Identified ICSD 00-011-0659	Identified 00-011-0651	Identified 00-010-0192	

Fig. 4.4 shows ^{31}P-{^{1}H} CP edited 2D ^{31}P RFDR spectrum. Signals from unaged ^{31}P species are suppressed; only correlations of protonated phosphate species are detected. Cross-correlated peaks are observed for the two unassigned resonances at -6.7 ppm (A) and -10.4 ppm (B). This indicates that both signals arise from protonated Q^1_H species that stem from one single phase.

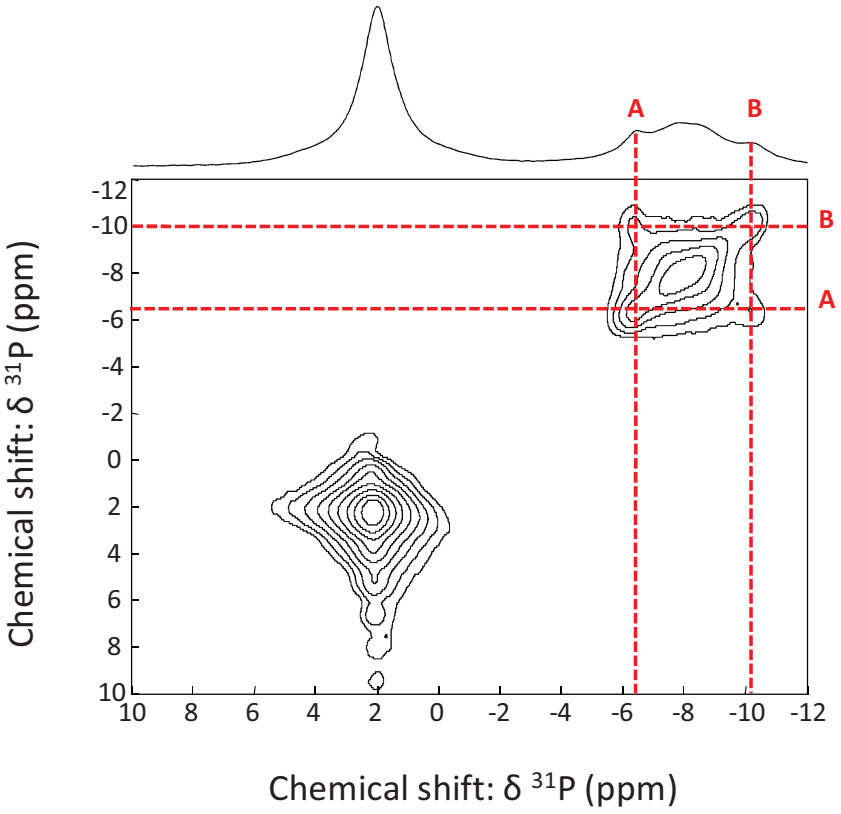

Figure 4.4:
^{31}P ^{1}H-^{31}P CP edited RFDR NMR spectrum of weathered $NaPO_3$ glass containing the not identified phase (figure 4.2c). The two signals at -6.7 ppm and -10.4 ppm are denominated A and B. Peaks on the diagonal show autoconnections B-B and A-A. The two off-diagonal signals A-B and B-A reveal that A and B arise from the same phase.

Fig. 4.5 shows a 2D ^{31}P-{^{1}H} CP NMR spectrum of aqueously attacked $NaPO_3$ glass. The resonances corresponding to the unidentified phase discussed above (A: -6.7 ppm and B: -10.4 ppm) are evident in this spectrum. They are correlated to the proton signal at -12 ppm and -14 ppm and can be attributed to Q^1_H sites with two different types of hydrogen bonds (Wenslow1998).

Another important observation from the ^{31}P-{^{1}H} CP MAS spectrum is that significant fractions of Q^1_H as well as Q^0_H groups are present in the weathered glass. Thus, in the following sections, the Q^1_H / Q^2_{Na} and the Q^0_H / Q^1_{Na} resonance region will be referred to as the Q^1_H and the Q^0_H resonance regions respectively, assuming that the generation of non-protonated depolymerized phosphate units upon weathering is negligible and that hydrolysis is the dominant process.

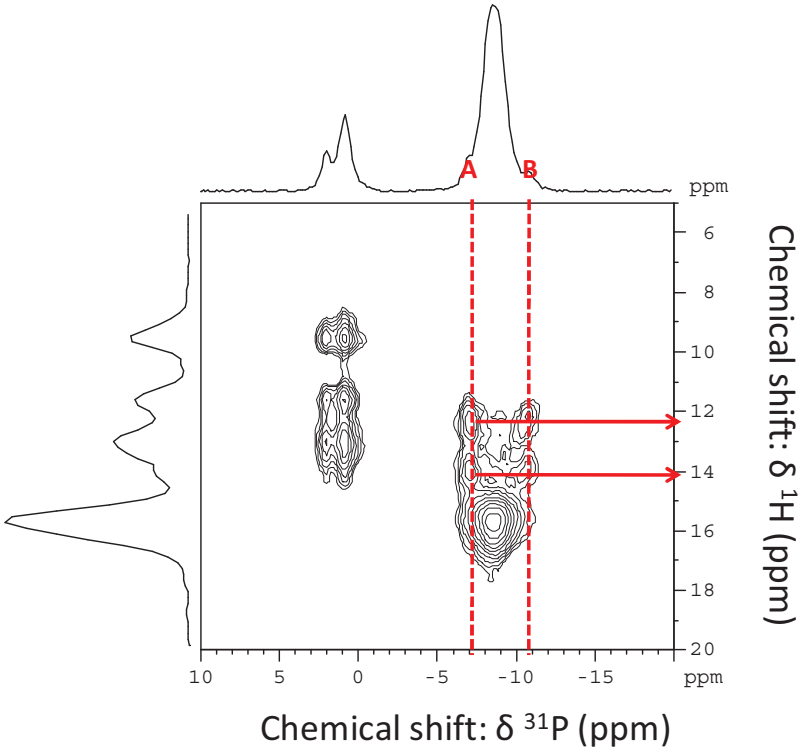

Figure 4.5:
2D ^{1}H-^{31}P CP MAS NMR spectrum of weathered $NaPO_3$ glass containing the not identified phase. The spectrum reveals the contributions of Q^1_H in the Q^1_H / Q^2_{Na} resonance region and the contribution of Q^0_H in the Q^0_H / Q^1_{Na} resonance region. The spectrum has been recorded at a static field of 9.4 T, MAS spinning speed 10 kHz (rotor diameter 4.0 mm).

Conclusion:

^{31}P-NMR and ^{31}P-{^{1}H} CP NMR data indicate depolymerization of the glass network as a function of weathering time. The Q^2 unit fraction decreases whereas the Q^1_H and Q^0_H unit fractions increase. This stands in agreement with the models for phosphate glass alteration under humid atmosphere proposed by Brow and by Tischendorf (Brow1990, Tischendorf2004).

- H_2O molecules from the vapor phase hydrate the phosphate chains.
- Subsequently, hydrolytic cleavage of P-O-P bonds occurs.
- The network progressively depolymerizes until isolated PO_4 entities are predominant in the material.

After prolonged weathering durations, the depolymerized network is almost entirely crystallized. It is noteworthy that isolated phosphate tetrahedra are the first species to reorganize in an energetically favorable crystalline state, followed by a small fraction of crystalline pyrophosphate phases. The dominant crystalline phase at the end of weathering is sodium dihydrogen orthophosphate, NaH_2PO_4. In general, this stands in agreement with previous weathering studies for more complex phosphate glass systems (Tischendorf2004). In these studies, XRD revealed the presence of hydrated crystalline orthophosphate layers on the glass surface. The absence of *hydrated* hydrogen phosphates, e.g. NaH_2PO_4*H_2O, in our

weathered glass samples can partly be attributed to sample storage under vacuum (Chapter 2), possibly leading to the desiccation of the water of crystallization.

4.1.2 Evolution of ^{1}H NMR spectra during weathering

Figures 4.6 – 4.8 show single-pulse 1D ^{1}H NMR spectra of the weathered $NaPO_3$ glass samples. The exposure times varied from 1 h to 70 h as indicated in the figures. The center band spectra are presented on top of each figure *(a)*. Larger spectral windows exhibiting the range of spinning sideband intensity are presented at the bottom of each figure (b). The latter shall be considered first.

At the early stage of weathering (*Fig. 4.6*), the proton concentration in the glass network is very small. The ^{1}H NMR data collected after 1 h of weathering corresponds merely to the ^{1}H NMR data of an empty rotor (Flambard2005, PhD thesis), introducing probe and rotor artifacts that are marked by an asterisk. Background intensity reaches from 60 to -60 ppm (*Fig. 4.6b*) and a distinct peak arises at about 0 ppm.
In the second and third weathering regime (*Fig. 4.7* and *Fig. 4.8*) the proton concentration in the attacked glass network increases. This leads to enhanced signal intensity and a weaker influence of the probe and rotor artifacts on the ^{1}H NMR spectra. However, they still can influence the phase correction. ^{1}H NMR spectra recorded for the samples weathered for 30 h and 40 h illustrate this (*Fig. 4.8b*).

The center band spectra (25 ppm to -15 ppm) allow for a distinction of the proton environments generated throughout the glass degradation process. Proton resonances are separated into two major chemical shift ranges following previous assignment by Wenslow and Mueller (Wenslow1998). Species such as molecular water that exhibit particularly weak hydrogen bonding give rise to signals in the range from 0-10 ppm. All signals exhibiting a ^{1}H chemical shift higher than 10 ppm are attributed to protons in stronger hydrogen bonding environments, e.g. in (P-OH…$^-$OP). In general, ^{1}H chemical shift correlates with the strength of hydrogen bonding (Xue2009, Alam2005, Hosono1992). Xue et *al.* have summarized these trends in detail in their review article (Xue2009): increasing hydrogen bonding strength is accompanied by decreasing [OH…$^-$O] distance and deshielding of the involved ^{1}H nucleus. This results in a higher chemical shift value.

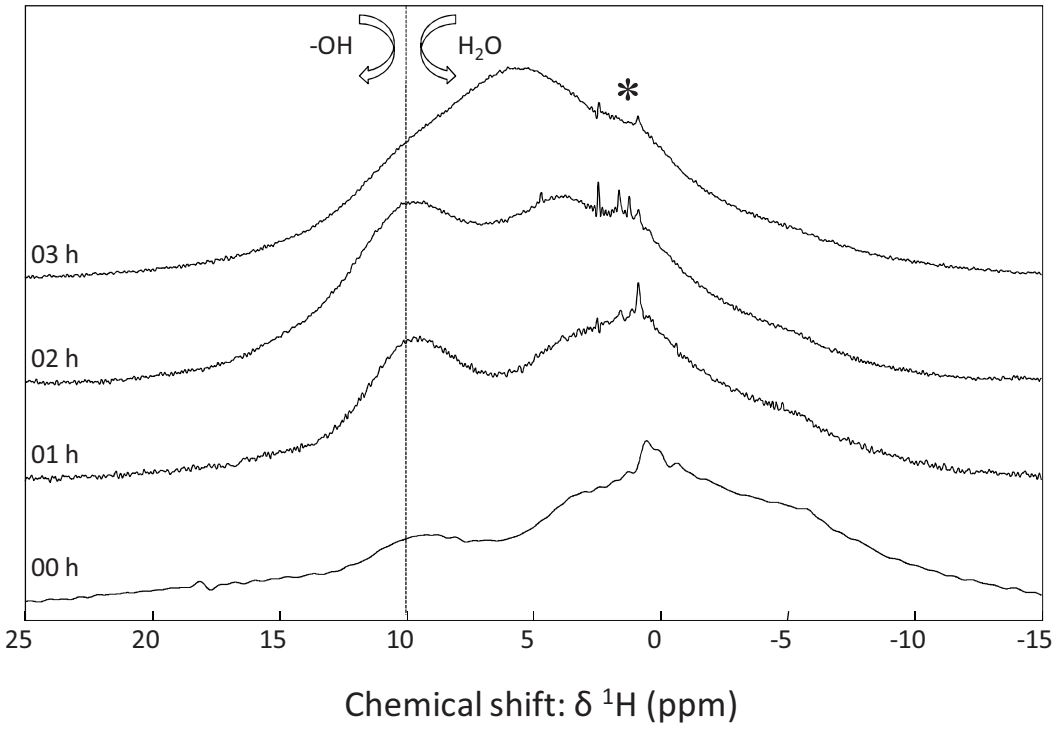

Fig. 4.6a:
1D ^{1}H center band NMR spectra of $NaPO_3$ glass during the first regime of weathering. Single-pulse spectra have been recorded at a static field of 9.4 T and a MAS spinning speed of 10 kHz (rotor diameter 4.0 mm). The asterisk marks rotor / probehead artifact signal.

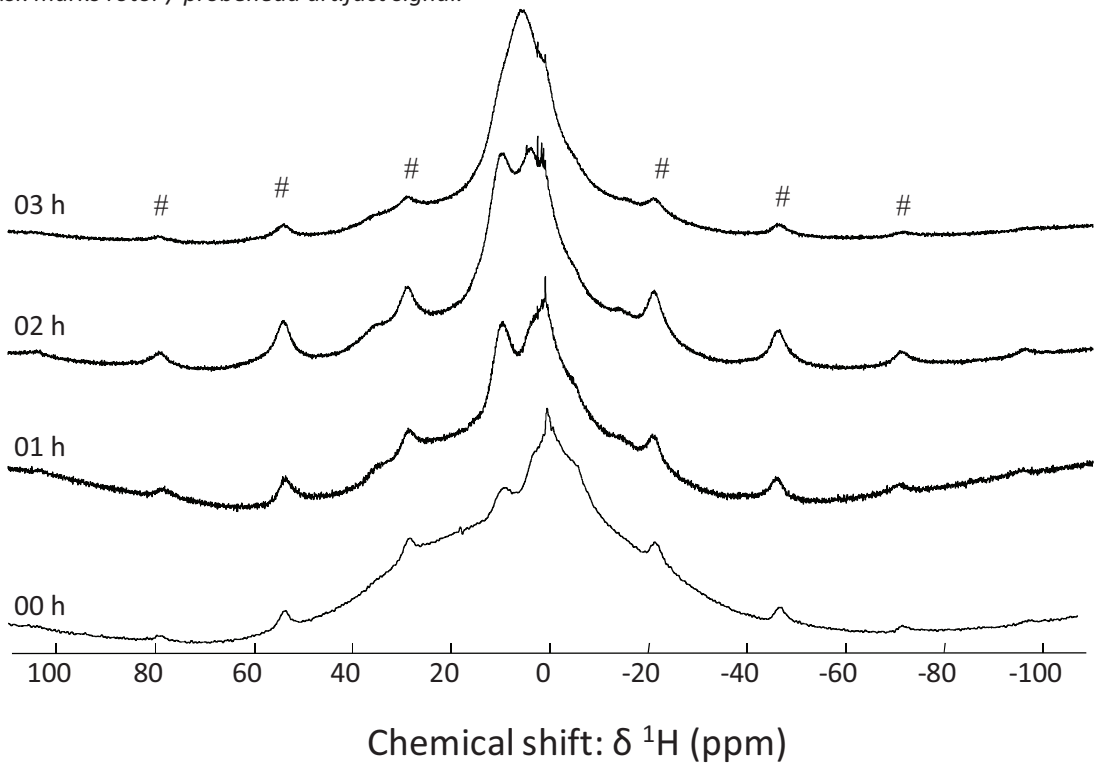

Fig. 4.6b:
1D ^{1}H NMR spectra of $NaPO_3$ glass during the first regime of weathering. Single-pulse spectra have been recorded at a static field of 9.4 T and a MAS spinning speed of 10 kHz (rotor diameter 4.0 mm). The asterisks mark spinning sidebands (ssb); only on the top spectrum the position of the respective ssb is represented.

In the first regime (0 h to 3 h, *Fig. 4.6a* and *b*), ^{1}H NMR spectra are characterized by broad resonances. A resonance contribution with its center at about 4 ppm can be observed. Its intensity is growing constantly. ^{1}H chemical shifts in this region have been assigned to adsorbed surface water molecules (Wenslow1998, Alam2005). Further, a resonance at around 10 ppm can be observed, increasing steadily throughout the first three hours of weathering. It has been assigned to ^{1}H environments involved in weak hydrogen bondings in hydroxyl groups (P-OH…$^{-}$O). These proton environments are generated upon hydrolytic cleavage of P-O-P bonds. Wenslow and Mueller attributed ^{1}H NMR around 10 ppm to intermolecular hydrogen bonding, e.g. between Q^{1}_{H} units at chain ends and Q^{2} backbone units in the same or a neighboring phosphate chain (Wenslow1998; Chapter 1). Finally, the observed signals stand in agreement with 1D ^{31}P NMR spectra (4.1.1), indicating beginning depolymerization of the phosphate network during the first weathering regime. In the 1D ^{1}H NMR spectrum of the sample weathered for 3 h, signal intensity in both regions has grown considerably and one broad peak results. Its maximum is shifted towards the region of H_2O ^{1}H resonances, indicating that protons from surface adsorbed H_2O molecules are the dominating species and that H_2O adsorption has increased. This points towards a possible saturation of the glass particle surface with water molecules.

In the second weathering regime (4 h to 8 h, *Fig. 4.7a* and *b*), resonances are still broad and stand therefore in contrast to the distinct crystalline signals that are present in the corresponding 1D ^{31}P NMR spectra (*Fig. 4.2b*). Since the proton concentration has increased, strong homonuclear dipolar ^{1}H-^{1}H coupling may be responsible for this lack of resolution in the collected ^{1}H NMR spectra. The signal at about 4 ppm is still predominant, supporting evidence for a high concentration of H_2O molecules at the glass surface. In addition, two resonances at about 11 ppm and 15 ppm are present. In a similar study, a ^{1}H NMR resonance around 15 ppm has been assignd to Q^{0}_{H} units with strong intramolecular hydrogen bonding (Wenslow1998). The spectral data recorded for the sample weathered for 4 h deviates from the observed trend in the second weathering regime. Hydroxyl group intensity due to network depolymerization is considerably high compared to samples weathered for 6 h and 8 h. This may be due to evolution of the sample during the recording of the spectrum and is thus considered as an experimental error.

In the third regime (30 h to 70 h, *Fig.4.8 a* and *b*), all ^{1}H resonances are still broad, revealing that single-pulse ^{1}H NMR spectra collected at a spinning speed of 10 kHz can only provide a rough estimation of the proton environments generated during attack. Resolution is not sufficient to discern and to identify crystalline contributions reliably. In this regime, the relative intensity of adsorbed surface water decreases steadily. ^{1}H resonances shift towards higher chemical shift values, indicating the generation of various (P-OH…$^{-}$O) environments either in amorphous or crystalline phases (Mercier1999) that accompanies progressing P-O-P network depolymerization.

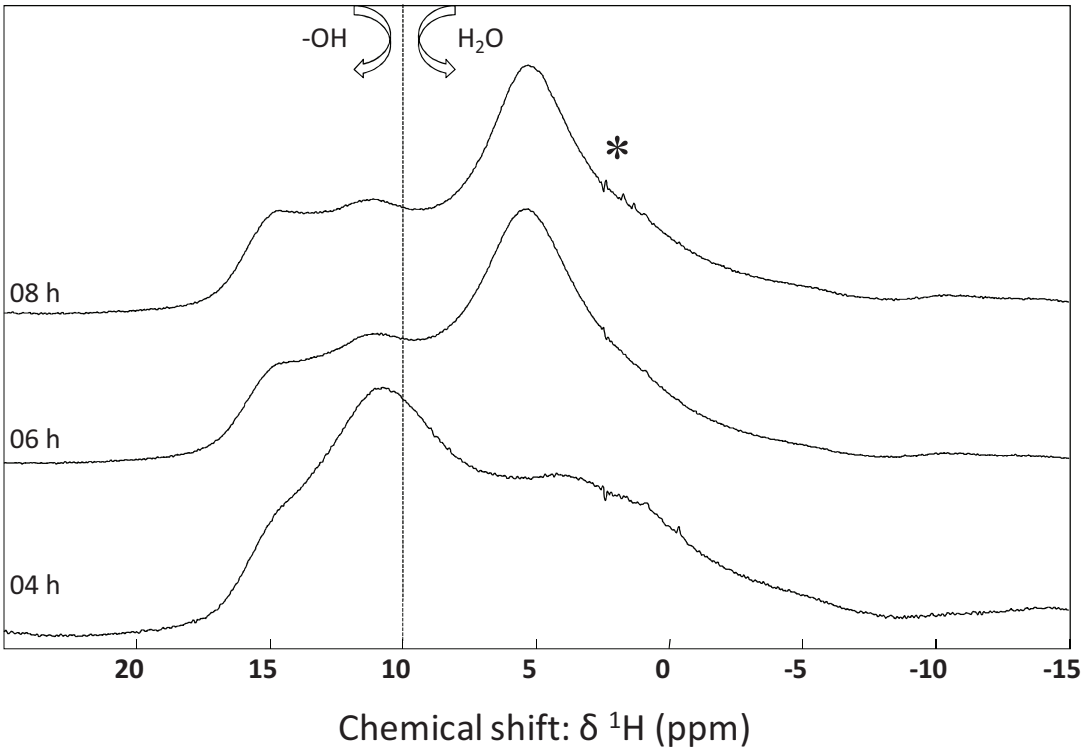

Fig. 4.7a:
1D ^{1}H center band NMR spectra of $NaPO_3$ glass during the 2nd regime of weathering. Single-pulse spectra have been recorded at a static field of 9.4 T and a MAS spinning speed of 10 kHz (rotor diameter 4.0 mm). The asterisk marks rotor / probehead artifact signal.

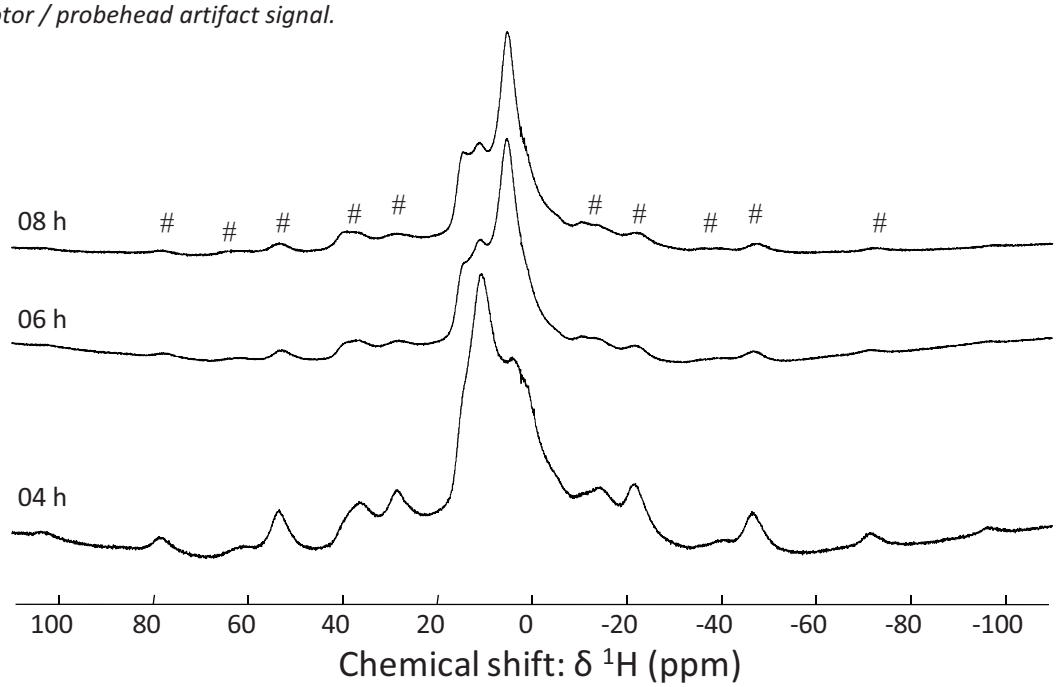

Fig. 4.7b:
1D ^{1}H NMR spectra of $NaPO_3$ glass during the 2nd regime of weathering. Single-pulse spectra have been recorded at a static field of 9.4 T and a MAS spinning speed of 10 kHz (rotor diameter 4.0 mm). The asterisks mark spinning sidebands (ssb); only on the top spectrum the position of the respective ssb is represented.

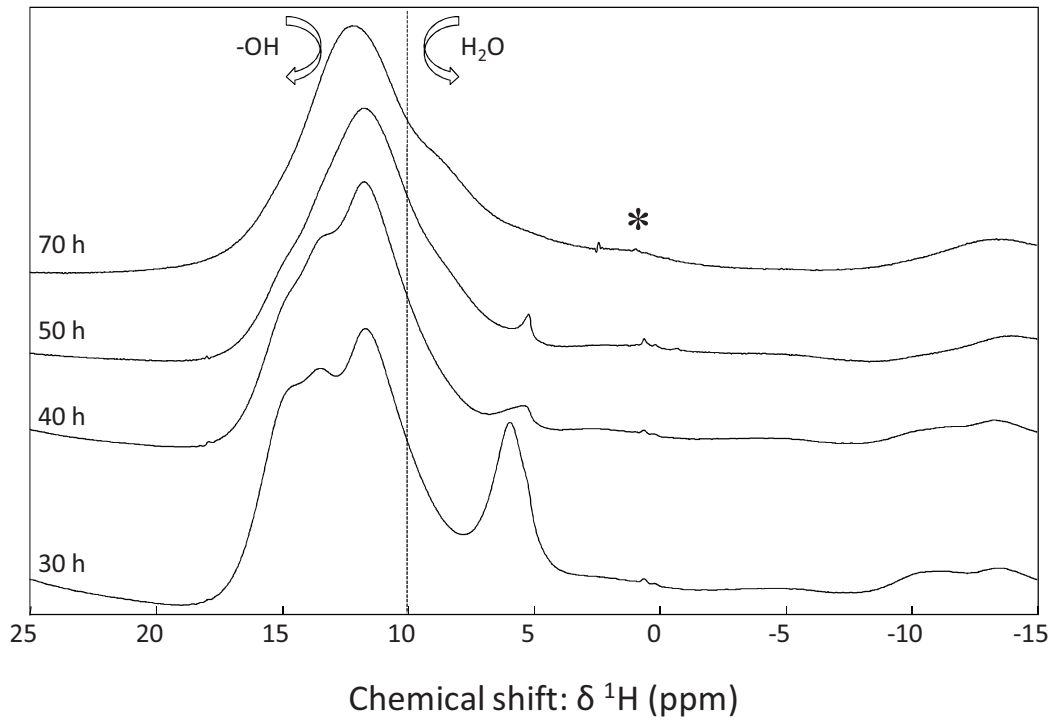

Fig. 4.8a:
1D ^{1}H center band NMR spectra of $NaPO_3$ glass during the 3rd regime of weathering. Single-pulse spectra have been recorded at a static field of 9.4 T and a MAS spinning speed of 10 kHz (rotor diameter 4.0 mm). The asterisk marks rotor / probehead artifact signal.

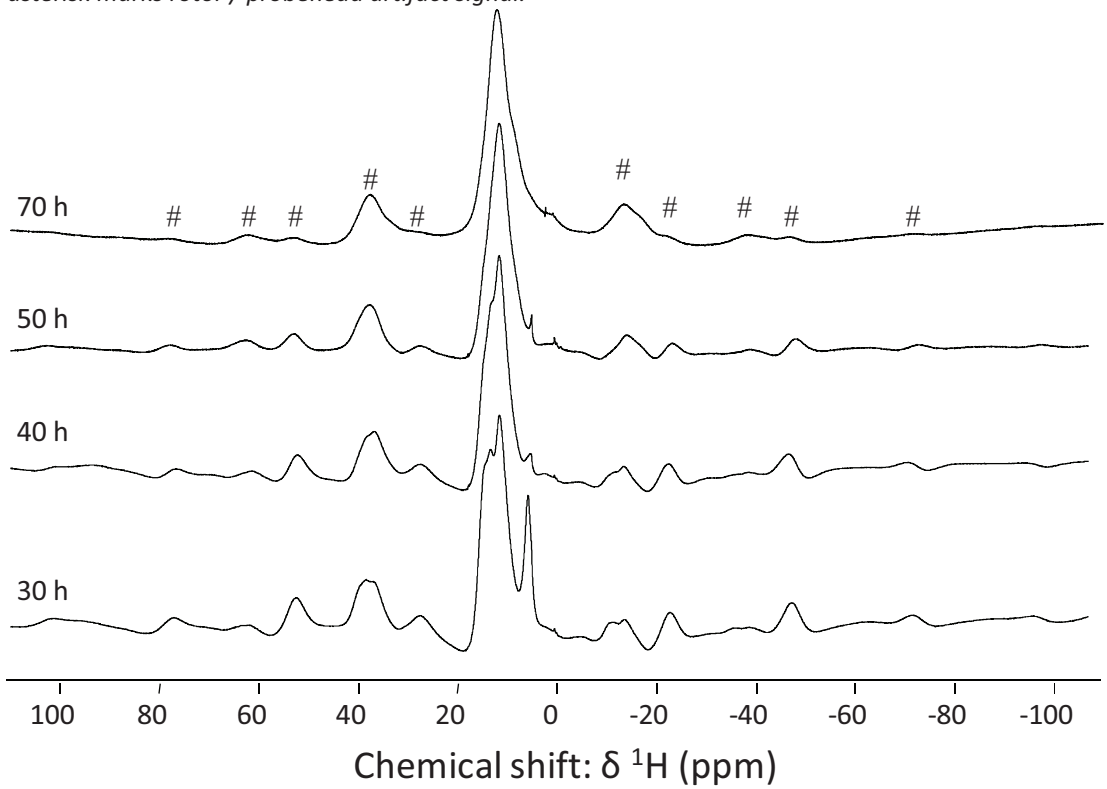

Fig. 4.8b
1D ^{1}H NMR spectra of $NaPO_3$ glass during the 3rd regime of weathering. Single-pulse spectra have been recorded at a static field of 9.4 T and a MAS spinning speed of 10 kHz (rotor diameter 4.0 mm). The asterisks mark spinning sidebands (ssb); only on the top spectrum the position of the respective ssb is represented.

In order to achieve insight into phase emergence, high resolution 1D ^{1}H NMR spectra for two selected weathered $NaPO_3$ samples have been recorded. The DEPTH sequence (see Chapter 2) has been employed to suppress rotor and probehead artifacts. Very high MAS spinning speeds (60 kHz) at high field (18.8 T) were employed to reduce spinning sideband intensities to a minimum and to obtain a maximum of resolution (Xue2009). *Fig. 4.9* depicts the resulting ^{1}H spectra of the two $NaPO_3$ samples weathered for 4 h and for 30 h.

Broad contributions from surface-adsorbed water molecules (4 ppm; 7 ppm) and from amorphous Q^{0}_{H} and Q^{1}_{H} species (14 ppm) are still visible in the spectrum of the sample weathered for 4 h. Nevertheless, resolution is enhanced remarkably, allowing for identification of emerging crystalline peaks (*Fig. 4.9*). In contrast to the single-pulse spectra presented previously, the high resolution ^{1}H NMR data can corroborate the observations from previously presented ^{31}P NMR data, since most of the crystalline signals with FWHM values < 1 ppm can be attributed to crystalline phases.

A crystalline contribution from $NaH_2PO_4*H_2O$ (2.1 ppm) can be identified in the sample weathered for 4 h. The resonance at 15.5 ppm has been assigned to $Na_2H_2P_2O_7$, based on reference data from pure crystalline $Na_2H_2P_2O_7$. Weak contributions stem from NaH_2PO_4 (9.6 ppm, 11.5 ppm, 12.7 ppm, 13.1 ppm; Xue2009).

With increasing weathering time (30 h) the intensity of water molecules decreases whereas the intensity of hydrogen bonded (-OH groups) ^{1}H nuclei increases. This stands in agreement with previously collected data. The peaks in the signal region between 10 ppm and 20 ppm could be resolved and attributed to crystalline hydrogen phosphate phases $NaH_2PO_4*H_2O$, NaH_2PO_4 and $Na_2H_2P_2O_7$.

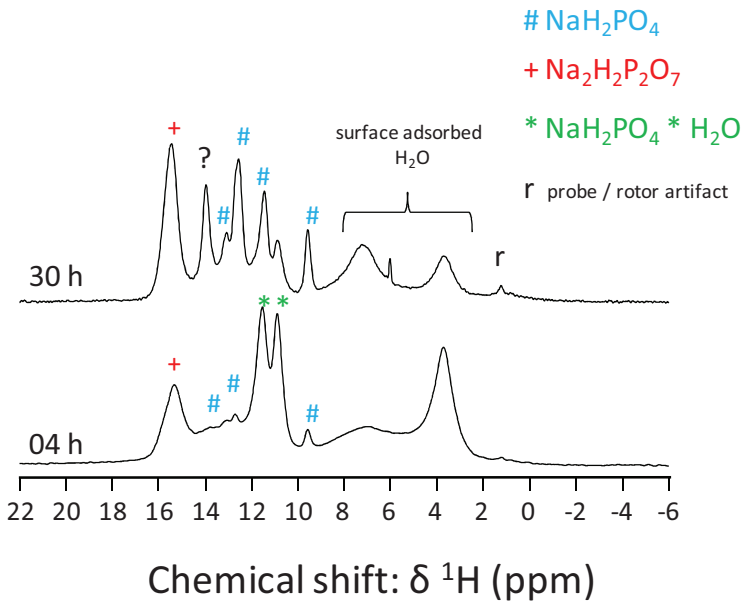

Fig. 4.9
High resolution 1D ^{1}H NMR spectra of weathered $NaPO_3$ glass. Spectra were recorded employing the DEPTH sequence, a static field of 18.8 T and a MAS spinning speed of 60 kHz (1.3mm rotor diameter) for the same samples that were used to collect the ^{1}H MAS NMR spectra at 9.4T (10 kHz; single-pulse).

Discussion:

The collected 1D ^{1}H NMR data stand in agreement with the results obtained from 1D ^{31}P NMR (Chapter 4.1.1). Considerably increasing intensity in the resonance region of surface adsorbed H_2O (center at about 4 ppm) for samples weathered for 3 h to 8 h (first and second weathering regime) indicates surface saturation of the glass powder particles exposed to water vapor. Subsequently, intensity of ^{1}H signals from protons involved in hydrogen bonding increases. Various ^{1}H environments in amorphous and crystalline phases are generated throughout this process. Crystallization progresses with increasing weathering time.
This corroborates the generally accepted model concept for aqueous attack on a phosphate glass under humid atmosphere (Tischendorf2004).
Single-pulse spectra collected at 9.4 T (MAS spinning speed 10 kHz, rotor diameter 4.0 mm) are quantitative, but suffer from a lack of resolution. Hence, a meaningful deconvolution of these spectra is not feasible. Moreover, crystalline phases cannot be detected, even if their presence has been confirmed in 1D ^{31}P NMR spectra of the same samples. In order to achieve sufficient resolution, the DEPTH sequence has been implemented in combination with high field (18.8 T) at very high MAS spinning speeds (60 kHz) for two of the weathered $NaPO_3$ glass samples. The enhanced spectral resolution allowed for identification of proton environments and crystalline phases formed throughout weathering. Finally, 1D ^{31}P NMR data have been confirmed by this advanced ^{1}H NMR technique. However, ^{1}H DEPTH NMR spectra are no longer quantitative.

4.2 A quantitative study of $NaPO_3$ weathering by ^{31}P NMR

4.2.1 Estimation of chain length

The weathering studies were initiated on pristine $NaPO_3$ glass. The spectrum for this glass is presented in *Fig. 4.1* and has been discussed previously (Section 4.1.1). Average chain lengths of 40 to 100 PO_4 units have been reported for this glass (Brow2000). This could be estimated by end group titration techniques (van Wazer1958), HPLC or by liquid- or solid-state NMR. Wiench et *al.* (Wiench2002) determined n_{av} for chain dominated zinc phosphate glasses from solid-state NMR spectra using the following equation:

$$n_{av} = \frac{Q^0 + Q^1 + Q^2}{Q^0 + \frac{1}{2}Q^1} \qquad \text{(IV-1)}$$

Their results based on quantitative analysis of 1D ^{31}P NMR spectra were in good agreement with HPLC results and theoretically predicted values. Equation (IV-1) was used to estimate the average chain length of pristine $NaPO_3$ glass. Resonances at about -20 ppm, -8 ppm and 0 ppm have been assigned to Q^2, Q^1_H (Q^1)

and Q^1_{Na} (Q^0) units respectively (*Fig. 4.1*). Substituting the integrated areas of the respective resonances in Equation (1), the average chain length is calculated to be $n_{av} \approx 67$.

4.2.2 Reaction orders

In order to estimate the relative Q^2 intensity, 1D ^{31}P NMR snapshots of weathered $NaPO_3$ have been deconvoluted over the entire range of spinning sidebands using the dmfit software (Massiot2002). *Tab. 4.2* lists the results that were obtained for the resonance at -20 ppm (Q^2 units) and for the resonance at -8 ppm (Q^1_H units). Their kinetics are analyzed with the aim to gain further insight into mechanistic details of $NaPO_3$ weathering.

Formal reaction orders have been obtained by plotting the evolution of the relative intensities (in %) of Q^2 - and Q^1_H fractions against weathering time (hours). *Fig. 4.10a* shows the time dependent evolution of Q^2 units. In *Fig. 4.10b* ln (Q^2) is plotted against weathering time (hours). A linear fit, indicative of first-order kinetics is possible only after 4 h of weathering. This implies that the first 4 h are needed to attain preponderance of hydrolysis. Principally, H_2O molecules are adsorbed on the surface of the $NaPO_3$ glass powder particles at this early stage. Evidence supporting this analysis has been presented when ^{31}P and ^{1}H NMR spectra were discussed (section 4.1.1 and section 4.1.2).
Subsequently, the relative Q^2 intensity diminishes constantly during the weathering process and reaches zero after 30 hours of weathering (*Fig. 4.10a*). Classically, first-order kinetics are associated with decay or decomposition reactions of the type:

$$A \rightarrow B + C + \ldots$$

where only one formal educt, "A", is present. Once the surface is saturated by adsorbed water molecules, as it is the case after 4 h of weathering, H_2O concentration can indeed be considered as large compared to the concentration of Q^2 units. As a result, the reaction between H_2O and the P-O-P bond:

$$A + B \rightarrow C + D$$

$$H_2O + (Q^2 - Q^2) \rightarrow 2Q^1{}_H$$

$$H_2O + (Q^2 - Q^1) \rightarrow 1Q^1{}_H + 1Q^0{}_H$$

which would theoretically give rise to second-order kinetics can be formulated in a first approach as (McQuarrie1997):

$$A \rightarrow B + C + \ldots$$

$$(Q^2 - Q^2) \rightarrow 2Q^1{}_H$$

$$(Q^2 - Q^1) \rightarrow 1Q^1{}_H + 1Q^0{}_H .$$

Tab. 4.2:
Relative intensities of Q^2, Q^1_H and Q^0_H / Q^1_{Na} units. Initial intensities of Q^1_H and Q^0_H / Q^1_{Na} are substracted in the corrected intensities (corrected). Corrected intensities are the basis of kinetics.

Weathering time (hours)	Q^2 (%)	Q^1_H (%)	Q^1_H (%) corrected	Q^0_H / Q^1_{Na} (%)	Q^0_H / Q^1_{Na} (%) corrected
0	96,63	2,95	0	0,43	0
1	94,83	4,6	1,65	0,57	0,14
2	85,93	9,07	6,12	5	4,57
4	78,25	12,91	9,96	8,84	8,41
6	42,97	33,45	30,50	23,59	23,16
8	29,63	37,54	34,59	32,83	32,4
15	6,08	42,95	40,00	50,96	50,53
30	0	46,01	43,06	53,99	53,56
40	0	35,74	32,79	64,26	63,83
70	0	7,33	4,38	92,67	92,24

Conclusion:

The kinetic data support a weathering model where hydrolysis becomes the dominant process and is accelerated after an initial phase glass surface saturation with water molecules. The acceleration can be explained by work published by Mercier *et al.* (Mercier1999) who observed higher surface adhesion rates for water molecules with increasing hydroxyl group concentration in the glass network. In addition, the determined reaction order indicates that the glass surface is highly saturated with water molecules when hydrolysis is accelerated.

While reaction kinetics can provide reaction orders, they are unable to provide information about the exact mechanism of a reaction (McQuarrie1997). A case in point is the hydrolysis of Q^2 units following first-order kinetics despite the involvement of two educts, H_2O and Q^2-Q^2 or Q^2-Q^1 bonds.

In the following section attempts are made to look beyond formal reaction orders and to understand, if there exist preferential pathways for hydrolytic attack.

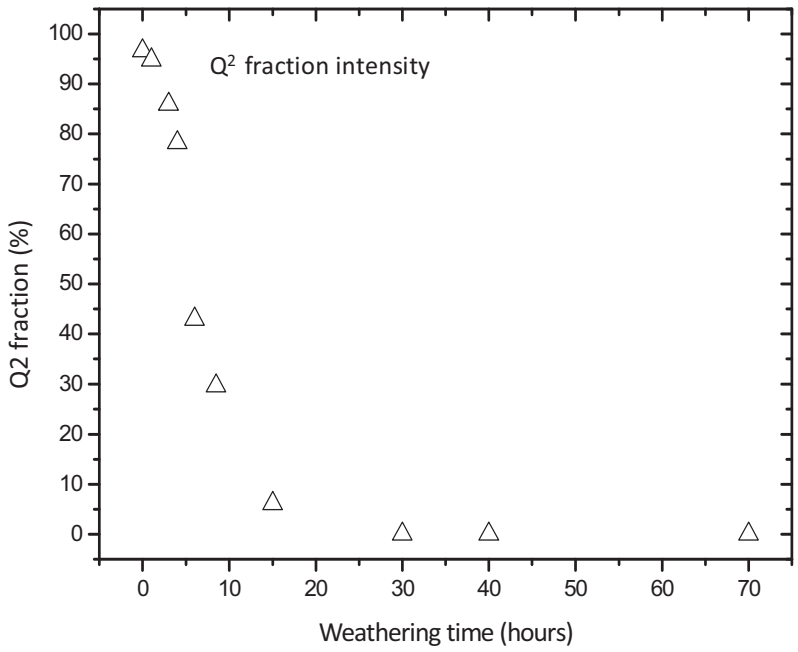

Fig4.10a:
Time-dependent evolution of the Q^2 unit fraction intensity in $NaPO_3$ glass weathered under H_2O saturation vapor pressure at 80°C.

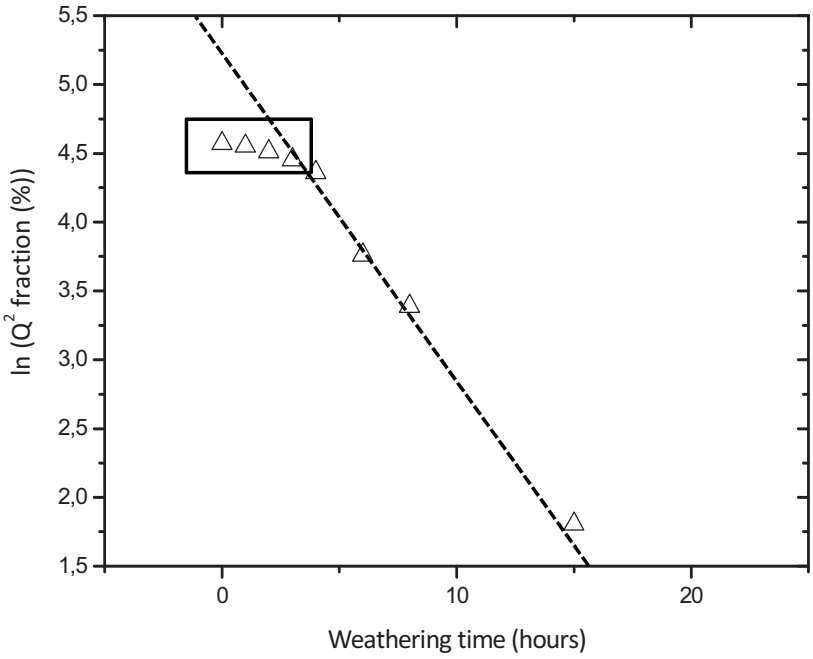

Fig. 4.10b:
Graphical analysis of the Q^2 decay from Fig.4.10a. Logarithmic plot of the time dependent evolution of the Q^2 unit fraction in $NaPO_3$ glass weathered under H_2O saturation vapor pressure at 80°C. After 4 h, the reaction follows first-order kinetics.

4.2.3 Sites of attack

Possible pathways for hydrolytic decomposition of the Q^2 backbones in sodium metaphosphate glass have been proposed by Wenslow and Mueller (Wenslow1998), although the authors have not provided quantitative analysis of their model mechanisms. The two possible scenarios are hydrolytic attack of P-O-P bonds at the phosphate chain ends (Q^2-Q^1) and hydrolytic attack at the interior of the phosphate chains (Q^2-Q^2). In the following paragraphs, the time dependent evolution of Q^2, Q^1_H and Q^0_H units for these scenarios shall be developed and subsequently be compared to experimental results.

a) First scenario: Attack at ends of phosphate chains

In the first scenario (*Fig. 14.11-1*), water attacks the polyphosphate anions at the chain ends. Either a Q^1_{Na} unit is transformed into a Q^0_H tetrahedron or a Q^1_H end unit is transformed into Q^0_H. Moreover, a new Q^1_{1H} unit is generated by transformation from a former Q^2 entity as illustrated by *Fig. 4.11-1* and equation (IV-2a) and (IV-2b). Formally, only the Q^2 and the Q^0 (Q^0_H and Q^0_{2H}) fractions show variations in intensity. Q^2 decreases by the same extent by which Q^0 grows. Hence, for a hydrolysis mechanism dominated by selective chain end attack, the 1D ^{31}P NMR spectra should show a clear increase of Q^0 (Q^0_H and Q^0_{2H}) intensity, whereas the Q^1_H intensity must stagnate.

$$-\frac{\Delta Q^1}{\Delta t} = \frac{\Delta Q^0{}_H}{\Delta t} \qquad -\frac{dQ^1}{dt} = \frac{dQ^0{}_H}{dt} \qquad \text{(IV-2a)}$$

$$-\frac{\Delta Q^1{}_H}{\Delta t} = \frac{\Delta Q^0{}_H}{\Delta t} \qquad -\frac{dQ^1{}_H}{dt} = \frac{dQ^0{}_H}{dt} \qquad \text{(IV-2b)}$$

$$-\frac{\Delta Q^2}{\Delta t} = \frac{\Delta Q^1{}_H}{\Delta t} \qquad -\frac{dQ^2}{dt} = \frac{dQ^1{}_H}{dt} \qquad \text{(IV-2c)}$$

b) Second scenario: Attack at the interior of phosphate chains

In the second scenario (*Fig. 4.11-2*), water attacks the polyphosphate anions in the inner regions of the backbone. By this formal scission at the interior of the phosphate chains, two Q^1_H units are generated from two former Q^2 units. In terms of the global ^{31}P intensity this must imply that Q^2 would decrease by the same amount by which Q^1_H increases.

$$-\frac{\Delta Q^2}{\Delta t} = \frac{\Delta Q^1{}_H}{\Delta t} \qquad -\frac{dQ^2}{dt} = \frac{dQ^1{}_H}{dt} \qquad \text{(IV-3)*}$$

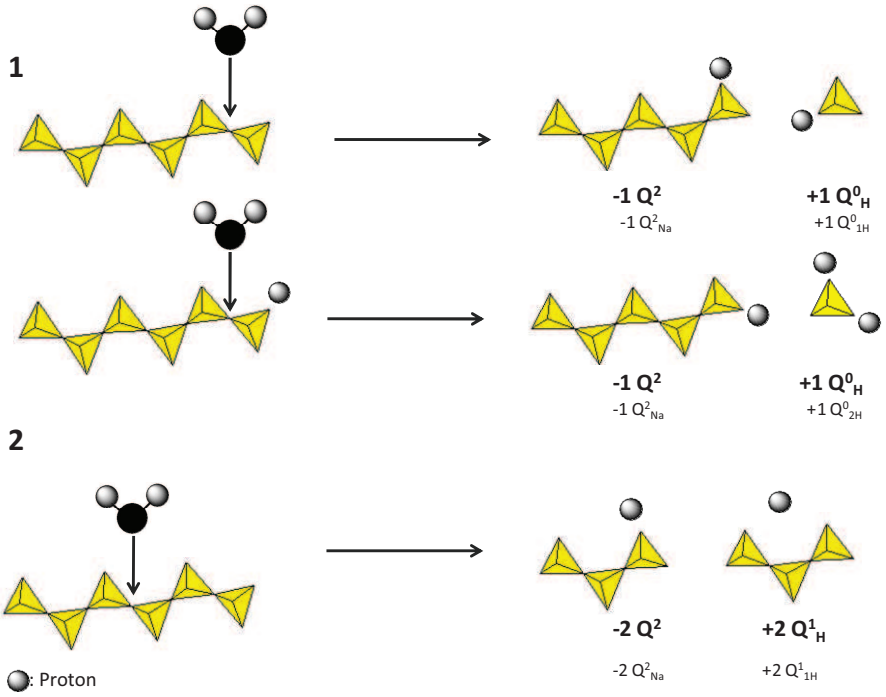

Fig. 4.11:
Two model scenarios for hydrolytic attack proposed by Wenslow and Mueller (Wenslow1998). Scenario 1: Attack at the ends of the metaphosphate chains. Scenario 2: Attack at the interior of the metaphosphate chains.
Please note that the conventional Q^n and $Q^n{}_H$ notation is given in bold letters, whereas a detailed notation is given in small letters for a better understanding.

It is noteworthy that if within one time unit equal numbers of Q^2-Q^1 (scenario 1) and Q^2-Q^2 (scenario 2) bonds are attacked, Q^2 decreases twice as fast in scenario 2 as compared to scenario 1. It is also noteworthy that in both scenarios, Q^2 decrease is always compensated by $Q^n{}_H$ increase.

As it has been mentioned above, the average chain length of the pristine $NaPO_3$ glass has been calculated as $n_{av} \approx 67$. Hence, the following average ratios are obtained for the structural units: $\frac{Q^1}{Q^2} = \frac{2}{65}$, and for the P-O-P bonds $\frac{Q^1 - Q^2}{Q^2 - Q^2} = \frac{2}{64}$, where "$-$" represents the P-O-P bond. Following this calculation, only about 3% of the P-O-P bonds in the pristine $NaPO_3$ glass are disposed at chain ends.

Therefore, if hydrolytic attack on P-O-P bonds were to be postulated non-selective, attack on (Q^2-Q^2) bonds is about 30 times more probable than hydrolytic attack on (Q^1–Q^2) bonds. During the early stage of the weathering process $n_{av} \approx 67$ ($n_{av} >> 5$) and hence $\frac{Q^2 - Q^2}{Q^2 - Q^1} >> 1$. In such a case, scenario 2 (attack at interior of phosphate chains) is expected to be prevalent.

The situation might change for prolonged weathering times, when $\frac{Q^2 - Q^2}{Q^2 - Q^1} = 1$, that is $n_{av} = 5$. At this juncture, assuming non-selective attack, both scenarios 1 and 2 become equally likely.

Fig. 4.12 allows for direct comparison of the Q^2 decay rate and the $Q^1{}_H$ increase rate (Eq. IV-3) during the early stage of weathering, where $\frac{Q^2 - Q^2}{Q^2 - Q^1} >> 1$. In the figure, the sign of $-\frac{\Delta Q^2}{\Delta t}$ has been inverted in order to facilitate comparison of the rates of formation and decay.

The approximate rate of loss of Q^2 intensity and the rate of gain of $Q^1{}_H$ intensity (*Tab. 4.2)* are represented by the slopes of the straight lines that are drawn as guides to the eye (*Fig. 4.12*). Please note that these lines only take into account the first 4 h of weathering that have been identified as the first weathering regime (*Section 4.1*). A greater number of Q^2 units decay per unit time than $Q^1{}_H$ entities appear in the same time interval. Therefore, a scenario where mainly (Q^2-Q^2) P-O-P bonds at the interior of the chains are attacked must be excluded (*Fig. 4.11*). As a result, neither selective attack of P-O-P bonds at the interior of the phosphate chains (Q^2-Q^2) nor completely non-selective attack are corroborated by experimental data.

As a result, attack at the end of the phosphate chains (Q^2-Q^1) must be considered and analyzed quantitatively in the following paragraphs.

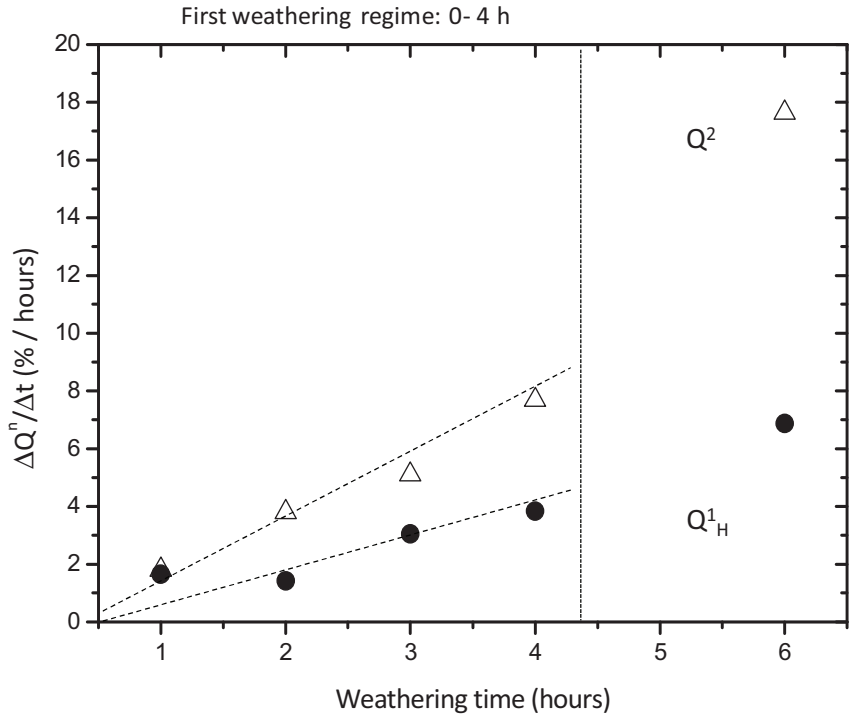

Fig 4.12:

Linear fit, representing the evolution of Q^2 and $Q^1{}_H$ units per time unit $\frac{\Delta Q^2}{\Delta t}$ and $\frac{\Delta Q^1{}_H}{\Delta t}$. Q^2 units are represented by white triangles, $Q^1{}_H$ units are represented by black circles.

Since linear fit functions can only provide an approximate estimation of decay and formation rates of the various structural units, a more precise approach has been used to obtain their respective decay and build-up rates. They are described by a polynomial fit. Polynomials are the most simple and important class of functions for the purpose of curve fittings. They are easy to compute with and evaluation at a point, differentiation or integration can be performed rapidly.

In our case polynomials have been employed in order to obtain a mean function representing the time dependence of the unit fractions of Q^2 and Q^1_H entities with sufficient exactitude (Lancaster1986). They were obtained by using the least squares deviation method. The exactitude of the fit was verified by visual inspection. Please note that the order of the polynomials was chosen to be as low as possible to describe the Q^n and Q^n_H evolution as exactly as possible.

Subsequent analysis of the differential functions of these polynomials furnishes information about the change of Q^2 - and Q^1_H intensity within infinitesimal time intervals. Thus the rates of change in Q^2 decay and Q^1_H generation could be extracted for various points on the time axis.

Tab. 4.3:
Changes of Q^n intensity per time unit. The values obtained by an approximate differentiation are confronted to those obtained by differentiating a polynomial fit $Q^n(t)$ of order four.

Weathering time (hours)	$\frac{\Delta Q^2}{\Delta t}$ $(\frac{\%}{h})$	$\frac{\Delta Q^1{}_H}{\Delta t}$ $(\frac{\%}{h})$	$\frac{\Delta Q^0{}_H}{\Delta t}$ $(\frac{\%}{h})$	$\frac{dQ^2}{dt}$ $(\frac{\%}{h})$	$\frac{dQ^1{}_H}{dt}$ $(\frac{\%}{h})$	$\frac{dQ^0{}_H}{dt}$ $(\frac{\%}{h})$
1	-1,8	+1,7	+0,1	-3,0	+1,7	+0,6
2	-3,8	+1,4	+2,3	-4,5	+3,2	+3,1
3	-5,1	+3,1	+2,1	-6,3	+3,5	+4,9
4	-7,7	+3,8	+3,8	-10,1	+6,3	+6,4
6	-17,7	+6,9	+7,4	-30,6	+19,2	+9,2

Fig. 4.13a represents the relative intensities of the Q^2- and the Q^1_H signal together with their corresponding fit functions (dashed plots). The time dependence of the structure during the first six hours of weathering can be described adequately by 4th order polynomials. Those polynomials allow for calculation of Q^2 and Q^1_H intensity at any point in time (h) and for calculation of the respective decay and built-up rates at any point in time. For completeness, the respective fit functions are given:

$$Q^2(t)=96,63-0,26t-1,99t^2+0,50t^3-0,07t^4 \quad \text{with} \quad \frac{dQ^2}{dt}=0,26-3,98t+1,50t^2-0,28t^3 \quad \text{(IV-4)}$$

and

$$Q^1_H(t)=0,031+1,23t+0,33t^2-0,11t^3+0,03t^4 \quad \text{with} \quad \frac{dQ^1_H}{dt}=1,23+0,66t-0,33t^2+0,12t^3. \quad \text{(IV-5)}$$

Indeed, the rate of reduction of Q^2 intensity is considerably higher than the increase of the Q^1_H signal (equation (IV-4)). This confirms results discussed above (*Tab. 4.2* and *Fig. 4.12)*: a significant amount of Q^2 structural units are *not* transformed into Q^1_H, even after short duration of weathering. Despite the predominance of long phosphate chains, cleavage of (Q^2-Q^2) bonds at the interior of chains does not seem to be prevalent. This more precise analysis of experimental data indicates once more that aqueous attack of phosphate tetrahedra is *not* completely non-selective. In the following section, attack on P-O-P bonds at the chain ends (*Fig. 4.11-1*) shall be considered.

It follows from equation (IV-2a) and (IV-2b) that attack on P-O-P bonds at the chain ends must result in an increase of Q^0 (Q^0_H and Q^0_{2H}) intensity. Indeed, it is observed that the signal intensity in the resonance region of Q^0 (Q^0_H and Q^0_{2H}; 0 ppm) does increase simultaneously with Q^1 (Q^1_H; -8.1 ppm) intensity.
In *Fig. 4.13b* the time dependent Q^2 and Q^0 (Q^0_H and Q^0_{2H}) evolution within the first six hours of weathering are presented, together with their corresponding fit functions (dashed plots). A 6th order polynomial had to be used to describe the time dependent evolution of Q^0 units during the first phase of weathering adequately.

$$Q^0(t)=0,50-2,62\,t+1,85\,t^2-0,17\,t^3+0,01\,t^4-1,10*10^{-4}\,t^5+6,57*10^{-7}t^6 \quad \text{(IV-6)}$$

$$\frac{dQ^0_H}{dt}=-2,62+3,70\,t-0,51\,t^2+0,04\,t^3-5,50*10^{-4}\,t^4+3,94*10^{-6}t^5$$

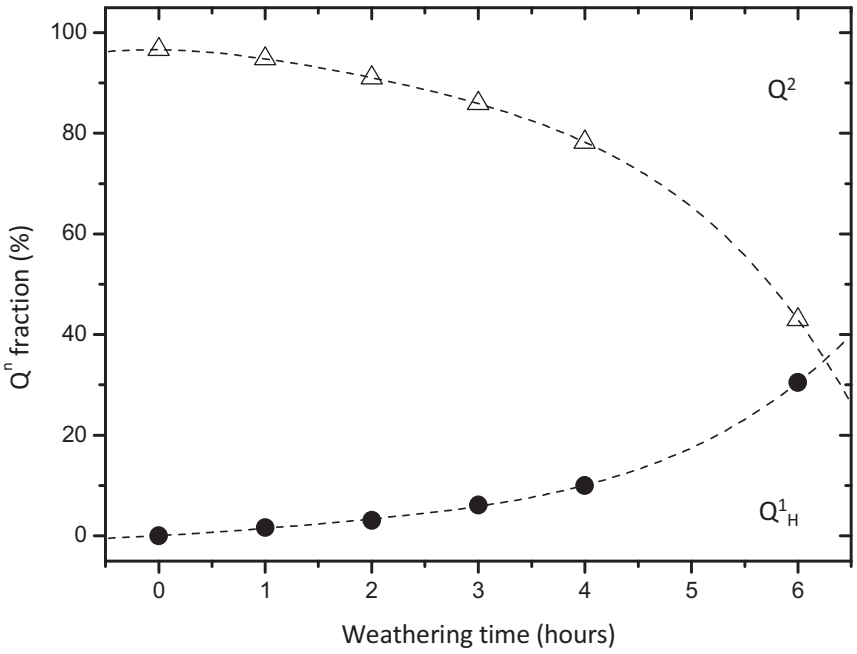

Fig. 4.13a:
Polynomial fits (dashed plots), describing the time dependent evolution of Q^2 (white triangles) and $Q^1{}_H$ (black circles).

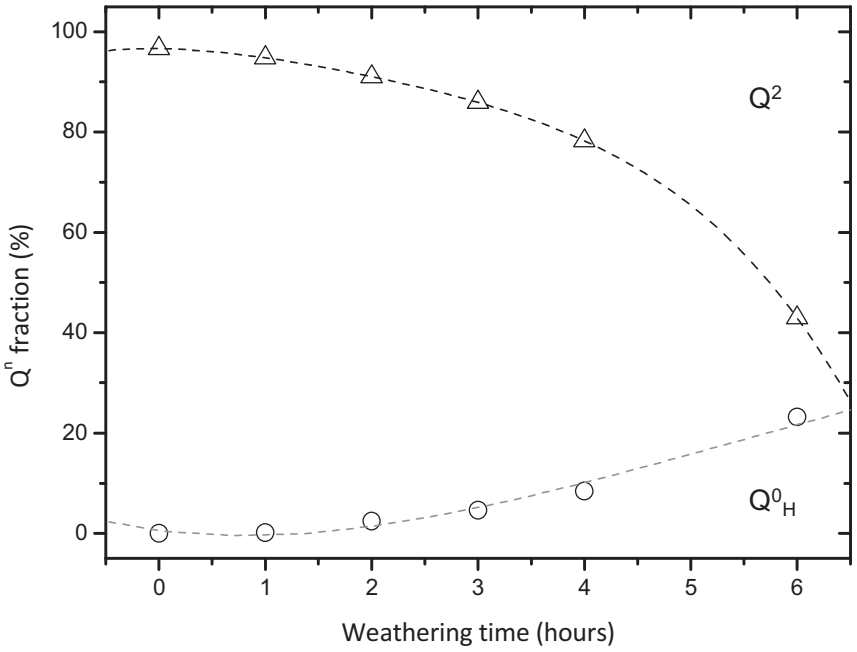

Fig. 4.13b:
Polynomial fits (dashed plots), describing the time dependent evolution of Q^2 (white triangles) and $Q^0{}_H$ (white circles).

Tab. 4.3 shows the rates of Q^2 decrease and those of Q^0_H increase after various weathering times. Besides Q^1_H generation, formation of protonated Q^0_H advances after an initiation time of approximately two hours at comparable rates. The Q^0_H growth rate and its increase are smaller than the observed decay rate and the decrease of Q^2 entities. This can be extracted from the values in *Tab. 4.2* and comparison of the evolution rates after different weathering times (*Tab. 4.3*).

Altogether, the rate of Q^2 signal loss is higher than the rate of Q^1_H increase. It is also higher than the rate of Q^1_H or Q^0_H increase. However, within the range of experimental error, the rate of Q^2 signal loss never corresponds to the sum of Q^1_H and Q^0_H increase.

This observation demonstrates that the simple consideration of the two model pathways elaborated above is not sufficient to understand the rates of Q^n fraction evolution. *Fig. 4.13c* illustrates an example. Signal intensity in the Q^0_H region can increase due to generation of Q^0_H units from aqueous attack at the ends of the phosphate chains (cleavage of Q^2-Q^1 bonds; scenario 1). Signal intensity in the Q^1_H region can increase due to generation of Q^1_H units from aqueous attack in the phosphate mid-chain region (cleavage of Q^2-Q^2 bonds; scenario 2). In parallel, dimeric Q^1_H units can be transformed into Q^0_H units instantaneously, causing the signal in the region at around -8 ppm to wane. Overall, the Q^n fraction evolution gives the impression of slightly predominant attack at the chain ends. However, in fact scenario 1 and scenario 2 are equally likely to occur in this example. A consecutively occurring process (concealed parallel process; cpp) is concealed. This can be misleading.

As a result, all trends elaborated for site selectivity have to be considered with care. Quantitative analysis of Q^n evolution *rates* has demonstrated that it is not possible to draw detailed conclusions about preferred sites of attack and reaction mechanisms.

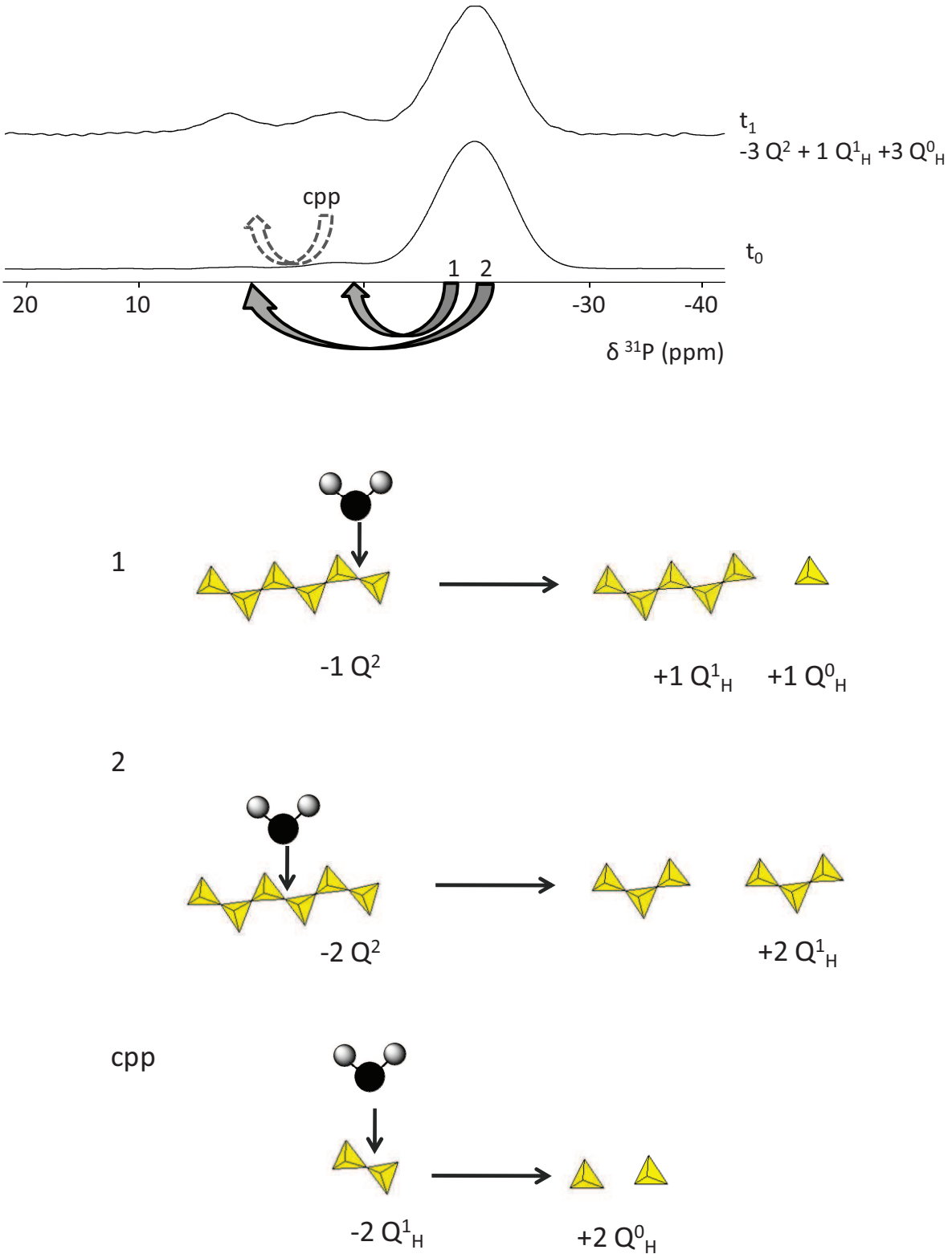

Fig. 4.13c:
Example illustrating how instantaneously occurring parallel processes (cpp) can be concealed by quantitative 1D ^{31}P NMR data. Analysis of apparent increase and decay rates points towards these concealed processes.
Top: apparent net evolution of 1D ^{31}P NMR data. Bottom: Processes occurring in this particular example.

4.2.4 Conclusion on the early stage of weathering from quantitative analysis of ^{31}P NMR:

Kinetics:

Exposure of $NaPO_3$ to humid ambient results in the cleavage of P-O-P bonds causing progressive depolymerization of the glass network as mentioned in Sections 4.1 and 4.2. This is in accordance with the work published by Brow (Brow1990). Hydrolysis reactions are not predominant until the surface of the glass powder is saturated with adsorbed H_2O as it has been proposed in a similar manner by Tischendorf (Tischendorf2004). Hydrolysis of $NaPO_3$ is expected to follow second-order kinetics. After surface saturation with H_2O molecules, the concentration of water is much greater than the relative concentration of Q^2 structural units and hydrolytic attack can be described satisfactorily by first-order kinetics. This model of water vapor attack on a phosphate glass surface stands in agreement with qualitative analysis of ^{31}P and ^{1}H NMR data (Chapter 4.1, Chapter 4.2).

Polynomial curve fitting, decay and formation rates of Q^2, Q^1_H and Q^0_H:

Quantitative analysis of 1D ^{31}P NMR data from the weathering snapshots indicates that the attack on the backbones of the phosphate network is not a purely non-selective, statistical process. If it were, then the generation of Q^1_H units would dominate the spectrum in the early stage of weathering, where Q^2-Q^2 bonds form the vast majority of P-O-P bonds to be attacked. However, experimental data does not support any selective weathering.
Experimental evidence (*Fig.4.13a* and *b*) shows that the intensity of the Q^0_H and Q^1_H resonances increases equally. This indicates that the rate of aqueous attack at chain ends is possibly higher than the rate of the same in the interior of the phosphate chains.
Nevertheless, analysis of the Q^n evolution rates points towards further scission processes that are running in parallel with scenario 1 and 2. Once reaction of water with the glass network has commenced, attack of pristine (Q^2-Q^2) bonds and further scission of (Q^1_H-Q^n) bonds resulting from depolymerization, can proceed in parallel. Hence, quantitative net results from 1D ^{31}P NMR data have to be considered with care, as it has been demonstrated on 4.2.3.

As a result, it is possible for the reaction kinetics and the polynomials fits obtained to conceal complex, interlinked processes (McQuarrie1997). Experiments employing ^{17}O as an isotopic probe are presented in Section 4.3. Together with the conclusion drawn in the section above, they will corroborate the model of complex processes occurring in parallel.

4.2.5 The final stage of the weathering process

The final phase of the weathering process is characterized by the absence of Q^2 units. $Q^0{}_H$ intensity increases linearly with time, while $Q^1{}_H$ intensity diminishes at the same rate. In *Fig. 4.14*, the evolution of the two species is plotted together with the corresponding fit functions (dashed lines).

$$Q^1{}_H(t) = 74,60 - 0,96t \qquad \text{with} \qquad \frac{dQ^1{}_H}{dt} = -0,96 \qquad \text{(IV-7a)}$$

$$Q^0{}_H(t) = 25,40 + 0,96t \qquad \text{with} \qquad \frac{dQ^0{}_H}{dt} = +0,96 \qquad \text{(IV-7b)}$$

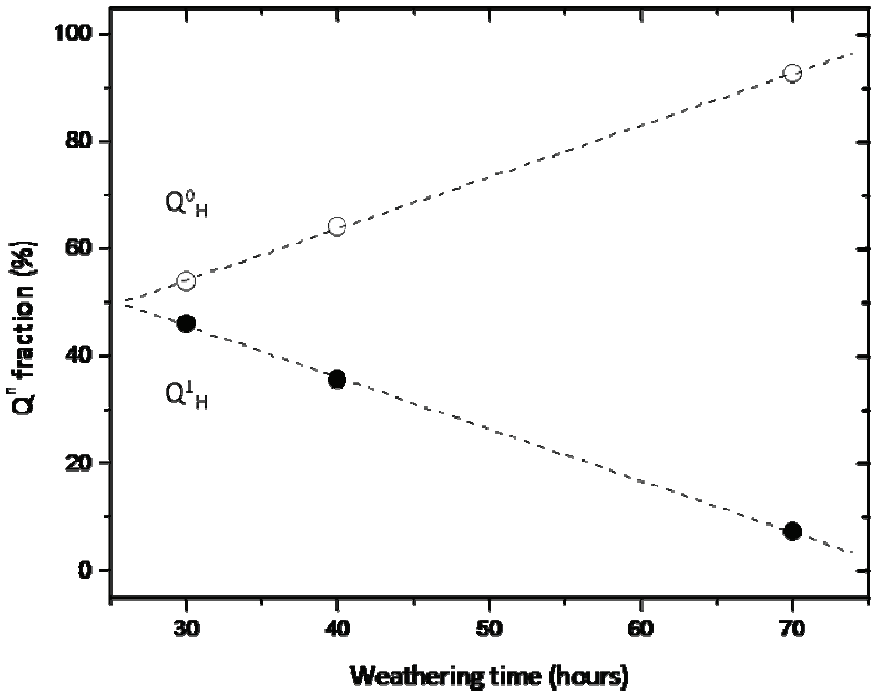

Fig. 4.14:
Evolution of $Q^1{}_H$ and $Q^0{}_H$ intensity for long term weathering (t >30 h). Linear fit functions describing the $Q^1{}_H$ (black circles) and the Q^0 (open circles) evolution during the last stage of the weathering process.

This observation stands in agreement with the final stage scenario illustrated in *Fig. 4.15*. After 30 hours of weathering there are no more Q^2 units present and hydrolytic attack takes place exclusively on dimeric Q^1 entities. $Q^1{}_H$ units are cut into $Q^0{}_H$ units. In the net reaction, two $Q^1{}_H$ units disappear and two $Q^0{}_H$ units are generated.

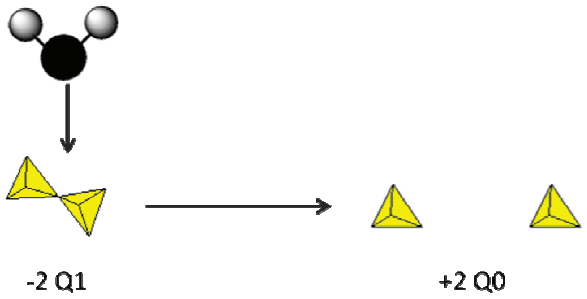

Fig. 4.15:
Model scenario for the final phase of the weathering. Q^1 units represent the highest degree of condensation. They are cut into Q^0_H species.

The experimental data indicates that the final stages of weathering are dominated by the conversion of Q^1 to Q^0.

4.3 A low abundant nucleus as selective isotopic probe: ^{17}O

Non-enriched $NaPO_3$ glass powder has been weathered in an atmosphere saturated by ^{17}O-enriched water vapor. Only the sites attacked by $H_2{}^{17}O$ vapor and their products, will contribute to the observed ^{17}O NMR signal.

2D 3QMAS at high field (18.8 T) is used to measure the isotropic chemical shift δ_{iso} and the quadrupolar parameters C_Q and η_Q could be extracted. It allows for characterization of the immediate structural environment of the newly incorporated ^{17}O sites as it has been demonstrated in Chapter 3.

In addition, 1D ^1H and ^{31}P NMR spectra of the enriched samples have been recorded as routine controls to verify the sample stability and the reproducibility of the assays. These spectra are presented before the discussion of the ^{17}O spectra.

4.3.1 1D ^{31}P NMR of $NaPO_3$ samples attacked by ^{17}O-enriched water vapor

The 1D ^{31}P NMR spectra of $NaPO_3$ glass attacked by enriched water are presented in *Fig. 4.16*. They display a continuous evolution that is in agreement with the 1D ^{31}P NMR spectra discussed previously (section 4.1.1). However, the rate of decrease of Q^2 signal intensity in this series of weathering assays is apparently higher than the one observed for the series of blank assays (*Fig. 4.2a-c* vs. *Fig. 4.16*). Also, crystallization seems to occur earlier than observed for the series attacked with non-enriched water.

These observations have been attributed to the fact that non-enriched samples could be checked immediately after generation whereas the enriched samples had to be stored under dynamic vacuum at room temperature for several days prior to analysis. Under these conditions, further reactions of the sample with water cannot be completely precluded.

The first crystalline NaH_2PO_4 (1.4 ppm and 2.7 ppm) resonances appear in the ^{31}P NMR spectrum of the sample which had been exposed to humid atmosphere for 4 h. In contrast to the weathering series presented in section 4.1, crystalline contributions can also be observed in the Q^1 (Q^1_H) resonance region after only 4 h of weathering (-6.7 ppm, -8.1 ppm and -10.4 ppm). These correspond to an unidentified phase (-6.7 ppm and -10.4 ppm, see section 4.1) and to $Na_2H_2P_2O_7$ (-8.1 ppm). The ^{31}P NMR spectrum recorded after 8 h of weathering under ^{17}O-enriched water vapor shows a broad non-symmetric resonance in the region around 2 ppm with possible crystalline contributions from NaH_2PO_4 and $NaH_2PO_4*H_2O$ (2.1 ppm). After 20 hours, the crystallinity of the weathered sample has considerably increased. The dominant crystalline contributions stem from NaH_2PO_4, $NaH_2PO_4*H_2O$ and $Na_2H_2P_2O_7$. In addition, the unidentified phase gives rise to sharp crystalline resonances.

To conclude, within the range of experimental error the observed evolution of the 1D ^{31}P NMR is identical to that for non-enriched samples. The higher degree of crystallization observed in samples attacked by ^{17}O-enriched water vapor is notably influenced by the duration of sample storage.

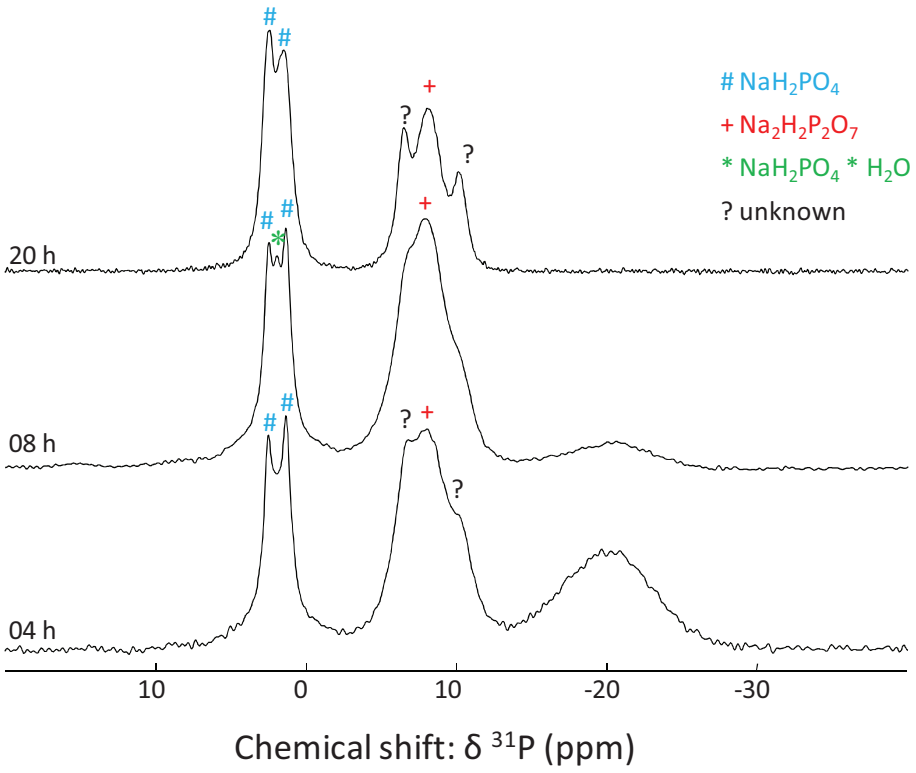

Fig. 4.16:
1D ^{31}P NMR spectra of non-enriched samples weathered under ^{17}O-enriched water vapor for 4 (bottom), 8 (middle) and 20 (top) hours. The spectra have been recorded at a static field of 18.8T and a MAS spinning speed of 20kHz.

4.3.2 1D ^{1}H NMR of $NaPO_3$ samples attacked by ^{17}O-enriched water vapor

1D ^{1}H spectra of the three samples attacked by ^{17}O-enriched water vapor for increasing weathering time are presented in *Fig. 4.17*. The spectra have been recorded at high field (18.8 T) and high MAS spinning speed (60 kHz) using the DEPTH sequence (Chapter 2; Chapter 4.1.2).

As it has already been observed for non-enriched $NaPO_3$ glass weathered under non-enriched water vapor, a continuous evolution from the glass towards the crystalline state is observed with increasing weathering time.

A broad signal in the range from about 4 ppm to 8 ppm is observed that may be assigned to surface-adsorbed water in the material. Broad ^{1}H NMR signals in the region from 12 to 14 ppm can be attributed to amorphous Q^0_H and Q^1_H units that are forming in the aqueously attacked glass (Mercier1999). In the course of phase emergence of crystalline hydrogen phosphates, crystalline Q^0_H and Q^1_H peaks appear in the same region.

As an example, after four hours of weathering, the ^{1}H site characteristic for crystalline $Na_2H_2P_2O_7$ (16 ppm) is already present. This stands in contrast to the observations for the series of non enriched samples, where the first crystalline phases observed were exclusively orthophosphates. Another weak signal can be attributed to NaH_2PO_4 at about 9.5 ppm. Its intensity increases with increasing weathering time. The presence of NaH_2PO_4*H_2O is confirmed from ^{31}P NMR. Indeed, there are three signals whose intensity decreases with increasing weathering time.

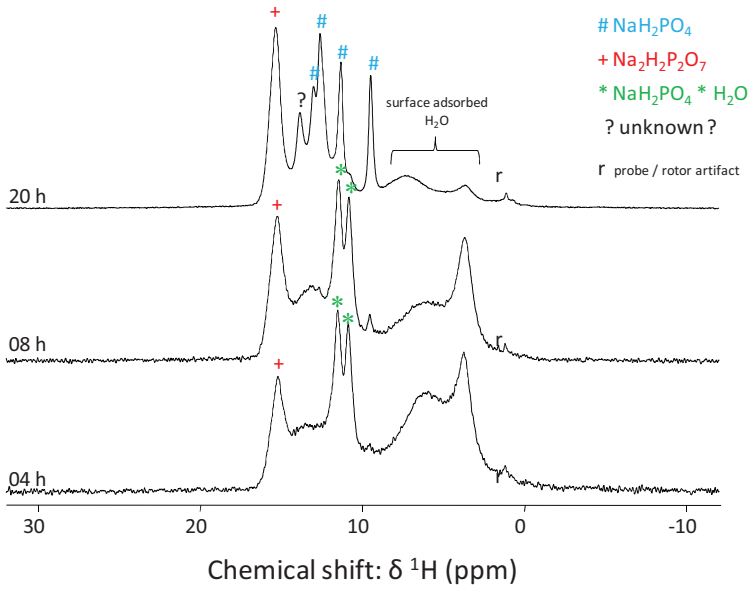

Fig. 4.17:
1D ^{1}H NMR spectra of non enriched samples weathered under ^{17}O-enriched water vapor for 4 (bottom), 8 (middle) and 20 (top) hours. The spectra have been recorded at a static field of 18.8 T and very high MAS spinning speed (60 kHz), implementing the DEPTH sequence to suppress probehead and rotor signals.

4.3.3 2D 3QMAS ^{17}O snapshots employing ^{17}O as a selective isotopic probe nucleus:

Fig. 4.18a, b and *c* show 2D ^{17}O 3QMAS spectra for non-enriched $NaPO_3$ glass weathered under ^{17}O-enriched water vapor. ^{17}O snapshots were recorded for different weathering times ranging from 4 h to 20 h. The observed evolution corroborates the results obtained from ^{1}H and ^{31}P NMR spectra of the same samples presented above.

Emergence of crystalline phases:

After 4 h of weathering, a weak resonance that can be attributed to the crystallographic oxygen site O3 in NaH_2PO_4 (see Chapter 3) is evident in the 2D ^{17}O 3QMAS spectrum. This signal at δ_{iso} = 80 ppm is highlighted in blue in *Fig.4.18a*. This phase can be observed well in the 1D ^{31}P MAS NMR (*Fig. 4.16*). O3 is a non-bridging oxygen (NBO) site. It is the only ^{17}O resonance that can be attributed to NaH_2PO_4 unambiguously. For several reasons not all of the eight sites of the ^{17}O-enriched crystalline NaH_2PO_4 reference can be identified in *Fig. 4.18a*. First, low sensitivity and low abundance of the probed nucleus as well as modest efficiency of triple quantum coherence excitation are constraints of the 2D 3QMAS experiment on ^{17}O. As an example, quadrupolar coupling constants C_Q for the different oxygen sites in NaH_2PO_4 vary from 4 MHz to 7MHz (Chapter 3), rendering uniform excitation difficult. Second, certain ^{17}O resonances are complex superpositions of oxygen sites of several crystalline phases. As an example, the NBO resonance region (highlighted as NBO in *Fig. 4.18a-c*; grey dashed bracket NBO) may cover NBO sites from NaH_2PO_4 as well as NBO sites from NaH_2PO_4*H_2O, NaH_2PO_4*$2H_2O$ and $Na_2H_2P_2O_7$ (see Chapter 3).
In the same spectrum (*Fig. 4.18a*), a resonance that is characteristic for bridging oxygen sites (BO) at δ_{iso} = 136 ppm, is detected and is highlighted in red. Superposition of the 2D 3QMAS NMR spectrum presented in *Fig. 4.18a* with the spectrum of crystalline ^{17}O-labeled $Na_2H_2P_2O_7$ reveals that the BO signal at δ_{iso} = 136 ppm most probably stems from this pyrophosphate phase. The corresponding peak in the ^{31}P NMR (*Fig. 4.16*; -8.1 ppm) also confirms the existence of crystalline $Na_2H_2P_2O_7$ in the sample.
We emphasize that this BO resonance can only arise from *re*condensation of formerly hydrolyzed P-O-P bonds since ^{17}O-enriched PO_4 tetrahedra are generated exclusively by aqueous attack from ^{17}O-enriched water vapor. Several studies on the temperature dependent transformation of hydrogen phosphate phases (Ghule2001, Schülke1983, Thilo1955) give evidence for possible condensation of orthophosphates at *T*=80°C to yield pyrophosphate phases. However, experimental evidence for this phenomenon occurring under weathering conditions cannot be achieved by employing common NMR probe nuclei such as ^{31}P or ^{1}H. It is a unique feature of ^{17}O to reveal this process.

Additionally, an oxygen resonance at δ_{iso} = 110 ppm can be observed in *Fig. 4.18a*. It is highlighted in green. This resonance can be assigned to $NaH_2PO_4*H_2O$. The pure hydrated phase $NaH_2PO_4*H_2O$ is difficult to access by micro-synthesis of the ^{17}O-labeled compound. Hence, the assignment of this resonance is based solely on the first-principles calculation approach presented in the previous chapter (Chapter 3).

After eight hours of weathering (*Fig. 4.18b*), the intensity of the bridging oxygen resonance at δ_{iso} = 136 ppm (red) is remarkably small. The oxygen site O3 of NaH_2PO_4 at δ_{iso} = 80 ppm (blue), also presents small signal intensity. However, it can be identified by its projection on the isotropic dimension (78 ppm).
In addition, the resonance at δ_{iso} = 110 ppm, which can be assigned to $NaH_2PO_4*H_2O$ (green), is well-developed and can clearly be observed.

After 20 hours of weathering (*Fig. 4.18c*), bridging oxygen resonances (red) have become stronger. Further the signal characteristic for site O3 in NaH_2PO_4 (blue) is also well expressed.
The ^{17}O signal intensity at δ_{iso} 110 ppm is markedly reduced. This is in agreement with ^{1}H MAS and ^{31}P MAS NMR spectra of this sample where contributions from $NaH_2PO_4*H_2O$, have also considerably diminished.

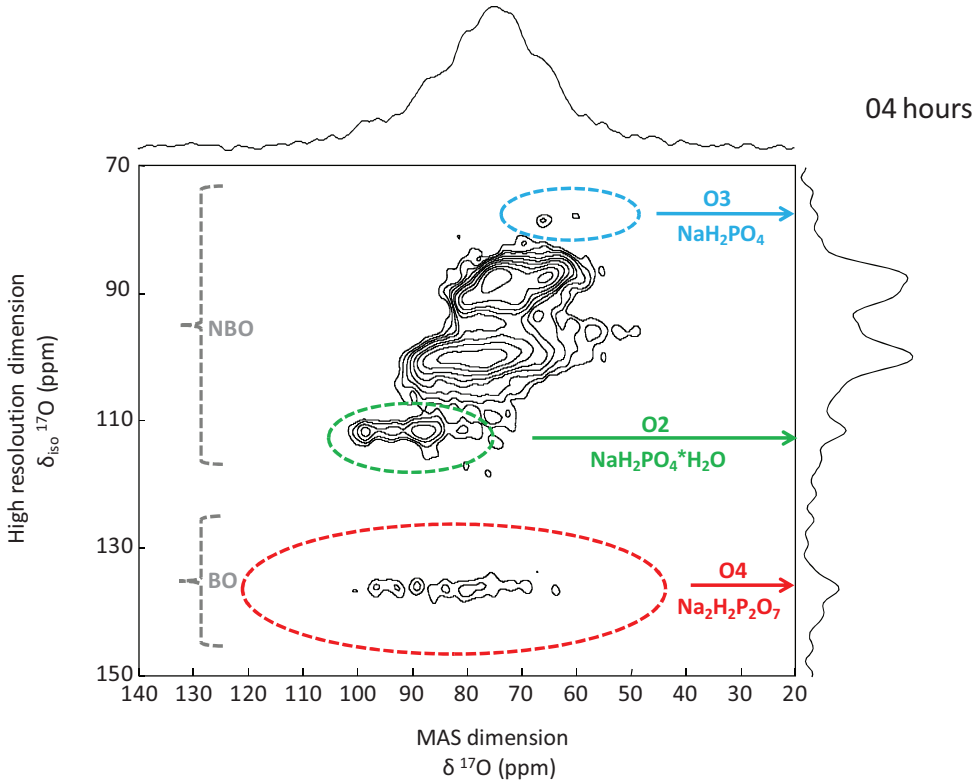

Fig. 4.18a:
2D ^{17}O 3QMAS snapshot of non-enriched $NaPO_3$ glass weathered for four hours under ^{17}O-enriched water vapor. NBO from NaH_2PO_4 (site O3; blue) and $NaH_2PO_4*H_2O$ (O2; green) as well as a BO resonance (red) are highlighted with dashed ellipses.

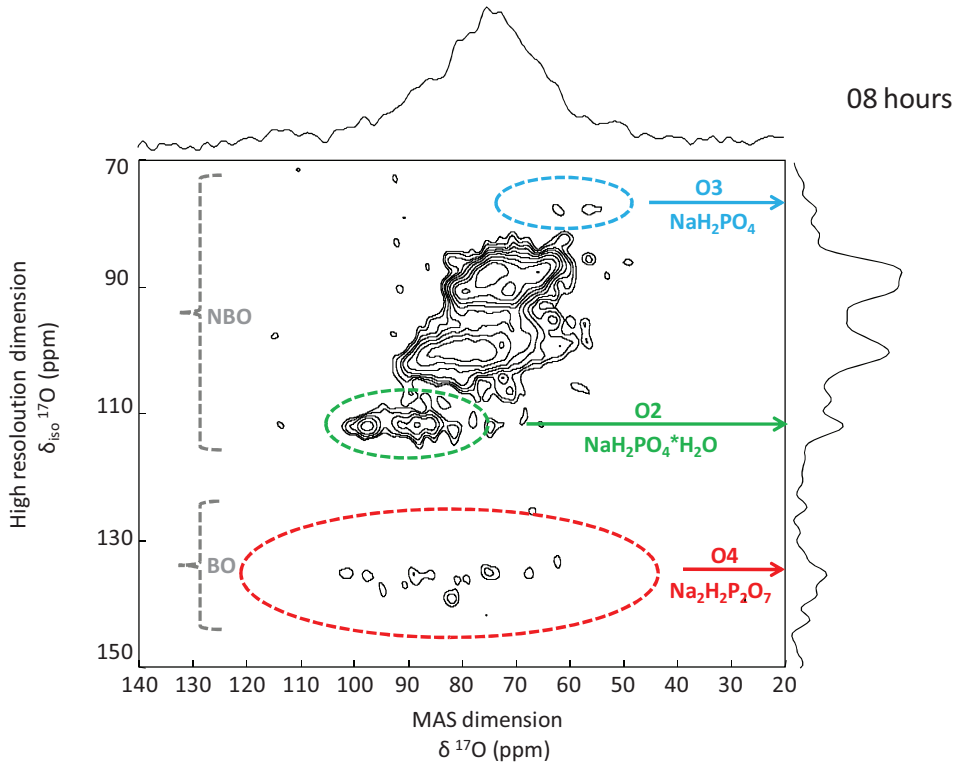

Fig. 4.18b:
*2D ^{17}O 3QMAS snapshot of non-enriched $NaPO_3$ glass weathered for 8 h under ^{17}O-enriched water vapor. NBO from NaH_2PO_4 (site O3; blue) and NaH_2PO_4*H_2O (green) as well as a BO resonance (red) are highlighted with dashed ellipses.*

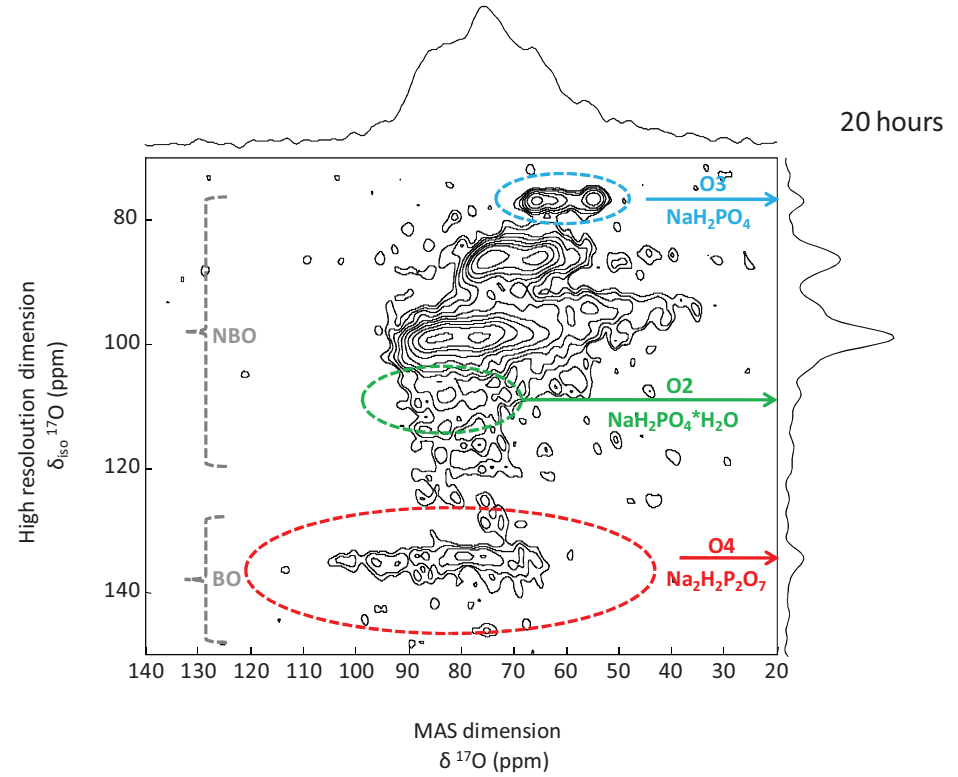

Fig. 4.18c:
*2D ^{17}O 3QMAS snapshot of non-enriched $NaPO_3$ glass weathered for 20 h under ^{17}O-enriched water vapor. NBO from NaH_2PO_4 (site O3; blue) and NaH_2PO_4*H_2O (green; vanishing) as well as a BO resonance (red) are highlighted with dashed ellipses.*

Oxygen environments during water incorporation:

In Chapter 3.2.3, 2D correlation maps (C_Q vs. δ_{CS}) have been elaborated. Based on these maps a visual inspection of ^{17}O 3QMAS data (*Fig. 4.18a-c*) allows for a further characterization of the oxygen environments.

During the early stage of weathering (4 h, 8 h), oxygen resonances appear mainly in the NBO signal region. C_Q values are moderate (around 5 MHz to 6 MHz) and δ_{CS} values reach from around 70 ppm to 100 ppm. Both are features characteristic for ionic bonds such as P-O…Na or P-O…H or P-O…(Na,H). In particular, the possibility to characterize the nature of O-H bonds further by ^{17}O merits interest for future studies.

After 20 h of weathering, rearrangement into crystalline phases has taken place. A broader variety of ^{17}O environments, e.g. those characteristic for ionic bonds with pure sodium environments, are present. Moreover, covalent P-OH bonds with high C_Q values (around 7 MHz) emerge.

Conclusion:

As a probe nucleus in the framework of a multinuclear NMR study, ^{17}O complements information from ^{1}H and ^{31}P NMR spectra. Thus, assignment of contributions from $NaH_2PO_4*H_2O$ in 1D ^{1}H spectra has been possible. The contributions from $NaH_2PO_4*H_2O$ have been detected in the ^{31}P NMR spectra of $NaPO_3$ glass weathered under ^{17}O-enriched water vapor for four hours (*Fig. 4.16*).

2D ^{17}O 3QMAS can be helpful in gaining new insights into the dynamics of the weathering process. Beyond pure assignment of resonances based on reference values, the ^{17}O 3QMAS data allowed for characterization of the ^{17}O environments that are present throughout weathering. This may be helpful for investigations *how* water depolymerizes the glass network. As an example, the quadrupolar parameters may provide additional information about H-O-H bonding angles that are not accessible from ^{1}H NMR data.

Based on NMR parameters that were obtained experimentally and by calculation in a previous work (see Chapter 3), *re*formation of bridging oxygen sites from formerly hydrolyzed sites could be observed. It is a unique property of ^{17}O to monitor this process, since the low-abundant nucleus can be employed as an isotopic probe.

The *re*condensation of P-O-P bonds under the present weathering conditions is one more process that remains concealed in 1D ^{1}H and ^{31}P NMR data.

Summary and Conclusion Chapter 4

Multinuclear solid-state NMR has been implemented as the major tool to obtain an as complete as possible idea of the fundamental processes and structural changes taking place during $NaPO_3$ weathering. The results are illustrated in *Fig. 4.19* and shall be summarized and discussed in the following paragraphs. The most important outcomes are highlighted in red.

Network evolution and preferred sites of attack (blue):

^{1}H NMR data and kinetic analysis of ^{31}P NMR data together with ^{1}H-^{31}P CP NMR give evidence for continuous network depolymerization. During an initial stage of weathering water molecules are adsorbed at the particle surface until a saturation state is reached. Simultaneously, the hydroxyl group concentration in the glass network grows, accelerating water molecule adhesion rates on the glass surface. After this preparation phase, the depolymerization occurs with accelerated rate.
The results of our studies corroborate the model of surface hydrolysis of phosphate glass networks under weathering conditions that is under an atmosphere saturated by water vapor. Weathering differs from phosphate glass alteration under solution conditions, where removal of entire phosphate chains and modifier cations into solution occurs (Tischendorf2004).

Crystallization phenomena (red):

Crystallization could first be observed after 4 h of weathering from 1D ^{31}P NMR. Isolated phosphate tetrahedra show a greater tendency to reorganize in the crystalline state and arise first in the NMR spectra. XRD data from this study and from the one presented by Tischendorf who observed hydrated phosphate layers on phosphate glass sample surfaces (Tischendorf2004) stand in agreement with this observation.
The fraction of crystalline phases in the former $NaPO_3$ glass increases steadily with prolonged weathering time. This indicates an increasing degree of phosphate glass surface corrosion. After 70 h of weathering, the 1D ^{31}P NMR spectrum shows mainly crystalline peaks. NMR providing a sample average, this indicates that the attacked glass surface layer grows. Consequently, localized crystalline colonies coalesce and migrate towards the interior of the particles. This corroborates data from Tischendorf who monitored the same process at the glass surface of a model amplifier glass (K_2O-Al_2O_3-P_2O_5 with additions of MgO / CaO / BaO) by employing scanning electron microscopy.

For a model phosphate glass exposed to physiological solution conditions (high ionic strength) Clément *et al.* (Clément1999) observed hydrolysis of the phosphate chains in the solution and subsequent precipitation and formation of a hydrated orthophosphate layer on the phosphate glass sample surface. Thus, phosphate glass surfaces seem to be predisposed to be transformed mainly into crystalline orthophosphate phases upon aqueous attack, either in solution or under weathering atmosphere.

Mechanistic analysis (green):

Quantitative analysis of deconvoluted 1D ^{31}P NMR data indicates a slight preference for hydrolytic attack on (Q^2-Q^1) bonds at the chain ends. However, polynomial analysis of built-up and decay rates of Q^2, Q^1_H and Q^0_H entities points towards a multitude of concealed processes that are occurring in parallel to the two model scenarios developed by Wenslow and Mueller (Wenslow1998). Thus, the apparent (Q^2-Q^1) site preference has to be considered with care, since a multitude of hydrolysis routes may lead to the respective structural units. To our knowledge, such a quantitative analysis of phosphate glass weathering has not been carried out so far.

As a low abundant isotopic probe, ^{17}O (green) proved to be helpful to reveal one of the concealed processes, namely the reformation of BO from formerly hydrolyzed P-O-P bonds. So far, recondensation under weathering conditions has not been considered. Under water vapor atmosphere, hydration of phosphate chains with subsequent hydrolysis of P-O-P bonds has been proposed by Tischendorf (Tischendorf2004); the reverse process has not been taken into account. The weathering temperatures used in our studies (80°C, water vapor) suggest a *re*formation of pyrophosphate units, but only the implementation of ^{17}O together with reference data obtained from synthesis of phase pure hydrogen phosphates and from first-principles calculations (see Chapter 2) could corroborate this thesis and provide an idea to what extent recondensation occurs.

In the case of silicate glass systems, the recondensation phenomen is also discussed controversely in the literature. Masui *et al.* (Masui2002) investigated the weathering of Na_2O-3 SiO_2 glass under the experimental conditions used in the present chapter. The authors concluded that the glass network decomposes slightly at the initial stage of hydration where low concentrations of H_2O are present and that significant recombination of Si-OH occurs above 20wt% of water content in the network.

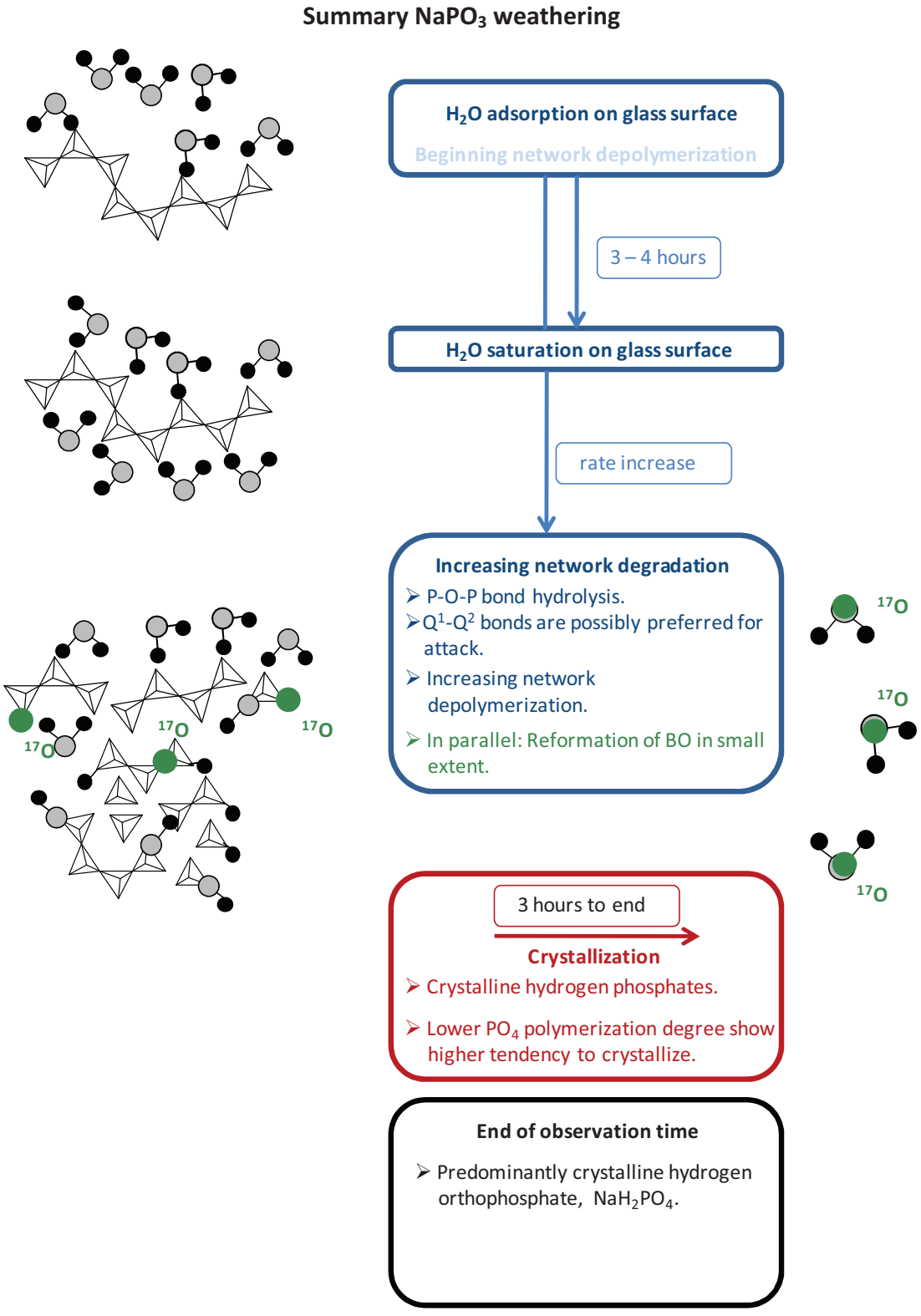

Figure 4.19:
Flowchart illustrating the results for $NaPO_3$ weathering studies from a pure multinuclear solid-state NMR analysis.

^{17}O as a probe nucleus:

$H_2{}^{17}O$ has been implemented as a selective marker for oxygen environments created throughout aqueous attack. ^{17}O 3QMAS has been employed to monitor the emrgence of their corresponding resonances. Based on NMR – structure relationships elaborated in Chapter 3, the environments corresponding to the observed resonances could be worked out. The unique combination of two / three NMR parameters of a quadrupolar nucleus provides information.
This may be of particular interest for further studies of the nature of water incorporation into the glass network.

Conclusion:

One of the aims of this study has been to demonstrate that a comprehensive approach to phosphate glass weathering is possible by employing solid-state NMR, exclusively. A combination of routine an advanced NMR techniques, with ^{31}P, ^{1}H and ^{17}O as probe nuclei helped us to monitor the fundamental structural changes that are occurring during the weathering of binary phosphate glass. The results of our studies stand in agreement with the outcome of former investigations (Wenslow1998, Alam2005). Aditionally, we gained a deeper understanding in details of the weathering process by a quantitative analysis and by implementing ^{17}O as a probe nucleus in the weathering process.
This understanding of the weathering process on an atomic level constitutes the basis for interpretation of macroscopic properties such as chemical durability of a phosphate glass.

In the following chapter, we shall extend our view on a 'durable' ternary system, namely Na_2O - Al_2O_3 - P_2O_5. Notably, we are interested in the structural role of aluminum during weathering, since increasing chemical durability in Na_2O-Al_2O_3-P_2O_5 networks is attributed to aluminum. However, even if the weathering of ternary phosphate glass systems containing Al_2O_3 has been investigated in the literature (Alam2005), ^{27}Al as a probe nucleus for monitoring the weathering these glasses has been neglected so far.

The ternary model system will be more complex than the binary one. Hence, the strategy for its study must be adapted and this constitutes an additional challenge that shall be confronted to in Chapter 5.

Bibliography Chapter 4

Alam2001
Alam, T.M., Lang, D.P.
Chemical Physics Letters (2001) **336 (5-6)** 385.

Alam2005
Alam, T.M., Tischendorf, B.C., Brow, R.K.
Solid State Nuclear Magnetic Resonance (2005) **27 (1-2)** 99.

Brow1990
Brow, R.K., Kirkpatrick, R.J., Turner, G.L.
Journal of Non-Crystalline Solids (1990) **116 (1)** 39.

Brow2000
Brow, R.K.;
Journal of Non-Crystalline Solids (2000) **263** 1.

Clark1979
David E. Clark and Carlo G. Pantano Jr. and Larry L. Hench
Corrosion of Glass (1979) Books for Industry and The Glass Industry,

Clément1999
Clément, J., Manero, J.M. Planell, J.A.
Journal of Materials Science: Materials in Medicine (1999) **10**, 429-432

Forler2010
Forler, N., Vasconcelos, F., Cristol, S., Paul, J.-F., Montagne, L., Charpentier, T., Mauri, F., Delevoye, L.
Phys. Chem. Chem. Phys. (2010), **12**, 9053-9062

Ghule2001
Ghule, A., Ramaswamy, M., Chang, H.
Inorganic Chemistry (2001) **40** 5917.

Hartmann1994
Hartmann, P., Vogel, J., Schnabel, B.
Journal of Non-Crystalline Solids (1994) **176 (2-3)** 157.

Hosono1992
Hosono, H., Yoshihiro, A., Deguchi, K.
Journal of Non-Crystalline Solids (1992) **142** 103.

Kirkpatrick1995
Kirkpatrick, R.J., Brow, R.K.
Solid State Nuclear Magnetic Resonance **5 (1)** (1995) 9.

Lancaster1986
Lancaster, P. and Salkauskas, K.
Curve and Surface Fitting, An Introduction (1986) Academic Press, San Diego

Masui2002
Masui, H., Chen, D., Akai, T., Yazawa, T.
Zeitschrift für Naturforschung (2002) **57a**, 473-478

McQuarrie1997
Donald A. McQuarrie (Publisher) and John D. Simon and John Choi
Physical Chemistry: A Molecular Approach (1997) Univ. Science Books.

Mercier1999
Mercier, C., Montagne, L., Sfihi, H., Palavit, G.
Journal of Non-Crystalline Solids (1999) **256 & 257** 124.

Schülke1983
Schülke, U., Kayser, R., Arndt, L.
Zeitschrift für anorganische und allgemeine Chemie (1983) **504** 77.

Thilo1955
Thilo, E., Grunze, H.
Zeitschrift für anorganische und allgemeine Chemie (1955) **281** 262.

Tischendorf2004
Tischendorf, B., Brow, R.;
XX. International Congress on Glass, Oct. 2004, Kyoto, Japan.

van Wazer1958
Van Wazer, J. R.
Phosphorus and its Compounds, Vol. 1, Interscience, New York 1958

Wenslow 1998
Wenslow, R.M., Mueller, K.T.;
Journal of Physical Chemistry B (1998) **102 (45)** 9033.

Wiench2002
Wiench, J.W., Tischendorf, B., Otaigbe, J.U., Pruski, M.;
Journal of Molecular Structure (2002) **602-603** 145.

Xue2009
Xue, X., Kanzaki, M.
Journal of the American Ceramic Society (2009) **92 (12)** 2803-2830.

Chapter 5

Structure and weathering of a ternary model phosphate glass investigated by solid-state NMR

CHAPTER 5

Structure and weathering of a ternary model phosphate glass (x Al_2O3 – (100-x) $NaPO_3$) investigated by solid-state NMR

In the following chapter, the hydration mechanism of “durable” phosphate glasses will be investigated. We will try to understand how the glass composition and structure can control and improve the resistance to water vapor attack.

To complete the results of the previous sections, we have chosen to focus on the previously investigated phosphate composition ($NaPO_3$) and to change the glass formulation by adding one oxide: Al_2O_3, which is known for a long time to improve the stability against water attack. It is worthy to note that iron oxide, Fe_2O_3, has also proven to be an efficient oxide to develop durable phosphate compositions but its paramagnetic character would have significantly disturbed and limited the application of the NMR techniques. The hydration mechanism of glasses in the xAl_2O_3- (100-x)$NaPO_3$ has thus been investigated in this section by monitoring the structural evolutions of the alumino-phosphate mixed network that occur during the exposition to water vapor.

As in Chapter 4, multinuclear solid-state NMR has been used to:

(i) investigate the structure of the pristine glasses (Section 5.1). ^{31}P and ^{27}Al 1D-MAS NMR has been used to characterize the local order of the phosphate and aluminate moieties. The poor resolution of the ^{31}P spectra has been overcome by the use of recent 2D MAS-NMR correlation technique (Dipolar-HMQC). The obtained results allow, in combination with recent data coming from the literature, developing a structural model describing the chemical nature of the mixed PAl moieties that constitutes the glass network.

(ii) monitor the structural evolution of the mixed moieties during the hydration process (Section 5.2). ^{1}H, ^{27}Al and ^{31}P MAS-NMR gave information about the protonated entities entering into the glass structure and about the chemical transformations of the phosphate and aluminate species as well. Additional information on the interaction between water and the alumino-phosphate network has been derived from 2D NMR techniques (D-HMQC, CP and REDOR). The global set of results allows understanding how the water reacts with the glass matrix and permits to propose a hydration mechanism for these durable phosphate glasses highlighting the impact of the mixed AlP moieties on the resistance against water vapor.

Experimental details Chapter 5

1D NMR spectra:

a) ^{1}H NMR

All 1D ^{1}H NMR experiments have been performed as high resolution experiments at 18.8 T with a resonance frequency of (ν_0 ^{1}H = 800.30 MHz). A 1.3 mm probe with MAS frequencies of 60 kHz was employed. For suppression of rotor and probe artifacts, the DEPTH sequence was used.
^{1}H chemical shift values are referred to adamantine.

b) ^{27}Al NMR

All 1D ^{27}Al NMR experiments have been recorded at 9.4 T (ν_0 ^{27}Al = 104.2 MHz), employing a 4 mm HX probe at a MAS spinning frequency of 10 kHz. One-pulse ^{27}Al spectra were acquired employing a radiofrequency amplitude of (ν_{RF} ^{27}Al) 20 kHz (determined on a liquid sample) , 2 µs pulse length, 64 transients and a relaxation delay of 1.0 s.
^{27}Al chemical shift values are referred to 1M $Al(NO_3)_3$.

c) ^{31}P NMR

All 1D ^{31}P NMR spectra have been recorded at 9.4 T (ν_0 ^{31}P = 161.9 MHz), employing a 4 mm HX probe at a MAS spinning frequency of 10 kHz. One-pulse ^{31}P NMR spectra were acquired using a 1.6 µs pulse length, a radiofrequency amplitude of (ν_{RF} ^{31}P) 50 kHz, 4 transients and a relaxation delay of 60 s.
^{31}P chemical shift values are referred to 85% H_3PO_4.

^{27}Al-{^{31}P} D-HMQC

The ^{27}Al-^{31}P D-HMQC spectrum has been recorded at 9.4 T on a 4 mm HXY probe with the following acquisition parameters: spinning frequency = 12.5 kHz, radiofrequency field on ^{27}Al channel = 4.4 kHz (determined on a liquid), radiofrequency field on ^{31}P channel = 80 kHz. The dipolar interaction has been recoupled with the SFAM1 pulse scheme during 1 ms by using a modulated rf field of 80 kHz and a 12.5 kHz frequency modulation allowing for the amplitude and phase double modulation. The 2D spectrum has been recorded with 2474 x 50 points using rotor synchronized conditions. Each slice

has been acquired with 2048 scans separated by a recycle delay of 0.5 s, leading to a complete experimental time of 14 h.

REDOR

a) ^{27}Al-{^{1}H} REDOR

^{27}Al-^{1}H REDOR was performed employing a HXY 4 mm probe at a spinning frequency of 10 kHz with radiofrequency amplitudes of (ν_{RF} ^{1}H) 58.8 kHz and (ν_{RF} ^{27}Al) 7.4 kHz. The 90° and 180° pulse lengths for ^{27}Al have been 11 µs and 22 µs, respectively. The recoupling pulse length on ^{1}H has been 8.5 µs. 512 transients were acquired, the relaxation delay was set to be 0.5 s.

b) ^{27}Al-{^{31}P} REDOR

^{27}Al-^{31}P REDOR was performed employing a HXY 4 mm probe at a spinning frequency of 10 kHz with radiofrequency amplitudes of (ν_{RF} ^{27}Al) 7.4 kHz and (ν_{RF} ^{31}P) 66.6 kHz. The 90° and 180° pulse lengths for ^{27}Al have been 11 µs and 22 µs, respectively. The recoupling pulse length on ^{31}P has been 7.5 µs. 512 transients were acquired, the relaxation delay was set to be 0.5 s.

^{1}H-{^{31}P} CP

The ^{1}H-^{31}P cross-polarization experiment was performed in a 4 mm HX probe at a spinning frequency of 10 kHz, using a CP contact time of 200 µs. CP transfer was effected at a radiofrequency amplitude of 45 kHz. During acquisition, ^{1}H high power decoupling at an amplitude of (ν_{RF} ^{1}H) 73.5 kHz has been used, employing spinal 64.

5.1 The structure of the pristine glass

In the following, the structure of sodium aluminum phosphate glasses along the composition line (100-x) $NaPO_3$-x Al_2O_3 will be studied (black circles; *Fig. 5.1*). These glass systems will be referred to as NaAlP-x, with x indicating the Al_2O_3 content in the batch composition (in mol %).

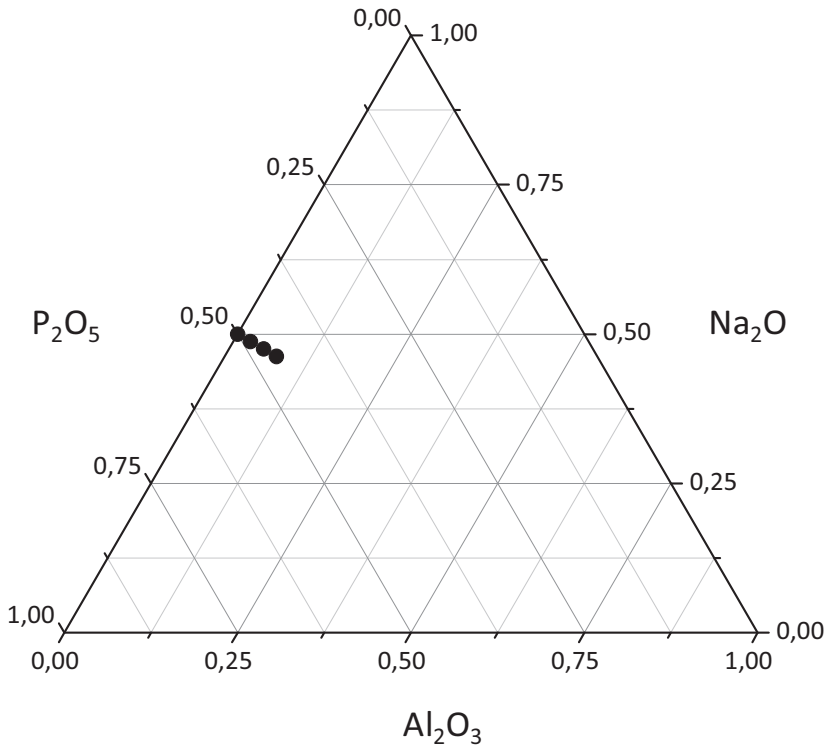

Fig. 5.1:
Composition line for the series of NaAlP-x glasses prepared in the frame of this work (black circles).

The sodium aluminophosphate glasses have been prepared following the protocol given in Chapter 2 at a melting temperature of 1050°C and a melting time of 30 minutes. The details of the preparation are given in *Tab. 5.1*. For the present series of NaAlP-x glasses, x varies from $0 \leq x \leq 7.5$ mol %. In the literature, glass compositions up to 25 mol % Al_2O_3 have been reported (Brow1993). However, the glasses reported in the present study contain low amounts of alumina to maintain a glass network mainly constituted by phosphate moieties. The amorphous nature of the glasses has been verified by XRD and their corresponding glass transition temperatures (T_g) have been measured by DSC. *Fig. 5.2* shows the evolution of the glass transition temperatures T_g vs. the Al_2O_3 glass content (x). Within the studied composition range, the addition of Al_2O_3 results in a very important and almost linear increase of T_g (e.g. +100 °C for insertion of 7.5% Al_2O_3). This trend is consistent with the one reported

in the literature (Brow1993) for the ternary aluminophosphate glasses of the same composition and for other alkali aluminophosphate systems (Wegner2008). The observed increase is associated to a strengthening of the network attributed to the connection of the sodium phosphate chains by aluminate species, leading to a more polymerized glass network.

Tab. 5.1:
NaAlP-x glass systems, nominal composition (mol %), preparation temperature (T_m), preparation time (t_m) and the glass transition temperature (T_g) determined by differential scanning calorimetry (DSC).

x	Na_2O (mol %)	Al_2O3 (mol %)	P_2O_5 (mol %)	T_m (°C)	t_m (min)	T_g (°C)
0	50.0	0	50.0	1050	30	288
2.5	48.75	2.5	48.75	1050	30	322
5.0	47.5	5.0	47.5	1050	30	349
7.5	46.25	7.5	46.25	1050	30	389

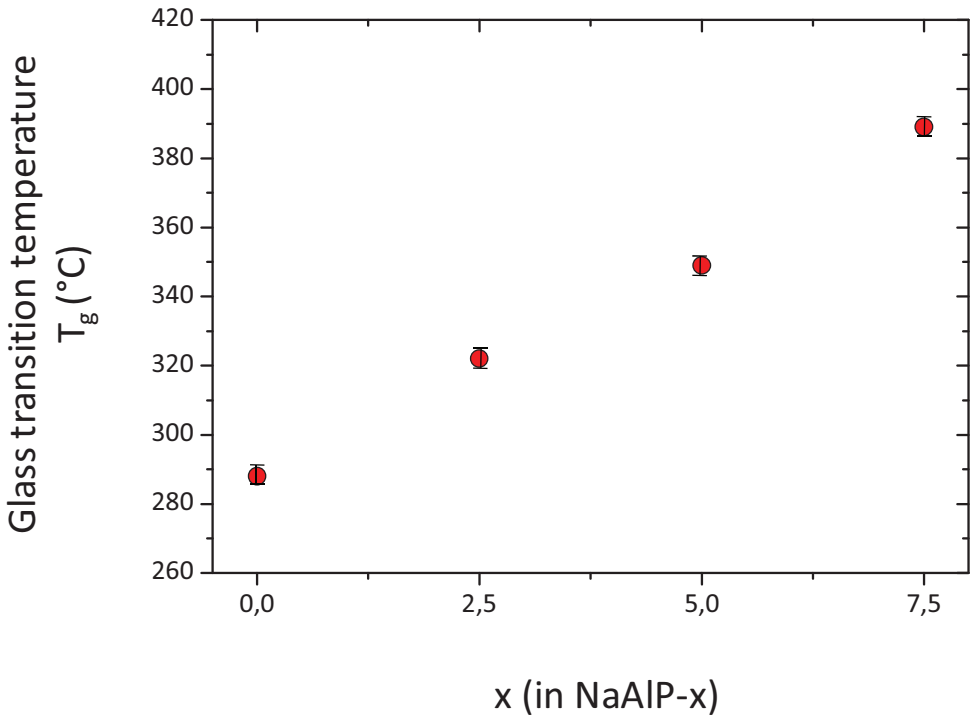

Fig. 5.2:
Glass transition temperatures (T_g) of the NaAlP-x composition series (x=0 to 7.5). The glass transition temperatures have been determined by differential scanning calorimetry (DSC) with a rate of 5°C/min and a maximum glass powder grain size smaller than 100 µm. The estimated error is in the range of +/-5°C and indicated by error bars.

5.1.1 1D ^{27}Al NMR results

Fig. 5.3 depicts the isotropic window of the ^{27}Al NMR spectra of the investigated compositions. All the spectra are dominated by an intense signal centered at -13 ppm, accompanied by low intensity signals at 13 and 45 ppm. These three signals have been attributed, on the base on ^{27}Al-{^{31}P} REDOR results obtained on similar glass systems by Wegner et al. (Wegner2008), to AlO6, AlO5 and AlO4 moieties surrounded by phosphate species, respectively. The signal at about 45 ppm can thus be assigned to $Al(OP)_4$ group, the signal at 13 ppm to $Al(OP)_5$ group and the signal at -13 ppm to $Al(OP)_6$ species.

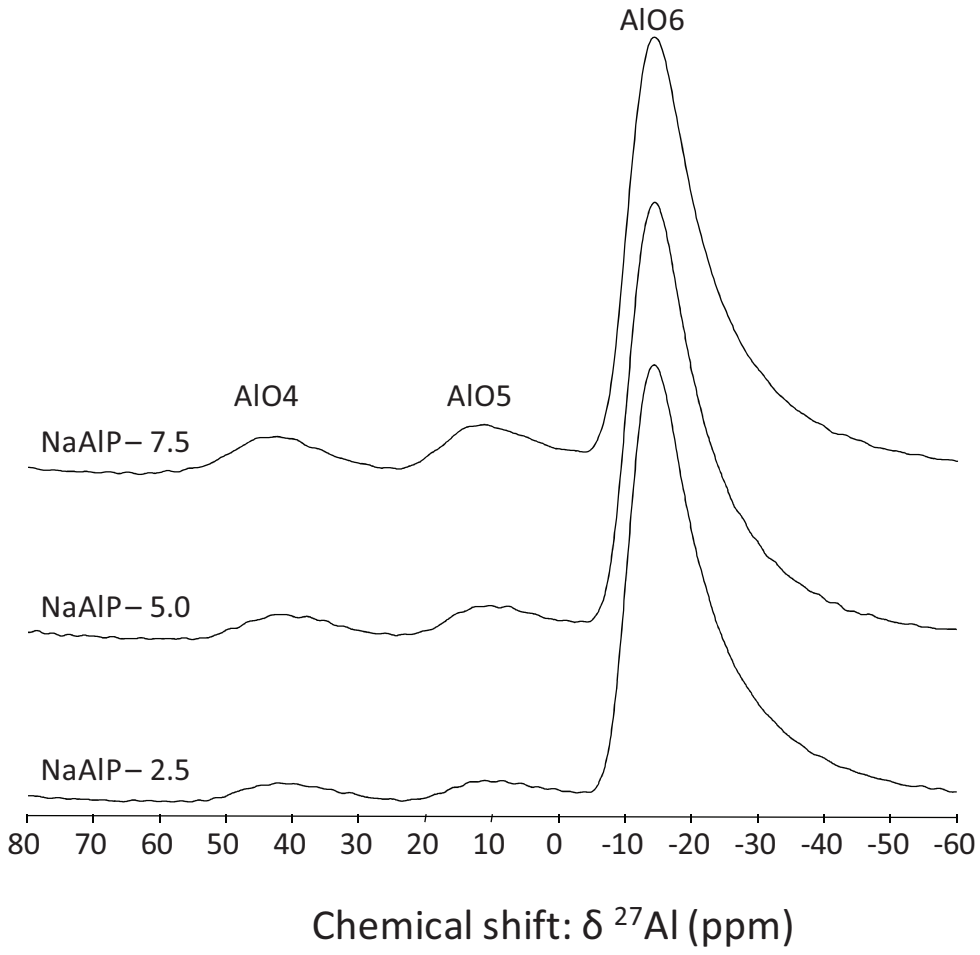

Fig. 5.3:
1D ^{27}Al NMR spectra of pristine glass samples of the NaAlP-x composition series (x=2.5 to 7.5). The spectra were recorded at a static field of 9.4 T, MAS spinning speed 10 kHz (rotor diameter 4.0 mm).

It is worthy to note that all ^{27}Al resonance lines are tailing towards high fields, a feature that is often observed in the spectra of quadrupolar nuclei in disordered solids. It results from the structural variations in the close environment of the probe nucleus. These variations, in turn, generate variations in the electric field gradient and thus in the observed quadrupolar parameters.

The Czjzek model (d'Espinoise de Lacaillerie2008) provides an analytical expression for the prediction of the lineshapes of quadrupolar nuclei in disordered solids. Hence, a more exact quantitative analysis of the corresponding spectra can be achieved by using the Czjzek model instead of the standard Gaussian model. Quantification of the different $Al(OP)_n$ species has been extracted from the MAS NMR analyses and is reported in *Fig. 5.4*. The latter figure shows that the proportions of AlO4 and AlO5 slightly increase at the expense of the AlO6 species when the global aluminium content increases in the glass formulation.

Tab. 5.2:
AlO4, AlO5 and AlO6 fractions obtained from deconvolution of the 1D ^{27}Al NMR spectra of the respective NaAlP-x glass systems. The Czjzek model has been employed for fitting. Errors are estimated to be +/- 2%.

x	AlO_4 fraction %	AlO_5 fraction %	AlO_6 fraction %
2.5	6	3	91
5.0	6	5	89
7.5	8	7	85

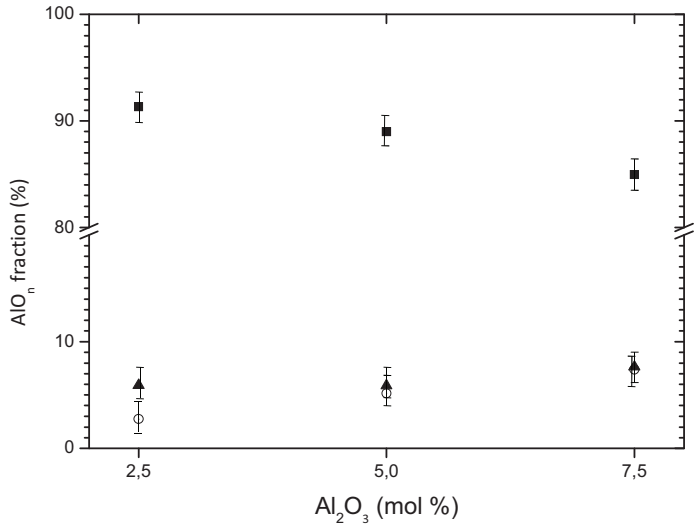

Fig. 5.4:
Evolution of the AlO_6 (black squares), AlO_5 (open circles) and the AlO_4 fractions (black triangles) with increasing Al_2O_3 content in the NaAlP glass network. The estimated error is of about 2% as indicated by error bars. Values are taken from Tab. 5.2.

The observed trend in ^{27}Al fraction evolution is consistent with published data (Brow1990, Lang2001, Wegner2008) for which AlO6 is found to be the major aluminum coordination state in low-Al_2O_3 content glasses. With increasing Al_2O_3 content the authors also observed an increase of aluminum in lower coordination, in particular close to the pyrophosphate composition ([O]/[P] = 3.5).

Brow (Brow1990) tried to explain this evolution around the pyrophosphate composition by the local charge compensation concept, assuming that the Al^{3+} coordination in phosphate glasses is governed by the need for local charge compensation at non-bridging oxygen (NBO) atoms. *Fig. 5.7* illustrates this model:

Near to the metaphosphate composition limit ([O]/[P] = 3.0) the glass structure is built up from long chains of PO_4 entities (Q^2). For each Q^2 species, the P-O bond involving a NBO (denoted as P-NBO) bears +1.5 valence units (VU) (corresponding to -0.5 VU at the NBO) and thus needs +0.5 VU to be perfectly compensated. Hence, AlO6 will dominate the glass structure, since, in six-fold coordination, each Al^{3+} provides +0.5 VU.

Near to the orthophosphate composition ([O]/[P] = 4.0), the dominating phosphate species are isolated phosphate tetrahedra, presenting 4 equivalent P-NBO bonds, bearing +1.25 VU ($5^+/4$) and thus requiring +0.75 VU at each NBO to be compensated. The required compensation is obtained by AlO4 tetrahedra, presenting +0.75 VU ($3^+/4$) at each corner. Between these two domains, the progressive evolution from AlO6 to AlO4 species occurs.

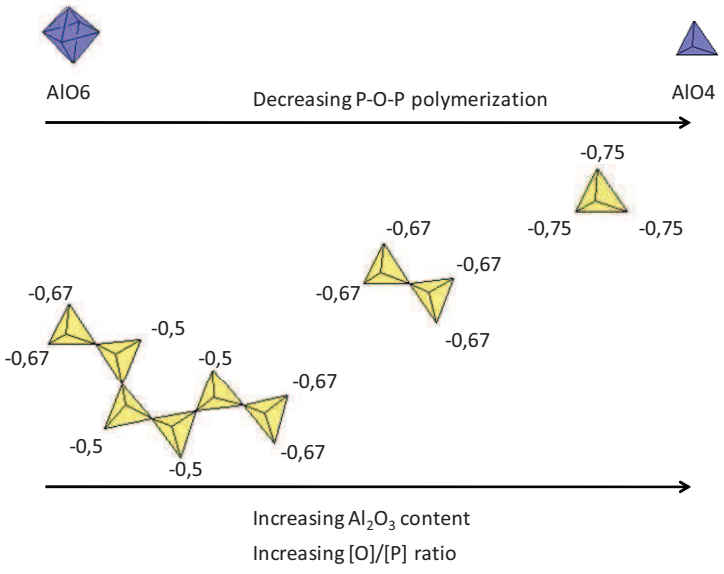

Fig. 5.5:
Illustration of the model of local charge compensation for aluminum phosphate glass networks. The overall [O]/[P] ratio determines the dominating phosphate anion species (poly-, pyro-, orthophosphate). This in turn determines the dominating negative valence units to be compensated locally at the non-bridging-oxygen atoms located at the interior and at the end of the phosphate chains. The higher the charge to be compensated, the lower the average coordination number of Al^{3+}.

This model is based on considerations of binary Al_2O_3-P_2O_5 glass systems. Therefore, it has to be treated with caution, since the present x Al_2O_3 – (100-x) $NaPO_3$ system contains large amounts of alkali that will change the compensation situation. However, the model of local charge compensation can be used as a starting point for discussion. In our case, it allows for explaining why the AlO6 is the major coordination state of aluminum in low-Al_2O_3 content glasses and why aluminum in lower coordination states increases with increases with increasing aluminum content.

5.1.2 1D ^{31}P NMR results

Fig. 5.6 depicts the isotropic window of 1D ^{31}P NMR spectra of NaAlP-x glass systems. The spectrum of pure sodium phosphate $NaPO_3$ (NaAlP-0) is dominated by a signal at about -20 ppm that has been assigned to Q^2 species, accompanied by weak resonances at about -7 ppm and at about +2 ppm showing the presence of Q^1_H and Q^1_{Na} sites (Chapter 4).

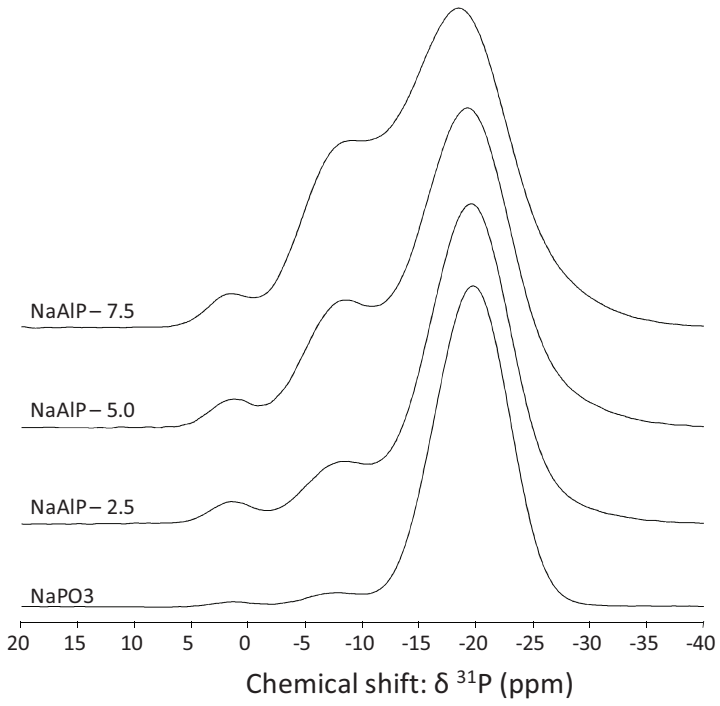

Fig. 5.6:
Center band 1D ^{31}P NMR spectra of pristine glass samples of the NaAlP-x composition series (x=0 to 7.5). The spectra were recorded at a static field of 9.4 T, MAS spinning speed 10 kHz (rotor diameter 4.0 mm).

The increase in aluminum content produces a significant development of a signal at -8 ppm as well as an increase of the signal at +2 ppm and a moderate decrease and a slight shift towards downfield of the signal at -20 ppm. The linear increase of the signal at -8 ppm with the increase Al_2O_3 content suggests that this site is associated to aluminum and thus precludes any association between this

signal and the Q^1_H resonance observed at about -7 ppm in $NaPO_3$ (NaAlP-0) glass. It is also worthy to note that the global Q^2 signal (at about -20 ppm in case of NaAlP-0) shifts towards more positive chemical shift values. This evolution could be due to progressive shortening of the phosphate chains (e.g., δ ^{31}P (ppm) of the middle unit in $Na_5P_3O_{10}$ is -8.9 ppm (MacKenzie2002)) but the observed increase of the signal linewidth and its maximum shift could also suggest an overlapping between the Q^2 resonance and another signal with a close chemical shift. The slight increase of the signal at +2 ppm indicates that the insertion of Al_2O_3 in the glass structure leads to a minor formation of Q^1 sites.

The broad resonance with its maximum at about -8 ppm has been interpreted by Brow and coworkers as a ^{31}P signal composed of phosphate tetrahedra connected towards aluminum, but without further indication of the number of connected phosphorous (n in the Q^n notation), the number of aluminium (m in the Q^n_m notation) or on the coordinated state of the connected aluminium (AlOx in the $Q^n_{m,AlOx}$ notation). Based on 1D ^{31}P chemical shift values, solely, further assignment to a particular $Q^n_{m,AlOx}$ species is complicated for several reasons :

(i) only a few $Q^n_{m,AlOx}$ crystalline references exist (Egan2000, MacKenzie2001) and thus only a few aluminophosphate environments can be characterized unambiguously on the basis of chemical shift values.

(ii) the addition of Al_2O_3 results in opposing, non-predictable effects (*Fig. 5.7*). On the one hand, depolymerization of the P-O-P network takes place with increasing [O]/[P] ratio (increasing Al_2O_3 content), leading to more deshielded chemical shift values. On the other hand, the presence of aluminate polyhedra linked to phosphate tetrahedra results in a shielding of the respective ^{31}P nuclei.

(iii) AlO4 linking leads to stronger shielding effects than AlO6 linking.

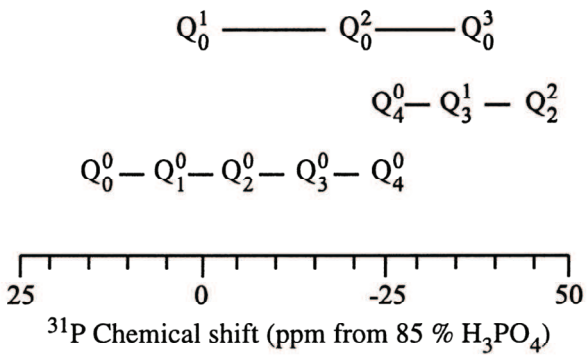

Fig. 5.7:
Schematic illustration of the overlapping chemical shift ranges for Q^n (Q^n_0) units and Q^n_m units in ternary Na_2O-Al_2O_3-P_2O_5 glass systems. From Egan et al. (from Egan2000).

To conclude, a very important variety of Q^n_m species can be generated by the insertion of aluminum in the phosphate matrix, leading to overlapping ^{31}P NMR signals whose positions cannot be predicted on a purely empirical basis (*Fig. 5.4, Fig. 5.5*). Thus, any assignment of 1D ^{31}P NMR spectra based on chemical shift references and empirical considerations (Brow1990, Brow1993) must be considered as tentative.

Previous studies reported in the literature have used 2D NMR techniques to obtain valuable information on the chemical nature of the mixed Q^n_m species that can be generated (Egan2000, Lang2001). Egan *et al.* (Egan2000) used a 2D ^{31}P-{^{27}Al} CP experiment to distinguish AlO4, AlO5 and AlO6 connectivity towards phosphorus in a x $NaAlO_2$ – (1-x) $NaPO_3$ glass series. Lang *et al.* (Lang2001) could reveal the presence of ^{31}P tetrahedra connected to ^{27}Al by ^{31}P-{^{27}Al} TRAPDOR. More recently, an advanced NMR protocol has been proposed in the literature (van Wüllen2007, Wegner2008) for the ternary system 50 K_2O - x Al_2O_3 - (50-x) P_2O_5. ^{31}P-{^{27}Al} CP HETCOR NMR was used to characterize ^{31}P-^{27}Al connectivity, ^{31}P-{^{27}Al} REAPDOR NMR and ^{27}Al-{^{31}P} REDOR to determine the number of ^{27}Al in proximity to ^{31}P and *vice versa*. Further, ^{31}P-J-RES NMR spectroscopy was helpful to determine ^{31}P polymerization. The outcome of these experiments was used to monitor the effects of increasing Al_2O_3 addition in the 50 K_2O – x Al_2O_3 – (50-x) P_2O_5 system. All the information extracted from the literature, including the ^{31}P MAS-NMR chemical shift values (Wegner2008) are summarized in *Fig. 5.8*.

In the following, this set of information shall be used to interpret the 2D NMR correlation spectrum, obtained with a more robust and efficient technique than CP-HETCOR, performed on the sample with nominal composition NaAlP-5.0 that we consider to be the most representative one of our system. This 2D correlation will help to better describe the mixed alumino-phosphate network of our glasses. Since the general feature of the ^{31}P NMR spectra is similar within the complete series (x= 2.5 to x = 7.5), we assume that the glass network structures of the other samples will be based on the same phosphate species that are present with different relative proportions.

	Exemplary site	Differentiated nomenclature	Chemical shift: δ ^{31}P (ppm)
Q^n		Q^0	---
		Q^1	0.5
		Q^2 (middle unit)	-17.9
	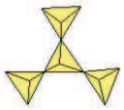	Q^3 (middle unit)	
Q^n_m Connectivity towards aluminum	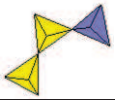	Q^1_{1AlO4}	-11.1
		Q^1_{2AlO4}	---
		Q^1_{3AlO4}	
	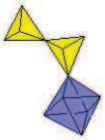	$Q^1_{1AlO5/6}$	-7.5
	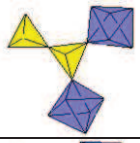	$Q^1_{2AlO5/6}$	-16.0
	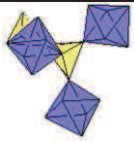	$Q^1_{3AlO5/6}$	---
	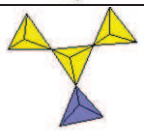	Q^2_{1AlO4}	---
	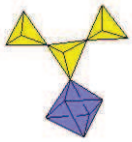	$Q^2_{1AlO5/6}$	---
	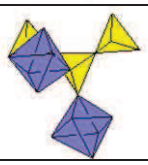	Q^2_{2AlO6}	[from -36.5 to -50.8]

Fig. 5.8:
The variety of Q^n and Q^n_m sites that may be present in pristine NaAlP-x glass systems.

5.1.3 2D correlation ^{27}Al-{^{31}P} D-HMQC

The NaAlP-5.0 glass structure has been investigated with the ^{27}Al-{^{31}P} D-HMQC technique which allows producing the through-space correlation spectrum reported in *Fig. 5.9a*. The 2D spectrum has been reported with the ^{27}Al and ^{31}P NMR spectra as direct and indirect projections, respectively. The 2D map exhibits an intense correlation signal between ^{31}P sites and AlO6. In addition, minor signal intensity corresponding to ^{31}P close to AlO5 and AlO4 can be observed. However, due to their very low intensity, the two latter contributions shall not be discussed in the following.

Fig. 5.9b shows the 1D NMR ^{31}P spectrum of NaAlP-5.0 (see *Fig. 5.6*) accompanied by the indirect slice of the 2D spectrum corresponding to the ^{31}P moieties close to AlO6 (*Fig. 5.9c*).

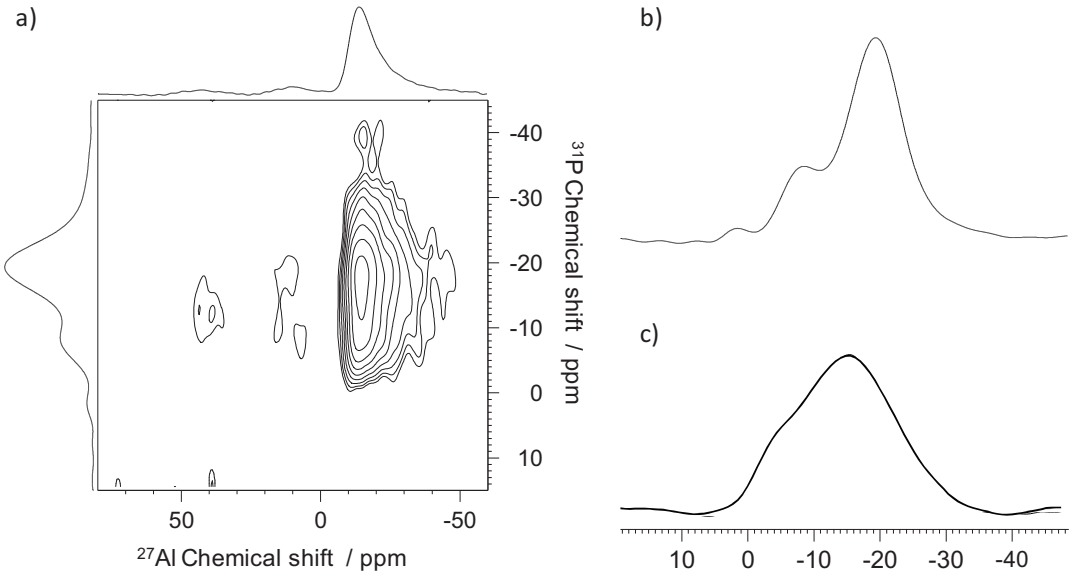

Fig. 5.9:
2D ^{27}Al-{^{31}P} D-HMQC spectrum of pristine NaAlP-5.0 glass (a) together with ^{27}Al and ^{31}P 1D NMR spectra as projections. Comparison between the 1D ^{31}P NMR spectrum (b) and the ^{31}P-AlO6 indirect slice (c) extracted from the 2D correlation spectrum.

The comparison between the 1D ^{31}P MAS-NMR acquisition and the ^{31}P-AlO_6 slice gives valuable information on the pristine glass structure:

i. The resonance observed at about +2 ppm in 1D ^{31}P NMR is of negligible intensity in the HMQC slice, corroborating our previous assignment to Q^1_0 entities.

ii. Different contributions between 0 and -30 ppm can be observed on the ^{31}P-AlO6 slice, indicating that the mixing between the phosphate and the aluminate moieties gives rise to different $Q^n_{m,AlO6}$ species. We confirm our first attribution of the signal at about -8 ppm to a ^{31}P connected to ^{27}Al and we determine that this site is connected to AlO6 moieties. Another contribution can also be observed at about -16 ppm, thus confirming our assumption concerning the possible overlapping between the Q^2 signal (-20 ppm) and another Q^n_m species that is unambiguously highlighted by our experiment.

iii. Signal intensity beyond - 30 ppm (ca. -32 ppm; *Tab. 5.3*) has been attributed to Q^3_0 entities, since this resonance is negligible in the AlO6 D-HMQC slice.

In order to go deeper in the structural determination, the ^{31}P-AlO6 slice has to be examined carefully. Additional information shall be provided by simulating this slice with the dmfit software (*Fig. 5.10*).

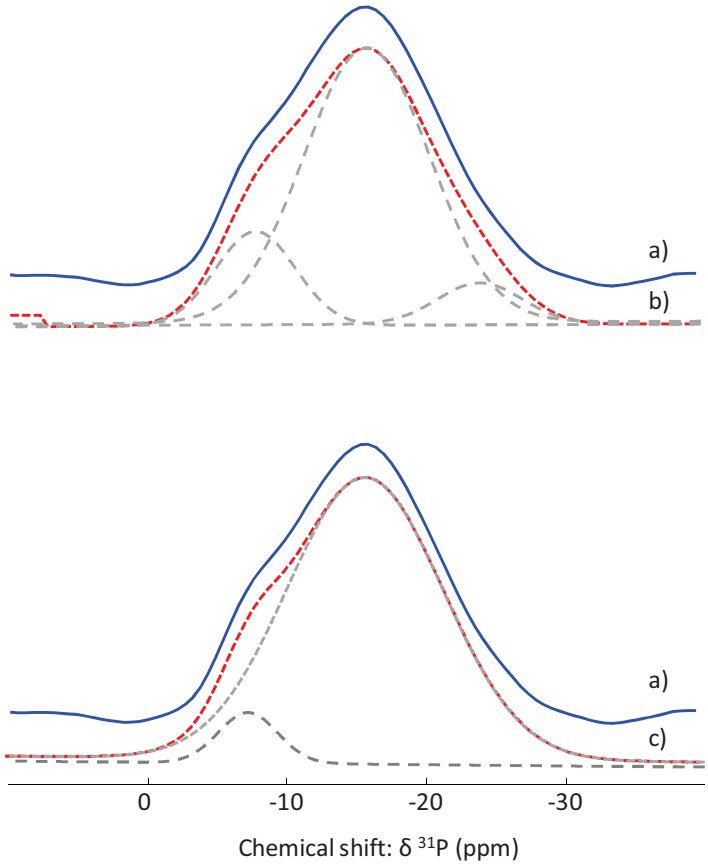

Fig. 5.10:
Multicomponent fitting (dmfit) of the ^{31}P-AlO6 D-HMQC slice. The experimental spectrum is shown on top of each fit Fig. 5.10 (a), the three- and two- components simulations are reported in Fig. 5b and 5c, respectively.

As reported in *Tab. 5.3a* and in *Fig. 5.10*, two and three components simulations correctly fit the experimental data. Nevertheless, we assumed that the three components model (*Fig. 5.10b*) is more suitable since

(i) it allows for simulating the slight shoulder noticed on the experimental spectrum at -24.0 ppm and

(ii) the FWHM of the second site in the two component model (*Fig. 5.10c*; FWHM: 12.5 ppm) is higher than the values reported in the literature for $Q^n_{m,AlOx}$ species. To conclude, we assumed, from the D-HMQC experiment, that the phosphate structure is composed by three phosphate species connected to AlO6 and three phosphate species surrounded by sodium ions, exclusively.

Tab. 5.3a:
Two and three components fit parameters of the AlO6 ^{27}A-l{^{31}P} D-HMQC slice. FWHM stands for full width at half maximum, 1,2 and 3 denote the sites. For full assignment see Tab. 5.3b; grey: two component model, white: three component model.

	1	2	3
δ ^{31}P	-7.2	-15.5	---
(ppm)	-7.6	-15.7	-24.0
FWHM	5.0	12.5	---
(ppm)	6.8	10.7	7.2

A more detailed insight of the Q^n_{mAlOx} species can now be extracted when our data are compared to previous work realized on the K_2O- Al_2O_3- P_2O_5 system. Indeed, the sites at -7.6 and -15.7 ppm can now be assigned to $Q^1_{1,AlO6}$ and $Q^1_{2,AlO6}$ moieties, respectively. Nevertheless, the signal at -24.0 ppm has not been reported previously and only assumptions can be made on its $Q^n_{m,AlOx}$ nature. According to its chemical shift values, $Q^2_{1,AlO6}$ or $Q^1_{3,AlO6}$ units are the most probable assignment for this particular signal, but we cannot conclude definitely about its chemical nature.

Fig. 5.11 shows the 1D ^{31}P NMR spectrum of pristine NaAlP-5.0 glass, accompanied by the simulation supported by the D-HMQC experiment presented above. The ^{31}P NMR envelope has been decomposed into six individual contributions (*Tab.5.3b*) by using the chemical shift and FWHM values deduced from the D-HMQC for the three ^{31}P-AlO6 sites and the chemical shift and FWHM values derived from previous studies on Na_2O-P_2O_5 binary system for the three sites only surrounded by sodium ions. Subsequently, the simulation has been performed by varying the relative intensity for each $Q^n/Q^n_{m,AlOx}$ species and by keeping all the other parameters as close as possible to the input data. The relative intensity of each species, obtained on the basis of this simulation procedure, are reported in *Tab. 5.3b*. They shall be used to describe the glass network.

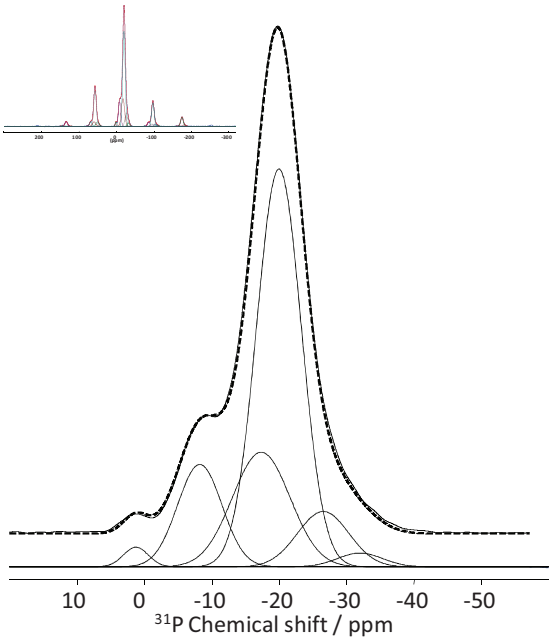

Fig. 5.11:
Deconvolution of the 1D ^{31}P NMR envelope of pristine NaAlP-5.0 glass. At the top of Fig. 5.11 the entire spectral window including the spinning sidebands is shown.

Tab. 5.3b:
Q^n and Q_{mAlO6} sites identified by 1D ^{31}P and D-HMQC NMR. FWHM stands for full width at half maximum, % indicates the relative intensity in %.

	1	2	3	4	5	6
δ ^{31}P (ppm)	+1.2	-8.3	-17.4	-20.0	-26.5	-32
FWHM (ppm)	4.4	7.7	10	7.8	9	7.8
%	1.5	12.0	15.5	60.5	7.5	3.0
Contribution from	Q^1_0	Q^1_{1AlO6}	Q^1_{2AlO6}	Q^2_0	Q^1_{3AlO6} (?)	Q^3_0

As expected, the phosphate network is mainly composed (60%) of Q^2_0 sites (like in the $NaPO_3$ structure) and octahedral alumina enters the network and forms Q^1_1 and Q^1_2 sites in similar proportions, showing the mixed character of the aluminophosphate network. In addition, a small amount of the site that could not be attributed on the basis of literature data (-24 ppm; Q^2_1 or Q^1_3) is also present. Even if these two species are expected to have close chemical shift values, their impact on the global ^{27}Al-^{31}P connectivity is very different, the Q^2_1 site being involved in a single P-O-Al bond, whereas the Q^1_3 site creates three P-O-Al linkages. This major difference has been exploited to assign the site at -24 ppm by using the following mathematical approach, focusing on the number of P-O-Al bonds required by the glass structure:

For the nominal composition NaAlP-5.0, the [Al]/[P] ratio is 10/95. Each Al^{3+} is surrounded by 6 P, requiring thus 60 P-O-Al bonds to complete its coordination. The simulation (*Tab. 5.3b*) indicates that 12% of the P is present as Q^1_1 species, 15.5% as Q^1_2 and 7.5% as Q^2_1 or Q^1_3. The contribution of Q^1_1 and Q^1_2 P species to the global P-O-Al linking is thus 40.85 P-O-Al [95*(12%*1+ 15.5%*2)]. In order to fully coordinated the $Al(OP)_6$ species, the third P-AlO6 site has to create 19.15 P-O-Al bonds [60-40.85]. Since this P site represents 7.125 P (7.5 % of 95 P), 1P has to be involved in 2.7 formal P-O-Al bonds, suggesting that the assignment of the signal at -24.0 ppm to a Q^2_1 site is unlikely. Therefore, we will assume that the Q^n_m site is the signature of a $Q^1_{3,AlO6}$ moieties, unless NaAlP-5.0 represents a series of low-Al_2O_3 content phosphate glasses.

5.1.4 Summary and discussion: pristine NaAlP-x glass

A structural model can finally be proposed at the light of the NMR investigations reported in this part. A schematic illustration that represents the different interconnections between phosphate and aluminate moieties (in case of NaAlP-5.0) is given in *Fig. 5.12*. The structures of the other glasses in the range of low-Al_2O_3 content will be qualitatively similar, but they will exhibit different relative proportions.

Our study has shown that the aluminum enters into the network by breaking phosphate chains and creating Q^1 sites with various numbers of connected AlO6 (1, 2 and 3). We did not highlight the presence of any Q^2 site connected to aluminum. We demonstrated that the presence of aluminum in the phosphate network reduces the phosphate chain length and reticulates the chains around octahedral AlO6 sites.

The insertion of Al_2O_3 also seems to disturb the Na^+ distribution since a few Q^3_0 and Q^1_0 entities have been observed in the glass structure. To conclude, it is worthy to note that the phosphate glass network can now be separated in two types:

(i) the residual Q^2 chains not connected to Al and

(ii) the end of chains connected to 1, 2 or 3 octahedral alumina,

the first type representing 60% of the global P network whereas the second type represents 35% (in the NaAlP-5.0 sample). In the second part of this chapter, the weathering mechanism will be investigated and we can expect different mechanisms for the two types of phosphorous.

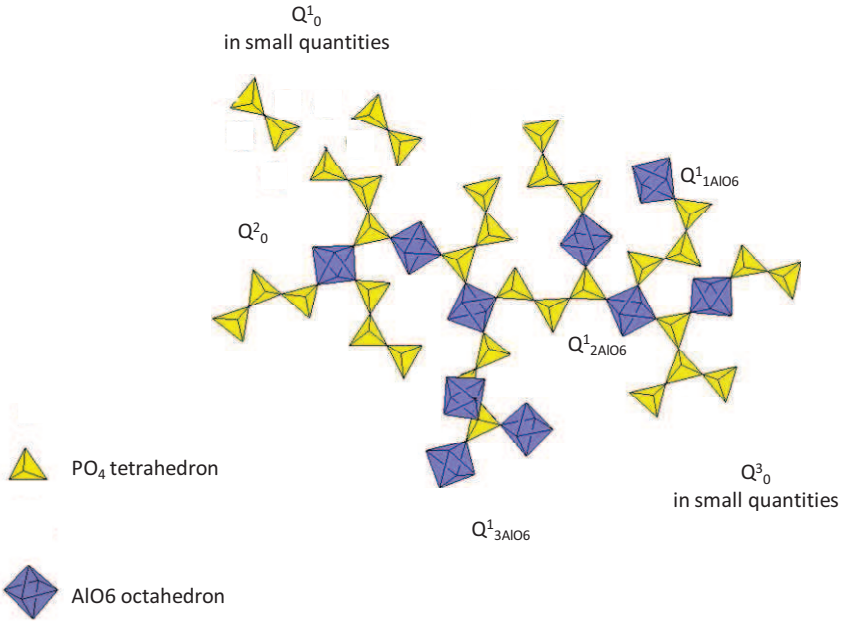

Fig. 5.12:
Schematic picture of the NaAlP-x glass structure. The schema is based on the structural investigation of glass with nominal composition NaAlP-5.0. Please note that only a restricted number of phosphate chains connected to AlO6 can be represented for reasons of clarity.

5.2 NaAlP-x glass weathering

In the following, the weathering mechanism of the aluminophosphate glass network has been monitored on the NaAlP-5.0 sample exposed to an atmosphere saturated by water vapor at 45°C (see Chapter 2.6 for details). 1D ^{1}H NMR provides direct information about the presence of protonated species whereas ^{31}P and ^{27}Al NMR monitor the evolution of the glass structure. Finally, heteronuclear correlation NMR techniques have been performed in order to provide additional information that allows for monitoring the weathering process of the aluminophosphate glass network and understanding the effect of P-O-Al bonds on the global durability.

5.2.1 1D ^{1}H NMR results

Fig. 5.13 depicts high resolution 1D ^{1}H NMR spectra of NaAlP-5.0 glass after 8 h, 16 h and 24 h of weathering. The spectra are accompanied by ^{1}H acquisitions performed on the pristine sample and on an empty rotor to characterize the ^{1}H signal background. A DEPTH sequence performed at very high field (18.8 T) and very high spinning frequency (60 kHz / 1.3 mm probe) has been employed to obtain well-resolved ^{1}H spectra.

Background signal (asterisk; *Fig. 5.13*), arising from probehead and rotor, can be observed between 0 and +2 ppm on all ^{1}H spectra. The clear presence of background signal, even after 24 h of weathering, suggests that the global amount of ^{1}H (and thus of water or hydroxyl groups) within the material structure does not attain very important values.

The ^{1}H spectrum of the pristine glass contains a weak signal (intensity lower than the background signal) centered at +4.8 ppm that highlights the presence of water adsorbed at the glass surface (Wenslow1998, Mercier1999, Alam2005). The intensity of the surface-adsorbed water resonance constantly increases with increasing weathering time. For prolonged intervals (> 8 h), the ^{1}H spectra also contain a large signal (between +10 and +17 ppm) in addition to the surface-adsorbed water peak (+4.8 ppm). Signal intensity in this region has been assigned to hydroxyl group -OH protons. In the case of weathered NaAlP-x glass, these hydroxyl groups could have been generated through P-O-P or P-O-Al depolymerization, giving rise to P-OH or Al-OH groups.

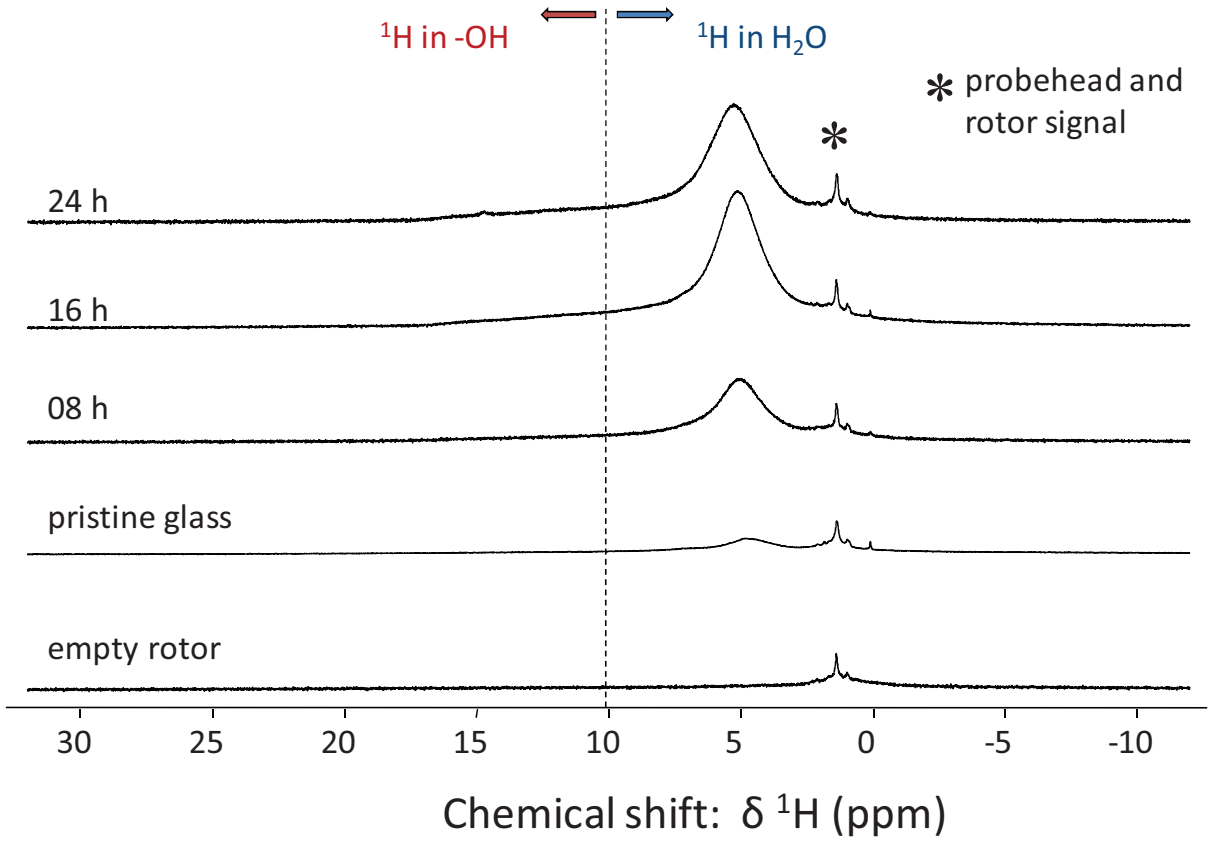

Fig. 5.13:
1D ^{1}H high resolution spectra of weathered NaAlP-5.0 glass. On top are the respective resonance regions for ^{1}H nuclei in surface-adsorbed water molecules (H_2O) and for hydroxyl groups (-OH) divided roughly (dashed plot) (Wenslow1998). The remaining probe / rotor background signal is marked by an asterisk. Left side of each spectrum: weathering time (hours).
The spectra were recorded at a static field of 18.8 T, employing the DEPTH sequence together with a MAS spinning speed of 62 kHz (rotor diameter 1.3 mm).

5.2.2 1D ^{27}Al NMR results

Fig. 5.14 depicts the isotropic window of the 1D ^{27}Al NMR spectra of NaAlP-5.0 glass samples after 4 h, 16 h and 24 h of weathering, accompanied by the acquisition performed on the pristine sample. The general feature of the spectra does not seem to be affected by the weathering. The three signals at +45 ppm, +13 ppm and -13 ppm previously reported and assigned to $Al(OP)_4$, $Al(OP)_5$ and $Al(OP)_6$ (Chapter 5.1) are still present. It appears thus that the 1D ^{27}Al MAS-NMR experiments reported here do not allow for highlighting new aluminate species that could have been formed during the weathering process. Nevertheless, a clear evolution can be observed concerning the relative proportions of the three signals. The spectra show an unambiguous increase of the octahedral species (-13 ppm) at the expense of the tetra- (+45 ppm) and pentahedral (+13 ppm) coordinated aluminum with increasing weathering time. The deconvolution using the Czjzek model is reported in *Tab. 5.4* and *Fig. 5.15* and clearly supports our observations.

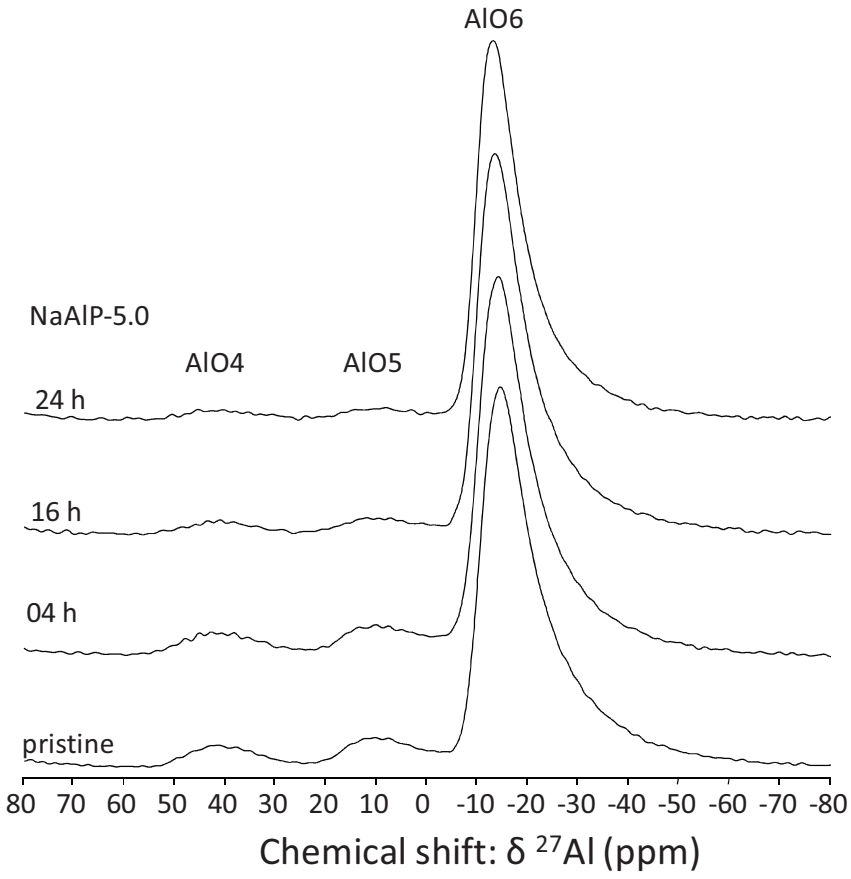

Fig. 5.14:
1D ^{27}Al spectra of pristine and weathered NaAlP-5.0 glass. The respective aluminum resonance regions are indicated on top, left side: weathering time (hours). The spectra were recorded at a static field of 9.4 T, MAS spinning speed 10 kHz (rotor diameter 4.0 mm).

Tab. 5.4:
AlO4, AlO5 and AlO6 fractions obtained from deconvolution of the ^{27}Al spectra of weathered NaAlP-5.0 glass (pristine glass, 4 h, 16 h and 24 h of weathering). The Czjzek model has been employed for fitting. Values of the pristine glass sample are taken from Tab. 5.2.

	AlO4 fraction %	AlO5 fraction %	AlO6 fraction %
pristine	6	5	89
04 h	7	6	88
16 h	4	3	93
24 h	2	2	94

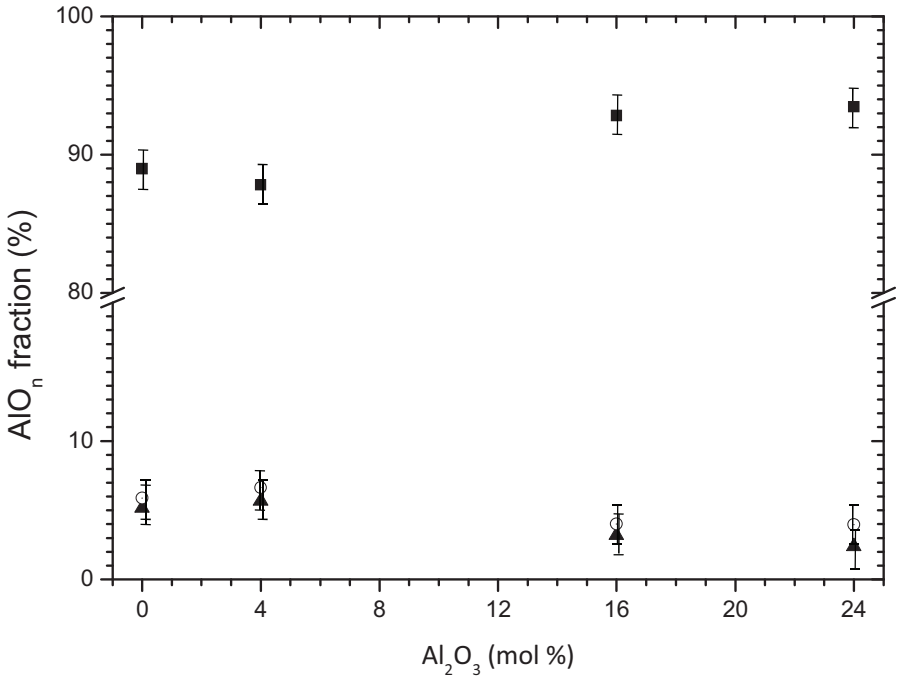

Fig. 5.15:
Evolution of the AlO6 (black squares), AlO4 fraction (black triangles) and of the AlO5 fraction (open circles) in NaAlP-5.0 glass with increasing weathering time. The estimated error is in the range of +/- 2 %. Values are taken from Tab. 5.4. Please note that values of the pristine glass reported in Tab. 5.4 are the same as in Tab. 5.2.

The 1D ^{27}Al NMR results show that weathering of the glass network induces an evolution of tetra- and pentahedrally coordinated aluminum towards the octahedral coordination state. We propose that the observed evolution originates from additional coordination of water or hydroxyl groups to tetra- and pentahedral species, as illustrated in *Fig. 5.16*. Thus, whereas AlO6 can be assigned to Al^{3+} coordinated to phosphate moieties, exclusively ($Al(OP)_6$), in the pristine glass, AlO6 resonances in the weathered glass can also arise from AlO6 species that are coordinated to one or two hydrated groups. In order to support or to reject this assumption, ^{27}Al-{^{1}H} correlation technique has been used on the NaAlP-5.0 sample weathered for 24 h. Among all correlation techniques, the ^{27}Al-{^{1}H} REDOR (Rotational Echo Double Resonance) (Chapter 2.3.5) has been employed because of its efficiency and its quantitative character. In order to monitor the effect of weathering attack on the chemical environment of AlO6, the REDOR technique has also been performed on the pristine sample.

Fig. 5.16 shows the ^{27}Al-{^{1}H} REDOR curves obtained for the pristine NaAlP-5.0 glass (black squares) and for the sample weathered for 24 h (white dots). The pristine sample is characterized by a very weak REDOR curve, showing only minor dipolar interaction between AlO6 and hydrated groups (H_2O, -OH). The experiment performed on the sample weathered for 24 hours produces a curve that shows a significant REDOR effect, indicating that hydrated groups are present in the vicinity of octahedral aluminum, thus supporting our previous assumption (*Fig. 5.16*).

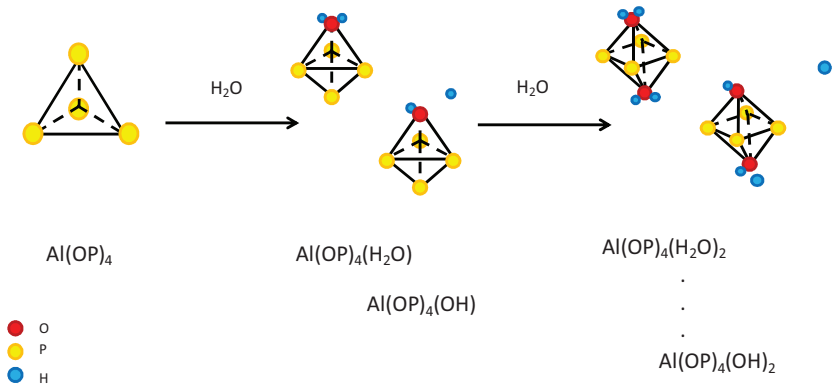

Fig. 5.16:
Generation of AlO6 octahedra in the course of NaAlP-5.0 glass weathering in humid atmosphere. The process is illustrated for proton coordination at Al(OP)$_4$ units exemplarily.

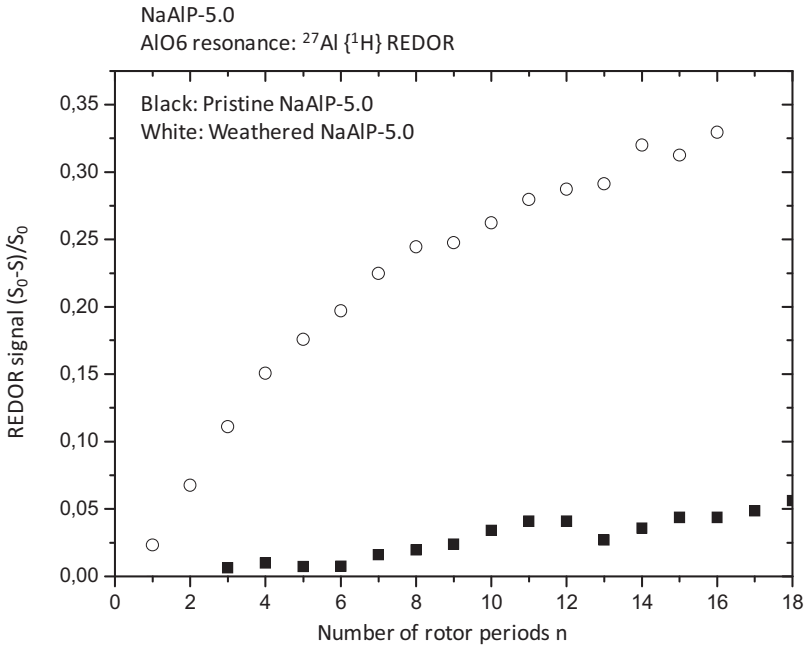

Fig. 5.17: ^{27}Al-{^{1}H} REDOR curves for pristine (black squares) and weathered NaAlP-5.0 glass (24 h, white circles). Observed nucleus: ^{27}Al with offset (parameter O1) on the AlO6 resonance. The spectra were recorded at a static field of 9.4 T, MAS spinning speed 10 kHz (rotor diameter 4.0 mm).

5.2.3 1D ^{31}P NMR results

Fig. 5.18 depicts the isotropic window of the 1D ^{31}P NMR spectra performed on the NaAlP-5.0 sample after 4 h, 16 h and 24 h of weathering, accompanied by the 1D ^{31}P NMR spectrum of the pristine sample.

The ^{31}P NMR acquisitions do not seem to be affected dramatically by the weathering attack, since the general spectrum feature appears to be constant during the hydration process. The only differences that can be highlighted concern:

(i) the decrease of the signal attributed to the Q^3_0 site at -30 ppm,

(ii) the slight increase of the signal attributed to the Q^1_0 site (3 ppm),

(iii) a more pronounced hollow between the regions at -8 and -20 ppm, probably resulting from different relative proportions within these regions.

It is worthy to note that the observed spectral evolution is related to the phosphate sites not connected to aluminum. In agreement with the results reported in Chapter 4, this suggests that these sites are attacked by water and give rise to P-OH group signals, whereas the P-AlO6 signals do not seem to change, indicating that the P-O-Al bonds are not affected by hydration. In the following, correlation NMR will be used to support these assumptions: the ^{27}Al-{^{31}P} REDOR technique shall be employed to monitor the evolution of the P-O-Al bonds and the ^{31}P-{^{1}H} CP MAS experiment will highlight the protonated species formed by the hydration process.

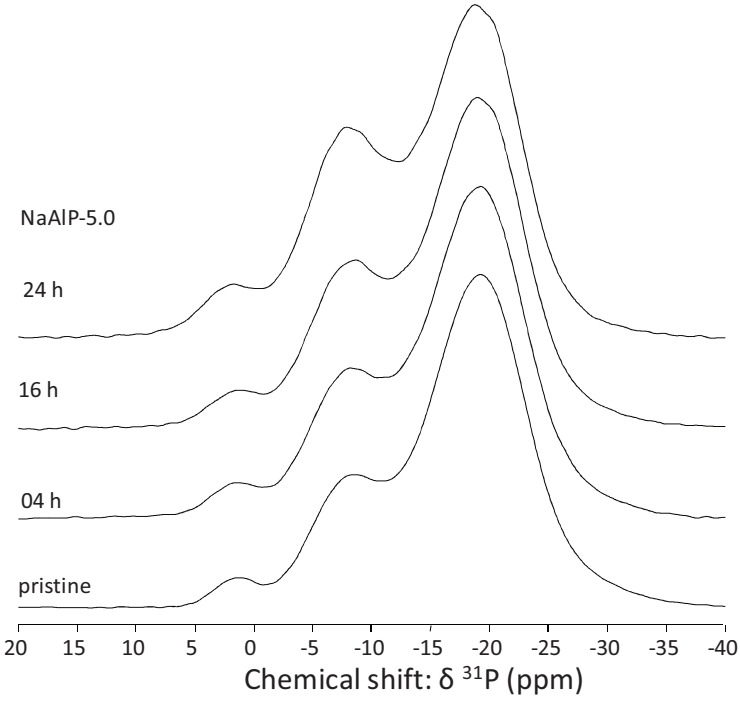

Fig. 5.18:
1D ^{31}P spectra of pristine and weathered NaAlP-5.0 glass. Left side: weathering time (hours). The spectra were recorded at a static field of 9.4 T, MAS spinning speed 10 kHz (rotor diameter 4.0 mm).

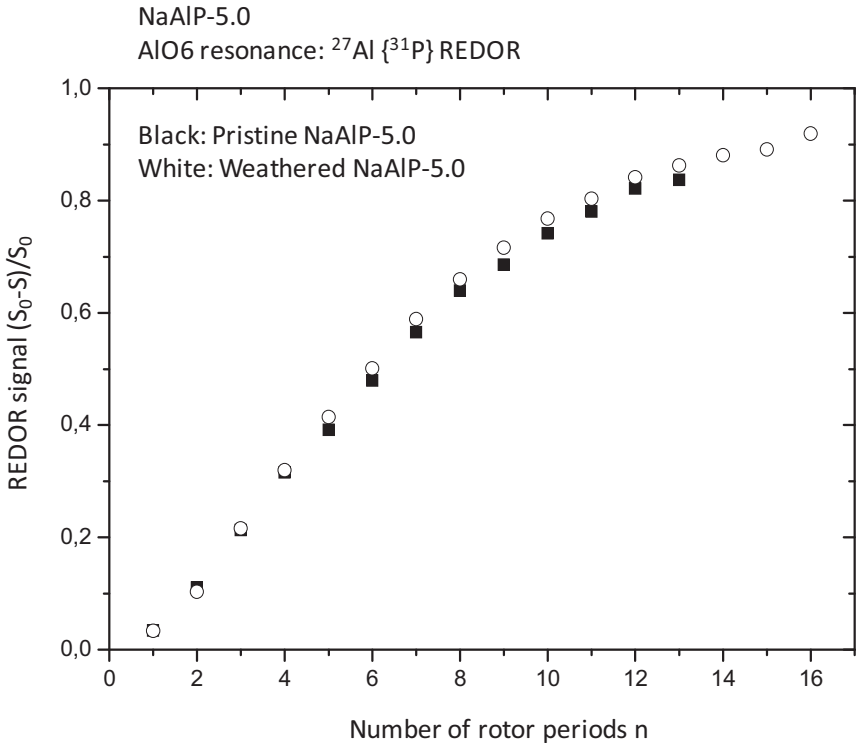

Fig. 5.19:
^{27}Al-{^{31}P} REDOR curves for pristine (black squares) and weathered NaAlP-5.0 glass (24 h, white circles). Observed nucleus: ^{27}Al with offset (parameter O1) on the AlO6 resonance. The spectra were recorded at a static field of 9.4 T, MAS spinning speed 10 kHz (rotor diameter 4.0 mm).

The stability of the P-O-Al bonds (and thus of the aluminophosphate network) against weathering attack has been monitored by the ^{27}Al-{^{31}P} REDOR experiment. Indeed, if the hydration induces P-O-Al bond cleavage, the number of P connected to AlO6 and thus the global ^{27}Al-^{31}P dipolar interaction should decrease. This decrease could be highlighted by comparing the REDOR curves of the pristine and the weathered samples, the REDOR curve exhibiting a lower slope than the pristine sample. These two curves are reported in *Fig. 5.19*. The similarity between the two curves clearly indicates that the ^{27}Al-^{31}P dipolar interaction is not significantly affected by the weathering. Hence, we conclude that the P-O-Al bonds are not broken by water during the observed weathering time interval.

The ^{31}P-{^{1}H} CP experiment has been used to highlight the presence of P-OH generated by hydrolytic attack of P-O-P bonds by water vapor. The respective CP spectrum is reported in *Fig. 5.20* and displays two main sites at +3 ppm and -7 ppm. Based on previous studies (see Chapter 4), the first peak has been attributed to Q^0_H and the second site can be assigned to Q^1_H species. These two moieties are the signature of the P-O-P bond cleavage and P-OH formation, occurring when water reacts with the phosphate network. The appearance of the Q^0_H signal also explains the global increase of the intensity of the signal at about +3 ppm in the spectrum.

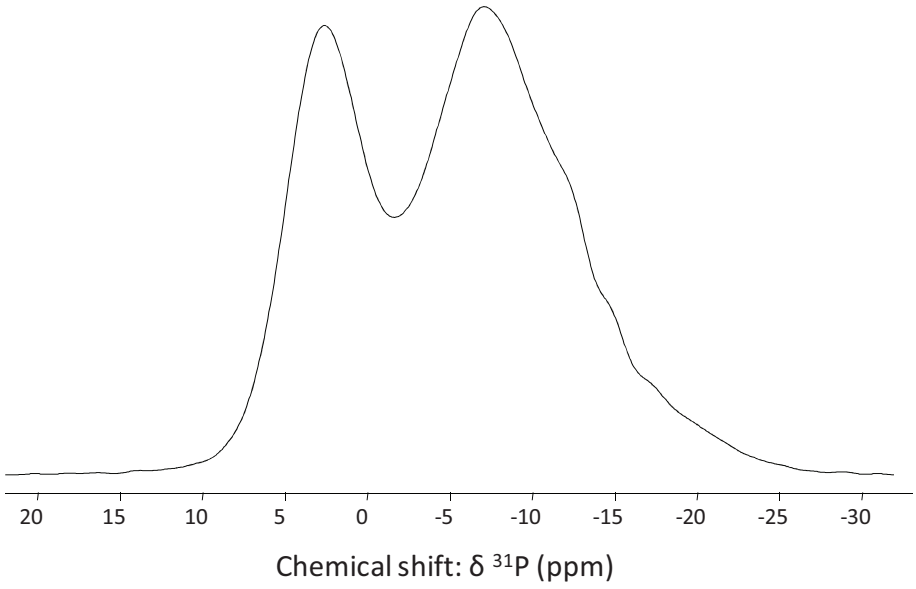

Fig. 5.20:
^{31}P-{^{1}H} CP MAS NMR spectrum of NaAlP-5.0 glass weathered for 24 h.

Based on all these results, a simulation of the 1D ^{31}P NMR envelope of the NaAlP-5.0 glass sample weathered for 24 hours has been carried out. It is reported in *Fig. 5.21*. The simulation has been done with 7 components: the Q^1_0 and Q^2_0 sites previously determined on the non hydrated sample, the Q^1_1, Q^1_2 and Q^1_3 sites connected to AlO6 previously determined on the pristine NaAlP-5.0 glass. Additionally, the two components of Q^1_H and Q^0_H components, determined from the ^{31}P-{^{1}H} CP MAS experiment have been added. Then, only the relative intensity of each species has been optimized and all the other parameters have been kept as close as possible to the input data previously determined from D-HMQC correlation NMR. The relative proportions are reported in *Tab. 5.5*.

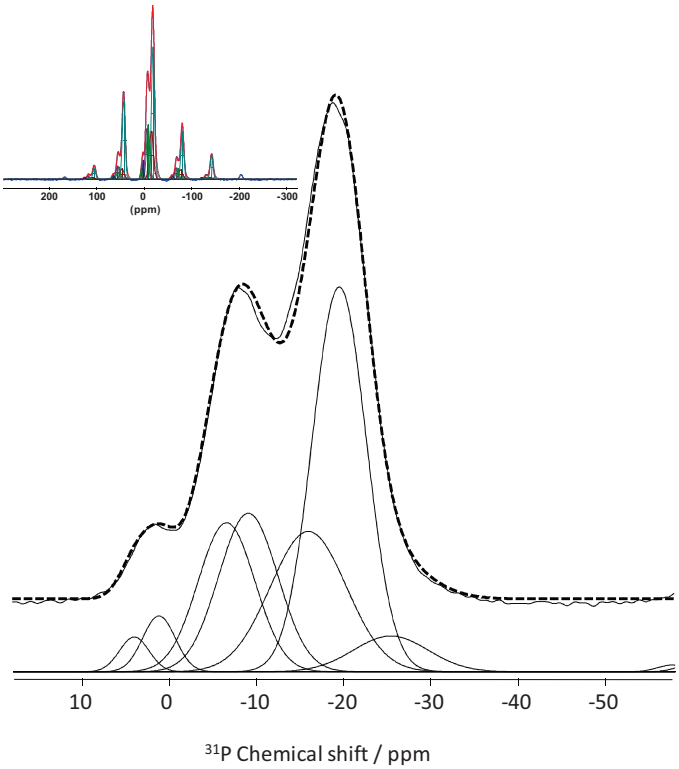

Fig. 5.21 :
Deconvolution of the 1D ^{31}P NMR envelope of weathered NaAlP-5.0 glass. At the top of Fig. 5.21 the entire spectral window including the spinning sidebands is shown. For further details see Tab. 5.5.

Tab. 5.5:
^{31}P species in weathered NaAlP-5.0 glass, % indicates the relative intensity in %. Quantification based on deconvolution of the spectrum of pristine glass (Tab. 5.3) and 1D ^{31}P-{^{1}H} CP MAS NMR. Please note that Q^1_0 and Q^1_H are represented by one site in the deconvolution.

Contribution from	Q^1_0	Q^2_0	Q^1_{1AlO6}	Q^1_{2AlO6}	Q^1_{3AlO6}	Q^0_H $Q^0_{m,H}$	Q^1_H $Q^1_{m,H}$
δ ^{31}P (ppm)	+1.2	-20.0	-8.3	-17.4	-26.5	+1.2	-8.5
FWHM (ppm)	4.4	7.8	7.7	10.0	9.0	4.4	8.0
% weathered	1.5	46.5	13.5	16.5	4.5	3.0	14.5
% in pristine	1.5	60.5	12.0	15.5	7.5	---	---

From the values of the *Tab. 5.5* one can determine that:

(i) the Q^2_0 intensity decreases, thus confirming that this site has been attacked to produce the Q^1_H observed in the spectrum at -8 ppm,

(ii) the P-AlO6 moieties intensities are more or less constant, confirming again their stability against water attack.

5.2.4 Summary and discussion on NaAlP-x glass weathering

From the complete set of NMR results reported here, we propose that the weathering of the aluminophosphate glass network principally occurs from the phosphate sites that are not connected to aluminum. Indeed, we could show that only the Q^2_0 and the Q^1_0 sites present in the glass structure are attacked by water during the weathering time, producing protonated species (Q^1_H, Q^0_H) through P-O-P bond cleavage. From the ^{27}Al-{^{31}P} REDOR experiment, we could also show that the P-O-Al bonds are not affected by water and that they are not destroyed by weathering attack. Connectivity with aluminum appears to protect the phosphate species from hydrolysis and hence to increase the chemical durability of the material.

Based on this conclusion, it appears that a very durable aluminophosphate glass composition should contain a maximum amount of P-O-Al bonds and a minimum amount of Q^2_0 and Q^1_0, the latter being easily attacked by water. Therefore, the continuous increase of the chemical durability with Al_2O_3 addition can be understood. Indeed, higher amounts of aluminum will induce more P-O-Al mixing at the expense of pure sodium phosphate moieties that will lead to a better global chemical durability. When all phosphate moieties are connected to aluminum, we can expect a constant chemical durability.

The conclusions reported here also support the formulation of the very durable phosphate glasses proposed by Day et al. (Day1998) for the immobilization of special radioactive wastes. These glass formulations are based on a binary iron phosphate 40 Fe_2O_3-60 P_2O_5 (Karabulut2003) producing a glass with a pyrophosphate structure ([O]/[P]=3.5) in which all the phosphate moieties are connected to at least one iron ion. Therefore, this composition does not contain any Q^2_0 moieties, easily being attacked by water and 100% of the phosphate entities are protected against hydrolytic attack since they are all connected to iron polyhedra.

5.3 Summary and Conclusion Chapter 5

In the present chapter, we have proposed a mechanism to explain the increase of the chemical durability produced by the addition of Al_2O_3 in the (100-x) $NaPO_3$-x Al_2O_3 glass formulation. Although this effect has been known for a long time, no structural study highlighting the impact of P-O-Al bonds on the global resistance of the glass against water has been reported, to our knowledge, so far.

In a **first step**, we have characterized the structure of glasses in the (100-x) $NaPO_3$-x Al_2O_3 system by using correlation NMR techniques. We have shown that the structure of the glass is built up from two types of phosphate moieties:

(i) P connected to AlO6 and thus involved in P-O-Al linkings and

(ii) P only surrounded by sodium and thus involved in P-O-P bonds, exclusively.

Further, we determined that the glass structure contains three type of P-AlO6 sites that differ by the number of connected aluminium (1,2 or 3), denoted as Q^1_1, Q^1_2 and Q^1_3, respectively.

In a **second step**, we could reveal that these two types of P exhibit opposite weathering behavior:

(i) the P-O-Al bonds do not suffer from hydration, as clearly indicated by the ^{27}Al-{^{31}P} REDOR experiment. Thus, their presence can be directly related to the improvement of the chemical durability.

(ii) the P-O-P bonds adopt the same behavior than in the $NaPO_3$ system (Chap. 4) and are thus easily attacked by water, producing protonated Q^1_H and Q^0_H sites as highlighted by the ^{31}P-{^{1}H} CP experiment.

At the light of our results, we finally propose that the chemical durability of the low-Al_2O_3 content aluminophosphate glass network has to be related to the amount of P-O-Al bonds inside the glass matrix: the higher the amount of P-O-Al, the better the chemical durability.

Of course, these conclusions would need **additional information** to be definitively confirmed. This information could come from various experiments:

(i) 2D ^{27}Al-{^{1}H} D-HMQC experiments would determine if aluminium is coordinated by H_2O or -OH groups.

(ii) ^{27}Al-{^{31}P} D-HMQC experiments performed on weathered samples would confirm their perfect stability under hydration.

(iii) Finally, new insights could come from ^{17}O NMR since this nuclei appears to be the perfect probe for the investigation of the weathering process. Some tests on the ^{17}O enrichment of aluminum phosphate glasses (that melt at higher temperature than pure sodium phosphate systems) have been realized in order to investigate the feasibility of this study.

Bibliography Chapter 5

Alam2005
Alam, T.M., Tischendorf, B.C., Brow, R.K.
Solid State Nuclear Magnetic Resonance (2005) 27 (1-2) 99-111

Amoureux2009
Amoureux, J.P, Trébosc, J., Delevoye, L., Lafon, O., Hu, B., Wang, Q.
Solid State Nuclear Magnetic Resonance (2009) **35 (1)**, 12-18

Brow1990
Brow, R.M., Kirkpatrick, R.J., Turner, G.L.
Journal of the American Ceramic Society (1990) **73 (8)**, 2293-2300

Brow1993
Brow, R.K.
Journal of the American Ceramic Society (1993) **76 (4)**, 913-918

Day1998
Day, D.E., Wu, Z., Hrma, P.
Journal of Non-Crystalline Solids (1998) **241**, 1

Egan2000
Egan, J.M., Wenslow, R.M., Mueller, K.T.
Journal of Non-Crystalline Solids (2000) **261 (1)**, 115-126

d'Espinose de Lacaillerie2008
d'Espinose de Lacaillerie, J.-B., Fretigny, C., Massiot, D.
Journal of Magnetic Resonance (2008) **192 (2)**, 244-251

Hosono1992
Hosono, H. Yoshihiro, A., Deguchi, K.
Journal of Non-Crystalline Solids (1992) **142**, 103

Karabulut2003
Karabulut, M., Metwalli, E., Day, D.E., Brow, R.K.
Journal of Non-Crystalline Solids (2003) **238**, 199-206

Lang2001
Land, D.P., Alam, T.M., Bencoe, D.
Chemistry of Materials (2001) **13**, 420-428

MacKenzie2002
MacKenzie, K.J.D., Smith, M.E.
Multinuclear Solid-State NMR of Inorganic Materials, Pergamon Materials Series Vol. 6
Elsevier Science (2002)

Mercier1999
Mercier,C., Montagne, L., Kostoj, V., Sfihi, H., Palavit, G.
Journal of Non-Crystalline Solids (1999) **256**, 124-129

Tischendorf2004
Tischendorf, B.C., Brow, R.K.
XX. International Congress on Glass, October 2004, Kyoto, Japan

Tricot2004
Tricot, G., Montagne, L., Delevoye, L., Palavit, G., Kostoj, V.
Journal of Non-Crystalline Solids (2004) **345-346**, 56-60

van Wüllen2007
van Wüllen, L., Tricot, G., Wegner, S.
Solid State Nuclear Magnetic Resonance **(2007) 32 (2)**, 44-52

Wegner2008
Wegner, S., van Wüllen , L., Tricot, G.
Journal of Non-Crystalline Solids (2008) **354 (15-16)**, 1703-1714

Wenslow1998
Wenslow, R.M., Mueller, K.T.
Journal of Physical Chemistry B (1998) **102 (45)**, 9033-9038

Xue2009
Xue, X., Kanzaki, M.
Journal of the American Ceramic Society (2009) **92 (12)** 2803-2830

General Conclusion

The present thesis has been dedicated to structural and mechanistic studies on the *weathering* of binary and ternary model phosphate glasses. Solid-state nuclear magnetic resonance has been employed as the major tool to investigate mechanistic details and structural changes that occur throughout weathering.

In the first part of this work, we have successfully validated a combined methodological approach for the study of phosphate glass weathering by ^{17}O NMR.

We have elaborated a reproducible synthesis route to obtain small amounts of two phase-pure ^{17}O-enriched crystalline hydrogen phosphates, NaH_2PO_4 and $Na_2H_2P_2O_7$, and collected the respective ^{17}O 2D 3QMAS data. In parallel, ^{17}O NMR parameters of both phases have been calculated by employing the GIPAW formalism and the corresponding ^{17}O 2D 3QMAS NMR spectra have been simulated. We could show that simulation results and experimental data stand in excellent agreement, thus validating the DFT / GIPAW calculation protocol for *hydrogen* phosphate phases. This gave us confidence to avoid costly and time demanding enrichment procedures and to investigate ^{17}O NMR data of two hydrated hydrogen orthophosphate phases, $NaH_2PO_4*H_2O$ and $NaH_2PO_4*2H_2O$, based on calculated / simulated ^{17}O NMR data, solely.

Further, we could draw systematic relationships between the NMR parameters of ^{17}O (shielding; quadrupolar) and the structural environment of the nucleus. We could show that 2D maps allow for a classification of ^{17}O environments from visual inspection of 2D 3QMAS data. This enabled us to characterize oxygen environments that are generated upon weathering of Na_2O-P_2O_5 ($NaPO_3$) phosphate glass.

Finally, we could simulate 2D ^{17}O 3QMAS NMR data of crystalline phase mixtures. This allowed for determination of the relative proportions of phases present in weathering snapshots of $NaPO_3$. Hence, the combined calculation-NMR approach allows for quantification of MQMAS NMR data of ^{17}O.

In the future, simulation of ^{17}O NMR data based on a DFT / GIPAW calculation approach may replace the costly synthesis of pure ^{17}O-enriched crystalline reference phases in our group. This may open the way towards a wide range of reference data that allows for further examination of relationships between NMR parameters of ^{17}O and its structural environment.

As an example, the present work focuses on the study of sodium and sodium hydrogen phosphate phases. With regard to the investigation of more complex ternary glass systems, we propose the investigation of sodium aluminum phosphates and sodium aluminum hydrogen phosphates. This is coherent with our fundamental interest in the understanding of the behavior of sodium aluminum phosphate glass systems for the storage of nuclear waste.

The second part of this thesis is dedicated to phosphate glass weathering studies of two model glass systems: $NaPO_3$ and (100-x) $NaPO_3$ * x Al_2O_3. With regard to the possible implementation of $H_2{}^{17}O$, we have carefully elaborated reproducible weathering conditions that employ very small amounts of water vapor.

For $NaPO_3$ we have worked out a qualitative model of phosphate glass weathering that is coherent with the one that is generally accepted.

We showed that weathering starts with an initiation phase where mainly phosphate chains are hydrated and the surface is saturated with water vapor (^{1}H NMR). Within the initiation phase, we found indications for commencing hydrolysis of the phosphate glass network (^{31}P NMR). At the end of this initiation phase, where the surface saturation with water molecules reaches its maximum, acceleration of the hydrolysis rate has been observed. Weathering of the phosphate glass leads to crystallization of the glass surface. After prolonged weathering times, it is mainly composed of orthophosphate phases.

We emphasize that phosphate glass corrosion studies in solution also lead systematically to crystalline hydrogen orthophosphate phases or *hydrated* crystalline hydrogen orthophosphate phases (Clément1999) after prolonged weathering times.

Further, we employed a quantitative and a polynomial fit analysis of 1D ^{31}P NMR data in order to work out whether preferred sites of attack on phosphate chains exist. Therefore, we based on the two model scenarios of aqueous attack that have been proposed by Wenslow and Mueller (Wenslow1998). Our analysis pointed towards a multitude of concealed processes that are running in parallel to the two model scenarios of initial attack at the interior or at the ends of the phosphate chains. Based on our polynomial analysis, we could show that the slight preference that we have found for attack of Q^2-Q^1 bonds may be misleading.

By employing $H_2{}^{17}O$ as a selective marker for the oxygen environments emerging upon water vapor attack on $NaPO_3$ glass, we were able to reveal one of the concealed processes: recondensation of phosphate units during weathering.

We emphasize that this phenomenon has never been reported for phosphate glass corrosion in solution or under weathering conditions, so far. Nevertheless, at these weathering temperatures (80°C), condensation of orthophosphate units is expected to occur (Ghule2001). For silicate systems, recondensation is discussed controversely.

Further, based on $H_2{}^{17}O$ vapor as a selective marker, we could describe the structural features of the oxygen environments that are emerging during the incorporation of water into the $NaPO_3$ glass structure under *weathering* conditions. Therefore, a visual inspection of the ^{17}O 2D 3QMAS NMR data and comparison with NMR-structure correlation maps (Chapter2) proved to be sufficient.

Masui et al. conducted a similar study on the weathering of Na_2O-3 SiO_2 glass (Masui2002). The authors employed ^{23}Na as a probe nucleus. The aim was to deduce the structural environment of ^{23}Na based on its NMR parameters. We believe that ^{17}O can provide information in greater detail, since it is directly involved in the process of water incorporation and it shows a larger variety of shielding and quadrupolar parameters. Therefore, we propose a combined ^{1}H and ^{17}O NMR study to elucidate the mechanism of water incorporation.

In an opening chapter, we extended our view on the structural study and the weathering of a ternary model glass system: (100-x)-x Al_2O_3 [NaAlP].

Based on 1D ^{31}P and ^{27}Al and data we could draw qualitative trends for the pristine glass structure with increasing Al_2O_3 content. Those trends are consistent with those found by Brow (Brow1993).

For the weathering network, we have found qualitative trends in ^{31}P NMR that we can assign tentatively to an increase of Q^1_H sites (^{1}H-^{31}P CP). Based on the outcomes of our studies on $NaPO_3$ weathering, we concluded that hydrolytic depolymerization of the P-O-P network occurs, when NaAlP glasses are exposed to weathering conditions.

Further, we have observed a systematic increase in the average aluminum coordination number upon weathering. ^{27}Al-^{31}P and ^{27}Al-^{1}H REDOR enabled us to conclude that this coordination number increase is possibly due to additional proton coordination on AlO4 and AlO5 sites throughout the weathering process.

We emphasize that an advanced NMR protocol is needed to identify all ^{31}P sites and all types of connectivity that are present in the ternary glass structure. Therefore, we propose the implementation of 2D homo- and heteronuclear correlation techniques.

With regard to future studies, we propose to use $H_2{}^{17}O$ as a selective marker. Notably, this would allow following the incorporation of water into the glass network. This, in turn, could elucidate the question whether H_2O molecules or –OH groups are possibly coordinated to aluminum throughout weathering. A combined calculation – NMR approach as it has been successfully validated and applicated for $NaPO_3$ is imaginable.